EVAPORATION OF WATER AS RELATED TO WIND BARRIERS

Completion Report
OWRR PROJECT NO. B-015 COLO

by

S. B. Verma

and

J. E. Cermak

Fluid Dynamics and Diffusion Laboratory
College of Engineering
Colorado State University

Submitted to

Office of Water Resources Research
U.S. Department of the Interior
Washington, D.C. 20240

June 30, 1971

The work upon which this report is based was supported in part by funds provided by the United States Department of the Interior, Office of Water Resources Research, as authorized under the Water Resources Research Act of 1964, Public Law 88-379, Agreement Number 14-01-0001-1436 (July 1, 1967 to June 30, 1971).

Environmental Resources Center
Colorado State University
Fort Collins, Colorado

Norman A. Evans, Director

U18401 0576176

CER 71-72SBV-JEC11

ABSTRACT

EVAPORATION OF WATER AS RELATED TO WIND BARRIERS

Local evaporation rates were measured from strips of saturated surfaces imbedded in wavy surfaces. Mean water vapor concentrations and mean velocity distributions were also measured over the wavy boundary. In the region far downstream of the leading wave, where the equilibrium boundary layer conditions were achieved, the average mass transfer coefficient was found to be a simple power function of the surface Reynolds number. Based on this result, the mass transfer data from this study correlated well with the mass transfer data from surfaces of various other geometries, e.g., evaporation data from water waves, evaporation data from flat plate and sublimation data from surfaces roughened with irregular pyramids and spanwise humps.

Turbulence intensities and Reynolds stresses were measured over the wavy surfaces. Measurements of wall pressures and wall heat flux distributions were obtained for a series of points along the surface.

Wind reduction factors were determined in the space between successive barriers. Measurements of turbulent shear stresses and mean velocity distributions along with the heat transfer rates in case of flow over equally spaced barriers has yielded valuable basic information concerning the boundary-layer flow over rough surfaces.

Verma, S. B. & J. E. Cermak
EVAPORATION OF WATER AS RELATED TO WIND BARRIERS
Completion Report to Office of Water Resources Research, Department of the Interior, June, Washington, D. C., June 1971, 211 p.
KEYWORDS--evaporation/moisture loss/mass transfer/soil erosion/wind barriers/corrugated surfaces/wavy boundary/fences/rough surfaces/field furrows/humidity profiles/turbulence/wall heat flux/wind reduction/wind tunnel.

TABLE OF CONTENTS

TABLE OF CONTENTS (Continued)

TABLE OF CONTENTS (Continued)

LIST OF TABLES

LIST OF FIGURES

LIST OF FIGURES - (Continued)

LIST OF FIGURES - (Continued)

LIST OF FIGURES - (Continued)

LIST OF FIGURES - (Continued)

LIST OF FIGURES - (Continued)

LIST OF SYMBOLS

Symbol		Dimension
a	Wave amplitude	L
B^{-1}	Reciprocal of sublayer Stanton number of Owen and Thomson (56)	---
C_f	Effective average skin friction coefficient	---
C_p	Specific heat at constant pressure	$HM^{-1}\Theta^{-1}$
C_v	Specific heat at constant volume	$HM^{-1}\Theta^{-1}$
d	Zero plane displacement	L
D	Molecular mass diffusivity	L^2T^{-1}
E	Evaporation rate per unit area	$ML^{-2}T^{-1}$
$f_+(z)$	Resistance to transport of momentum	---
g	Acceleration due to gravity	LT^{-2}
G	Shape factor (Eq. 2-19)	---
H	Form factor also heat flux	$HL^{-2}T^{-1}$
h	Wave or fence height	L
I	Current	amp
k	Kármán constant	---
K_c	Mass transfer coefficient = mass transfer rate per unit area/Δq	$ML^{-2}T^{-1}$
K_x, K_y, K_z	Exchange coefficients of water vapor x, y, z directions	L^2T^{-1}
K_M	Exchange coefficient of momentum	L^2T^{-1}
K_h	Exchange coefficient of heat	L^2T^{-1}
L	Monin-Obukhov length = $\frac{u_*^3}{k \frac{g}{T} (\frac{H}{\rho c_p})}$	L
L_e	Latent heat evaporation	HM^{-1}

LIST OF SYMBOLS (Continued)

Symbol		Dimension
ℓ	Characteristic length	L
m,n	Exponents	--
p	Pressure	$ML^{-1}T^{-2}$
Pr	Prandtl number	--
q	Specific humidity $(\frac{\text{gm of water vapor}}{\text{gm of dry air}})$	--
q_{amb}	Ambient specific humidity	--
q_s	Surface air humidity	--
q_∞	Specific humidity in free stream	--
q'	Fluctuations in q	--
q_*	Friction specific humidity	--
Δq	$q_s - q_\infty$	--
R	Resistance of film or wire	ohm
R_l	Wind reduction factor	--
R_e	Reynolds number	--
$r_+(z)$	Resistance to transport of mass	--
$(Re_*)_o$	Surface Reynolds number (based on u_* and z_o) = $u_* z_o/\nu$	--
Sc	Schmidt number = ν/D	--
Sh	Sherwood number = $E\ell/\rho D(\Delta q)$	--
$(Sh)_h$	Sherwood number based on $h = Eh/\rho D(\Delta q)$	--
$(Sh)_o$	Sherwood number based on $z_o = Ez_o/\rho D(\Delta q)$	--
$T_{t'}$	Temperature	θ
T_s	Surface air temperature	θ
T	Ambient air temperature	θ
T_*	Friction temperature	θ
t	Time	T

LIST OF SYMBOLS (Continued)

Symbol		Dimension
U,V,W	Mean velocity components in x,y,z direction	LT^{-1}
u',v',w'	Velocity fluctuations in x,y,z direction	LT^{-1}
u_*	Friction velocity	LT^{-1}
x	Distance along longitudinal direction	L
y	Distance along lateral direction	L
z	Distance in vertical direction: above effective zero plane in the case of waves and above the wall in case of fences	L
z_c	Distance above wave crest in vertical direction	L
z_T	Distance above wave bottom in vertical direction	L
z_o	Roughness parameter	L
z_{om}	Hypothetical length parameter associated with humidity profile	L
z_{ot}	Hypothetical length parameter associated with temperature profile	L
α	Molecular thermal diffusivity	L^2T^{-1}
δ	Boundary layer thickness for momentum transfer	L
δ_m	Mass boundary layer thickness	L
δ_t	Temperature boundary layer thickness	L
δ^*	Displacement thickness	L
θ	Momentum thickness	L
μ	Coefficient of dynamic viscosity	$ML^{-1}T^{-1}$
ν	Coefficient of kinematic viscosity	L^2T^{-1}
ρ	Mean mass density	ML^{-3}
τ	Shear stress	$ML^{-1}T^{-2}$
λ	Wave length	L

LIST OF SYMBOLS (Continued)

Symbol		Dimension
ε	Shift of origin below the roughness tops	T^{-1}
Ω	Angular velocity	T^{-1}
$( )_o$	Reference quantity	--
Δ	A length parameter (Eq. 2.18)	L

CHAPTER I

INTRODUCTION

A wind break or barrier is any device designed to obstruct wind flow and intended for protection against any ill effects of wind (43). Protection against ill effects of wind primarily means reduction of wind speed below the dangerous level for a particular kind of crop, reduction of evaporation of water, reduction of heat transfer from air-water and air-soil interface, etc. A number of previous studies, e.g., Bates (1930, 1945), Cheyney (1931), Denuyl (1936) etc., have outlined the value of windbreaks by showing that rows of trees had beneficial effects on crops in reducing wind speed, moisture loss and heat transfer. Preliminary field and wind-tunnel observations (66) indicate that furrowed surfaces (microridging) effectively reduce wind erosion and improve seed germination. McGinnies (1959) conducted a field study and his results indicated that furrows if deep enough can have pronounced effects on increasing soil moisture content and improving the seedling stand. A practical field microridge roller was developed by Hyder and Bement (1969) to furrow a wind-swept field and provide protection for seeds planted between microridges. Van Eimern (1964) and Chepil (1965) suggested roughening the ground between successive wind breaks to further reduce the ravages of wind.

In semi-arid regions of the United States much effort and thought is being given to procedures which will maximize productive use of available soil-moisture and maximize snow retention without stimulating wind erosion of the soil. Before the control of processes such as

evaporation and soil erosion from bare and vegetated currugated soil surfaces can be accomplished in the field, additional knowledge is required on how the local boundary conditions and adjacent wind barriers affect the local flow. Systematic field studies on how various spacings and configurations of solid barriers and soil corrugations affect the local transfer coefficient could be made, but such studies would be extremely costly in time and money. Therefore, laboratory studies of these variables using a properly designed wind tunnel were initiated at Colorado State University.

Turbulent flow over rough surfaces is considered. To help understand the transfer processes more completely, the study was conducted in two parts. The first part concentrated on the flow over corrugated areas (wavy surfaces) and the second dealt with the flow over equally spaced fences. Briefly, the main objectives of the study were:

1. to determine the local mass and heat-transfer coefficients over corrugated surfaces for several corrugation sizes and ambient flow conditions,
2. to obtain detailed distributions of mean and turbulent velocity fields, humidity and temperature above the corrugated surfaces,
3. (a) to develop, by using the acquired experimental data, a general model of mass transfer mechanism in terms of the various pertinent flow parameters, and
   (b) to correlate the mass transfer data obtained from saturated fixed corrugated surfaces with mass transfer data from saturated surfaces of various other geometries

(e.g., flat plate, water waves, solid irregular surfaces, etc.),

4. (a) to correlate the form drag of fences to the free stream mean velocity and the spacing between the fences, and

   (b) to find the optimum arrangement for multiple wind breaks.

CHAPTER II

THEORETICAL AND EXPERIMENTAL BACKGROUND

This chapter deals with the basic concepts of mass and momentum transfer in turbulent flows. A brief review of pertinent literature with particular reference to flows over rough surfaces is given.

2.1 Turbulent Flow Over a Rough Solid Surface

Assume that the flow field under consideration is incompressible with small temperature differences. Then, fluid properties may be assumed constant (Rosenhead (1963)). The Navier-Stokes equations (Hinze (1959)) are then

$$\rho \frac{DU_i}{Dt} = - \frac{\partial p}{\partial x_i} + \mu \frac{\partial}{\partial x_j} D_{ij} \tag{2.1}$$

where i and j can have values of 1, 2, or 3. D_{ij} is the deformation tensor for a point in the flow with

$$D_{ij} = \frac{\partial U_i}{\partial x_j} + \frac{\partial U_j}{\partial x_i} \quad . \tag{2.2}$$

The incompressibility condition gives

$$\frac{\partial U_i}{\partial x_i} = 0 \quad . \tag{2.3}$$

Now let the 1-direction be the x-axis in the longitudinal direction, with the 2-direction representing z in the vertical direction. The 3-direction is the y-axis which is lateral to the flow and projects out of the plane.

Let the velocity in the x-direction consist of a temporal mean U and a fluctuation value of u'. The velocities in the y and z direction are fluctuating values v' and w', respectively. The fluctuating values have zero mean by definition, or

$$\overline{u'} = \overline{v'} = \overline{w'} = 0 \tag{2.4}$$

where an overbar represents time averaging.

Introducing these definitions into the instantaneous equations of motion and averaging with respect to time, using the conventional boundary-layer approximations (Rotta (1962)), gives

$$U \frac{\partial U}{\partial x} + W \frac{\partial U}{\partial z} = - \frac{1}{\rho} \frac{\partial p}{\partial x} + W \frac{\partial^2 U}{\partial z^2} - \frac{\partial}{\partial z} (\overline{u'w'}) - \frac{\partial}{\partial x} (\overline{u'^2} - \overline{w'^2}) \tag{2.5}$$

$$\frac{\partial U}{\partial x} + \frac{\partial W}{\partial z} = 0 \tag{2.6}$$

and

$$\frac{p}{\rho} = \frac{p_a}{\rho} - \overline{w'^2} \tag{2.7}$$

The second and third terms of the right-hand side of Eq. (2.5) are the shear-stress terms. Let τ be the total shear stress, then

$$\frac{\tau}{\rho} = \nu \frac{\partial U}{\partial z} - \overline{u'w'} \quad . \tag{2.8}$$

The flow over a rough wall can be expected to be turbulent everywhere.

Thus, viscous transport of momentum can be assumed negligible compared to turbulent transport, or

$$\mu \frac{\partial u}{\partial z} << -\rho\overline{u'w'} \quad . \tag{2.9}$$

Eddy viscosity is defined as

$$-\overline{u'w'} = K_M \frac{\partial \bar{u}}{\partial z} \quad , \tag{2.10}$$

and is analogous to the absolute molecular viscosity in

$$\tau = \mu \frac{\partial u}{\partial z} \quad . \tag{2.11}$$

An eddy viscosity is postulated since the present knowledge of turbulent flows does not allow the analytical determination of $\overline{u'w'}$. Thus, comparison between similar flows, for one with the K_M known, gives an indication of the K_M for another, more complicated flow.

2.2 Boundary-Layer Flows with a Rough Wall

Turbulent shear flow considered in two-dimensions and with steady mean velocities can be represented by the "law of the wall" for a considerable region near the smooth wall:

$$U/u_* = f(zu_*/\nu) \tag{2.12}$$

where u_* is called the shear velocity and is equal to $\sqrt{\tau/\rho}$, where τ is the wall shear stress. For values of $zu_*/\nu > 50$, the universal law becomes

$$U/u_* = (1/k)\ \ln\ (zu_*/\nu) \quad + C_1 \tag{2.13}$$

where k and C_1 are experimentally determined constants. The flow near a smooth wall is dominated by the laminar-like shear flow and the law of the wall reduces to

$$U/u_* = zu_*/\nu \quad . \tag{2.14}$$

The derivation of the logarithmic law can be accomplished by several methods. Malkus (1961) used dimensional arguments, while assumptions involving a region of constant stress near the wall were used by van Driest (1956) and Reichardt (1951). Coles (1956) suggested expanding the "law of the wall" to include a function

$$h(x,y) = (\pi/k)\omega \quad (z/\delta) \ , \tag{2.15}$$

which would describe the flow outside of the logarithmic portion, which is usually a region within 0.2 times the boundary layer-thickness.

The value of u_* or $\frac{u_*}{U_\infty} = \sqrt{C_f/2}$ plays a very important role in the character of the turbulent boundary layer, since the wall shear supplies the energy to the turbulence. Also, all length ratios in a turbulent shear flow are dependent on the value of $\sqrt{C_f/2}$ since

$$\delta^* = \sqrt{C_f/2}\ \Delta \tag{2.16}$$

$$\theta = \Delta\ \sqrt{C_f/2}\ [1-G\ \sqrt{C_f/2}] \tag{2.17}$$

where

$$\Delta = \delta \int_0^\infty \frac{(U_\infty - U)}{u_*} \, d(z/\delta) \tag{2.18}$$

$$G = \int_0^\infty \frac{(U-U_\infty)^2}{u_*} \, d(z/\Delta) \quad . \tag{2.19}$$

The length Δ is a length determined from the universal plot of the velocity defect $(U_\infty - u)/u_*$ and z/δ. The parameter G is a shape factor.

Introducing roughness at the wall increases the wall friction. Consequently, the logarithmic wall law is shifted downward and to the right in a U/u_* vs. $\log \frac{zu_*}{\nu}$ plot. Roughness changes the wall law to

$$\frac{U}{u_*} = A \log \frac{zu_*}{\nu} + C - \frac{\Delta U}{u_*} \tag{2.20}$$

where $\Delta U/u_*$ is called the roughness function, and measures the downward shift of the logarithmic velocity profile. For fully rough flows, where viscous effects have been removed, the inner law must be independent of the viscosity; thus, Eq. 2.20 must give

$$\frac{\Delta U}{u_*} = A \log \frac{Ku_*}{\nu} + D \quad , \tag{2.21}$$

where K specifies the roughness height. The Clauser form of the roughness function above has been used by Hama (1954) and Perry and Joubert (1963). The form and orientation of the roughness elements used

by Hama (1954), Perry and Joubert, Betterman (1966) and Liu, et al. (1966) have been screens or square rods perpendicular to the mean flow. Recently, Perry, et al. (1969) have extended the rough-wall analysis to closely spaced roughness elements. The roughness function $\Delta U/u_*$ is given by

$$\frac{\Delta U}{u_*} = \frac{1}{k} \log\left[\left(\frac{\alpha K+\varepsilon}{\nu}\right) u_*\right] + C \tag{2.22}$$

where αK is the height above the roughness elements at which the inner flow

$$\frac{U}{u_*} = f(z_c/K)$$

and the outer flow

$$\frac{U}{u_*} = \frac{1}{k} \ln \frac{(z_c+\varepsilon)u_*}{\nu} + A - \frac{\Delta U}{u_*} \tag{2.23}$$

blend. For flow over a "K" type roughness, vortices of scale K are shed from between the roughness elements. Flow above these elements would then be characterized by "large" values of αK compared to the origin shift ε. Thus,

$$\frac{\Delta U}{u_*} = \frac{1}{k} \log \frac{Ku_*}{\nu} + C_2 \tag{2.24}$$

where C_2 is a new constant. Large values of αK are achieved by large values of α, which is analagous to the outer edge of the

"viscous sublayer", $zu_*/\nu = \alpha$. The value of α would be expected to be larger than the smooth wall result since u_* is much larger for a rough wall.

Closely spaced roughness elements do not shed vortices into the flow, resulting in the "skimming" type flow of Morris (1955). For this flow, α would be small since the viscous layer would be near the top of the roughness elements. Thus,

$$\frac{\Delta U}{u_*} = \frac{1}{k} \ln \frac{\varepsilon u_*}{\nu} + C_3 , \tag{2.25}$$

where $\varepsilon > aK$ in Eq. 2.22 above.

Depending on the shape, size, and spacing of the roughness elements, the roughness function could depend on either K, the roughness size, or ε, the shift of the origin below the roughness tops.

In general, the displacement length ε is retained in meteorology (Stearns (1970)) but the roughness function is neglected since roughness sizes (1 m at most) are small compared to the thickness of the constant-flux layer (20 to 200 m) (Lumley and Panofsky (1964)).

When the velocity profile is correlated with

$$\frac{U}{u_*} = \frac{1}{k} \ln \frac{(z_c + \varepsilon K)u_*}{\nu} + A - \frac{U}{u_*} , \tag{2.26}$$

arbitrary choices of ε may give incorrect values of z_c since the two parameters are not independent. For a smooth wall, ε is zero and u_* can be determined by several methods (Schraub and Kline (1965)).

Rough-wall flows present a problem, since two related parameters are involved: ε and C_f. Perry and Joubert (1963) use a wake-alignment method and the momentum integral equation to obtain the values of u_* and ε. However, they comment that a better method should be devised.

The slope of the log profile is $5.6\sqrt{C_f/2}$, and using the momentum integral technique gives C_f. Then, ε can be determined approximately by adding values to the vertical coordinate measured from roughness element tops. When the data points give a straight line for distances below 0.25, the "correct" value of ε has been determined. However, this type of approximate method does not always give consistent results as observed by Perry and Joubert.

The best method presently available for determining C_f in a rough-wall turbulent boundary layer is to pressure tap the roughness elements and use the moment balance over one roughness element. The details of this method are given in Appendix (B). Using the value of C_f thus determined, the slope of the logarithmic portion of the velocity profile is fixed and values of ε can be added to the coordinate of z_c until the data points in the lower 20% of the velocity profile gives a straight line with the correct slope of $5.6\sqrt{C_f/2}$. When the slope of the logarithmic velocity profile $5.6\sqrt{C_f/2}$ and the shift of origin ε are determined by this method, the velocity data points (u,z) can be correlated with the logarithmic velocity profile.

2.3 Turbulence in Boundary Layers

The determination of the turbulent intensities $\sqrt{\overline{u'^2}}/U_\infty$ and $\sqrt{\overline{w'^2}}/U_\infty$ and the turbulent shear stress $-\rho\overline{u'w'}$ involve the complete

solution to the averaged Navier-Stokes equation. Consequently, empirical correlations have been developed which relate to other measured quantities.

The intensities $\sqrt{\overline{u'^2}}/U_\infty$ and $\sqrt{\overline{w'^2}}/U_\infty$ for turbulent boundary layers over rough surfaces have rarely been reported and empirical correlations do not exist. However, for the turbulent shear stress, solutions to the equation

$$U \frac{\partial U}{\partial x} + W \frac{\partial U}{\partial z} = \frac{\partial}{\partial z} (-\overline{u'w'}) \tag{2.27}$$

for the outer flow results in an equation for the stress $-\rho\overline{u'w'}$ (107). The outer flow is assumed universal in the form

$$(U_\infty - U)/u_* = f(z/\delta) \tag{2.28}$$

resulting in the distribution

$$-\overline{u'w'} = u_*^2 \exp [-b(z/\delta)^2] \tag{2.29}$$

where b is an empirical constant. The value of b has been obtained from the measurement of Klebanoff (1959) for a smooth wall, and is 1.77. The applicability of the above analysis for rough walls has not been established.

The constant b is given by

$$b = \frac{U_\infty \delta}{z K_m} \frac{d\delta}{dx} \tag{2.30}$$

where K_m is the eddy viscosity, defined by

$$-\overline{u'w'} = K_m \frac{\partial}{\partial z} (U_\infty - U) \ . \tag{2.31}$$

The above relation for the turbulent shear stress is expected to hold for $z/\delta < 0.6$, since the boundary layer is intermittent above this level. For low values of z/δ (say, $z/\delta < 0.2$), the additional assumption of

$$\frac{U_\infty - U}{U_\infty} \ll 1 \tag{2.32}$$

does not hold. The analysis in this form for the turbulent shear stress has not been examined for rough walls and the corrugated surfaces.

2.4 Concept and Application of K-theory - Diffusion Equation

The two-dimensional boundary-layer flow of an incompressible fluid is considered. Let $q(x,y,z,t)$ be the concentration of a diffusing substance, e.g., the amount of water vapor associated with unit weight of dry air, with q' the fluctuation of q. Then, the equation of diffusion can be written as follows:

$$\frac{\partial q}{\partial t} + U \frac{\partial q}{\partial x} + V \frac{\partial q}{\partial y} + W \frac{\partial q}{\partial z} = \frac{\partial}{\partial x} \left(K_x \frac{\partial q}{\partial x}\right) + \frac{\partial}{\partial y} \left(K_y \frac{\partial q}{\partial y}\right) + \frac{\partial}{\partial z} \left(K_z \frac{\partial q}{\partial z}\right), \tag{2.33}$$

in which K_x, K_y, and K_z are the exchange coefficients for mass transfer in the three directions. These exchange coefficients are obtained from the assumption of proportionality between the respective

diffusion fluxes and the concentration gradients, e.g.,

$$\overline{u'q'} = - K_x \frac{\partial q}{\partial x}, \quad \overline{v'q'} = - K_y \frac{\partial q}{\partial y} \quad \text{and} \quad \overline{w'q'} = - K_z \frac{\partial q}{\partial z} . \tag{2.34}$$

For a steady and two-dimensional problem with $V = W = 0$ when the longitudinal dispersion term is neglected, because of its smallness relative to the corresponding term in the z-direction and the convective term, the diffusion equation reduces to

$$U \frac{\partial q}{\partial x} = \frac{\partial}{\partial z} \left(K_z \frac{\partial q}{\partial z}\right) . \tag{2.35}$$

Equation (2.35) can be solved analytically only if the functional form of the exchange coefficient K_z and the velocity profile are known. Many scientists have solved this equation by assuming various forms of K_z and U. A detail review on these works can be found in (20) or (110).

O. G. Sutton (1934) investigated the problem of evaporation from a saturated or free liquid surface, of finite extent downwind, level with the earth's surface, and of such dimensions that no detectable variation of wind structure was produced. To formulate the problem mathematically, he assumed that for an infinite cross wind saturated strip, of length x_o downwind and situated at ground level $(z = 0)$, the appropriate boundary conditions were:

$$\left.\begin{aligned} &\lim_{z \to 0} q(x,z) = q_s \text{ (a constant)} \quad (0 < x \leq x_o) \\ &\lim_{z \to \infty} q(x,z) = 0 \qquad\qquad (0 \leq x \leq 0) \\ &\lim_{x \to 0} q(x,z) = 0 \qquad\qquad (0 < z) \end{aligned}\right\} \tag{2.36}$$

He hypothesized the following functional form for the correlation coefficient R_ξ

$$R_\xi = \left(\frac{\nu}{\nu + \overline{w'^2}\xi}\right)^n \tag{2.37}$$

with the requirement that ν be small compared to $\overline{w'^2}\xi$. Then, assuming $K_z = K_M$, Sutton used Taylor's theory of diffusion by continuous movements, and Prandtl's mixing length theory to obtain:

$$K_z = \frac{(0.251)^{1-n}}{1-n} \nu^n \left[\left(\frac{\partial U}{\partial z}\right)^3 \left(\frac{\partial^2 U}{\partial z^2}\right)^{-2}\right]^{1-n} .$$

Substituting this expression into $K_z \frac{\partial u}{\partial z} = \frac{\tau}{\rho}$ = constant, which simply means that the shear stress is invariant with height in the lower atmosphere, the following familiar power law of velocity was recovered

$$\frac{U}{U_1} = \left(\frac{z}{z_1}\right)^{\frac{n}{2-n}} . \tag{2.39}$$

Hence, Sutton was able to obtain an analytical solution of the diffusion equation with the above functional forms of K_z and U.

Sutton's theory, though applicable to aerodynamically smooth surfaces only, has received considerable experimental and some theoretical attention. Evaporation measurements of many investigators, e.g., Himus (1929), Hine (1924), Powell and Griffith (1935), and Thiesenhausen (82), agree reasonably well with Sutton's theory.

In 1943, Pasquill (78) modified Sutton's theory by replacing ν by D, the molecular diffusivity of water vapor, to obtain better agreement with his wind tunnel results.

Yih (1952) presented a solution of Eq. 2.35, using a procedure similar to that first used by Blasius and later by Goldstein (1939) and Mangler (1943) in their analysis of boundary-layer problems. Kohler (1950) had obtained the same solution in an attempt to solve Eq. 2.35 by Sutton's theory. Cermak (1953) adapted Kármán's (1939) equation for heat transfer,

$$\frac{1}{C_H} = \frac{2}{C_f} + 5\left(\frac{2}{C_f}\right)^{1/2} \{\sigma-1 + \ln [1 + \frac{5}{6} (\sigma-1)]\}, \qquad (2.40)$$

to vapor transport by writing instead of C_H ,

$$C_e = E/\rho g U_\infty \Delta q \qquad (2.41)$$

Assuming a 1/7 power relationship of velocity distribution, he finally obtained the following equation for the range of $10^3 \leq R_x \leq 10^5$:

$$N^{-1} = \frac{6.23\ R_x^{-8/9}}{\left(\frac{x_1'}{x_1}\right)^{4/45}} - \frac{3.77\ R_x^{-1}}{\left(\frac{x_1'}{x_1}\right)^{1/10}} , \qquad (2.42)$$

in which $\tau = C_f\ \rho\ \frac{U_\infty^2}{2}$, $Q = C_H\ \rho C_p\ U_\infty \Delta\ T$, $R_x = \frac{u_* x}{D}$, $N = \frac{E' x}{D \Delta q}$, x_1 = distance downstream from the beginning of evaporation boundary, x_1' = distance downstream from the leading edge of boundary, and E' = evaporation weight/time x area.

Before this, Frost (1946) had attempted to extend the considerations to hydrodynamically rough surfaces. He developed a form for K_z that included the roughness parameter. In his work, he assumed that the mixing length over a rough surface can be written as

$$\ell_1 = z^{1-m} z_o^{m} \tag{2.43}$$

in which z_o = roughness parameter and m = constant. The shear stress, which is given by

$$\tau = \rho \, \ell_1^2 \, (\frac{\partial U}{\partial z})^2 \tag{2.44}$$

then becomes

$$\frac{\tau}{\rho} = z^{2-2m} z_o^{2m} (\frac{\partial U}{\partial z})^2 \tag{2.45}$$

Again, assuming the constancy of shear stress in the lower 30 meters of the atmosphere, and integrating, the relation

$$U = \frac{1}{m} \sqrt{\tau/\rho} \; (\frac{z}{z_o})^m \tag{2.46}$$

is obtained. Thus, the assumption in Eq. 2.43 is compatible with the power law

$$\frac{U}{U_1} = (\frac{z}{z_1})^m \tag{2.47}$$

for a wind profile similar to Eq. 2.39. Next, using

$$K_z = \ell_1^2 \frac{\partial U}{\partial z} \tag{2.48}$$

and Eqs. 2.43 and 2.47, Frost solved the diffusion equation analytically to obtain the evaporation rates from rough surfaces.

In an effort to include the effect of atmospheric stability, Deacon (1948) proposed a general wind profile,

$$U = \frac{u_*}{k(1-\beta_1)} \left[\left(\frac{z}{z_o}\right)^{1-\beta_1} - 1\right] \tag{2.49}$$

for rough flow, in which the boundary requirement is that $\frac{U}{u_*} = 0$ at $\frac{z}{z_o} = 1$. The limiting values in Eq. 2.49 are $0.75 \leq \beta_1 \leq 1.25$, where

$$\left.\begin{aligned} &\beta_1 < 1 \quad \text{For stable conditions,} \\ &\beta_1 = 1 \quad \text{for neutral conditions,} \\ \text{and} \quad &\beta_1 > 1 \quad \text{for unstable conditions.} \end{aligned}\right\} \tag{2.50}$$

Then, the relation $\tau = \rho K_z \frac{\partial U}{\partial z} = \text{constant}$ and Eq. 2.49 can be used to obtain a form for K_z that enables the diffusion Eq. 2.35 to be solved.

Calder (1949) also studied the problem of evaporation from smooth and rough surfaces, of a finite extent downwind, in a turbulent flow. In a so-called "aerodynamically smooth flow", the drag exerted on the fluid by the boundary surface is a function of the Reynolds number only, and, except for a region very close to the surface, the distribution of mean velocity is represented by the law

$$\frac{U}{u_*} = \frac{1}{k} \ln \frac{u_* z}{\nu} + 5.5 \quad . \tag{2.51}$$

On the other hand, for "aerodynamically rough flow," the drag is independent of the Reynolds number and is proportional to the square of velocity with the mean velocity distribution

$$\frac{U}{u_*} = \frac{1}{k} \ln \left(\frac{z-d}{z_o}\right) \quad \text{for} \quad z \geq z_o + d \tag{2.52}$$

in which d is the zero-plane displacement, z is measured from the base of the roughness, and z_o is called the roughness parameter. Because of the intractibility of certain mathematical developments, Calder chose to use the relations,

$$\frac{U}{u_*} = q'' \left(\frac{u_* z}{\nu}\right)^{\alpha} \tag{2.53}$$

and

$$\frac{U}{u_*} = q''' \left(\frac{z-d}{z_o}\right)^{\alpha} \tag{2.54}$$

in place of Eq. 2.51 and 2.52, respectively. In Eq. 2.53 q'' and α depend on the range of $\frac{u_* z}{\nu}$ such that Eq. 2.53 agrees approximately with Eq. 2.51, and similarly, q''' and α also will depend on the range of $(z-d)/z_o$ such that Eq. 2.54 agrees with the more accurate Eq. 2.52. Also, in the turbulent layer over a smooth or a rough surface, there is a region not too far removed from the surface in which the turbulent shear stress, given by

$$\tau = \rho K_M(z) \frac{\partial U}{\partial z} \tag{2.56}$$

can be regarded as effectively independent of the distance from the surface. From Eqs. 2.53 and 2.54, one can easily obtain

$$\tau_o = \left(\frac{U}{q''}\right)^{2/1+\alpha} \left(\frac{\nu}{z}\right)^{2\alpha/1+\alpha} \tag{2.57}$$

for smooth surfaces, and

$$\tau_o = \rho \frac{U^2}{q'''^2} \left(\frac{z_o}{z}\right)^{2\alpha} \tag{2.58}$$

for rough surfaces. Equations 2.57 and 2.58 are special cases of a more general equation

$$\tau_o = \varepsilon \rho U^{2\beta} \left(\frac{\delta}{z}\right)^{2\alpha\beta} \tag{2.59}$$

in which

$$\beta = \frac{1}{1+\alpha}, \quad \delta = \nu, \quad \text{and} \quad \varepsilon = \left(\frac{1}{q''}\right)^{2/1+\alpha} \tag{2.60}$$

for smooth surfaces,

and

$$\beta = 1, \quad \delta = z_o, \quad \text{and} \quad \varepsilon = 1/q'''^2$$

for rough surfaces.

Thus, Calder was able to adopt a uniform mathematical treatment for both smooth and rough surfaces. In both cases, using

$$\frac{U}{U_1} = \left(\frac{z}{z_1}\right)^{\alpha} \tag{2.61}$$

in which U_1 is the velocity at a standard height z_1, an expression for $K_M(z)$ was obtained applying Eqs. 2.56, 2.59 and 2.60. Calder assumed that the concentration of vapor over a rough surface, which is saturated, was constant over a plane at a distance from the datum plane equal to the zero plane displacement d of the velocity profile. At this distance, turbulence can be regarded as first becoming operative. Thus, the boundary conditions (2.36) were assumed valid for a rough surface also, if the plane $z = 0$ is at a distance d from the datum plane of height reference in the velocity profile equation. He treated the infinitely crosswind strip of evaporating surface defined by $z = 0$, $0 < x \leq x_o$, as an aggregate of elemental, continuous, infinite, crosswind, line sources of vapor. And finally, assuming $K_M(z) = K_z(z)$, Calder obtained the expressions for vapor concentration distribution $q(x,z)$ and the evaporation rate. His expression for vapor concentration above a smooth saturated strip is identical with the one first obtained by O. G. Sutton (1934).

Phillip (1959) and Rider et al. (1963) studied the problem of horizontal transport of heat and moisture in the lower atmosphere. They solved the steady state two-dimensional equations of diffusion of heat and moisture using energy-balance considerations. Their solution has some formal similarity to the solution obtained for the evaporation problem by Sutton (1934) and Calder (1949). The analyses by Sutton and

Calder, however, neglected energy-balance considerations and required that the surface temperature of the evaporating surface be known. In the study pursued by Rider et al. (1963), because the energy balance was taken into account, the surface temperature of the downwind wet area emerged as part of the solution.

2.5 Semi-empirical Theories of Turbulent Diffusion

In a fully turbulent flow, that is a flow in which molecular diffusion is largely outweighed by turbulent mixing, the mean upward vertical flux F of an entity S per unit mass of the fluid, is given by

$$F = \rho\overline{w's'} = - \rho K \frac{\partial \overline{S}}{\partial z} , \qquad (2.62)$$

in which w' and s' are the fluctuations in the vertical component of velocity, and concentration, respectively, $\overline{S}$ is the averaged concentration of the entity, ρ is the density of the fluid, and K is the eddy diffusivity. The justification of Eq. 2.62 rests mainly on empirical grounds and is based on the mixing length approach to atmospheric diffusion, which has an analogy with the molecular motion.

The turbulent shear stress, which is given by $\tau = -\rho\overline{u'w'}$, can also be interpreted as a transport of the x-momentum across a plane normal to the vertical z-axis, and so Eq. 2.62 gives

$$\tau = - \rho\overline{u'w'} = \rho K_M \frac{\partial \overline{U}}{\partial z} \qquad (2.63)$$

in which K_M is the eddy momentum diffusivity defined before in Section 2.1. In the constant flux-layer, one can define a friction velocity u_* such that

$$\tau = \rho\, u_*^2 \tag{2.64}$$

in which u_* is assumed to be independent of z for a given wind velocity profile. For a nearly neutral case, dimensional analysis of these variables leads to an expression for the vertical gradient of mean wind speed U,

$$\frac{\partial U}{\partial z} = \frac{u_*}{kz} \tag{2.65}$$

in which k is a dimensionless constant. Integration of the above equation gives the known logarithmic velocity profile

$$\frac{U}{u_*} = \frac{1}{k} \ln \frac{z}{z_o} \quad (z > z_o) \tag{2.66}$$

where z_o is termed as the roughness length, and k as Kármán's constant. For rough surfaces, if z_T is measured from the base of the roughness rather than from the level of the zero mean wind which may be somewhat higher, it is necessary to introduce a zero-plane displacement d so that Eq. 2.66 becomes

$$\frac{U}{u_*} = \frac{1}{k} \ln \frac{z_T - d}{z_o} \tag{2.67}$$

which is the same as Eq. 2.52. The roughness length z_o incorporates the previously defined roughness function $\Delta U/u_*$, such that

$$\frac{1}{k} \ln z_o = \frac{\Delta U}{u_*} - 5.0 - \frac{1}{k} \ln \frac{u_*}{\nu} \quad . \tag{2.68}$$

On the basis of the assumption that the eddy viscosity, eddy diffusivity and eddy conductivity are determined by the first and second differential coefficients of the mean velocity U, mean humidity q, and mean potential temperature T, Björgum (1953) obtained the following relations for the constant flux layer:

$$q - q_s = q_* \ln \frac{z}{z_{om}} \tag{2.69}$$

and

$$T - T_s = T_* \ln \frac{z}{z_{ot}} \tag{2.70}$$

in which z is measured from the effective zero plane, given by $z = z_T - d$. The zero plane displacement d is the same as in the corresponding case of velocity profile (Eq. 2.67) and z_T is measured from the base of the roughness. The quantities q_* and T_* are known as the friction humidity and friction temperature respectively; z_{om} and z_{ot} may be considered as hypothetical length parameters.

For the turbulent transport of water vapor in the constant flux region, one can write

$$E = \rho \overline{w'q'} = - \rho K_z \frac{\partial q}{\partial z} \quad . \tag{2.71}$$

Combining Eq. 2.71 with Eqs. 2.63, 2.64, 2.65 and 2.67, one obtains

$$E = - \rho \, k \, \beta \, u_* q_* \tag{2.72}$$

in which $\beta = K_z/K_M$. In an analogous fashion, the following equation can be written for the turbulent transport of heat,

$$H = \rho \, C_p \, \overline{w't'} = - \rho \, C_p \, K_h \frac{\partial T}{\partial z} = - \rho \, C_p \, \beta' k u_* T_* \tag{2.73}$$

in which t' is the potential temperature fluctuation, K_z the eddy conductivity, C_p the specific heat at constant pressure and $\beta' = K_h/K_M$.

In regard to ratio K_z/K_M (or K_h/K_M), the experimental results obtained, both in field and laboratory, are contradictory and the question is far from settled. The work of Swinbank (1955) suggests a value of 0.7 for K_h/K_M, while that of Rider (1954) suggests about 1.3, for neutral conditions. Pasquill (1949) found that in neutral and stable conditions, but not under unstable conditions, measured K_z and calculated K_M values were essentially equal within 10 percent. Laykhtman and Ponomareva (1969) obtained the following relation which agreed satisfactorily with the measurements of other authors:

$$\frac{K_h}{K_M} \simeq \begin{cases} 0.8 \quad \text{for} \quad -0.03 < \dfrac{z}{L} + 0.10 \\ 3.2 \; z/L^{\,0.35} \quad \text{for} \quad -0.8 < \dfrac{z}{L} < -0.03, \\ 3.0 \quad \dfrac{z}{L} < -0.8 \quad . \end{cases} \tag{2.74}$$

in which L is the Monin-Obukhov length.

Most of the formulae for evaporation used primarily for meteorological observations, however, rely mainly on the identity of K_z and K_M ; some of these are discussed in the following text.

2.5.1 The Thornthwaite and Holzman formula (1939) - By combining Eqs. 2.63, 2.64, and 2.71 and assuming $K_z = K_M$, one arrives at the equation

$$E = - \rho \frac{u_*^2}{(\frac{\partial U}{\partial z})} \frac{\partial q}{\partial z} , \tag{2.75}$$

which can be written in the constant flux layer as

$$E = \rho u_*^2 \frac{q_1 - q_2}{U_2 - U_1} . \tag{2.76}$$

Under neutral conditions in the lower atmosphere, using the logarithmic velocity profile $U/u_* = (1/k)(\ell n\ z/z_o)$ in Eq. 2.76, we obtain

$$E = \rho k \frac{u_*(q_1 - q_2)}{\ln(\frac{z_2}{z_1})} \tag{2.77}$$

which can also be written as

$$E = \rho k^2 \frac{(U_2 - U_1)(q_1 - q_2)}{(\ln\ z_2/z_1)^2} \tag{2.78}$$

The above formula was first derived by Thornthwaite and Holzman (1939).

Similarly, if one uses the logarithmic profile $U/u_* = (1/k)\ \ell n(\frac{z-d}{z_o})$ one can easily obtain the relation

$$E = k^2 \frac{(U_2-U_1)(q_1-q_2)}{\left(\ln \frac{z_1-d}{z_1-d}\right)^2} . \qquad (2.79)$$

This equation was first suggested by Pasquill (1949 a and b) and later used by Rider (1954) to calculate evaporation from an oat field.

Since velocity profiles (2.66) and (2.67) are only applicable in neutral conditions, Eqs. 2.78 and 2.79 are also subject to this restriction. However, Pasquill (1949) has shown that the Deacon (1948) generalized wind profile law (Eq. 2.49) provides a satisfactory basis for the modification of Eq. 2.79 for unstable conditions. The modified equation is

$$E = \frac{\rho k^2 (1-\beta_1)^2 (q_1-q_2)(U_2-U_1) z_o^{2(1-\beta_1)}}{(z_2-d)^{1-\beta_1} - (z_1-d)^{1-\beta_1\ 2}} \qquad (2.80)$$

In stable conditions, Rider (1954) has shown that Eq. (2.49) does not hold and its use would lead to an underestimation of the eddy diffusivity for momentum and, hence, of that for vapor.

2.5.2 Flux equations using surface conditions - The methods just discussed for measuring evaporation flux demand observations at two atmospheric levels by refined techniques and may not be used on a synoptic basis. If one level is the surface itself, large humidity differences would be available for measurements, with a reduction in errors, especially in the observations at a water surface (for land surfaces, there is always the problem of defining surface conditions

accurately). Sheppard (1959) used $K_z = ku_*z$ in the following equation:

$$E = - \rho(D + K_z) \frac{\partial q}{\partial z} \tag{2.81}$$

to obtain:

$$E = \frac{\rho k u_* (q_s - q)}{\ln \frac{ku_* z}{D}} \quad \text{for} \quad z >> \frac{D}{ku_*} \tag{2.82}$$

in which D is the molecular diffusivity of water vapor.

Sverdrup (1946) decided to neglect D in Eq. 2.81 and assumed $K_z = ku_*(z+z_o)$. Thus, on integration of Eq. 2.81, he obtained:

$$E = \frac{\rho k u_* (q_s - q)}{\ln \frac{z+z_o}{z_o}} \quad \text{for} \quad z \geq z_o \ . \tag{2.83}$$

To estimate vertical vapor flux from a hydrodynamically rough sea surface, Montgomery (1940) assumed the existence of a three-layer model described below:

1. a laminar layer of very small thickness, above the surface of the water;

2. an "intermediate" layer of height I (about the height of the waves), in which the stress as represented by the friction velocity u_{*k} is constant, with the velocity distribution in this layer given by Eq. 2.51, and

3. the normal turbulent boundary layer, above the "intermediate" layer, in which the friction velocity remains constant at a different value u_{*R} ($u_{*R} > u_{*R}$). By requiring continuity in wind speed, a relation between the two friction velocities was obtained. Montgomery, postulating the distribution of water vapor in the "intermediate" layer

as being nearly the same as in the case of smooth water surface, expressed the humidity q_I at the top of the intermediate layer as

$$q_s - q_I = \frac{E_o}{\rho k u_{*k}} \left(\frac{\lambda_1 \nu k}{D} + \ln \frac{k u_{*k} I}{D}\right) , \tag{2.84}$$

in which E_o is the rate of evaporation and λ_1 is a nondimensional constant defined by the equation

$$\delta = \frac{\lambda_1 \nu}{u_{*k}} \tag{2.85}$$

with δ as thickness of the laminar layer. Montgomery found $\lambda_1 = 7.8$. For the turbulent layer, where the friction velocity is supposed to be equal to u_{*R}, Montgomery wrote:

$$E_o = - \rho k u_{*R} z \frac{dq}{dz} . \tag{2.86}$$

Integrating the above equation with respect to z, between the top of the "intermediate" layer and any height z, and eliminating q_I with the help of Eq. 2.84, Montgomery obtained

$$q_s - q = \frac{E_o}{\rho k u_{*R}} \left[\ln \frac{z}{I} + \frac{u_{*R}}{u_{*k}} \left(\frac{\lambda_1 \nu k}{D} + \ln \frac{k u_{*k} I}{D}\right)\right] \tag{2.87}$$

Defining, for a height $b (b > I)$, the evaporation coefficient,

$$\Gamma_b \equiv \frac{1}{q_s - q_b} \frac{dq}{d \ell n z} = \left[\ln \frac{b}{I} + \frac{u_{*R}}{u_{*k}} \left(\frac{\lambda_1 \nu k}{D} + \ln \frac{k u_{*k} I}{D}\right)\right]^{-1}$$

we get

$$E_o = \rho k\, u_{*R}\ \Gamma_b\ (q_s - q_b)\ . \tag{2.89}$$

Later, Norris (1948) also used the concept of three-layer model to obtain evaporation rates from extensive surfaces of water; but he differed from Montgomery as far as the distribution of water vapor in the outer turbulent layer was concerned. Norris pointed out that by assuming the equality of eddy diffusivities for momentum and water vapor, except for the small difference in D and ν, one uses the same friction velocity for a rough surface for both properties [K_z (vapor) $= D + ku_{*R}(z+z_o) \simeq \nu + ku_{*R}(z+z_o) = K_M$]. Hence, once the eddy diffusivities are conceded to be the same, it follows that the distribution of water vapor and velocity must obey similar laws. Based on this argument and proceeding in Montgomery's manner, Norris arrived at the following expression for evaporation rate

$$E = \rho k\, u_{*R}\ \Gamma_b (q_s - q_b) \tag{2.90}$$

in which

$$\Gamma = \frac{1}{q_s - q_b}\frac{dq}{d\ell nz} = \ell n\ \frac{b}{I} + \frac{u_{*k}}{u_{*k}}\left(\frac{\lambda_1 \nu k}{D} + \ln\ \frac{ku_{*k}I}{D}\right)\Big] \ -1\ . \tag{2.91}$$

2.6 Dimensionless Correlations for Mass Transfer

Traditionally, data on mass transfer have been expressed in terms of the mass-transfer coefficient K_c in an analogy with the corresponding problem of heat transfer. Correlations of such data have generally

taken the form of empirical expressions relating the dimensionless groups Sh, Re, and Sc, in which Sh is the Sherwood number, Re the Reynolds number, and Sc the Schmidt number. A considerable amount of work has been done in an effort to develop these dimensionless correlations for mass transfer rates from aerodynamically smooth surfaces in turbulent flows. The Chilton-Colburn formula (23), which indicates a mass transfer dependency to $Re^{0.8}$, has been extensively used for obtaining mass-transfer information from smooth flat plates. Gilliland and Sherwood (1934) found, for vaporization of a liquid into air in a wetted column,

$$Sh = 0.023\ Re^{0.83}\ Sc^{0.44} \quad . \tag{2.92}$$

In electrochemical mass transfer for cathode reduction at limiting current conditions, it was observed by Elder et al. (1964) that the mass transfer rate varied with $Re^{0.6}$; Arvia et al. (1964) found that it was proportional to $Re^{0.5}$. Smolsky and Sergeyev (1962) investigated heat and mass transfer by the evaporation of various liquids (water, acetone, benzol, and butanol) from a free surface into a turbulent air stream and concluded that

$$Sh = 0.094\ Re^{0.8}\ Sc^{0.33}\ Gu^{0.2} \tag{2.93}$$

in which, Gu is the Gukhman number given by

$$Gu = \frac{T_a - T_w}{T_a} \quad , \tag{2.94}$$

with T_a and T_w the dry and wet bulb temperatures of the free stream respectively.

Relatively little has been published to date on the effect of roughness on the rates of heat and mass transfer. Moreover, results from different investigators sometimes disagree either partly or completely. In connection with their work on flow through rough tubes, Nunner (1956), Smith and Epstein (1957), and Dipprey and Serbersky (1963) found that the presence of roughness increased the heat (or mass) transfer rates. On the other hand, Pohl (1933), and Kolar (1965) found the opposite, especially at high Re.

Levich (1962) proposed that if the height of roughness elements was greater than the thickness of the viscous sub-layer, but less than that of the turbulent boundary layer, the hydrodynamic situation may be modified in such a way that a decrease of the mean mass transfer would result. He came to this conclusion after considering the following. In turbulent flow, he postulated two zones in the hydrodynamic boundary layer -- a viscous sublayer near the solid interface in which momentum transfer occurs mainly because of friction, and a turbulent boundary layer further outside where the exchange of momentum takes place by turbulent eddies. In a similar fashion, a diffusion sublayer exists where mass is transferred mainly by a molecular mechanism; further outside there is a concentration boundary layer where mass transfer occurs because of turbulent mixing. The diffusion sublayer usually will develop around the roughness peaks. However, a separation in the flow over individual protrusions will also occur in the case where the roughness height is greater than the thickness of the viscous sublayer, but less than that of the turbulent boundary layer. Levich proposed a

theoretical correlation for the mass transfer rate in terms of friction velocity, difference of surface and free-stream concentrations, and fluid properties (for $Sc \gg 1$):

$$E' = \frac{D(\Delta q)\ u_*^{1/2}\ Sc^{1/4}}{\nu^{1/2}\ h^{1/2}} = \frac{(\Delta q)\ D^{3/4}\ u_*^{1/2}}{\nu^{1/4}\ h^{1/2}} \qquad (2.95)$$

in which h is the height of roughness, Δq the difference of free stream and surface concentrations, D the molecular diffusivity, and $E' = K_c(\Delta q)$. Since $u_* = (\frac{C_f}{2})^{1/4}\ U_\infty$, Eq. 2.95 reduces to

$$\frac{E'\ell}{D(\Delta q)} = (\frac{C_f}{2})^{1/4}\ Re^{1/2}\ Sc^{1/4}\ (\ell/h)^{1/2} ,$$

or

$$(Sh)_\ell = (\frac{C_f}{2})^{1/4}\ Re^{1/2}\ Sc^{1/4}\ (\frac{\ell}{h})^{1/2} \qquad (2.96)$$

in which ℓ is a characteristic length, $(Sh)_\ell = E'\ell/D(\Delta q)$, and $Re = \ell U_\infty/\nu$.

Although Levich's model presents a basic approach of the problem of mass transfer from rough surfaces, its applicability is limited to cases which satisfy the condition $Sc \gg 1$. Equation 2.96 agrees with the results obtained by Mahato and Shemilt (1968) in their experiments with the corrosion of commercial iron pipe by water under isothermal turbulent flow conditions, where the concept of mass transfer is that of the transfer of a depolarizer (dissolved oxygen, $Sc \simeq 238$) to the cathodic sites on the corroding pipe. On the other hand, Lai's (1969) evaporation data, from his experiments on small water waves ($Sc \simeq 0.60$),

did not correlate well with Levich's equation (2.96). Lai obtained a variation of Sherwood number as $Re^{0.85}$ insteady of $Re^{0.5}$.

In addition, the derivation of equation 2.96 does not take into account the fact that protrusions themselves extending into the boundary layer are in a somewhat favored position from the standpoint of diffusion. Therefore, Eq. 2.96 gives somewhat low values for the mass transfer rate. Secondly, it is to be noted that the true surface area of a rough body with a large number of protrusions may greatly exceed the apparent surface area. Thus, in computing the diffusional flux, Eq. 2.96 should be multiplied by a factor to take care of the area differences.

Kolar (1961) and (1965) presented a theoretical analysis of heat and mass transfer in the turbulent flow of fluids through smooth and rough tubes. His theoretical consideration was based on description of the hydrodynamic relations on the phase boundary employing quantities and relations derived in the statistical theory of turbulence. He assumed the following: (1) the fluid at the interface consists of vortex elements of dimension λ_o and fluid velocity $U_{\lambda o}$ with

$$\lambda_o = \left(\frac{\nu^3}{\varepsilon}\right)^{1/4} \quad \text{or} \quad \frac{\lambda_o U_{\lambda o}}{\nu} \simeq 1 \,, \tag{2.97}$$

in which λ_o is the local degree of turbulence, $U_{\lambda o}$ is the velocity in fluctuation of dimension λ_o, ε is the energy dissipation per unit mass per unit time, and ν is the kinematic viscosity and (2) within these vortex elements, heat (or mass) is transferred by molecular mechanisms. On solving the appropriate differential equation with

relevant boundary conditions, he obtained for the heat transfer coefficient the following relation

$$h = 2\left(\frac{\alpha}{\pi \tau_e}\right)^{1/2} \tag{2.98}$$

in which α = thermal diffusivity and

$$\tau_e = \frac{\lambda_o}{U_{\lambda o}} \quad . \tag{2.99}$$

According to assumption (1), τ_e is the period of time when part of the surface of the vortex element is in contact with the medium in which the heat transfer occurs. Thus, Eq. 2.98 indicates that the rate of heat transfer is inversely proportional to the time the vortex element is in contact with the surface. Combining Eqs. 2.97, 2.98, and 2.99, one obtains

$$\frac{hd}{k} = \frac{2}{\sqrt{\pi}} \left(\frac{d}{\lambda_o}\right) (Pr)^{0.5} \quad . \tag{2.100}$$

Kolar, then, made use of his experimental data to evaluate λ_o and obtained the relation,

$$\frac{hd}{k} \simeq \left(\frac{u_* d}{\nu}\right) (Pr)^{0.5} \quad ,$$

or

$$Nu \simeq (Re_*)_d \, Pr^{0.5} \quad , \tag{2.101}$$

in which $(Re_*)_d = u_* d/\nu$. He obtained good agreement between his experimental results on flow through tubes and the above relation. Thus, relation (2.101) depicts the mechanism of heat transfer, as well as mass transfer on parallel lines, of flow through smooth tubes and through tubes with various forms of surface roughness.

On theoretical grounds and by analysis of their experiments on mass and heat transfer in flow over rough surfaces, such that $\frac{u_* h_1}{\nu} > 100$ (where $h_1 = 30 z_o$ = the equivalent sand roughness), Owen and Thomson (1963) postulated that

$$B^{-1} = \alpha_1 \left(\frac{u_* h_1}{\nu}\right)^m \sigma^n \qquad (2.102)$$

where

$$\frac{\rho U(z)(q_s - q)}{E} = \frac{U(z)}{u_*} \left[\frac{U(z)}{u_*} + B^{-1}\right] , \qquad (2.103)$$

$\sigma = \frac{\nu}{D(\text{or } \alpha)}$, m and n are constants to which values 0.45 and 0.8 were assigned. In Eq. 2.102, α_1 was suggested to be a constant for each experimental arrangement, but varied according to the type of roughness.

Chamberlain (1966 and 1968) conducted some wind tunnel experiments on the transport of a radioactive vapor of thorium B and water vapor, to and from some rough surfaces. He analyzed his results in the light of the empirical formula (2.102) derived by Owen and Thomson (1963).

2.7 Similarity of Laboratory and Field Data

The increasing need to study environmental problems in areas of complex boundary conditions has motivated serious efforts to simulate

atmospheric boundary layers in the laboratory (15). Simulation of the entire atmospheric boundary layer in an "exact" sense does not appear to be possible. However, comparisons of data obtained in appropriate wind tunnels with corresponding data measured in the atmospheric surface layer have shown good similarity.

The similarity requirements are expressed in terms of dimensionless parameters which should be nearly equal for both the model and prototype, if similarity is to exist. These requirements are summarized as follows (detailed discussions of these requirements are given in (14) and (15)):

Type of Similarity	Requirement
A. Geometrical	1. Undistorted scale model
B. Dynamic	1. Rossby No. -- $\bar{U}_o/(L\Omega)$
	2. Richardson No. -- $g\Delta TL/(T_o\bar{U}_o^2)$
	3. Reynolds No. -- $\bar{U}_oL/\nu$ or $\bar{U}_oL/K_M$
C. Thermal	1. Prandtl No. -- $k/(C_p\mu)$
	2. Specific heat ratio -- C_p/C_v
	3. Richardson No. -- $g\Delta TL/(T_o\bar{U}_o^2)$
D. Boundary Conditions	1. Surface temperature and roughness distributions.
	2. Vertical distribution of velocity and temperature in approach flow
	3. Pressure variation in direction of mean flow

Fundamental difficulties arise in attainment of exact similitude for only two of the requirements. These are equality of Rossby numbers and equality of Reynolds numbers for the model and the atmosphere.

Consequently, the motions under consideration must not be influenced strongly by rotation of the earth. For air motion strongly influenced by city geometry and/or complex topographical features less than about 10 miles in extent, relaxation of Rossby-number equality does not appear to introduce significant differences in model and prototype flow patterns.

Reynolds number similarity based on the viscosity of air is neither practical nor essential for many model-studies, such as wind loads on buildings and structures, shelter belts, dispersion of smoke from chimneys, etc. Two alternatives have been offered by different authors. Nemoto (1961) evolves an "eddy" Reynolds number defined as

$$R_{e_k} = \frac{UL}{K_M} \tag{2.104}$$

as a similarity parameter. It is obviously not a practical criterion because the eddy diffusivities are not known accurately in either the field or in the wind tunnel. On the basis of assumptions of local isotropy and identity of rates of energy dissipation in the two flows, Nemoto (1961) expresses the Reynolds number criterion for modeling wind velocity as

$$\frac{U_{\infty M}}{U_{\infty p}} = \left(\frac{L_M}{L_p}\right)^{1/3} . \tag{2.105}$$

This is much more plausible form of Reynolds number similarity and has the effect of scaling down the wind velocity instead of requiring it to be increased for the model as was the case with ordinary Reynolds number. The above approach to Reynolds number similarity disregards the

effects of surface terrain on flow phenomena. The fact that the turbulent flow of air in the surface layer over an urban area is invariably aerodynamically rough, opens up a new possibility. It has been established that an aerodynamically rough flow is similar to any other aerodynamically rough flow irrespective of its velocity, roughness length and kinematic viscosity. In other words, the velocity of flow, roughness length and viscosity can be varied independently of each other. Thus if the flow over the model is rough, the Reynolds number need not be modeled. This freedom is essential in that if the flow over the model is not rough, its turbulence characteristics would be considerably different from those in the atmosphere.

In addition to the various similarity parameters mentioned above, the boundary conditions should be reproduced faithfully. Of importance, specially in case of simulation of wind-break sheltering effects, is the criterion pointed out by Jensen (1958) that the roughness parameter for the tunnel-floor must be scaled to the roughness parameter in nature, i.e.,

$$\frac{z_{op}}{z_{om}} = \frac{L_p}{L_m} \tag{2.106}$$

where z_{op} is the roughness parameter in nature, z_o is the roughness parameter in the wind tunnel, and L_p/L_m is the scale ratio from prototype to model. The model must of course be entirely immersed in the turbulent boundary layer of the tunnel as is possible in the CSU wind tunnels used for this investigation.

The foregoing discussion has summarized pertinent investigations on mass and momentum transfer from smooth and rough surfaces. The information

on mass and momentum transport from rough surfaces is very limited. In view of this and because of the difficulty of controlling the variables encountered in field research and because of the great amount of time and money involved, laboratory investigation of this problem was initiated at the Fluid Dynamics and Diffusion Laboratory of Colorado State University.

CHAPTER III

EXPERIMENTAL EQUIPMENT AND PROCEDURES

Experiments were conducted in the Colorado State University wind tunnel and the U.S. Army Meteorological wind tunnel. Both tunnels are located in the Fluid Dynamics and Diffusion Laboratory at the Engineering Research Center of Colorado State University. Drawings of these wind tunnels are given in Fig. 1 and 2, respectively and Table 1 summarizes their performance characteristics. The experimental equipment and measuring techniques are discussed in the following sections.

3.1 Physical Arrangement in the Experiments

Experiments were performed with two different physical arrangements in the wind tunnel. A series of sinusoidal waves were chosen to represent the corrugations and a series of equally spaced fences were used to represent a row of impermeable wind breaks. These two arrangements are described below in detail.

3.1.1 Wave assembly - Figure 3 shows the layout of the experimental arrangement used in this study. The experiments on waves were conducted in the CSU wind tunnel. The measurements were taken on sinusoidal waves cut in three sizes (λ = 4.2 in. and h = 1.70 in., 1.0 in. and 0.50 in.)[1]. These waves were cut from styrofoam[2] blocks with a single shaper blade on a horizontal milling machine at the Engineering Research Center workshop. Figure 4 shows photographs of the three different sizes of waves and the shaper blades used to cut these waves. The styrofoam waves

---

[1] λ and h denote the wave length and height of a wave.

[2] Styrofoam is the commercial name for polystyrene foam.

were laid in aluminum pans (Figs. 3 and 5), which were of sizes convenient for moving. Aluminum channel supports were spot welded to the bottom of these pans; the waves were later screwed down in sets to these channel supports to keep them from floating when the pans were filled with water. An asseumbly of six pans was used (Figs. 3 and 5). The first pan contained a set of 4 1/2 waves, the next four contained 5 waves each, and the last pan contained 3 1/2 waves, in addition to a specially built wave, called the evaporation metering wave (described in section 3.6). These pans were placed adjacent to each other in the wind tunnel (as shown in Fig. 3), and a sheet of felt was positioned very carefully over the waves, following their contour. Small stainless steel pins were used to tack the felt to the waves. The ends of the waves toward the walls of the wind tunnel were sealed. When positioning the individual styrofoam waves in the pans, care was taken to leave a small (about 1/32 in. wide) crack between each wave to allow water to flow up from the bottom of the pans (Fig. 5); thus the continuity of the wavy surface was not disturbed. Once the pans containing the waves were assembled, they could be conveniently moved in or out of the wind tunnel. Distilled water was supplied from a reservoir (shown in Fig. 5) to the bottom of each pan. The water level was maintained so that water came to the top of the crack in the troughs of the waves (Fig. 5). Before beginning a run, the felt surface was saturated with water; it was observed that the felt remained wet everywhere as long as the desired water level in the pans was maintained.

Local heat transfer measurements were made by replacing the evaporation metering wave in above set up by a similar styrofoam wave

on which a flush mounted heated film could be located (details given in section 3.7). No water was supplied to the pans so that all the waves were dry.

The surface upstream of the waves was raised by the addition of a false floor (approximately 4 3/16 in. high). Also, just upstream of the false floor, a 6 ft wide aluminum sheet was placed to provide a smooth transition from the contraction section to the false floor (Fig. 3). A 9 1/2-in. wide strip of steel brushes were positioned across the entire width of the wind tunnel between the aluminum sheet and the false floor at a distance of about half an inch from the leading edge; the brushes were used for tripping the turbulent flow and thickening the boundary layer. Downstream, at the end of the pan assembly, 2 1/2 styrofoam waves and a 6 ft wide sloping surface were located to provide a smooth transition from the end of the waves to the wind-tunnel floor (Fig. 3).

3.1.2 Fence assembly - The experiments on equally spaced fences were conducted in the U.S. Army meteorological wind tunnel. Fence elements were made from commercial aluminum angle beams, measuring 1" x 1" x 1/8". One side of the angle beam was machine sharpened to 45^{o} and the sharp edged side stood vertically as a fence, the other side served as the foot of the fence (refer to Fig. 6). All fences were cut 6 ft long; conner fillets were used to insure all fences extended to the full tunnel width. The front edge of the first fence was located at $x = 0$, which indicates the leading edge of the aluminum floor or 40 ft from the wind tunnel entrance. From the first fence downstream, all fences were fixed on a 1/2 in. thick plywood floor. The spacing between each fence was chosen at a constant value L for each run. The

plywood floor was made to cover the total test section. Double stick scotch tape was inserted between the fence foot and the plywood floor and 3/8 in. wood screws were used to fasten fences on the floor. Half inch wooden strips were glued to the bottom of the plywood to elevate it one inch above the original aluminum floor. In order to measure the stagnation pressure at the foot of each fence, three 1/16 in. ID pressure taps were drilled in front of each fence through the plywood floor. One pressure tap was drilled at the wind-tunnel center line, the other two were drilled 12 in. to the right and to the left of the center line. Plastic tubes were connected to the pressure taps and let outside to the tunnel through the space between the plywood floor and the aluminum floor.

The 1 in. high plywood floor was extended 16 ft downstream from $x = 0$ and 10 ft transition extended farther upstream to elevate the original floor to a 1 in. height. A sketch of the floor assembly is shown in Fig. 6.

Pressure tapped fences, which were used to measure the form drag of fences, have the same shape and dimensions as the other fences except some pressure holes were drilled. Two tapped fences were made--one for measuring the stagnation pressure on the front surface of a fence and another used to measure the separation pressure on the rear surface of a fence. Seven pressure holes were drilled on the first fence, with each hole spaced 1/8 in. in the vertical direction. And since the separation pressure was constant over the height of the fence (see Plate, 1964, and Nagabhushanaiah, 1961), only three pressure holes were drilled on the second fence (Fig. 6). Three sets of such pressure holes

were drilled on both tapped fences, one set was at the center line and the other two were located 12 in. right and left from the center line.

Pressure gradients over that part of the test section which was covered with fences were adjusted to nearly zero.

3.2 Log of Experiments

The list of primary measurements with different physical set ups is given below.

Physical Set Up	Primary Measurements
Wave Assembly (Wet)	Distribution of mean velocity, mean humidity, mean temperature, and local mass transfer coefficient.
Wave Assembly (Dry)	Distribution of mean velocity, turbulence, wall pressure and local heat transfer coefficient. Drag measurements and visualization.
Fence Assembly (Dry)	Distribution of mean velocity turbulence, wall pressure and local heat transfer coefficient. Drag measurements.

3.3 Measurement of Mean Velocity and Turbulence

3.3.1 Mean velocity - Mean velocity profile at different longitudinal stations were measured by pitot tubes. Hot wires were also employed to cross check the values obtained by pitot tube measurements.

Near roughness elements, significant pressure gradients exist both in x and z directions (56), with the pressure gradient in the lateral direction being approximately zero because of the assumed two dimensionality of the flow. The velocity measured by a conventional pitot tube must involve an error because of the presence of the above mentioned pressure gradients. In view of this, both the dynamic and static taps were put on two different arms held along the y-axis ((56) and (110)) in order to obtain approximately zero pressure gradients

between the two taps. Both the total and static heads were measured by connecting the dynamic and static taps to the P_x and P_{ref} pressure terminals, respectively, of an electronic pressure meter. The D.C. output of this pressure meter was proportional to the pressure difference $(P_x - P_{ref})$ in mm Hg. An integrator built at the Fluid Dynamics and Diffusion Laboratory at Colorado State University (56), in conjunction with a D.C. amplifier and a digital voltmeter, was used to obtain the averages of the pressure meter output. Calibration details of these instruments are described in references (56) and (110).

3.3.2 Turbulence - Three types of hot-wire arrangements were used to measure the various statistical quantities of turbulence, that is, a single wire, placed normal to the flow for measuring $\overline{u'^2}$, the x-wire, and a rotating wire for measuring $\overline{u'w'}$ and $\overline{w'^2}$. Constant temperature hot-wire anemometers were used. The details of these hot-wire measurements were described in references (5) and (56).

3.4 Measurement of Moisture Content

The moisture content of the air flow was measured by sampling the gas stream through a specially built sampling probe (see Figs. 11 and 12), connected to a dew point hygrometer (Cambridge Systmes, Model 992), at a constant flow rate maintained by a vacuum pump built in the hygrometer. During an experimental run, the background humidity changed, although very slowly, with time because the recirculating air gradually absorbed additional moisture. Also, the surface air humidity changed slightly. Two stainless steel sampling probes were used simultaneously to measure both the local moisture content in the boundary layer and the free-stream moisture content. The sampling lines connecting the sampling

probes to the dew point hygrometer consisted of 1/4 O.D. teflon tubing with stainless steel swagelok fittings and a three-way stainless steel valve. The surface air humidity was determined by measuring the surface air temperature, T_s by a copper-constantan thermocouple, after assuming that it was equal to the saturated humidity at temperature T_s.

The dew point hygrometer, utilizing a thermoelectrically cooled optically sensed mirror, directly measures the temperature at which the vapor adjacent to a surface of water is in equilibrium with the vapor in the sample gas. This is the dew point temperature of the gas; the moisture content of the gas can be determined from this using some standard relations (see Appendix A). A simplified block diagram of the hygrometer along with an interior view of the instrument is shown in Figs. 13 and 14. In addition to the thermoelectrically cooled mirror which has an internal thermometer, the dew-point sensor contains an optical sensing bridge for sensing the dew formation. The amplifier unit consists of solid-state amplifiers and control components for amplifying the output of the optical sensing bridge, and controlling the mirror. The temperature of the mirror, representing the dew point temperature, is determined by a platinum resistance thermometer. The details of the working and calibration of this instrument are given in (110).

3.5 Measurement of Mean Temperature

All temperature measurements were taken with copper-constantan thermocouples. A precision potentiometer (Leeds-Northrup Co., type K-3), in conjunction with an accurate galvanometer, a standard cell and a set of batteries, was used to measure the output of each thermocouple.

In the temperature profile $(T-T_s/T_\infty-T_s$ vs height) measurement, three thermocouples were simultaneously used, to measure the local temperature in the boundary layer, the free-stream temperature, and the surface air temperature, respectively. The free stream and surface air temperatures had to be measured along with the local temperature at every point of measurement so that the changes in ambient and surface temperatures could be taken into account. The surface thermocouple was positioned very carefully on the surface of the wave at each measurement station.

Every thermocouple used in this study was calibrated in a temperature calibrator. This calibrator consists of an insulated oil bath equipped with a heater, a cooling coil, a thermostat, and a set of precision thermometers. All thermocouples were calibrated before and after the experimental runs in the wind tunnel. This was done to check for any suspected drift in the stability of the batteries or the standard cell used. No appreciable differences were noted.

3.6 Measurement of Local Evaporation Rates

Local mass transfer coefficients were determined by measuring the actual volume of water that had evaporated from different sections of a saturated wavy surface in a given time. These measurements were taken from a specially designed "evaporation metering wave", in an approximately fully developed boundary layer, located about 10 ft from the initial upstream wave (Fig. 3). This special wave facilitated the direct measurements of local evaporation rates. These rates could be determined with the aid of an "automatic feed and metering system". Both the

"evaporation metering wave" and the "automatic feed and metering system" are described subsequently.

3.6.1 Evaporation metering wave - A detailed drawing of the evaporation metering wave is shown in Fig. 7. Taken from a top view, the wave (of wavelength = 4.2 in.) was divided into eight sections of equal width with thin (0.020 in.) copper baffles comprising both the sides and the bottom of each section. The copper channels (which consisted of the above mentioned copper baffles) were fixed to an aluminum block with the top edges of the channels forming the desired sinusoidal profiles. The dimensions of these copper channels and the aluminum block were computed so that when combined they resulted in a sinusoidal-shaped wave of desired amplitude and wavelength (Fig. 7 and 8). Strips of blotter paper (0.022 in. thick) were cut to fit vertically in these channels; the tops of the blotter papers were carefully sanded to form a continuous surface. Water from separate burettes, belonging to the automatic feed and metering system described later, was supplied to the bottom of these sections through brass tubings. It was carried to the top of the blotters by capillary action. Thus, the blotter surface was kept completely wet as long as the water supply was maintained. Brass screens (18 x 14 mesh, 0.011 in. diameter wire) were placed at the bottom of each section to keep the blotter papers in position. The dimensions of these screens were designed so that the water travelled equal distances through the blotter capillaries at every part of the wave. Figure 6 shows the relative positions of the screens, tubings, copper channels, etc., in the wave. The presence of the thin copper walls prevented the longitudinal transport of water from one section of the wave to another. From a top view, the measuring wave was 2 ft long. Two

additional waves (called the buffer waves), each also 2 ft long, were provided on each end of the measuring wave (Fig. 3). These buffer waves were also kept wet to minimize lateral diffusion of water vapor. Care was taken to seal the ends and sides of the metering wave to avoid any leaks. To measure the surface air temperatures, copper-constantan thermocouples were mounted on the wave surface in each section. The thermocouple beads were placed in the center of the top surface of the blotters; their leads ran 1/4 in. downward from the surface and then along the horizontal length of the wave between two blotter layers, to minimize conduction errors.

Metering waves of three sizes, namely λ = 4.2 in. and a = 0.85 in., 0.5 in., and 0.25 in., were built separately. Figure 7 shows the dimensions for a typical case.

3.6.2 Automatic feed and metering system - A photograph of the automatic feed and metering system is shown in Fig. 9. This system maintains and measures the supply of water to each of the eight sections of the metering wave; it is similar to the one used by Cermak and Lin (1955), and Nelson (1957). Figure 8 shows the arrangement needed for one typical wave section. Each wave section was linked to a graduated burette, which in turn was connected to its own water bottle. These burettes were closed by rubber stoppers at the top; two brass tubes (0.092 in. O.D.) were inserted in each through holes in the rubber stoppers. The bottom end of tube A (Fig. 10) was used to control the water level in the corresponding wave section. The pressure difference, created by the water loss from evaporation at the top of the wave section, was compensated for by drawing water from the burette automatically. This volume of water drawn from the burette was replaced by the ambient

air coming through tube A. Thus, the evaporation of water from each wave section took place at ambient pressure and the amount of water that evaporated from each section in a given time was measured from the drop of water level in the corresponding graduated burette. Burette readings were corrected to account for the volume occupied by the brass tube A in each burette.

3.7 Measurement of Wall Heat Flux and Local Shear Stress

Wall heat flux was measured by a point source (1 mm x 0.2 mm) of heat (Fig. 15). The heated element was a Disa 55A90 flush-mounted film operated at a small overheat (ΔT from 10 to 45^{o}C) by a Disa 55D01 constant resistance anemometer. The overheat ΔT equals the difference $T_f - T_a$, where T_f is the film temperature (assumed constant on the film surface) and T_a is ambient temperature. The resistance ratio R_H/R_c was determined for a specified overheat, ΔT, by the following relation

$$R_H/R_c = 1 + \alpha'\Delta T \ . \tag{3.1}$$

R_H and R_c are the hot and cold resistances, respectively, of the film and α' is the temperature-resistance coefficient, equal to 0.3%/^{o}C (calibrated). The changing ambient temperature of the tunnel air was measured by a Yellow Springs Tele-Thermometer model 405.

The wall-heat flux in the form $I^2R/\Delta T$ can be related to the shear stress τ through a calibration of the form

$$\frac{I^2R}{\Delta T} = M\tau^{1/3} + P \ , \tag{3.2}$$

where M and P can be found from calibration as described later. The use of flush-mounted heated films for shear stress measurements was recently investigated by Bellhouse and Schultz (1966, 1967, 1968) and Brown (1967). The calibration, Eq. 3.2, describes the behavior of the film for zero pressure-gradient flows. Brown extended the calibration for flows with pressure gradients to

$$\tau + \frac{5}{18} L\frac{dp}{dx}\frac{1}{Nu} = \frac{19}{10}\frac{\mu^2}{\rho(Pr)^2}\frac{1}{L^2}Nu^3, \tag{3.3}$$

where Nu = Nusselt number of film, L is a characteristic length and Pr is the Prandtl number of fluid. However, the velocity profile must be represented by

$$\left.\begin{aligned} U &= \frac{\tau_w}{\mu} z + \frac{1}{2\mu}\frac{dp}{dx} z^2 \\ &\text{and} \\ W &= 0 \quad . \end{aligned}\right\} \tag{3.4}$$

Under these conditions, the film could be used up to separation.

The film was calibrated on a circular cylinder at $Re_d = 10^5$ in a uniform stream using the values of τ obtained from many sources, ((1), (28), (32), (95)). Two typical calibrations are shown in Fig. 15 and 16. Note should be ade of the following results: First, the calibration

$$\frac{I^2R}{\Delta T} = M\,\tau^{1/3} + P \tag{3.5}$$

holds for ΔT constant, as noted by others ((6) and (12)). Second, the intercept P is a function of ΔT. Consequently, the film was recalibrated for a range of ΔT's. The resulting values of I^2R, ΔT and $\tau^{1/3}$ were used to correlate the film response to

$$I^2R = \tau^{1/3}(A + B\Delta T + C(\Delta T)^2) + (D + E\Delta T + F(\Delta T)^2). \quad (3.6)$$

Estimates of A, B, C, D, E and F within 10% are

$$A = -3.9 \times 10^{-2} \qquad B = 5.6 \times 10^{-3}$$
$$C = -8.0 \times 10^{-5} \qquad D = 7.0 \times 10^{-2}$$
$$E = 5.7 \times 10^{-4} \qquad F = 1.5 \times 10^{-5} .$$

Using these values for the constants, τ can be obtained from measurements of I^2R and ΔT. The response Eq. 3.6 was used to "predict" the shear stresses for the calibrations shown in Fig. 16. The "predicted" and calibration shear stresses are shown in Fig. 17. In general, the response equation gives stresses within $\pm$ 10% of the calibration stresses when the measured calibration I^2R's and ΔT's are used in the equation. Although these results may be misleading, the response of the film to changing ΔT could be checked no other way. The slope $M = A + B\Delta T + C(\Delta T)^2$ is given (12) by

$$M = kW_1 \frac{(\rho\sigma)^{1/3}}{1.9\mu^2} L^{2/3} \quad (3.7)$$

where W_1 and L are the width and length of the film. The effective length, L_e, of the film can be determined from Eq. 3.7, and for

$M \cong 2 \times 10^{-3}$ (watts/C)/$(psf)^{1/3}$, $L_e \cong 2L$, in agreement with Brown (1967). Also, the slope M is a weak function of the ambient temperature (12), and $A + B\Delta T + C(\Delta T)^2$ gives the correct variation with changes in ambient temperature.

The goal was to determine areas of erosion and strong shear, which would be detrimental to seeds on the micro-ridges, by measurements of heat loss and wall pressure. An attempt to correlate the heat losses to shear stress was also made. The results of this part of the measurements are presented in Chapter IV.

3.8 Measurement of Drag Force

3.8.1 Waves - The drag force on the waves was determined in two ways; first, by integrating the wall-pressure distribution, and secondly, by using a shear plate.

The pressure distribution on the surface of the waves was measured by a special pressure tapped wave, placed at the 27th wave position. This pressure tapped wave has the same shape and dimensions as other styrofoam waves except that 17 equispaced holes were drilled across the midsection of the wave. Each pressure tap was in turn connected to an electronic pressure meter. The meter measured the difference in the wall pressure at that point on the wave and the static pressure at a reference height in the free stream. Fig. (69) shows the wall pressure distributions along the surface of the waves. Details of the computation of average skin-friction coefficient C_f are given in Appendix B.

So that drag force could be directly measured on different kinds of surfaces, Hsi and Nath (1968) had previously designed a special shear plate. This shear plate is made of aluminum with dimensions of 0.635 cm x 59.6 cm x 59.0 cm. This plate was separated from the foundation

plate by three chrome-steel balls (0.635 cm diameter). Two stainless steel restoring arms, 0.317 cm x 1.27 cm x 45.6 cm each, were used. One end of the arm was attached to the shear plate and the other to the foundation plate. Four semi-conductor strain gages, one on each side of the restoring arm, were installed at 1.27 cm from the end of the restoring arm which was attached to the foundation plate. The shear plate moved back and forth in a horizontal plane only; it had a natural frequency of six cycles per second. The construction of the shear plate has been described in detail in (42).

If a horizontal force was applied to the shear plate, the plate would be displaced according to the spring constant of the restoring arms and the magnitude of the applied force. The shear plate would return to its original position after the applied force was removed. An 8 volt D.C. power supply and a D.C. micro-ammeter in conjunction with a digital voltmeter and a digital printer were used to measure the shear plate readout.

Three 23.5 in. pieces of styrofoam wave were attached by masking tape to the top of the shear plate. The shear plate was put in the wind tunnel so that the above wave pieces would occupy the 26^{th}, 27^{th}, and 28^{th} wave positions; other styrofoam waves were put on each side and at each end of these pieces to maintain the continuity of the wavy surface. Care was taken to properly seal the ends and sides of these pieces. The shear plate was calibrated on location by applying a known horizontal force to the plate and recording the bridge output. These measurements were conducted on all the wave sizes.

3.8.2 Fences - The drag force on the fences was measured by means of two tapped fences; one was the "stagnation fence" and another was the

"separation fence" (Section 3.1). The stagnation pressure acting on the upwind surface of a fence was measured through seven pressure taps on the stagnation fence. The stagnation pressure at the lowest point of the fence was measured through the pressure tap drilled through the plywood floor (Section 3.1). Stagnation pressure measurements at $z = 7/8"$, $6/8"$, $5/8"$, $4/8"$, $3/8"$, $2/8"$, $1/8"$, and $z = 0$ were recorded. By substituting the separation fence for the stagnation fence, the separation pressure on the lee side of the fence was measured. Separation pressures were measured at $z = 2/8"$, $4/8"$, and $7/8"$. Constant separation pressure was found in the z direction which is in agreement with Plate and Nagbhushanaiah.

The form drag D_f of a fence was obtained graphically:

$$D_f = \int_0^h (p_f - p_b)\, dz \tag{3.8}$$

where

h = fence height = 1 inch,

p_f = pressure measured by the stagnation fence, and

p_b = pressure measured by the separation fence = constant for each fence.

3.9 Visualization of Flow Pattern

To get a qualitative picture of the flow pattern in the troughs of the waves, a visualization study was made. Air motions were traced by releasing smoke near the waves, and visible records were obtained by means of pictures taken from a 35 mm still camera. The smoke was produced by passing moist air through a container of titanium-tetrachloride

located outside the wind tunnel floor by means of a tygon tube terminating at suitable locations near the waves. Figures 62 and 63 show some of the photographs taken during this study.

CHAPTER IV

RESULT AND DISCUSSION

The results of various measurements on the waves and fences are presented. Emphasis is placed on the region far downstream from the leading wave or fence, because at this location the momentum boundary layer in each case is approximately fully developed and equilibrium boundary layer conditions are obtained. Average mass and momentum transfer characteristics from these surfaces are considered. Variation of local mass and heat transfer coefficients are investigated in an effort to maximize the available moisture and heat for plant growth. The results are compared with certain other pertinent investigations in this subject. Applications of this study in practical situations are discussed.

4.1 Mean Velocity Distribution and Drag Measurements

4.1.1 Waves - The dimensionless velocity profiles (U/U_∞ vs z_c/δ) at different longitudinal positions are plotted in Figs. 18, 19 and 20, in which z_c is the height measured above the respective wave crest and δ is the boundary-layer thickness, where δ is defined by $U_\delta = 0.99\ U_\infty$. Figures 18, 19 and 20 clearly show the changes in the velocity profiles above the waves proceeding downstream. But for stations downstream of 22nd crest, all non-dimensional velocity profiles approximately collapse into a single curve. In addition the quantities $\frac{u_*}{U_\infty}$ and $\frac{dp_\infty}{dx}$ became almost constant for $x \geq 7$ ft, where x is measured from the start of the leading wave (see Figs. 24 and 25). This means that the boundary layer reached its equilibrium condition for

$x \geq 7$ ft (94). Plots of relevant boundary-layer parameters, e.g., boundary layer thickness δ, displacement thickness δ^*, momentum thickness θ and form factor H, are shown in Figs. 21, 22 and 23.

Measuring form drag on the waves by two different methods, namely, integrating wall pressure distributions, and using a shear plate was discussed in Section (3.8). Table 2 gives the values of the effective skin-friction coefficient C_f obtained from both methods in the far downstream region. The agreement of results from these two different methods in most cases is within 20 to 25 percent.

Friction velocities were obtained primarily from the measurements of velocity profiles. The results from drag force measurements were used to cross-check these values. In order to obtain u_* and z_o, it was assumed that the velocity distributions followed the logarithmic profile

$$\frac{U}{u_*} = \frac{1}{k} \ln \frac{z}{z_o} \qquad z > z_o \qquad (4.1)$$

for nearly neutral conditions (see page 61). In Eq. 4.1, z is the height measured from effective zero plane given by $z = z_T - d = z_c + \varepsilon$ and $\varepsilon = h - d_c$ is the height measured above the respective wave crest, d is the zero plane displacement, and h the wave height. The value of d was estimated by a method similar to the one used by Perry et al. (1969). The velocity profiles on wave crests in the far downstream region were first plotted on the $\frac{U}{U_\infty}$ vs z_c axes. An estimate of the required slope of the final logarithmic distribution $(2.5 \ln \frac{C_f}{2})$ was then calculated using values from the drag measurement results. Values of ε were then added to the abscissa of the raw profile in a trial-and-

error process until a value of ε was obtained that gave a straight line, in the lower part, with a slope close (within 10 to 15 percent) to the above predetermined value of $2.5 \ln \frac{C_f}{2}$. The values of $d(= h - \varepsilon)$ so obtained are given by $\frac{d}{h} = 0.5$, 0.25 and 0 for waves A, B, and C, respectively, with $\frac{h}{\lambda} = 0.41$, 0.24 and 0.12. This means, from the bottom of the waves, the effective zero plane is raised by a half and a quarter of the wave height for the steepest and the intermediate waves, but remains unchanged for the shallowest one, which seems reasonable.

Considering the above and using Eq. 4.1, values of u_* were computed for different longitudinal positions assuming d constant with fetch. Figure 25 shows the variation of friction velocity with fetch for all three wave situations. The results indicate that the friction velocity initially undergoes a rapid change when the air first encounters the change of roughness, and then adjusts itself in the far downstream region. This type of response in the wall shear stress has been predicted by many investigators and is consistent with that measured by Yeh (1970).

Having obtained the u_* values, values of z_o were obtained by using equation 4.1. In the far downstream region, the values of z_o varied from 0.03 to 0.175 in. for the three wave sets, which are comparable, at least with regard to the order of magnitude, to the results obtained in investigations above similar surfaces [e.g., Chamberlain (1968), and Owen and Thomson (1963)].

In the evaporation experiments, a temperature gradient was set up as heat was transferred from the air to the evaporating surface

(see Section (4.4) also). However, the gradient of windspeed in the lowest few inches (above the wave crests) was large, and a typical value of the Richardson number $= \frac{g}{T} \frac{\frac{\partial T}{\partial z}}{(\frac{\partial U}{\partial z})^2}$ for $1 \text{ in.} < z_c < 4 \text{ in.}$ was found of the order of 10^{-3}. The Monin-Obukhov parameter $L = \frac{u_*^3}{k \frac{g}{T} (\frac{H_o}{\rho C_p})}$ (with $H_o \simeq L_e E$, see Section 4.4), was of the order of 10^3 cm. This means that an error of about 2 to 3 percent is involved in estimating u_* by using the relation (4.1). Thus, the effect of stability on the velocity profile could be neglected.

4.1.2 Fences - Figures 26 and 27 show a typical set of velocity profiles above fences at different longitudinal positions and the corresponding boundary-layer parameters. The boundary layer deviates from the initial profile (at station $x = -4$ ft) when it encounters the fences. But for $x > 9$ ft all nondimensional velocity profiles collapsed into a single curve. This means that the boundary layer reached its equilibrium condition for $x > 9$ ft.

Measurements of form drag of fences were discussed in Section (3.8) and Eq. 3.7 was used to determine the form drag where

$$D_f = \int_o^h (p_f - p_b) dz \ . \qquad (3.7)$$

The form drag coefficient is defined as

$$c_D = \frac{D_f}{\frac{1}{2} h \rho U_\infty^2} \qquad (4.2)$$

If the distance between fence L is not large, the shear stress acting on the floor between adjacent fences is negligible when compared to the form drag acting on the fences. It is possible to assume that the average wall shear stress can be expressed as

$$\tau_o = \frac{1}{L} D \tag{4.3}$$

and the average drag coefficient of wall shear stress is

$$C_f = \frac{\tau_o}{\frac{1}{2}\rho U_\infty^2} = \frac{h}{L} c_D \quad . \tag{4.4}$$

The shear velocity is defined as

$$u_* = \sqrt{\frac{\tau_o}{\rho}} = \sqrt{\frac{D}{L\rho}} = U_\infty \sqrt{\frac{C_f}{2}} \tag{4.5}$$

Values of measured c_D, C_f, and u_* for all six runs are shown in Table 3. Also in Table 3, both u_* and τ are listed where u_τ's are the shear velocities obtained from the slopes of the semi-log plots, U vs $\log z$.

As found by Nikuradse (1933) and Hama (1954), when Reynolds number R_x is high, $R_x = U_\infty x/\nu$, C_f is independent of R_x and is a function of κ or $R_\kappa = \kappa U_\infty/\nu$ (refer to page 580 of Schlichting, 1968). At a distance far downstream from the leading fence, the important length scale in the multiple fence flow model is L and h. Since h is held constant in the present study, the length scale must be L. The measured C_f for each run at the largest x is plotted in Fig. 28, and the relation between C_f and R_L is found to be

$$C_f = 0.282\ R_L^{-0.258} \tag{4.6}$$

where $R_L = U_\infty L/\nu$. The application range of Eq. 4.6 is suggested to have the L/h ratio between 5 and 20.

The form-drag coefficients of the leading fence c_{Do} are compared to the empirical relation given by Plate (1965). Figure 33 shows good agreement between the present data and Plate's empirical relation

$$c_{Do} = 1.05\ (\frac{h}{\delta})^{2/7}$$

where c_{Do} is the form drag coefficient of the leading fence.

4.2 Turbulence

4.2.1 Waves - The turbulent intensities $\sqrt{\overline{u'^2}}/U$ and $\sqrt{\overline{w'^2}}/U_\infty$ for the last wave position for a typical case are shown in Fig. 30. The intensity profiles are similar for a wave for positions 15, 20, 24, and 25, and are also similar between the three waves. The measurements of Liu, et al. (1966) and Corrsin and Kistler (1954) are also shown for comparison.

The following approach was used to obtain turbulent stress. The momentum integral equation for any surface z above a boundary is

$$\frac{\tau}{\rho} = \frac{d}{dx}\int_z^\infty U(U_\infty - U)dz + \frac{dU_\infty}{dx}\int_z^\infty (U_\infty - U)dz - W(U_\infty - U). \tag{4.7}$$

The values for the terms were evaluated using the mean velocity profiles. The first term is analogous to a local momentum thickness,

while the second term is the pressure gradient-displacement thickness term. From the mean velocity profiles, the vertical velocity W, given by

$$W = - \frac{d}{dx} \int_{z_c}^{z} U \, dz \qquad (4.8)$$

from the two-dimensional continuity equation, is negligible when used in the last term, compared to the first two terms.

The resulting non-dimensional turbulent stress profiles are shown in Fig. 31, for the 25^{th} wave downstream for a typical case. The stresses using the momentum integral approach give values of the wall stress within $\pm$ 15% of the value obtained using the pressure-integration method. The profile shape for all three cases is similar. The measurements over square rods perpendicular to the mean flow by Lin et al. (1966) and over water waves by Karaki and Hsi (1968) are also shown for comparison.

In addition, one of the assumptions under which the logarithmic velocity profile law can be derived is existence of a constant shear stress layer above the boundary. Although the stresses for the corrugated wall are not constant (τ/τ_o decreasing to approximately 0.8 at $y/\delta = 0.2$), the use of the pressure-integrated values of c_f still give reasonable correlation to the logarithmic velocity profile law. The same conclusion was reached by Perry and Joubert (1963). In addition, using the values $5.76 \sqrt{c_f/2}$ in the logarithmic velocity profile law gave reasonable values for the origin shift; the effective origin shifted downward as the wave-height decreases.

4.2.2 Fences - The turbulence distributions over fences of a typical run are shown in Fig. 32. "Over shoots" are found to exist in

all turbulence quantities. Both $\overline{w'^2}$ and $\overline{u'w'}$ increase immediately when flow encountered the fences. But one can see from Fig. 32 that at station $x = 0$, $\overline{u'^2}$ almost retained its initial quantities and the increase of $\overline{u'^2}$ occurs later. At a certain distance downstream from the leading fence, the distribution of each turbulence component is similar. Again this is an indication of the existence of the equilibrium turbulent boundary layer.

The turbulence intensities $\overline{u'^2}$ and $\overline{w'^2}$ at $x = -4$ ft are plotted in Fig. 33. For a comparison, Klebanoff's (1954) smooth wall measurements are also plotted in Fig. 33.

The turbulent shear stress $\overline{u'w'}$ at $x = -4$ ft near the wall is plotted in Fig. 38. The shear velocity u_* determined from mean velocity profile measurements is also shown in Fig. 34. There appears to be good agreement between u_*^2 and $-\overline{u'w'}$ within a $\pm$ 5% difference. A nearly uniform stress region is also found in the lower portion of a smooth wall turbulent boundary layer.

Unlike the smooth wall case, the turbulent shear stress $-\overline{u'w'}$ near a rough wall does not have a uniform region. This can be found in Fig. 35 where Fig. 35 is the plot of $-\overline{u'w'}$ vs z for Stations I(11), I(9), and I(7). The corresponding u_*^2 for each station is also shown. Correlations between u_*^2 and $-\overline{u'w'}$ still exist. The maximum value of $-\overline{u'w'}$ is comparable to u_*^2.

4.3 Mean Humidity Distributions

Profiles of mean humidity at various stations on the saturated wavy surface were obtained by simultaneously measuring local, free stream, and surface air humidities. It has been shown (e.g., Chamberlain

(1966)) that evaporation from saturated surfaces is equivalent to evaporation from a free liquid surface; so, the air humidity at the evaporating surface can be determined by assuming that it is equal to the saturated humidity q_s at T_s where T_s is the surface temperature.

To account for variation in free-stream and surface humidities, the humidity profiles were plotted in terms of $\frac{q-q_\infty}{q_s-q_\infty}$ vs height z_c, where q, q_∞, and q_s are the local, the free stream, and the surface air humidities, respectively. Figures 36, 37, and 38 show plots of $\frac{q-q_\infty}{q_s-q_\infty}$ vs height for various crest positions. These plots indicate that variations of humidity at various stations have been obtained with reasonable accuracy and relatively little data scatter. The value of the nondimensional humidity $\frac{q-q_\infty}{q_s-q_\infty}$ at a particular height, encounters a noticable increase with fetch downstream as expected, because of more and more water vapor effluxing from the wave in the boundary layer. The thickness of the mass (or humidity) boundary layer, δ_m can be defined as the height where the non dimensional humidity $\frac{q-q_\infty}{q_s-q_\infty}$ becomes equal to 0.01. The development of a typical mass boundary layer is shown in Fig. 39.

The vertical distributions of humidity at different longitudinal positions were plotted in semi-logarthmic form, as shown in Figs. 40, 41, and 42. Except for large heights, most of the data points, taken at a station, form a straight line indicating that these humidity profiles follow logarithmic distributions. This result is consistent with the observations made in both field and laboratory experiments by Montgomery (1940), Pasquill (1949), and Lai (1968). The humidity profiles in the far downstream region were then plotted with $\frac{q-q_s}{q_*}$ vs $\frac{z}{z_{om}}$ axes (Figs. 43, 4, and 45), in which z is again the height

measured from the effective zero plane, which is the same as for velocity profiles. The experimental data seem to be well correlated by the line

$$q-q_s = q_* \ln \frac{z}{z_{om}} \tag{4.9}$$

in which z_{om} is a length parameter, and q_* is the friction humidity (Section 2.5).

In the far downstream region, vertical humidity profiles were also measured at various positions inside the troughs of the waves. Figures 46, 47, and48 show these humidity distributions. Shown in Figs.49, 50, and 51 are the enlarged views of the lower portion of the corresponding profiles near the surface of the wave. This is presented to display contrast in behavior of humidity variation at different positions on the wave surface. Using these profiles, isoconcentration lines (i.e., lines of $\frac{q-q_\infty}{q_s-q_\infty}$ = constant) were drawn inside the troughs of each wave in the far downstream region (shown in Figs.52, 53, and 54). From these isoconcentration plots, one can conclude the following: the humidity gradient is relatively high just upstream of a crest and it starts decreasing quite rapidly downstream of the crest along the curvature of the wave. In the middle of the trough, the humidity gradient is relatively small, but passing this region it again starts increasing until just before the next crest. This result facilitates understanding the effect of the flow structure on the variation of local evaporation rates along the surface of waves (Section 4.5).

4.4 Mean Temperature Distributions

Nondimensional temperature profiles $\frac{T-T_s}{T_\infty-T_s}$ vs height at various crest positions of the saturated wave surface were computed and some typical results are plotted in Fig. 55. As mentioned, free stream and surface air temperatures, T_∞ and T_s respectively, were measured along with the local temperature $T(z)$ to account for changes in ambient and surface temperatures. Figure 43 shows a typical development of temperature boundary layer, where δ_t is defined by $\frac{T_{\delta_t}-T_s}{T_\infty - T_s} = 0.99$. From Fig. 59 it appears that these temperature distributions follow logarithmic variation except for the outer region. In case of temperature profiles also, one can define a friction temperature T_* given by the equation

$$T - T_s = T_* \ln \frac{z}{z_{ot}} \quad , \tag{4.10}$$

in which z is the height above the effective zero plane, with the same definition as used in the velocity and humidity profiles, and z_{ot} is a hypothetical length parameter (10).

An estimate of the flux of sensible heat H can be obtained by using the equation

$$H = - \rho C_p k u_* T_* \quad , \tag{4.11}$$

in which u_* and T_* are the friction velocity and the friction temperature respectively, ρ is the density, C_p the specific heat and $\beta' = \frac{K_h}{K_M}$ has been assumed to be unity (Eq. 2.73)). If no heat is conducted below or radiated from above to the waves, H should be equal

to $L_e E$, where L_e is the latent heat of vaporization, and E is the evaporation rate per unit area. A relatively small amount of heat was conducted upwards through the floor of the wind tunnel and this was calculated (in a typical case) to be about 10 percent of the heat lost by vaporization $L_e E$. The long wave radiation downward from the roof of the tunnel was estimated to be about 6 percent of $L_e E$, by assuming black body radiation. Using Eq. 4.11, the sensible heat was computed to be approximately equal to 84 percent of the heat transferred by vaporization.

Vertical temperature profiles were also measured at various positions inside the troughs of the waves in the far downstream region. Figures 56 and 57 show a typical case of these temperature distributions. From these profiles, isotherms (i.e., the line of constant $\frac{T-T_s}{T_\infty-T_s}$) were also drawn inside the troughs (Fig.58). The variation of temperature gradients, along the wave surface, is quite similar to the corresponding variation of humidity gradients.

4.5 Local Mass Transfer Coefficients

In this section, results of measurements on local mass transfer coefficients over wavy surfaces is presented, along with other relevant experimental observations. Flow inside the troughs of the waves is very complex, and is characterized by high turbulent intensities. Measurements of various flow characterisitcs in such flows are delicate and difficult to interpret. However, to facilitate future research it was considered worthwhile to attempt to measure the local mass transfer behavior. The mass transfer data reported in this study reveal some interesting features. An explanation of the behavior inside the troughs

primarily in a qualitative sense is presented and some practical aspects of the results discussed.

Local evaporation rates were measured from various positions on the surface of the specially designed wave located in the far downstream (approximately fully developed) region (Section 3.6). These measurements were taken with all upstream waves completely wet, at various ambient air speeds for waves of all three sizes. The ambient and surface air humidities were also simultaneously measured. The mass transfer coefficients were defined as $\frac{E}{q_s - q_\infty}$, in which E is the local evaporation rate per unit area, and $(q_s - q_\infty)$ is the difference of surface and ambient air humidities.

The result for all cases are plotted in Figs. 59, 60, and 61. As discussed in Section 3.6, actual measurements were conducted on only one evaporation metering wave of each size. Therefore, results in Figs. 59, 60, and 61 have been projected to the next consecutive wave to facilitate a better understanding of the process. The nature of local mass transfer distribution for air speeds ranging from 10 to 40 fps, for each of the three wave sets, is essentially the same, indicating that the flow pattern for each wave remains unchanged in the corresponding range of Reynolds numbers. In each case, the evaporation rate shows a maximum just upstream of a crest and undergoes a minimum slightly downstream of that crest. At a given ambient speed (e.g., 20 fps), the ratio of maximum to minimum mass transfer rates varies approximately from 3.6 for wave A to 2.40 and 2.10 for waves B and C, respectively. After reaching the minimum, the evaporation rates show relatively little variation inside the trough in the case of steeper waves (A and B) as

compared to the shallowest wave (C). Before explaining this behavior, some other pertinent results should be considered.

Photographs taken for visual studies are shown in Figs. 62 and 63. The most noticeable feature of the flow is the vortex (or roller) seen in the troughs of the waves; this vortex is more significant in the steeper wave (Wave A). In general, certain distinct characteristics of the flow can be identified (Fig. 64). In addition to the presence of vortex region 'v', one can also see that the region marked 's' is the place where the flow separates. It is also noticed that the region 'a' is the approximate vicinity where the airflow contacts the wave surface. As seen in the photographs (Figs. 62 and 63), the flow on the upstream portion of the wave trough is much quieter than on the downstream portion where certain degree of unsteadiness is observed, especially near the place where the flow contacts the wave surface.

Also, the results of wall-pressure measurements, for all three wave sets, are shown in Fig. 65. A general feature noticed is a maximum in all these curves upstream of a wave crest approximately near region 'a' where the flow contacts the surface and a minimum near region 's' where the flow possibly separates. Also, pressure in the trough of wave A remains relatively constant as compared to the shallower waves (B and C).

In light of what has just been presented, an explanation of the local mass transfer behavior can be made. The variations of local mass-transfer coefficients for all three wave sets, at a given ambient speed ($\simeq$20 fps), have been plotted together in Fig. 66 to facilitate comparison. The minimum in evaporation-rate distribution occurs in region 's' where the flow is suspected of separating; this is the same

region where the minimum of pressure distribution is also exhibited (Fig. 65). Downstream from this minimum, in region 'v', the evaporation rate for steeper waves is found to be smaller than for shallower waves. Also, in the case of waves A and B, the evaporation rates are relatively constant in region 'v' as compared to the situation in wave C. As displayed in the visualization pictures, the vortex in the steeper wave (A) is much better defined than the vortex in the shallower wave (C). In case of steeper waves, a given particle of air in region 'v' tends to remain in that region for a relatively longer time and keeps on picking up more and more moisture, thus reducing the evaporation rates as compared to the corresponding case of shallower waves. Thus, the build up of high humidity in the vortices, which is greater for steeper waves, tends to reduce the moisture transfer more effectively in the case of waves A and B than in wave C. As mentioned before, flow on the upstream portion of a trough is much quieter than on the downstream portion where a certain degree of unsteadiness is noticed, especially near the place where air flow contacts the wave surface (Figs. 62, 63 and 64). The evaporation rates become significantly larger on the downstream portion of wave troughs and peak at a maximum in the vicinity of region 'a'. In this region, the incoming dry air contacts the wave surface, thereby removing relatively larger amounts of moisture. Another distinct feature noticed in Fig. 66 is the shift in the maxima of evaporation rates of the shallower waves in the upstream direction. The corresponding shift in the wall pressure maxima can also be noted (Fig. 65). This indicates that the region where the dryer air comes in contact with the wave surface is reached sooner for the shallower waves than the steeper ones, which is reasonable. After this maximum, the

evaporation rate decreases sharply and drops to a minimum in region 's'. This can be attributed to a relatively low shear occurring there and also to the fact that the low moisture-content air coming in contact with the wave surface in region 'a' picks up relatively more moisture as it flows along the wave before reaching the region 's' and so is left with lesser capacity to hold the moisture.

To reiterate with regard to humidity distribution in wave troughs, as discussed in Section 4.3 (see Figs. 52, 53, and 54), a typical set of isoconcentration lines can be drawn as shown in Fig. 67. This figure reveals, as also indicated in Section 4.3, that the humidity gradient is fairly low in region 'v', but later it increases toward region 'a', reaching a maximum just upstream of a crest. After this maximum, the humidity gradient again starts decreasing rapidly downstream of the crest. This presentation substantiates the conclusions drawn previously in connection with the variation of local mass-transfer coefficients. Measurements of local evaporation rates from the "evaporation-metering wave" were also taken when all upstream waves were kept completely dry. Typical results are shown in Fig. 68. For this dry condition also, the local evaporation rates exhibited almost the same behavior discussed previously. An overall increase in evaporation by 10 to 15 percent resulted because the upstream was dry instead of wet.

The above measurements were repeated with the measuring wave turned around. The results matched within 5 to 10 percent, indicating that the effect of a possible texture difference of surfaces of different wave sections is negligible.

An important conclusion to be drawn from the results reported in this section is that the various sets of independent measurements, e.g.,

the local evaporation rates, the wall-pressure distributions, the vertical humidity profiles inside the troughs, and the visualization studies, are mutually consistent.

4.6 Wall Heat-Flux Profiles

4.6.1 Waves - Local heat loss from a point source of heat on the wavy surface was measured by surface-mounted heated films. The relation between the heat flux and the wall shear stress will be discussed later.

The heat flux profiles, in the form I^2R are given in Fig. 69 and 70 for a small (7 mm x .2 mm) element approximately $35^{o}C$ above ambient temperature. The three dimensional vortex between the waves removes heat from the element and produces large values of I^2R in the troughs (Fig. 73). There is a scarcity of data in this area, no exact comparisons can be made with the work of others. However, measurements of local mass transfer using an area source of water vapor (Section 4.5) can be used as a qualitative comparison with the wall heat flux profiles obtained from a point source of heat. On a qualitative basis, the observations of the heat flux agree with the mass flux measurements. The separated flow after the crest removes less heat from the wave surface than the flow at the wave crests. Consequently, there is a drop in I^2R after the crest. As the next crest is approached along the wave surface, the values of I^2R increase.

4.6.2 Fences - Local heat flux profiles for fences are shown in Fig. 71 for all flow conditions. In this figure, P = dissipation factor = $\frac{I^2R}{\Delta T}$ and $\Delta P = P - P_o$ where P_o is dissipation factor at zero air velocity and $\Delta T = T_f - T_a$, where T_f is the film temperature and T_a is ambient temperature. The maximum reduction in heat transfer

or the minimum ΔP occurs within h distance downwind from each fence. Also shown in Fig. 72 is the distribution of local static pressure coefficient $C_p = \frac{p-p_o}{\frac{1}{2}\rho U_\infty^2}$, where p is the local static pressure and p_o is the reference static pressure. The general nature of these distributions are very similar to the corresponding case of waves, explained in previous sections.

4.7 Shear-Stress Measurement on the Wavy Surface

Variation of the shear stress can be estimated, provided the assumptions underlying the use of the calibration are met. (See section 3.7). Using the calibration of the surface film, τ (shear stress) versus I^2R (power lost by the film) with ΔT (the overheat) as a parameter can be plotted. As the flow pattern depicted in Fig. 64 indicates, the assumptions of negligible vertical velocity, negligible pressure gradient, and laminar-like flow at the surface are definitely not met. However, assuming the wall shear stress is still related to I^2R through the calibration performed on a circular cylinder, the shear stress can be determined and is given in Figs. 74 and 75.

The separation area just downstream of each wave crest is marked by a drastic reduction in the shear stress. The troughs area indicates a large shear but this apparent shear is a consequence of the large heat flux, not strong two-dimensional flow. The three-dimensional flow is most noticable for wave A, as wave C has a very small vortex flow between the crests. After the trough region the shear stresses increase to the large value at the next crests. Shear stresses on wave C follow a sinusoidal pattern along the wave profile. Kendall (1970) has observed

the same sinusoidal pattern for waves with small h/λ values. However, his sinusoidal waves did not have a separation region in the troughs.

4.8 Average (Mean) Evaporation Rates from an Uniformly Saturated Wavy Surface

4.8.1 Computation of average evaporation rates: Average evaporation rates, in the fully developed region, were obtained by direct measurements (by averaging the results of local evaporation measurements - Section 4.5). Knowing the velocity and humidity profiles, two other methods were employed to compute evaporation rates for various longitudinal positions. Variation of evaporation rate with fetch in the approach flow was obtained. The reliability of these two methods was cross-checked with the directly measured values, at least in the fully developed region.

The first method, which may be called the mass balance method, makes possible the evaluation of evaporation rates by using the equation

$$E = \frac{d}{dx} \int_0^{\delta} \rho U(z) \, [q(z) - q_\infty] \, dz \, . \qquad (4.12)$$

This equation can be obtained by considering a mass balance on a control volume in the air (30), or by simply integrating the two-dimensional diffusion equation with respect to z and neglecting the vertical velocity at the interface. To find the experimental values of evaporation rates from the above equation, values of $\rho U[q-q_\infty]$ were plotted vs height z_c. Curves for a typical case are shown in Fig. 76. An optical planimeter was used to obtain the value of the integral $\int_0^{\delta} \rho U[q-q_\infty]dz$. The value of evaporation rates were obtained by using Eq. 4.12.

This method requires measuring slopes of the curve $\int_0^{\delta} \rho U[q-q_\infty]dz$ vs x; therefore, measurements at a number of closely spaced longitudinal positions are needed to obtain the evaporation rates accurately. In view of this, this method was used to evaluate the evaporation rates in the fully developed (far downstream from the leading wave) region only. In order to obtain the estimates of evaporation rates at different longitudinal positions in the approach flow, the following method was used.

The second method, which may be called the profile method, is based on Eq. 2.72, described in Chapter II. The values of friction velocity u_* and friction humidity q_* can be obtained from measured mean velocity and mean humidity profiles as described in previous sections. The vapor flux at the surface can be obtained from Eq. 2.72 by assuming the validity of the assumption $K_z \approx K_M$ near the surface.

Figures 77, 78, and 79 show the variation of evaporation rates with fetch for all of the three cases. In general, the evaporation rate, in the beginning, increases rapidly to a maximum near the fourth or fifth crests and then decreases, leveling off in the far downstream region. When the air first encounters the presence of waves, there is a sudden increase in the shear (as exhibited by the u_* variation in Fig. 25), which causes an increase in the evaporation rates in the beginning. Also, when the relatively dry air contacts the first few waves, it absorbs much more moisture than it does in the downstream region. The evaporation rate later decreases and becomes contant in the far downstream region, in a fashion similar to that seen in the friction velocity variation. This kind of variation is compatible with results reported in some other studies, e.g., Marciano and Harbeck (1952).

In the far downstream region, the results obtained from the first and second methods of evaluating evaporation rates were compared with direct measurements; the first method agreed within 10 percent and the second, for most cases, within 20 percent (Table 4). Considering that these two methods used entirely different sets of measurements than those used for direct evaporation measurements, the agreement is encouraging.

4.8.2 Correlation of evaporation data - Evaporation from a saturated surface may be influenced by certain variables:

(1) physical properties, dynamic and vapor characteristics of the ambient air,

(2) characteristics of the evaporating surface, and

(3) properties of the evaporating liquid.

For a fully developed boundary layer under near neutral conditions, with no lateral diffusion present, a dimensional analysis of the evaporation problem leads to

$$\frac{E\,\ell}{\rho D(q_s - q_\infty)} = f\left[\frac{u_* \ell}{\nu}\ ,\ \frac{\nu}{D}\right] , \qquad (4.13)$$

in which E is the evaporation rate per unit of projected area, ρ is the density, D is the molecular diffusivity, ν is the kinematic viscosity, u_* is the friction velocity, $(q_s - q_\infty)$ is the difference of surface and ambient air humidities, and ℓ is a characteristic length.

As shown in Section (4.1), an approximately fully developed boundary layer was obtained near the evaporation metering wave. The effect of lateral diffusion was minimized by keeping the buffer waves, located at both ends of the metering wave, completely wet during the

course of an experimental run. It also has been shown in Section (4.1) that conditions in this study can be treated as nearly neutral with a negligible effect of stability on u_* . Thus, the evaporation data of the present study can be correlated on the basis of Eq. 4.12. As the first step for correlating the evaporation data, the height h of a wave was taken as the characteristic length. The computed values of Sherwood numbers, $(Sh)_h = \frac{Eh}{(q_s - q_\infty)}$, and the corresponding Reynolds numbers, $(Re_*)_h = \frac{u_* h}{\nu}$, for all three wave sets at different free stream speeds are given in Table 5. Figure 80 shows a plot of $(Sh)_h$ vs $(Re_*)_h$ and the data is correlated by the line

$$(Sh)_h = 0.10\ (Re_*)_h^{0.84} \tag{4.14}$$

where $\frac{\nu}{D}$ (=Sc) is included in the constant 0.10. In connection with the above relation there have been numerous values proposed for the exponent to the Reynolds number for the transport of mass or heat from different kinds of surfaces. Based on their heat transfer measurements for flow through rough tubes, Kolar (1965) and Nunner (1956) found values of 0.986 and 1.0, respectively, for the exponent to the Reynolds number formed from the friction velocity and diameter of the tube. On the other hand, Levich (1962) obtained [rewriting Eq. 2.95]:

$$\frac{Eh}{\rho D(q_s - q_\infty)} \approx (\frac{u_* h}{\nu})^{1/2}\ (Sc)^{1/4} \approx (Re_*)_h^{1/2}\ (Sc)^{1/4}, \tag{4.15}$$

in which h is the height of the protrusions. It should be noted that Levich's analysis is restricted only to cases where $Sc >> 1$; his results are in agreement with Mahato and Shemilt's (1968) results (with

Sc ≃ 238). In trying to correlate his data on evaporation from water waves (Sc ≃ 0.6) with Levich's correlation (2.63), Lai (1969) reports a $Re^{0.84}$ dependence on the Sherwood number. In view of these various dependences reported in the literature, the relation $(Sh)_h \simeq (Re_*)_h^{0.84}$ of Eq. 4.12 can be considered reasonable.

The applicability of relation (4.12) is restricted to wavy surfaces. In an attempt to make the correlation more general, roughness parameter z_o was used as the characteristic length. Using the average values of u_* and z_o in the far downstream region, the values of $(Sh)_o = \frac{Ez_o}{\rho D(q_s - q_\infty)}$ and $(Re_*)_o = \frac{u_* z_o}{\nu}$ were computed for all the three sets at different free stream speeds; they are tabulated in Table 6. Figure 81 shows a plot of these values, and the relation

$$(Sh)_o = 0.055\ (Re_*)_o^{0.90} \tag{4.16}$$

gives the best fit correlation for all the different sets of data. The advantage of this correlation is that it is applicable to evaporation from any type of surface, some examples of which are considered in the next few sections.

4.8.3 Comparison with evaporation data from water waves - Lai (1969) measured evaporation from small amplitude wind generated water waves at different ambient conditions. He reported his evaporation data along with the corresponding values of the friction velocity u_* and the roughness parameter z_o obtained from the relation

$$\frac{U}{u_*} = \frac{1}{k}\ \ell n \frac{z}{z_o}\ , \tag{4.17}$$

where U is the air speed, k is the Kármán constant, and z is the height above mean level. In attempting to correlate Lai's data with the data obtained in the present study, the following considerations can be made. Consider the simplified case of a long train of waves of constant form with amplitude a and length λ moving at a constant speed or celerity c. The wind blows over these waves with a velocity U which varies with height z, i.e., $U = U(z)$, but remains constant with time and direction. The flow is unsteady and the boundary conditions are different from those of a fixed set of solid waves. To reduce this situation to a steady one, a coordinate system moving at the same speed as the waves is introduced. When viewed from the moving coordinate system, the wave profile is stationary, so this transformation makes boundary condition correspond approximately to the rigid waves. The introduction of this moving coordinate system does not affect the values of u_* reported by Lai (1969), but it does modify the roughness parameter:

$$\frac{(z_o)\ \text{moving coordinate}}{(z_o)\ \text{fixed coordinate}} = e^{\frac{kc}{u_*}} \quad . \tag{4.18}$$

Using this modification, values of $(Sh)_o = \frac{Ez_o}{\rho D(q_s - q_\infty)}$ and $(Re_*)_o = \frac{u_* z_o}{\nu}$ were computed from the set of data, (taken in the approximately fully developed region), reported by Lai (1969). The results are shown in Fig. 82. As shown, the evaporation data from the water waves and those from the fixed waves are reasonably well correlated by Eq. 4.15. Therefore, this relation can be used to obtain estimates of evaporation rates from water waves, provided necessary modifications are made.

4.8.4 Comparison with evaporation data from a flat plate - Cermak and Lin (1955) reported evaporation results from their experiments on a smooth flat plate. To correlate their data with that of the present study, one needs the values of the friction velocity u_* and the roughness parameter z_o corresponding to each evaporation run.

The values of u_* reported by the authors were based on the relation

$$\frac{U}{u_*} = \frac{1}{k} \ln \frac{zu_*}{\nu} + \text{constant.} \qquad (4.19)$$

For a smooth flat plate, designating z_o as the roughness parameter may be misleading. However, for the sake of evaluating Eq. (4.15), z_o may be assumed to have that value of z for which the extrapolated value of U is zero. This procedure for obtaining z_o for a flat plate has been previously used by Cermak and Koloseus (1953) and Chamberlain (1968). Using the values of u_* and z_o thus obtained, along with the evaporation data obtained from a flat plate located in a fully developed boundary layer (17), the values of Sherwood number = $\frac{Ez_o}{\rho D(q_s - q_\infty)}$ and Reynolds number = $\frac{u_* z_o}{\nu}$ were computed; the results are shown in Fig. 83. The line representing Eq. (4.15), which correlated the data from the solid and water waves, can be extrapolated to correlate the evaporation data from a flat plate reasonably well.

4.8.5 Comparison with sublimation data from different rough surfaces - Owen and Thomson (1963, p. 327) measured sublimation rates of camphor from surfaces roughened by two types of glass: "one was mottled by irregular pyramids in relief and the other reeded, with the generators of the reed running perpendicular to the stream ...". To correlate

their sublimation data with the evaporation data, one must account for the difference in molecular diffusivities of the camphor and water vapors which can be incorporated in the non dimensional Schmidt number, $Sc = \frac{\nu}{D}$, analogous to the Prandtl number in the corresponding heat transfer case. Thus a correlation of the type

$$(Sh)_o \simeq (Re_*)_o^m (Sc)^n \tag{4.20}$$

can be attempted, in which $(Sh)_o = \frac{Ez_o}{\rho D(\Delta q)}$ where E is the mass transfer rate per unit area and Δq is the difference of the surface and ambient concentrations. A variety of values, ranging from 0.25 to 0.5, for the exponent n have been used in the literature.

From their experiments on evaporation of various liquids, Smolsky and Sergeyev (1962) reported a value of 0.44 for n as did Gilliland and Sherwood (1934). Levich (1962) and Mahato and Schmilt (1968) used $Sc^{0.25}$ in their correlation. In heat transfer experiments, Chilton and Colburn (1934), Reynolds et al. (1958), and many others report a $Pr^{0.33}$ dependence, whereas Kolar (1965) obtained a $Pr^{0.5}$ dependence on the Nusselt number. In this study, $n = 0.33$ has been chosen for correlating the sublimation data with the evaporation data. Figure 84 shows a plot of $\frac{(Sh)_o}{(Sc)^{0.33}}$ vs $(Re_*)_o$ for the sublimation data of Owen and Thomson (1963) with the evaporation data of this study. The line

$$\frac{(Sh)_o}{(Sc)^{0.33}} = 0.064\ (Re_*)_o^{0.90} \tag{4.21}$$

correlates both of these data well.

The foregoing presentation indicates that the mass transfer parameter $(Sh)_o$ for a wide variety of uniformly saturated surfaces, may be considered as uniquely determined by the surface Reynolds number $(Re_*)_o$ and the Schmidt number Sc. This implies that the roughness of the surface can influence $(Sh)_o$ only insofar as u_* and z_o are influenced. The importance of this result is embodied in the fact that by knowing the velocity profile above a surface, one can predict the mass transfer rates with reasonable accuracy for different ambient conditions, provided the surface and ambient concentrations are known.

4.8.6 Comparison with some results based on field observations - Norris (1948) investigated the problem of evaporation from extensive surfaces of water. As mentioned previously, his analysis was based on the three-layer model which was also used by Montgomery (1940). On physical grounds Norris differed from Montgomery concerning the distribution of water vapor in the outer turbulent layer above rough surfaces. For evaporation from a rough surface, Norris presented the relation

$$E = \rho k\, u_{*R}\, \Gamma_b (q_s - q_b) \ , \tag{4.22}$$

in which

$$\Gamma_b = \left[\ell n \frac{b}{I} + \frac{u_{*k}}{u_{*R}} \left(\frac{\lambda_1 \nu k}{D} + \ell n \frac{k u_{*k} I}{D} \right) \right]^{-1} \ . \tag{4.23}$$

Equations 4.21 and 4.22 have previously been presented as Eqs. 2.57 and 2.58. Equation 4.22 could be simplified to

$$\Gamma_b = [\ell n \frac{b}{\alpha z_o}]^{-1}, \tag{4.24}$$

in which $\ell n\alpha = 1.76 \frac{u_{*k}}{u_{*R}}$ with u_{*k} and u_{*R} being the friction velocities inthe intermediate and turbulent layers of the three-layer model over a hydrodynamically rough surface. From actual calculations for many wind profile data, Norris reported an approximate value of 0.88 for $\ell n\alpha$.

In connection with estimating evaporation losses from lakes, reservoirs, or any other water surfaces of finite extent, let us assume that the value of mean humidity measured at 10 meters above the water surface is approximately representative of the ambient humidity. This assumption is compatible with the considerations made in (65).

Determinations of wind profile over the sea (93) indicate that the sea surface is hydrodynamically rough at wind velocities exceeding 6 m/sec as measured at a height 6 to 12 meters above the sea surface. The roughness length z_o of the sea surface has been found to be about 0.6 cm, regardless of wind velocity. On the other hand, for hydrodynamically rough lake surface, z_o was found to vary from 0.55 to 1.55 cm for the wind velocity ranging from 1 m/sec to 15 m/sec measured at an 8 meter level from the water surface (93). For computation of Γ_b in Eq. 4.23, an average value of z_o equal to 0.8 cm was chosen.

Using the above assumptions, the values of $\frac{Ez_o}{\rho D(q_s - q_{amb})}$ were computed for various values of $\frac{u_* z_o}{\nu}$ from Norris' results. A line representing these values is shown in Fig. 85, along with the correlation

$$\frac{Ez_o}{\rho D(q_s - q_{amb})} = 0.055 \left(\frac{u_* z_o}{\nu}\right)^{0.90} . \qquad (4.25)$$

Agreement is within 10 to 15 percent for the range of $\frac{u_* z_o}{\nu}$ considered.

It turns out that Norris' results are not very sensitive to the chosen level for measuring ambient humidity. For example, a change of this level from 10 to 20 meters makes a difference of 5 to 8 percent only in the values of $\frac{E}{q_s - q_{amb}}$.

Based on empirical relations derived from field observations, Kondo (1962) obtained estimates of evaporation losses from natural water surfaces for various ambient conditions. Kondo (1962) tabulated the values of $\frac{E}{q_s - q_{10m}}$ with the corresponding U_{10m} , u_* and z_o values for various stability conditions, where q_{10m} and U_{10m} are the humidity and velocity measured at 10 m above the water surface. Again, assuming that q_{10m} approximately represents the ambient humidity over a lake or reservoir surface, the values of $\frac{Ez_o}{\rho D(q_s - q_{amb})}$ and $\frac{u_* z_o}{\nu}$ were computed from Kondo's results for near neutral conditions. Figure 89 shows a line representing these values plotted along with relation 4.24. Except for low $\frac{u_* z_o}{\nu}$ values, the agreement is reasonable. For example, the evaporation losses predicted by the relation (4.24) are within 10 to 15 percent of Kondo's results for $200 < \frac{u_* z_o}{\nu} < 500$.

The preceding comparisons indicate relation (4.24) is of considerable practical significance. With the help of simple meteorological measurements, namely, windspeeds at a few levels, surface temperature and ambient humidity, using relation (4.24), one can reliably estimate the evaporation losses from field situations, e.g., lakes, reservoirs irrigated areas, etc. Marciano and Harbeck (1952) concluded, as did

Holzman (1943), that evaporation can be accurately predicted by neglecting stability, that is, by exclusively using adiabatic equations. Therefore, it appears that the application of relation (4.24) may also be extended to stratified conditions.

4.8.7 Comparison with some results related to Reynolds analogy - The rate of mass transfer immediately near a surface, regardless of the regularity of the surface, is controlled by a purely molecular property (i.e., molecular diffusivity in the flowing fluid) of the substance (e.g., water vapor). However, the stream-wise pressure forces (the bluff body effect) acting on individual roughness elements of the surface, in case of an aerodynamically rough flow, are large enough to render the simultaneous transfer of momentum independent of the molecular viscosity of the fluid. A dimensionless number B^{-1} given by

$$B^{-1} = r_+(z) - f_+(z) = \frac{\rho u_* [q_s - q]}{E} - \frac{U(z)}{u_*} \tag{4.26}$$

has been used [Chamberlain (1966), Chamberlain (1968) and Owen and Thomson (1963)] to measure the discrepancy between the transport of mass and momentum transfer to, or from, a surface. Based on dimensional analysis and experimentation, Owen and Thomson (1963) presented a relation for B^{-1} given by

$$B^{-1} = \alpha_1 \left(\frac{30 u_* z_o}{\nu}\right)^m (\nu/D)^n \quad \text{for} \quad \left(\frac{30 u_* z_o}{\nu}\right) > 100 \ , \tag{4.27}$$

where m and n were assigned the values 0.45 and 0.8, respectively, and α_1 was suggested to be a constant for each experimental arrangement, but varied according to the type of roughness.

Values of B^{-1} and $u_* z_o/\nu$ were computed from the experimental data obtained in this study. Figure 86 shows a plot of these values for $u_* z_o/\nu > 40$, along with the data points from Chamberlain's wind-tunnel experiments on evaporation from artificial grass (18) and various other surfaces with cylindrical and wavelike roughness elements (19). The results show that, for the range of $u_* z_o/\nu$ considered, B^{-1} is always positive, indicating that the resistance to momentum transfer is usually less than the resistance to a simultaneous mass transfer to, or from, a surface. Although, for a given value of $u_* z_o/\nu$ the value of B^{-1} will depend upon the type of roughness elements, the B^{-1} values obtained in this study are of the same order of magnitude as the values obtained by Chamberlain (1968), especially in the case of his evaporation experiments with cylindrical and wavelike surfaces. In the range $50 < u_* z_o/\nu < 400$, B^{-1} values, in this study, do not seem to vary with $u_* z_o/\nu$, as much as indicated by Owen-Thomson's model (Eq. 4.25). A similar observation can be made from most of Chamberlain's data [(18) and (19)], especially when one chooses to examine the variation of $u_* z_o/\nu$ for one type of roughness elements at a time.

4.9 Implications Relative to Sheltering Effects and Efficient Use of Water by Plants

4.9.1 Use of field corrugations to reduce moisture loss - The results of this study are of importance in agricultural applications, especially in connection with using furrows to reduce moisture loss. A model of a field furrow is shown in Fig. 87. For the furrow orientation, as shown in this figure, the moisture loss is fairly low $([E/q - (E/q)_{min}]/[E/q_{max} - (E/q)_{min}] \quad 0.25)$ in the region D;

so, from an evaporational point of view, this region would be favorable for planting seeds. Another important consideration in connection with seed germination is the availability of reasonably moderate soil temperatures. A typical set of distributions of surface temperature over the wavy surfaces of this study is shown in Fig. 88. As expected, the surface temperature is relatively higher in the region for planting seeds, which is quite favorable for seed germination and seedling establishment.

As previously indicated the evaporation losses from the bottom of waves A and B are respectively 30 to 40 percent and 20 to 25 percent less than the evaporation loss from the bottom of the shallowest wave C. This result is consistent with the results of a set of field experiments conducted by McGinnies (1959). His results indicated that furrows, if deep enough, can have a pronounced effect on increasing soil moisture content and improving the seedling stand. The increase in moisture content (and thus a proportional decrease in evaporation loss), as found in his experiments, by increasing the depth to width ratio of the furrows, was of the same order of magnitude as the results of this study.

Improvements in the sense of reducing moisture loss by furrowing the field is so significant that the method deserves careful examination for range seeding, especially when soil moisture is critical for seed germination and seedling emergence.

4.9.2 Wind break effects - (a) Fences: A wind reduction factor can be defined as

$$R_1 = \left(1 - \frac{U[z]}{U_o[z]}\right) \times 100 \ , \qquad (4.28)$$

where $U[z]$ is the local wind speed measured after placing fences, and $U_o[z]$ represents the local wind speed measured in clear tunnel. The values of U_o used in this analysis are measured at $x = -4$ ft. Figure 89, 90, and 91 are plots of constant R's for L = 6 in., 12 in. and 18 in., respectively. The wind reduction pattern is not affected by the ambient velocity. Furthermore, all six runs show that a constant R_1 is reached at a distance about 110 h downwind from the leading fence, and that this distance is independent of L. A summary of the asymptotic heights at various wind reduction factors, R_1, for all three L's are as follows:

	20%	30%	40%	50%	60%
L = 6 in.	6.8h	4.8h	3.1h	2.0h	1.4h
L = 12 in.	6.4h	4.2h	2.9h	1.6h	----
L = 18 in.	6.0h	3.4h	1.9h	1.1h	----

Figure 92 shows the wind reduction pattern between fences for Case II (U_∞ = 30 fps, L = 6 in.) and Fig. 93 is a same plot of Case I (U_∞ = 30 fps, L = 12 in.). Since the wind reduction pattern found in this study is dependent on L only, and for a more general flow condition the flow in rough region is dependent on h as well (56), a possible modeling law can be written as

$$\frac{h_p}{h_m} = \frac{L_p}{L_m} . \tag{4.29}$$

An obvious result can be found from Figs. 89 through 93 that a smaller L can provide a higher rate of wind reduction at a given height. However, when applying this result to design the wind breaks, a smallest

L may not be necessary. For example, if a 40% of wind reduction within a 3h height is needed, $L = 12h$ will be an optimum arrangement; but when the wind reduction $R > 70\%$ is needed for $y < h$, fences must be placed for L less than 6h.

(b) Waves: Wind speed is reduced more at any height above the wavy surface than for a comparable height above a smooth surface. The wind reduction factor

$$R_1 = (1 - \frac{U}{U_o}) \times 100$$

of Eq. 4.28 can be used as a measure of this percentage reduction. The reference velocity U_o is the velocity for the smooth surface upstream of the roughened surface. This wind reduction factor is shown in Figs. 94, 95, and 96 for the corrugated surface. The wind speed is reduced the most at any height by the largest wave (Wave A), as would be expected. Also, the rapid growth of the boundary layer is evident from the change in wind speed between the start of the waves ($\lambda = 0$) and approximately the 15^{th} wave crest. After the 15^{th} crest, the reduction in wind speed changes slowly at any height above the wave crests.

The reduction in wind speed is achieved by a loss of momentum at the wavy surface, measured by local skin friction coefficient, C_f. Consequently, the increased C_f for the wavy surface, as compared to smooth surface values, should also be accounted for, since surface friction promotes soil erosion. Therefore, a modified wind reduction factor

$$R_f = \frac{u_*}{u_{*o}} (1 - \frac{U}{U_o}) \times 100$$

is suggested to take account of the increased friction (u_*/u_{*_o}) and the wind reduction $(1 - U/U_o)$. The corrugated surface values of u_* are 2 to 3 times the values for a smooth surface u_{*_o}. If roughening a surface did not increase the surface shear, the above two wind reduction factors would be the same. The values of R_f are shown in Fig. 97 for the 25^{th} wave crests.

The largest wave gives the best windbreak effect for two reasons: 1) The wind speed is reduced the greatest for this wave, and 2) vortices are created between the wave crests. Both effects provide sheltering for seeds in the troughs. The vortices have a small velocity (49) and do not remove the seeds. This sheltering also prevents moisture loss from the wavy surface (110), providing further growth potential for seeds and small plants.

CHAPTER V

CONCLUSIONS

For equilibrium boundary layer situations, the following can be concluded:

1. Corrugated surfaces and successive fences are excellent wind breaks which retard blowing of soil and promote retention of moisture to improve seed germination.

2. For uniformly saturated surfaces, the mass-transfer parameter $(Sh)_o$, for a wide variety of geometrical characteristics, depends primarily upon the surface Reynolds number $(Re_*)_o$ and the Schmidt number Sc. This implies that the roughness of the surface can influence mass transfer (evaporation, sublimation etc.) rates only insofar as the aerodynamic parameters u_* and z_o are influenced.

3. Based on the experimental data of this study, the following relation is proposed for obtaining estimates of evaporation losses from saturated surfaces such as lakes, reservoirs, or irrigated areas:

$$\frac{Ez_o}{\rho D(q_s - q_{amb})} = 0.055 \left(\frac{u_* z_o}{\nu}\right)^{0.90} . \qquad (5.1)$$

Evaporation rates given by Eq. (5.1) represent an upper bound for evaporation from partially saturated surfaces.

4. The vertical humidity profiles over wave crests were found to follow a logarithmic distribution and the results reveal that one can obtain reasonable estimates of humidity by using the relation:

$$q - q_s = q_* \ln \frac{z}{z_{om}} . \qquad (5.2)$$

5. The mass-transfer rates from various locations on the wavy surface are intimately related to the flow structure inside the wave-troughs. The buildup of high humidity in the vortices formed in the troughs, tends to reduce the moisture transfer. These vortices are significantly more effective in reducing the evaporation loss from the bottom of the steeper waves as compared to the shallower ones. This substantiates that furrows, if deep enough, can have pronounced effects on decreasing the moisture loss. Furrowing the field offers another advantage in terms of providing relatively higher soil temperature at the bottom, which is favorable for seed germination.

6. In case of flow over fences, the average drag coefficient C_f was found to be correlated with the Reynolds number $R_L = \frac{U_\infty L}{\nu}$ based on the fence spacing as follows:

$$C_f = 0.282\ R_L^{-0.258} \quad .$$

Also the form drag coefficients of the leading fences were found to be in good agreement with Plate's (1965) empirical relation.

7. In case of flow over fences, the wind reduction factor R was found to depend on the fence spacing L and to be independent of the ambient velocity. In general, the highest values of R at a given height were found for the smallest fence spacings. However, it was not necessary to place the fences at the smallest spacing in order to obtain an optimum arrangement of wind breaks.

REFERENCES

REFERENCES

1. Achenbach, E. (1968) "Distribution of local pressure and skin friction around a circular cylinder in cross-flow up to Re 5 x 10^6," J. Fluid Mech., 34, #4, p. 625.

2. Arvia, A. J., J. S. W. Carrozza and S. L. Marchiano (1964), "On the mechanism of turbulent flow in mass transfer controlled electrochemical reactions," Electrochemical Acta, Vol. 9, No. 11.

3. Bates, C. G. (1930), "The windbreak as a farm asset," (revised), U. S. Dept. of Agric., Farmers Bulletin #1405.

4. Bates, C. G. (1945), "Shelterbelt Influence, Part I, General description of studies made," J. of Forestry, 43, p. 88 and "Part II, The value of shelterbelts in house-heating," J. of Forestry, 43, p. 176.

5. Beebe, P. S. (1971), "Turbulent flow over a wavy boundary," Ph. D. Dissertation (to be published), Colorado State University, Fort Collins, Colorado.

6. Bellhouse, B. J. and D. L. Schultz (1966), "Determination of mean and dynamics skin friction, separation and transition in low-speed flow with a thin-film heated element," J. of Fluid Mech., 24, p. 379.

7. Bellhouse, B. J. and D. L. Schultz (1967), "The determination of fluctuating velocity in air with heated thin film gauges," J. of Fluid Mech., 29, p. 289.

8. Bellhouse, B. J. and D. L. Schultz (1968), "The measurement of fluctuating skin friction in air with heated thin-film gauges," J. of Fluid Mech., 32, p. 675.

9. Betterman, D. (1966), "Contribution a l'etude de la convection forcee turbulente le long de plaques rugueuses," Int. J. of Heat Mass Transfer, 9, p. 153.

10. Björgum, O. (1953), "On the velocity temperature and humidity profiles in the lower atmosphere," Quarterly Journal of Royal Meteor. Soc., Vol. 79.

11. Brown, G. L. (1967), "Theory and application of heated films for skin friction measurements," Heat Transfer and Fluid Mechanics Institute Proceedings, p. 361 (D.B. Olfe and C. W. van Atta, eds.), Stanford Univ. Press.

12. Brown, G. L. (1967), "The application of heated surface films to aerodynamics measurements in boundary layers," Ph.D. Thesis, Magdalen College, Univ. of Oxford.

13. Calder, K. L. (1949), "Eddy diffusion and evaporation in flow over aerodynamically smooth and rough surfaces," Quarterly Journal of Mechanics and Applied Mathematics, Vol. 2.

14. Cermak, J. E., "Laboratory simulation of the atmospheric boundary layer," AIAA Paper No. 70-151, presented at AIAA 3rd Fluid and Plasma Dynamics Conference, Los Angeles, California, 29 June-July 1970.

15. Cermak, J. E. and Arya, S. P. S., "Problems of atmospheric shear flows and their laboratory simulation," Boundary-Layer Meteorology, Vol. 1, pp. 40-60, 1970

16. Cermak, J. E. and H. J. Koloseus (1953), "Lake Hefner model studies on wind structure and evaporation," Report No. 54JEC20, Department of Civil Engineering, Colorado State University, Fort Collins, Colorado.

17. Cermak, J. E. and P. N. Lin (1955), "Vapor transfer by forced convection from a smooth, plane boundary," Report No. 55JEC1, Colorado State University, Fort Collins, Colorado.

18. Chamberlain, A. C. (1966), "Transport of gases to and from grass and grass-like surfaces," Proceedings of Royal Society Vol. A290.

19. Chamberlain, A. C. (1968), "Transport of gases to and from surfaces with bluff and wavelike roughness elements," Quarterly Journal of Royal Meteor. Soc., Vol. 94.

20. Chaudhry, F. H. (1969), "Turbulent diffusion in a stably stratified shear layer," Ph.D. Dissertation, Colorado State University, Fort Collins, Colorado.

21. Chepil, W. S. (1965), "Transport of soil and snow by wind," Agricultural Meteorology, Meteorological Monograph, 6, #28.

22. Cheyney, E. G. (1931), "Establishment, growth, and influence of shelterbelts in the prairie region of Minnesota," Univ. of Minn. Agricultural Expt. Station Bulletin #285.

23. Chilton, T. H. and A. P. Colburn (1934), "Mass transfer (absorption) coefficients -- Prediction from data on heat transfer and fluid friction," Ind. Eng. Chem., 26.

24. Coles, D. (1956), "The law of the wake in the turbulent boundary layer," J. of Fluid Mech., 1, p. 191.

25. Corrsin S. and A. L. Kistler (1954), "The free stream boundaries of turbulent flow," N.A.C.A. T.N. 3133.

26. Deacon, E. L. (1948), "Vertical profiles of mean wind velocity in the surface layers of the atmosphere," Porton Technical Paper No. 39, British Ministry of Supply, London.

27. Denuyl, D. (1936), "The zone of effective windbreak influence," J. of Forestry, 34, p. 689.

28. Dimopoulos, H. G. and T. J. Hanratty, (1968), "Velocity gradients at the wall for flow around a cylinder for Reynolds numbers between 60 and 360," J. Fluid Mech., 33, #2, p. 303.

29. Dipprey, D. F. and R. H. Sebersky (1963), "Heat and momentum transfer in smooth and rough tubes at various Prandtl Numbers," International Journal of Heat and Mass Transfer, Vol. 6.

30. Eckert, E. R. G. and R. M. Drake, Jr.,(1959), "Heat and mass transfer," McGraw Hill Book Company, Inc., New York.

31. Elder, J. P. and G. Wranglen (1964), "Mass transfer at plane plate electrodes," Electrochemical Technology, Vol. 2, No. 1-2.

32. Fage, A. and V. M. Falkner (1931), "Further experiments on the flow around a circular cylinder," Aero. Research Council, Reports and Memoranda No. 1369.

33. Frost, R. (1946), "Turbulence and diffusion in lower atmosphere," Proceedings Royal Society, Vol. A186.

34. Gilliland, E. R., and T. K. Sherwood (1934), "Diffusion of vapors into air streams," Ind. Eng. Chem., 26.

35. Goff, J. A. and S. Gratch (1948), "The humidity ratio (mixing ratio) of moist air at saturation," Special Report, University of Pennsylvania Thermodynamics Research Laboratory, Navy Contract NOBS-2477.

36. Goldstein, S. (1939), "A note on the boundary layer equations," Proceedings Camb. Phil. Soc., 35.

37. Hama, F. R., (1954), "Boundary layer characteristics for smooth and rough surface," Annual meeting of the Soc. of Naval Architects and Marine Engrs., p. 333.

38. Himus, G. (1929), "The evaporation of water in open pans," presented at conference on Vapor Absorption and Adsorption sponsored by Inst. of Chem. Eng., London.

39. Hine, T. B. (1924), "Rate of evaporation of liquids in a current of air," Physical Review, Vol. 24.

40. Hinze, J. (1959), Turbulence, McGraw-Hill, New York.

41. Holzman, B. (1943), "Influence of stability on evaporation," Annals New York Academy of Science, Vol. 44.

42. Hsi, G. and J. H. Nath (1968), "Wind drag within a simulated forest canopy field, Colorado State University Report No. CER68-69GH-JHN6.

43. Huschke, R. E. (1959), "Glossary of meteorology," American Meteorological Society, Boston, Mass.

44. Hyder, D. N. and R. E. Bement (1969), "A micro-ridge roller for seedbed modification," J. of Range Management, 22, p. 54.

45. Jensen, M. (1958), "The model-law for pehnomena in natural wind," Ingeniren, 2, p. 121, Denmark.

46. von Kármán, T. (1939), "The analogy between fluid friction and heat transfer," Trans. American Society of Mechanical Engineers, 61.

47. Karaki, S. and E. Y. Hsu (1968), "An experimental investigation of the structure of a turbulent wind over water waves," Civil Engrg. Dept. Stanford University, Tech. Report 88.

48. Kendall, J. M. (1970), "The turbulent layer over a wall with progressive surface waves," J. of Fluid Mech., 41, p. 259.

49. Kistler, A. L. and F. C. Tan (1967), "Some properties of turbulent separated flows," Phys. of Fluids, 10, p. 165.

50. Klebanoff, P. S., (1954), "Characteristics of turbulence in a boundary layer with zero pressure gradient," NAXA TN 3178.

51. Klebanoff, P. S. (1955), "Characteristics of turbulence in a boundary layer with zero pressure gradient," N.A.C A. Report 1247.

52. Kohler, H. (1950), "On evaporation from snow surfaces," Arkiv für Geofysik. Bandl, nr. 8.

53. Kolar, V. (1961), "Heat and mass transfer in a turbulent medium," Collection of Czechoslovak Chemical Communications, Vol. 26.

54. Kolar, V. (1965), "Heat transfer in turbulent flow of fluids through smooth and rough tubes," International Journal of Heat and Mass Transfer, 8.

55. Kondo, J. (1962), "Evaporation from extensive surfaces of water," The Science Reports of Tôhuko University, 5th Series, Vol. 14, No. 3, The Faculty of Science, Tôhuko University, Sendai, Japan.

56. Kung, R. J. (1970), "Boundary layer development over equally spaced fences," Ph.D. Dissertation, Colorado State University, Fort Collins, Colorado.

57. Lai, J. (1969), "Evaporation from small wind waves," Ph.D. Dissertation, Colorado State University, Fort Collins, Colorado.

58. Laykhtman, D. L. and S. M. Ponomareva (1969), "On the ratio of the turbulent transfer coefficients for heat and momentum in the surface layer of the atmosphere," Izv. Atmos. and Oceanic Phys. Vol. 5, No. 12.

59. Levich, V. G. (1962), "Physicochemical Hydrodynamics," Prentice-Hall, Inc., Englewood Cliffs, N. J.

60. Liu, C. K., S. J. Kline and J. P. Johnston (1966), "An experimental study of turbulent boundary layer on rough walls," Mech. Engrg. Dept. Stanford University Report MD-15.

61. Lumley, J. L. and H. A. Panofsky (1964), The structure of Atmospheric Turbulence, Interscience, New York.

62. Mahato, B. K. and L. W. Shemilt (1968), "Effect of surface roughness on mass transfer," Chem. Eng. Sci., Vol. 23.

63. Malkus, W. V. R. (1961), "Similarity arguments for fully developed turbulence," Nuovo Climeto, 22, p. 376.

64. Mangler, W. (1943), "Die ahnlichen Lösungen der Prandtlschen Grenzsich--tgleichungen," Zeitsch. Ang. Math. und Mech., Vol. 23.

65. Marciano, J. J. and G. Earl Harbeck, Jr. (1952), "Mass-transfer studies," Water Loss Investigations: Vol. 1 - Lake Hefner Studies Technical Report, Geological Survey Circular 229, U. S. Department of Interior.

66. Marlatt, W. and D. Hyder (1969), "The effect of microridging and wind erosion from grass seedbeds," Presented at the Eighth National Conference on Agricultural Meteorology of the American Meteorological Society, May 21-23, 1968, Ottawa, Canada.

67. McGinnies, W. J. (1959), "The relationship of furrow depth to moisture content of soil and to seedling establishment on a range soil," Agronomy Journal, Vol. 51.

68. McVehil, G. E., G. R. Ludwig, and T. R. Sundaram (1967), "On the feasibility of modelling small scale atmospheric motions," Cornell Aeronautical Laboratory, Inc., Report No. ZB-2328P-1.

69. Montgomery, R. B. (1940), "Observations of vertical humidity distribution above the ocean surface and their relation to evaporation," Papers in Physical Oceanography and Meteorology, Vol. VII, No. 4, Massachusetts Institute of Technology and Woods Hole Oceanographic Institution, Cambridge and Woods Hole, Massachusetts.

70. Morris, H. M. (1955), "Flow in rough conduits," Trans. A.S.C.E. 120, p. 373.

71. Nagbhushanaiah, H. S., (1961), "Separation flow downstream of a plate set normal to a plane boundary," Ph.D. dissertation, Colorado State University, Fort Collins, Colorado

72. Nelson, D. F. (1957), "The effect of shape of a plane, smooth saturated surface on evaporation rate," M.S. Thesis, Colorado State University, Fort Collins, Colorado.

73. Nikuradse, J., (1933), "Stromungsgesetze in rauhen rohren," Forsch. Arb. Ing.-Wes., No. 361, also NACA TM 1292 (1950).

74. Nemoto, S. (1961), "Similarity between natural wind in the atmosphere and model wind in a wind tunnel (I, II, & III), Papers in Meteorology and Geophysics, Vol. 12, No. 2.

75. Norris, R. (1948), "Evaporation from extensive surfaces of water roughened by waves," Quarterly Journal of Royal Meteorol. Soc., Vol. 74.

76. Nunner, W. (1956), "Heat transfer and pressure drop in rough tubes," V.D.I. Forsch. Series B, 22.

77. Owen, P. R. and W. R. Thomson (1963), "Heat transfer from rough surfaces," Journal of Fluid Mechanics, 15.

78. Pasquill, F. (1943), "Evaporation from a plane, free-liquid surface into a turbulent air," Proceedings Royal Society, Vol. A182.

79. Pasquill, F. (1949a), "Eddy diffusion of water vapor and heat near ground," Proceedings Royal Society, Vol. 198A.

80. Pasquill, F. (1949b), "Some estimates of the amount and diurnal variation of evaporation from a clayland pasture in fair spring weather," Quarterly Journal of Royal Meteorol. Soc., Vol. 75.

81. Perry, A. E. and P. N. Joubert (1963), "Rough wall boundary layers in adverse pressure gradients," J. of Fluid Mech., 17, p. 193.

82. Perry, A. E., W. H. Schofield and P. N. Joubert (1969), "Rough wall turbulent boundary layers," Journal of Fluid Mechanics, Vol. 37, Part 2.

83. Phillip, J. R. (1959), "The theory of local advection: I," Journal of Meteorology, 16.

84. Plate, E. J., (1965), "The drag on a smooth flat plate with a fence immersed in its turbulent boundary layer," ASME, Paper No. 64-FE-17.

85. Pohl, N. (1933), "Einfluss der Wnadrauhig--keit auf den wäermeübergang an Wasser," Forsch. Ing., Vol. 4, No. 5.

86. Powell, W. and E. Griffith (1935), "The evaporation of water from plane and cylindrical surfaces," Trans. Inst. Chem. Eng., London, Vol. 13.

87. Reichardt, H. (1951), "Vollstandige darstellung der turbulent geshwindikeitsverteilung in glatten leitungen," Z.A.M.M., 31, p. 208.

88. Reynolds, W. G., W. M. Kays and S. J. Kline (1958), "Heat transfer in the turbulent incompressible boundary layer, II -- the step temperature distribution," N.A.S.A. Memo 12-2-58W.

89. Rider, N. E. (1954a), "Evaporation from an oat field," Quarterly Journal of Royal Meteorol. Soc., Vol. 80.

90. Rider, N. E. (1954b), "Eddy diffusion of momentum, water vapor and heat near the ground," Phil. Trans., Royal Society, Vol. A246.

91. Rider, N. E., J. R. Phillip and E. F. Bradley (1963), "The horizontal transport of heat and moisture -- a micrometeorological study," Quarterly Journal of Royal Meteorol. Soc., Vol. 89.

92. Rosenhead, L. (1963), Laminar Boundary Layers, Claredon, Oxford.

93. Rossby, C. G. (1936), "On the momentum transfer at the sea surface," Papers in Physical Oceanography and Meteorology, 4, No. 3.

94. Rotta, J. C. (1962), "Turbulent boundary layer in incompressible flow," Progress in Aero. Sci., Vol. 2, Pergamon Press, the MacMillan Co., New York.

95. Schlichting, H. (1968), "Boundary layer theory," Sixth Edition, McGraw-Hill Book Co., New York.

96. Schraub, F. A. and S. J. Kline (1965), "A study of the structure of the turbulent boundary layer with and without longitudinal pressure gradient," Mech. Engrg. Dept. Stanford University, Report MD-12.

97. Sheppard, P. A. (1958), "Transfer across the earth's surface and through the air above," Quarterly Journal of Royal Meteorol. Soc., Vol. 84.

98. Smith, J. W. and N. Epstein (1957), "Effect of wall roughness on convective heat transfer in commercial pipes," American Institute of Chemical Engineers Journal, Vol. 3.

99. Smolsky, B. M. and G. T. Sergeyen (1962), "Heat and mass transfer with liquid evaporation," International Journal of Heat and Mass Transfer, Vol. 5.

100. Stearns, C. R. (1970), "Determining surface roughness and displacement height," Boundary Layer Meteorology, 1, p. 102.

101. Sutton, O. G. (1934), "Wind structure and evaporation in a turbulent atmosphere," Proceedings Royal Society, Vol. A146.

102. Sverdrup, H. V. (1946), "The humidity gradient over the sea surface," Journal of Meteorology, Vol. 3.

103. Swinbank, W. C. (1955), "Eddy transport in the lower atmosphere," Commonwealth Scientific and Industrial Research Organization, Division of Meteorological Physics (Melbourne), Technical Paper No. 2.

104. Thiesenhausen, R. (1930), "Untersuchungen uber die Wasserverdungstungs-geschwindigkeit in Abhangigkeit von der Temperatur des Wassers, der Luftfeuchtigkeit und Windgeschwineligkeit," Gesundheits Ingenieur, Vol. 53.

105. Thornthwaite, C. W. and B. Holzman (1939), "The determination of evaporation from land and water surfaces," Monthly Weather Review, Vol. 67.

106. Threlkeld, J. L. (1962), "Thermal environmental engineering," Prentice Hall, Inc., Englewood Cliffs, N. J.

107. Townsend, A. A. (1956), The Structure of Turbulent Shear Flow, Cambridge Univ. Press, Cambridge.

108. van Driest, E. R. (1956), "On turbulent flow near a wall," J. Aero. Sci., 23, p. 1009.

109. van Eimern, J. (1964), Windbreaks and Shelterbelts, Technical Note #59, World Meteorological Organization, Geneva.

110. Verma, S. B. (1971), "Mass transfer from rough surfaces," Ph.D. Dissertation, Colorado State University, Fort Collins, Colorado.

111. Yih, C. S. (1952), "On a differential equation of atmospheric diffusion," Trans. AGU, Vol. 33, No. 1.

112. Yeh, F. F. (1970), "Air flow over roughness discontinuity," Ph.D. Dissertation, Colorado State University, Fort Collins, Colorado.

APPENDICES

APPENDIX A

Dew point temperature t_d is a saturation temperature of moist air defined (106) mathematically by the solution $t_d(p,q)$ of the equation:

$$q_s(p,t_d) = q \ , \tag{A-1}$$

in which p is the barometric pressure, q is the humidity ratio or the weight of water vapor associated with unit weight of dry air, and q_s is the humidity ratio of saturated air. Practically speaking, t_d is the temperature of incipient condensation when moist air is cooled at constant pressure. It is the lowest temperature at which a given humidity ratio q may exist for a certain barometric pressure.

The humidity ratio at saturation q_s is defined (35) by

$$q_s = 0.62197 \frac{f_s \, p_s}{p - f_s p_s} \ , \tag{A-2}$$

in which p_s is the saturation pressure of pure water, and f_s is a coefficient. The coefficient f_s differs only moderately from unity and varies more or less slowly with pressure p and temperature T so that it is a quantity that is amenable to easy interpolation. Goff and Gratch (35) presented a chart representing the coefficient f_s as a function of temperature T (^{o}F) for each of a number of equally spaced pressures p (in. Hg); the part of the chart that is pertinent to this study is given in Table 7.

APPENDIX B

Measurement of drag on waves was discussed in Sections (3.8), and (4.1.1). The form drag D (per ft of wave in the lateral direction) is given by (Fig. B-1)

$$D = \int_{-\lambda/2}^{\lambda/2} (-p_w) \sin\theta \ ds \ , \qquad \text{(B-1)}$$

in which p_w is the wall pressure at a point on the wave surface, θ is the angle that the normal to the curve at that point makes with the vertical direction and ds is the elemental curve length as shown in Fig. B-1.

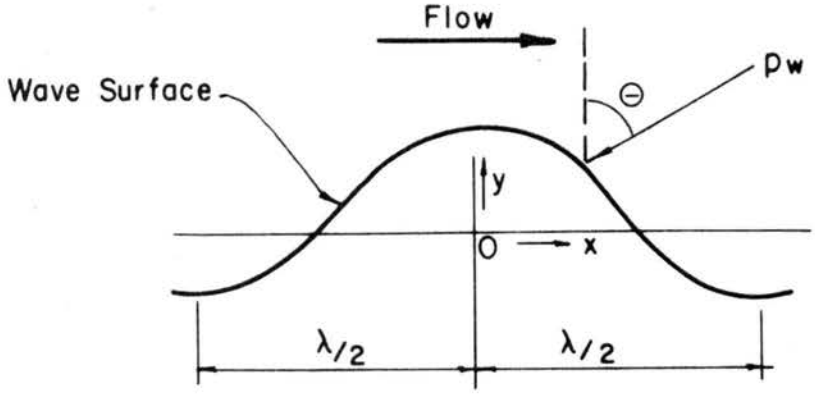

Figure B-1

The equation of the curve representing the wavy surface is

$$y = a \cos \frac{2\pi x}{\lambda} \ , \qquad \text{(B-2)}$$

in which a and λ are the amplitude and wavelength respectively.

Then the quantities ds and $\sin\theta$ (Eq. B-1) can be estimated by

$$ds = 1 + \left(\frac{dy}{dx}\right)^2 \, ds = 1 + \left(\frac{2a\pi}{\lambda}\right)^2 \sin^2 \frac{2\pi x}{\lambda} \, dx$$

$$\sin\theta = \frac{\left(\frac{2a\pi}{\lambda}\right) \sin \left(\frac{2\pi x}{\lambda}\right)}{1 + \left(\frac{2a\pi}{\lambda}\right)^2 \sin^2 \frac{2\pi x}{\lambda}} \quad . \tag{B-3}$$

Using Eqs. (B-3) in Eq. (B-1), one obtains

$$D = - \frac{2a\pi}{12\lambda} \left[\int_0^{\lambda/2} p_w \sin \frac{2\pi x}{\lambda} \, dx + \int_{-\lambda/2}^{0} p_w \sin \frac{2\pi x}{\lambda} \, dx \right] , \tag{B-4}$$

in which ds is in inches.

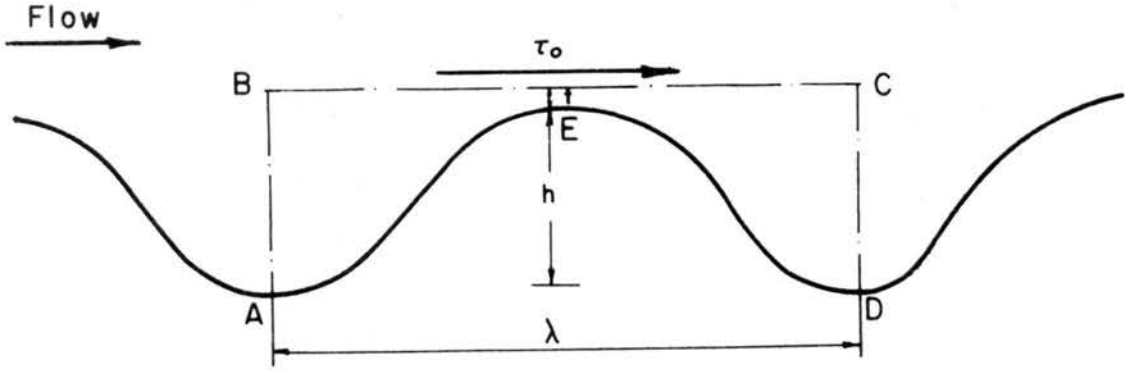

Figure B-2

The effective skin friction coefficient C_f was determined by considering a force balance on a control volume ABCDE around a single wave as shown in Fig. B-2. This method is primarily based on the procedure

Perry et al. (82) used for evaluating wall shear stress in case of flow over a series of cavities. As shown in Fig. B-2, the effective wall shear stress τ_o is assumed to act along a surface BC positioned at a distance t above the crest of the waves, where t is small compared with h. The shear on the surface AED is assumed to be negligible as compared with the acting pressure forces. Flow patterns in successive troughs are assumed to be negligibly different, and, hence, streamwise momentum in through face BA equals the momentum efflux through CD. Pressure patterns along the centerlines of two adjacent troughs are assumed to be similar. However, the values of the pressure distributions on the centerline of one trough will be lowered below that in the preceding trough by the amount the free stream static pressure has decreased in that wavelength. Neglecting the change in free stream static pressure over a wavelength, the force balance leads to

$$\frac{D}{2a \quad \frac{1}{2}\rho U_\infty^2} = \frac{\tau_o \lambda}{2a \quad \frac{1}{2}\rho U_\infty^2} \quad . \tag{B-5}$$

Using Eq. (B-4) in Eq. (B-5), the effective skin friction coefficient C_f $(= \frac{\tau_o}{\frac{1}{2}\rho U_\infty^2})$ was determined. A difference of 2 to 3 percent was obtained in the value of C_f if the change in static pressure over a wavelength were taken into account. The values of C_f were also cross checked with the shear plate measurements, again by using the concept of force balance just described.

TABLES

Table 1

Performance characteristics of the Army Meteorological and the Colorado State University Wind Tunnels

Characteristic	Army Meteorological Wind Tunnel	Colorado State University Wind Tunnel
1. Dimensions		
Test-section length	27 m	9.2 m
Test-section area	.4 m^2	3.4 m^2
Contraction ratio	9.1	9.1
Length of temperature controlled boundary	12 m	3.1 m
2. Wind-tunnel drive		
Total power	200 kw	75 hp
Type of drive	4-blade propeller	16-blade axial fan
Speed control: coarse	Ward-Leonard DC control	single-speed induction motor
Speed control: fine	pitch control	pitch control
3. Temperatures		
Ambient air temperature	5°C to 95°C	not controlled
Temp. of controlled boundary	5°C to 205°C	ambient to 95°C
4. Velocities		
Mean velocities	approx. 0 mps to 3˜ mps	approx. 1 mps to 27 mps
Boundary layers	up to 50 cm	up to 20 cm
Turbulence level	low (about 0.1 percent)	low (about 0.5 percent)
5. Pressures	adjustable gradients	not controlled
6. Humidity	controlled from approx. 20% to 80% relative humidity under average ambient conditions.	not controlled

Table 2

Effective average skin friction coefficient C_f (waves)

(Far downstream region)

	U_∞ (ft/sec)	Wall Pressure Integration	Shear Plate
Wave A	39.70	0.0210	0.0205
	19.60	0.0218	0.0175
Wave B	40.1	0.0195	------
Wave C	39.70	0.0110	0.0160
	19.80	0.0126	0.0170

Table 3

Drag coefficient of fences and average shear velocities

Station	U_a (fps)	c_D	c_f	U_* (fps)	U_τ (fps)	Station	U_a (fps)	c_D	c_f	U_* (fps)	U_τ (fps)
I(0)*	29.98	.508	.0423	4.36	3.196	IV(0)	44.90	.478	.0398	6.337	---
I(1)	30.20	.0415	.0035	1.256	5.246	IV(1)	45.10	.0620	.0052	2.289	7.921
I(2)	30.28	.247	.0206	3.073	3.574	IV(2)	44.81	.220	.0183	4.291	5.243
I(3)	30.40	.221	.0184	2.916	3.481	IV(4)	45.24	.196	.0163	4. 88	5.385
I(5)	30.38	.199	.0166	2.768	2.328	IV(6)	45.70	.174	.0145	3.889	3.492
I(7)	30.46	.176	.0147	2.612	2.530	IV(8)	44.88	.154	.0128	3.593	3.391
I(9)	30.60	.167	.0138	2.543	2.439	IV(10)	44.73	.144	.0120	3.459	3.365
I(11)	30.88	.161	.0134	2.531	2.469	IV(12)	45.17	.142	.0018	3.474	3.377
I(13)	31.16	.158	.0131	2.526	2.456						
						V(0)	45.06	.476	.0265	5.183	---
						V(1.5)	45.37	.185	.0103	3.248	---
II(0)	30.38	.505	.0842	6.232	---	V(3)	45.52	.172	.0095	3.130	---
II(0.5)	30.61	--	--	--	---	V(6)	45.15	.235	.0130	3.644	3.205
II(1)	30.30	.0663	.0110	2.252	3.804	V(9)	44.94	.199	.0110	3.340	3.165
II(1.5)	30.66	.112	.0186	2.958	4.950	V(12)	45.01	.195	.0108	3.309	3.170
II(2)	30.57	.108	.0180	2.900	4.429						
II(2.5)	30.77	.111	.0185	2.959	4.140						
II(3)	30.59	.111	.0185	2.942	4.012	VI(0)	29.51	.487	.0271	3.432	---
II(4)	30.56	.103	.0172	2.834	3.631	VI(1.5)	29.97	.185	.0103	2.151	---
II(5)	30.82	.099	.0165	2.799	3.231	VI(3)	29.94	.297	.0165	2.720	---
II(6)	30.44	.0972	.0162	2.740	2.676	VI(6)	29.67	.234	.0180	2.392	2.319
II(8)	30.61	.0950	.0158	2.723	2.663	VI(9)	29.78	.216	.0120	2.309	2.250
II(10)	30.95	.0943	.0157	2.743	2.582	VI(12)	29.89	.212	.0118	2.293	2.243
II(10.5)	30.97	.0942	.0157	2.744	2.585						
II(11)	31.11	.0942	.0157	2.756	2.695						
III(0)	44.43	.475	.0791	8.836	---						
III(1)	44.60	.0825	.0138	3.699	8.339						
III(2)	44.77	.0802	.0134	3.661	6.228						
III(4)	45.27	.103	.0172	4.200	4.881						
III(6)	44.77	.0948	.0158	3.979	3.904						
III(10)	44.43	.0151	.0142	3.741	3.667						
III(12)	44.67	.0849	.0141	3.757	3.663						

*Distances from the leading edge are given in paranthesis.

Table 4

Comparison of Average Evaporation rates $E/(q_s-q_\infty)^*$ obtained from Different Methods

(Far Downstream Region) (Upstream Waves Wet)

Waves	U_∞ cm/sec	Direct Measurements	First Method (Mass Balance Method) $E = \frac{d}{dx}\left\{\int_0^\delta \rho U(q-q_\infty)dz\right\}$ x 10^3	Second Method (Profile Method) $E = -\rho k u_* q_*$ x 10^3
A	596.49	3.900	3.620	3.280
B	595.58	3.265	3.160	3.315
C	595.27	3.450	3.320	2.240

* E (gm/cm^{2}sec) = Average evaporation rate (based on projected area)

q_s-q_∞ ($\frac{\text{gm water vapor}}{\text{gm dry air}}$) = Difference of surface and ambient air humidities

Table 5

Data for Correlation $(Re_*)_h$ vs $(Sh)_h$

Waves	U_∞ cm/sec	u_* cm/sec	h=2a cm	$(Re_*)_h = \frac{u_* h}{\nu}$	$(Sh)_h = \frac{En}{\rho D(q_s - q_\infty)}$
A	302.97	32.72	4.318	856.27	23.95
A	596.49	64.42	4.318	1685.85	62.49
A	1208.23	130.49	4.318	3414.88	92.13
B	304.19	29.81	2.54	458.89	14.85
B	595.58	58.37	2.54	898.54	30.77
B	915.01	89.67	2.54	1380.37	43.68
B	1204.87	118.08	2.54	1817.72	54.07
C	301.75	22.18	1.27	170.72	8.20
C	595.27	43.75	1.27	336.74	16.26
C	1210.97	89.01	1.27	685.11	26.30

Table 6

Data for Correlation $(Re_*)_o$ vs $(Sh)_o$

Waves	U_∞ cm/sec	u_* cm/sec	z_o cm	$(Re_*)_c = \frac{u_* z_o}{\nu}$	$(Sh)_o = \frac{E z_o}{\rho D(q_s - q_\infty)}$	$\frac{(Sh)_o}{(Sc)^{1/3}}$
A	302.97	32.72	0.4445	88.15	2.47	2.90
A	596.49	64.42	0.4445	173.54	6.43	7.54
A	1208.23	130.49	0.4445	351.53	9.48	11.11
B	304.19	29.81	0.358	64.68	2.09	2.45
B	595.58	58.37	0.358	126.65	4.34	5.09
B	915.01	89.67	0.358	194.56	6.157	7.22
B	1204.87	118.08	0.358	256.20	7.62	8.93
C	301.75	22.18	0.0813	10.92	0.525	0.615
C	595.27	43.75	0.0813	21.56	1.04	1.22
C	1210.97	89.01	0.0813	43.86	1.68	1.97

Table 7

Values of f_s [Goff and Gratch (1948)]

	Atmospheric Pressure		
T^oF	23 in. Hg	24 in. Hg	25 in. Hg
32	1.003484	1.003616	1.003749
42	1.003497	1.003623	1.003751
52	1.003543	1.003666	1.003789
62	1.003626	1.003745	1.003864
72	1.003749	1.003865	1.003979
82	1.003909	1.004021	1.004134
92	1.004104	1.004216	1.004326

FIGURES

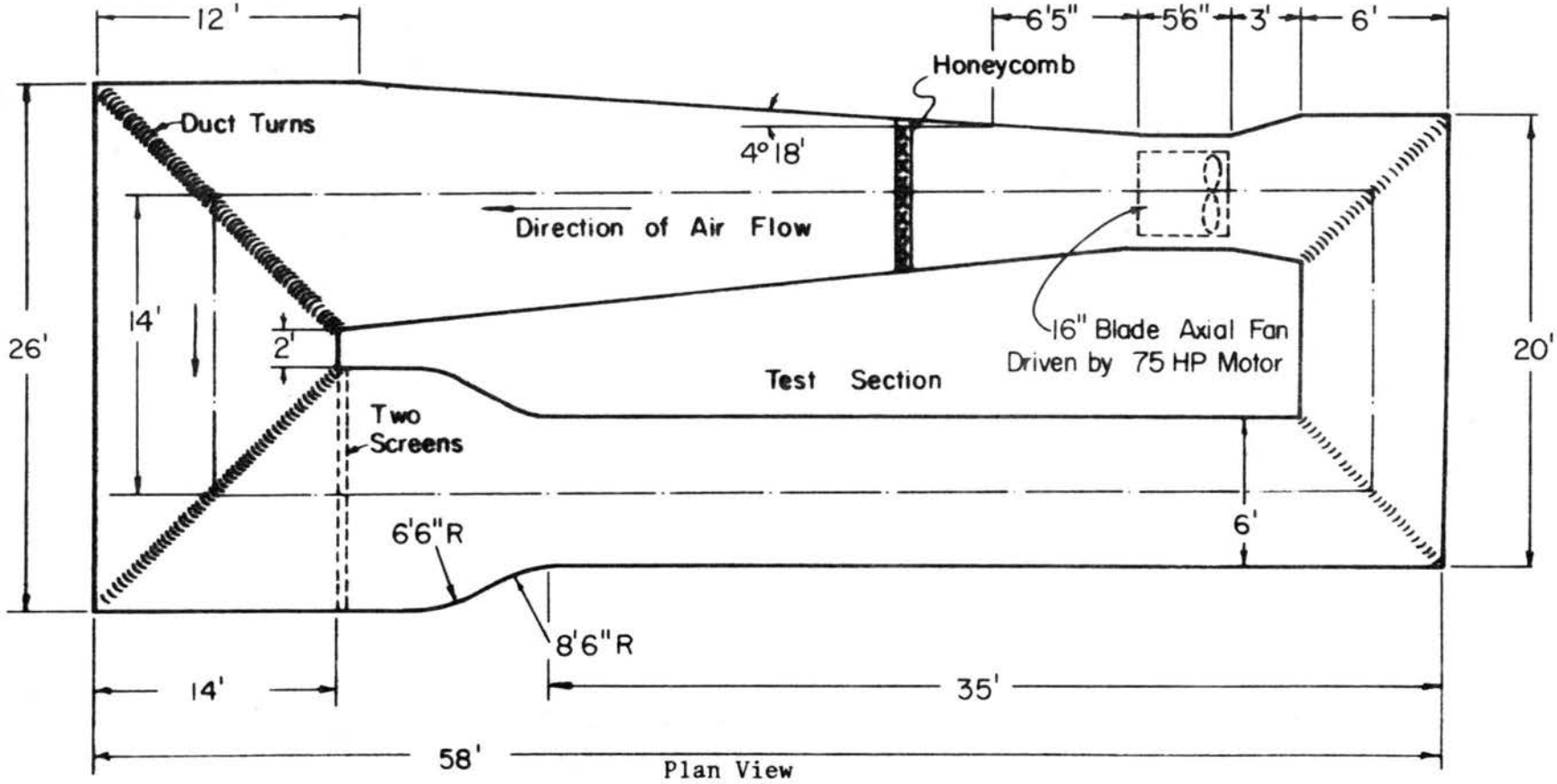

Fig. 1. Colorado State University wind tunnel.

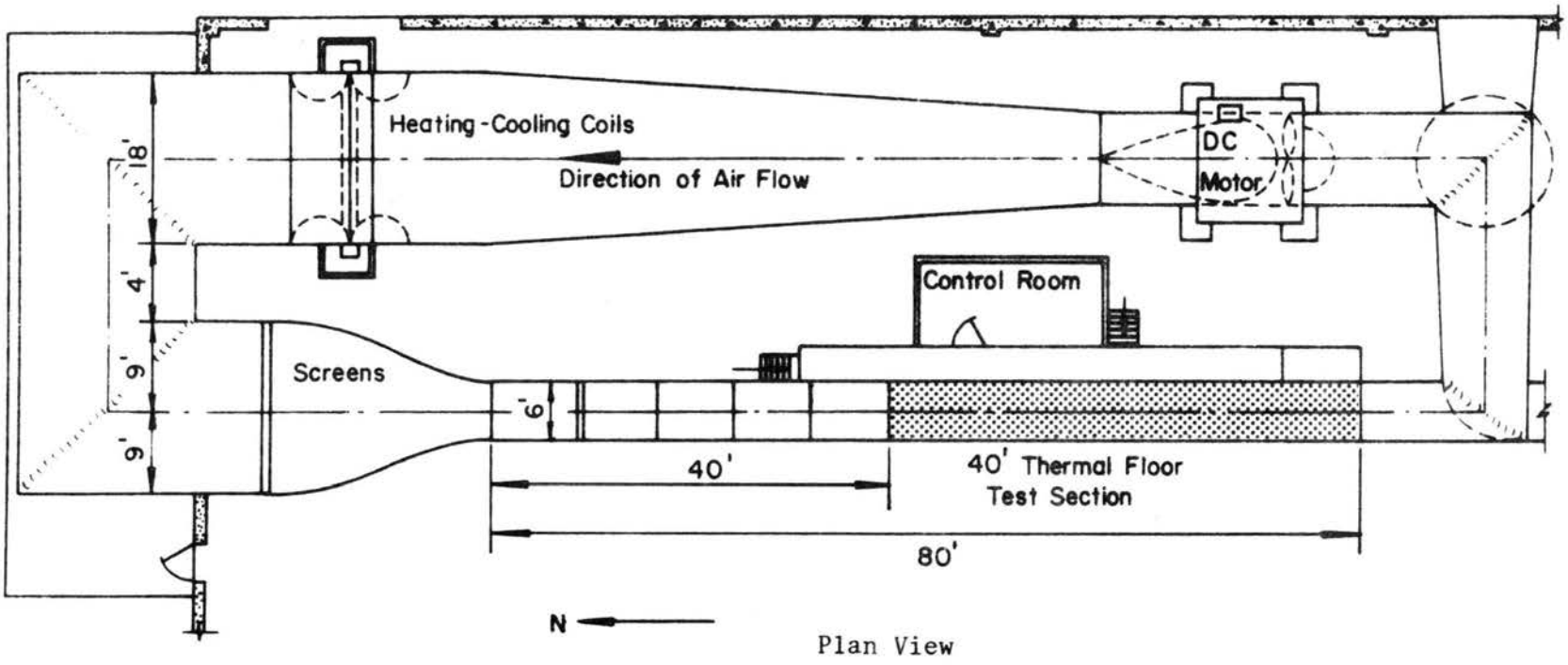

Fig. 2. The U. S. Army meteorological wind tunnel.

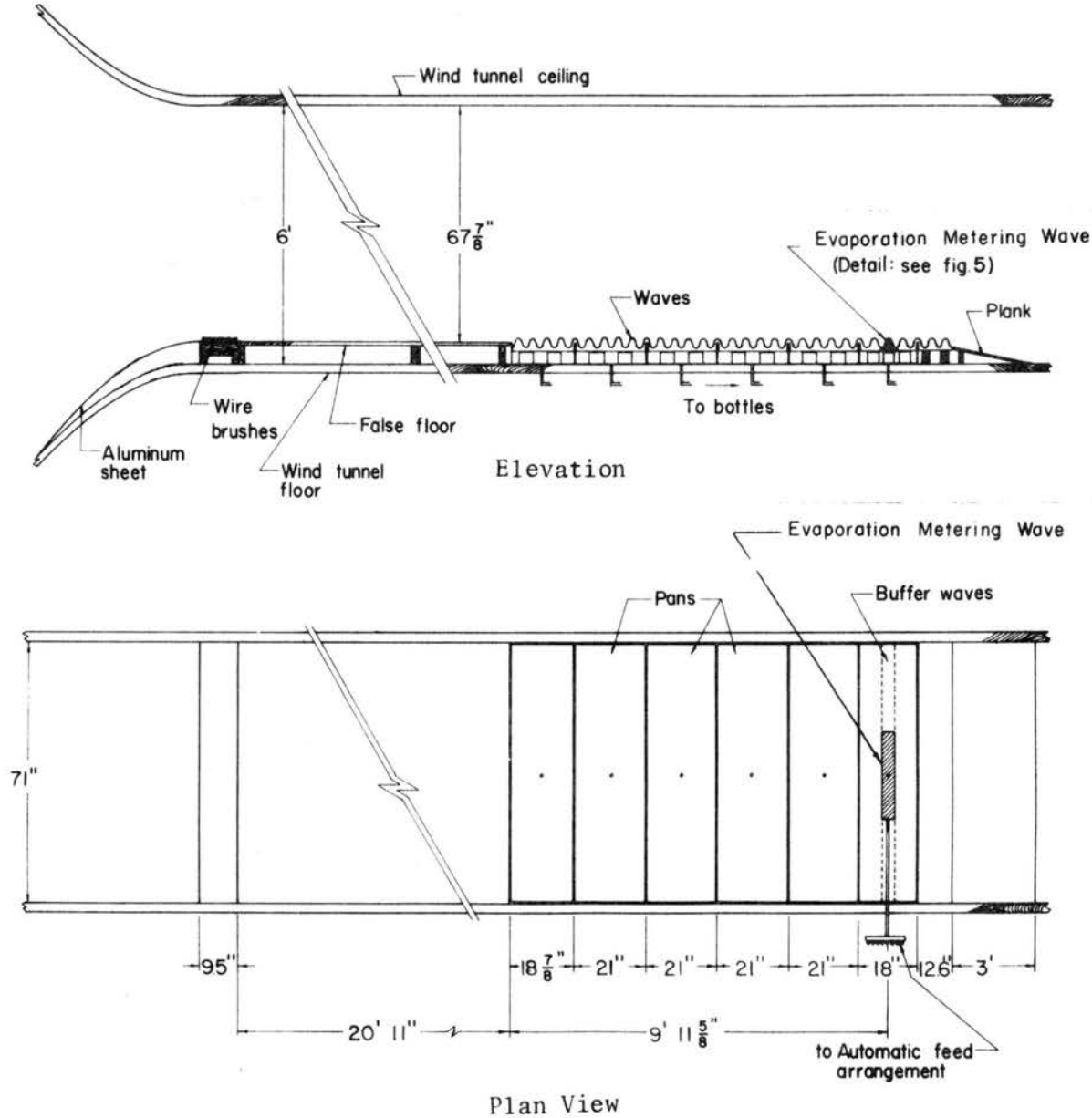

Fig. 3. Experimental arrangement (wave assembly) in wind tunnel.

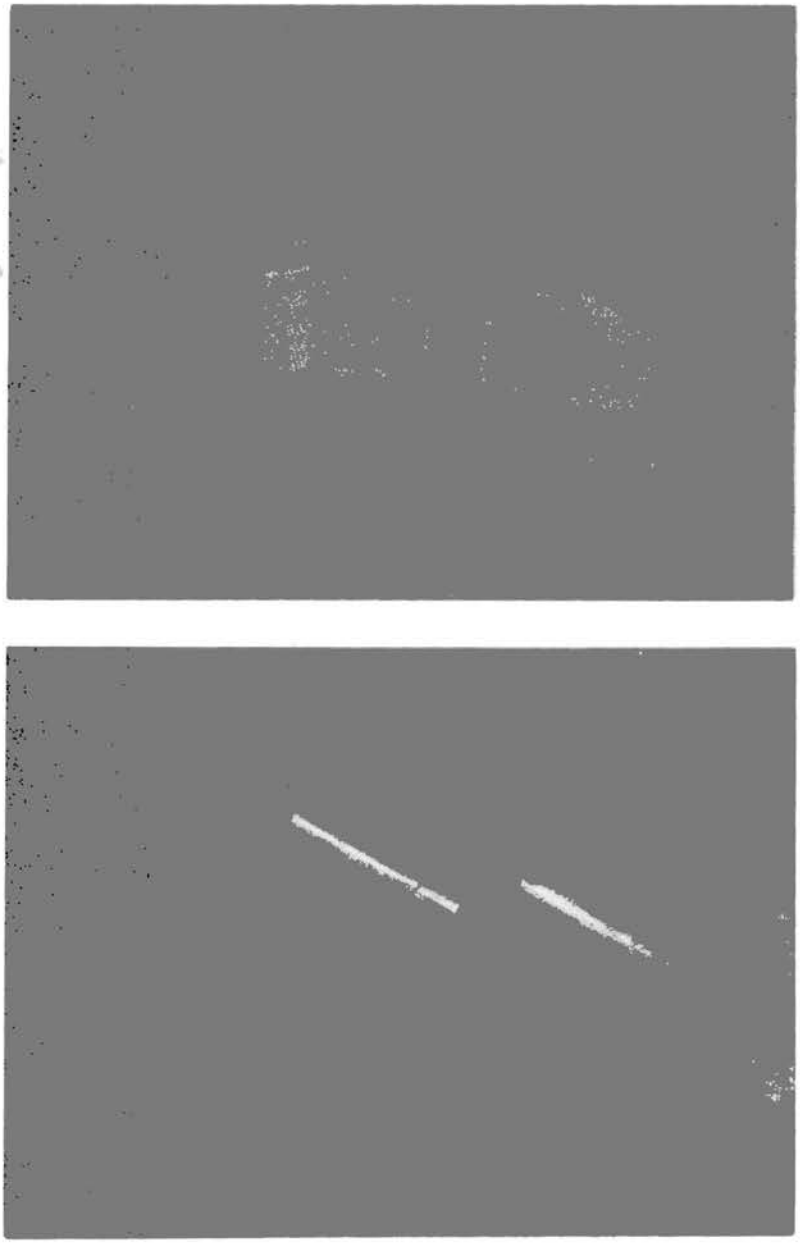

Fig. 4 Waves and shaper blades.

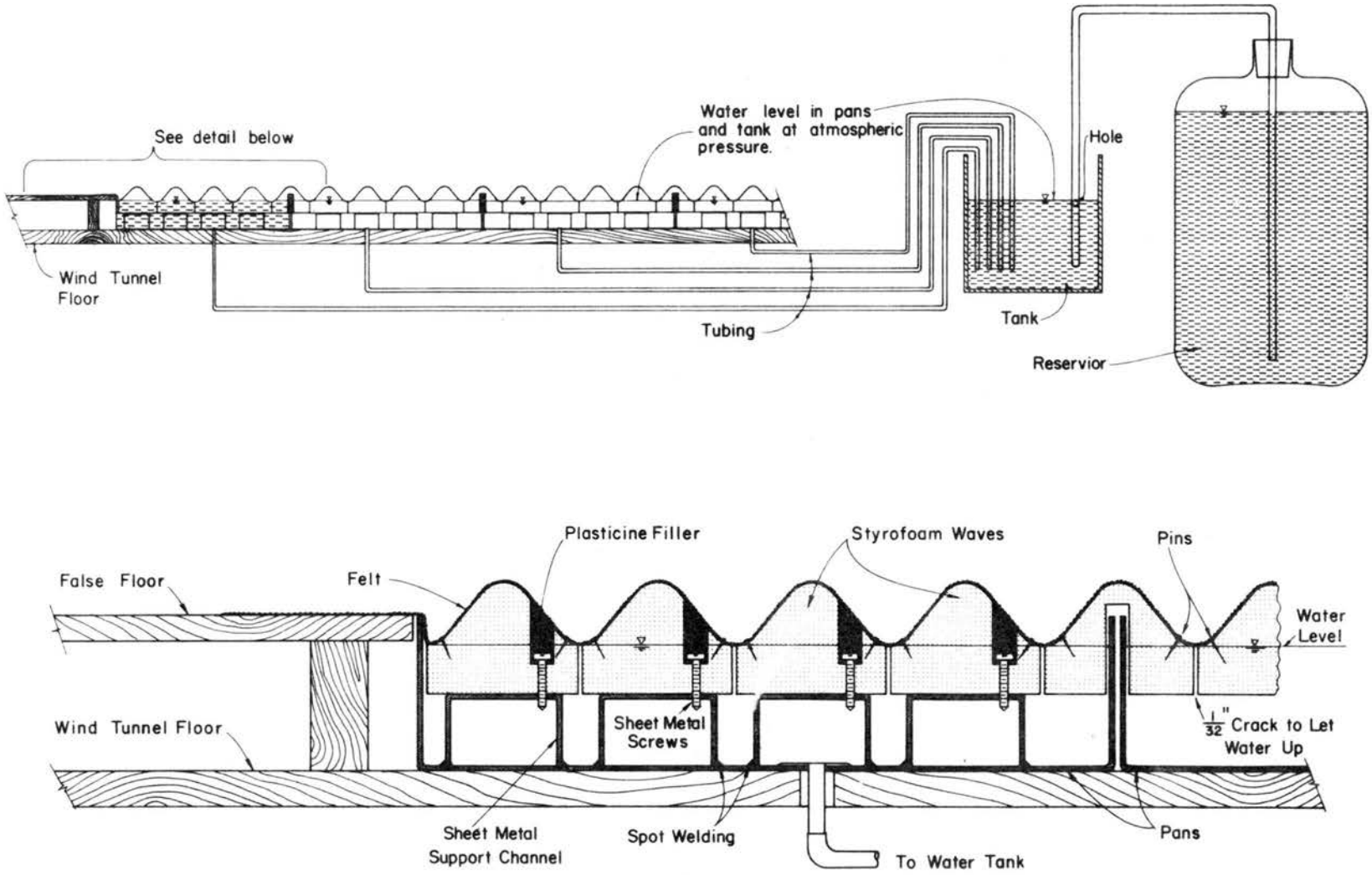

Fig. 5. Details of Figure 3 (schematic).

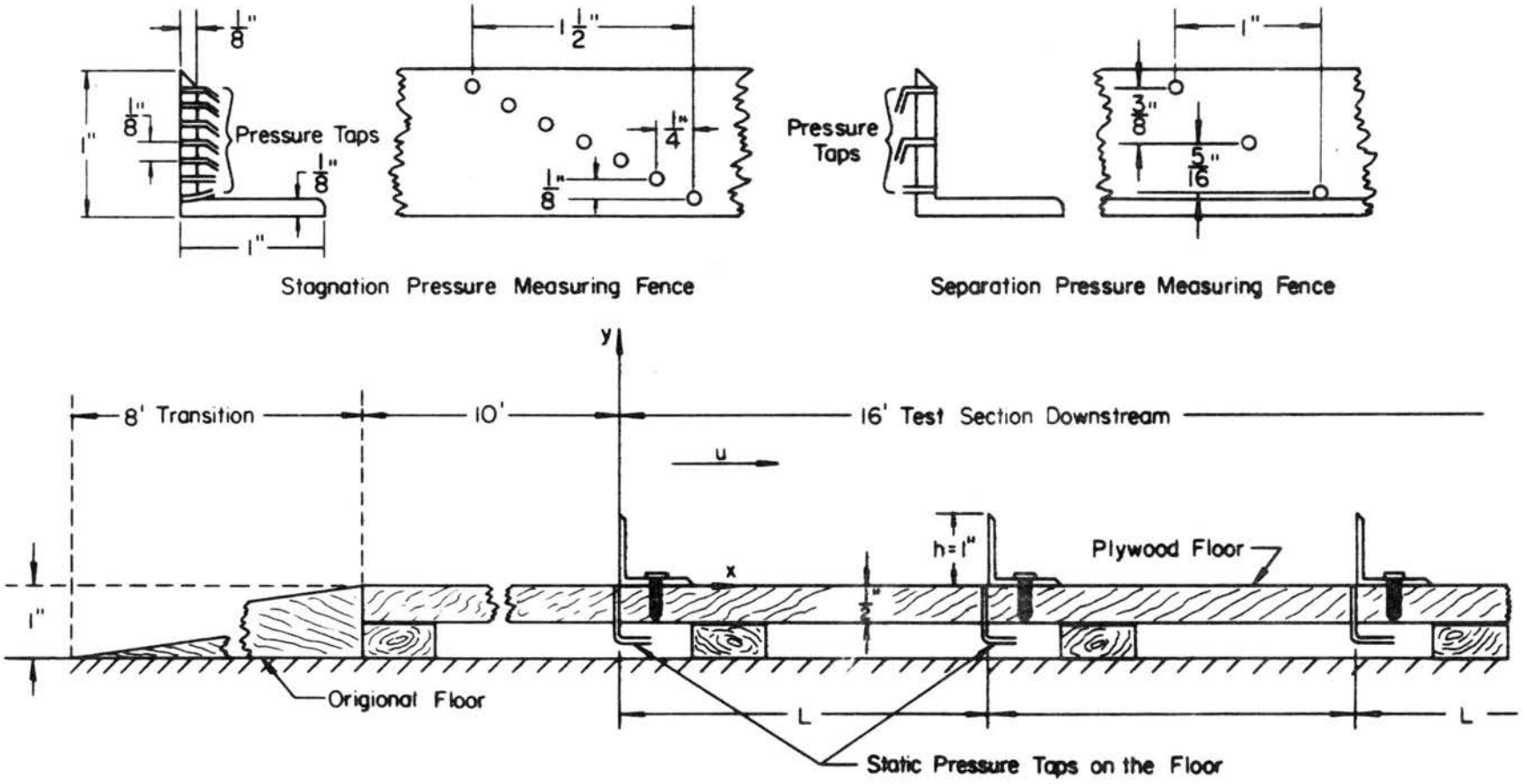

Fig. 6. Sketch of floor and fence assembly.

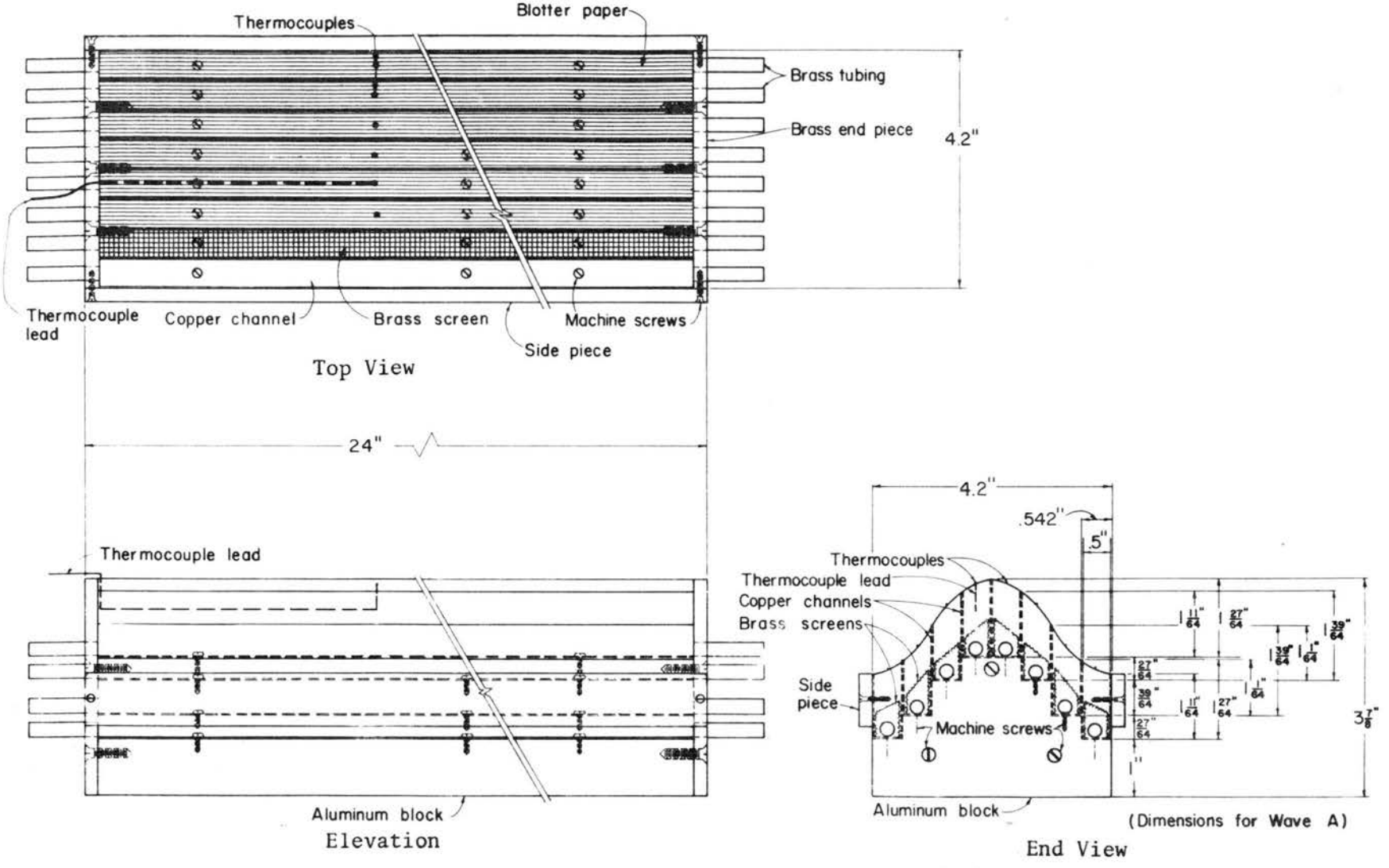

Fig. 7. Evaporation metering wave.

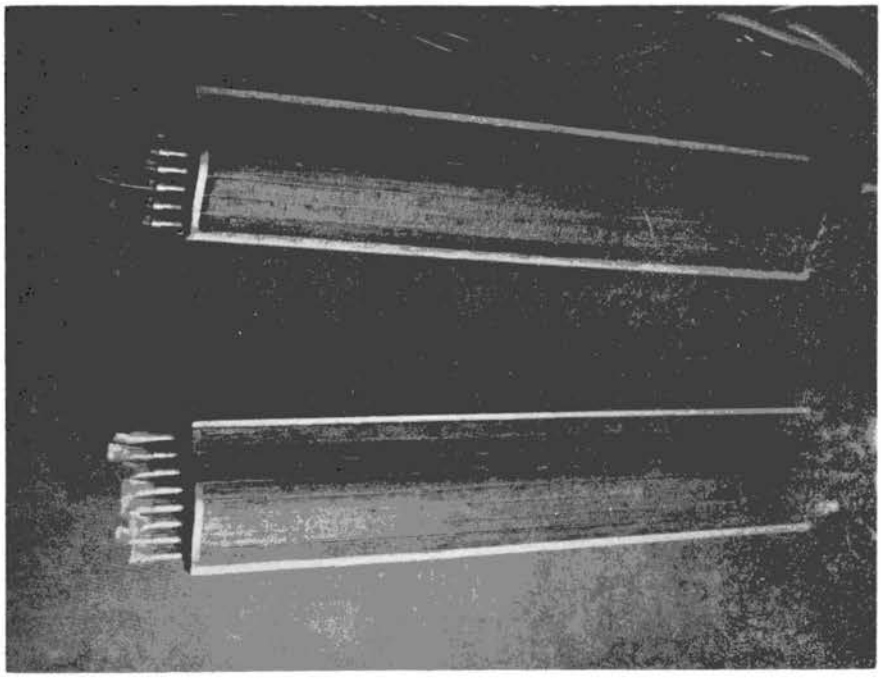

Fig. 8 Photograph of evaporation metering waves B and C.

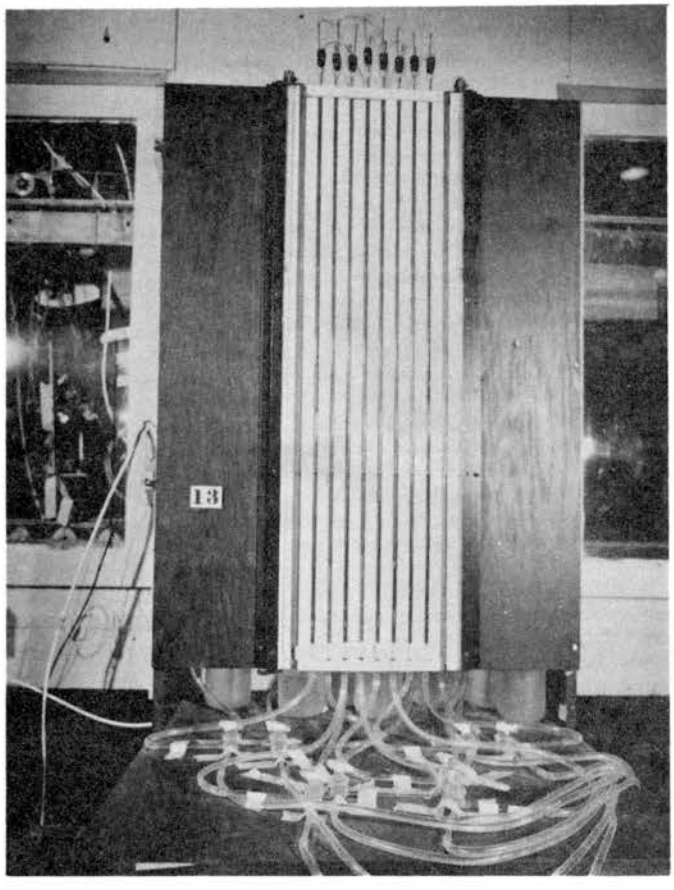

Fig. 9 Photograph of automatic feed and evaporation metering system.

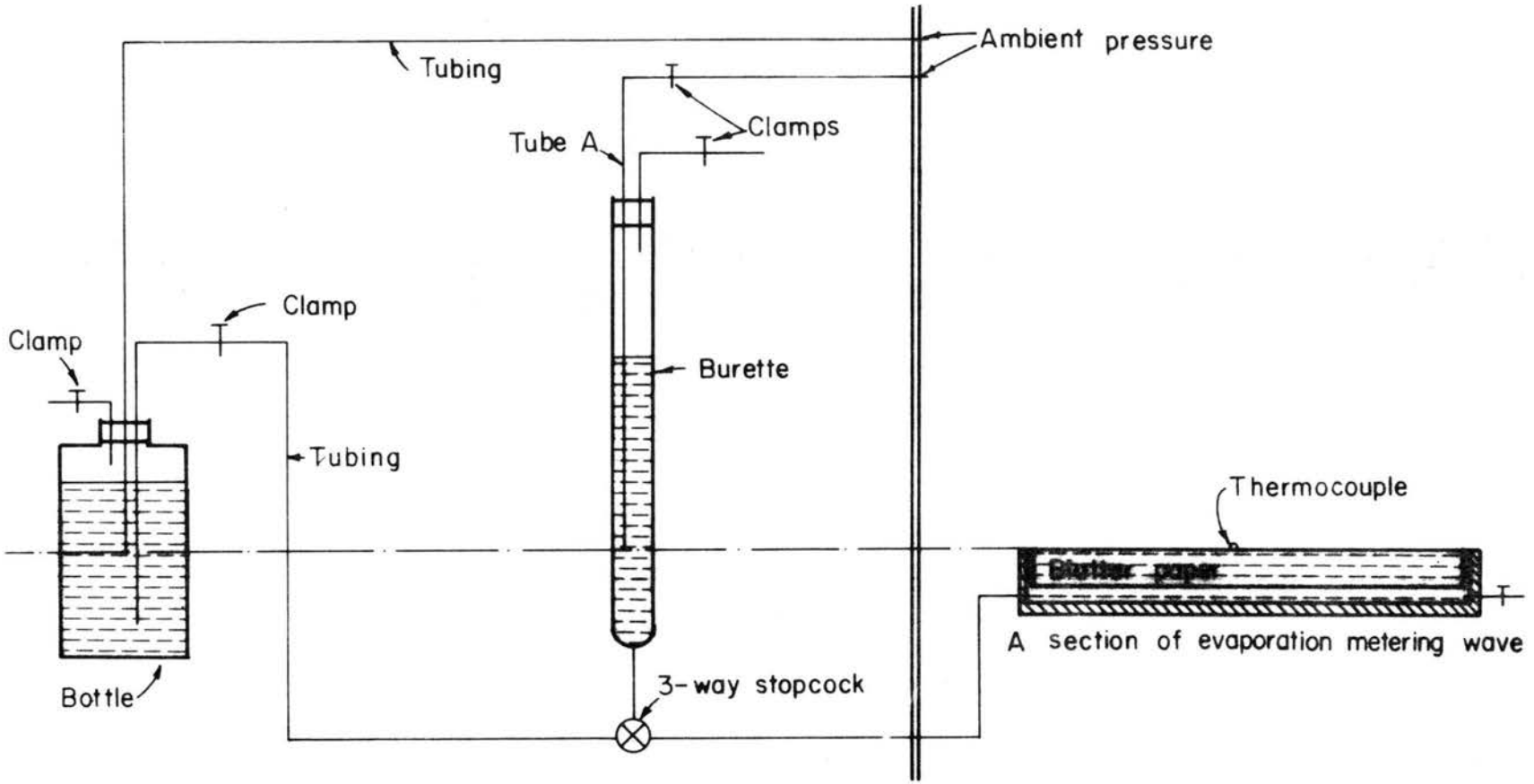

Fig. 10. Part of automatic feed and metering system (typical for each wave section).

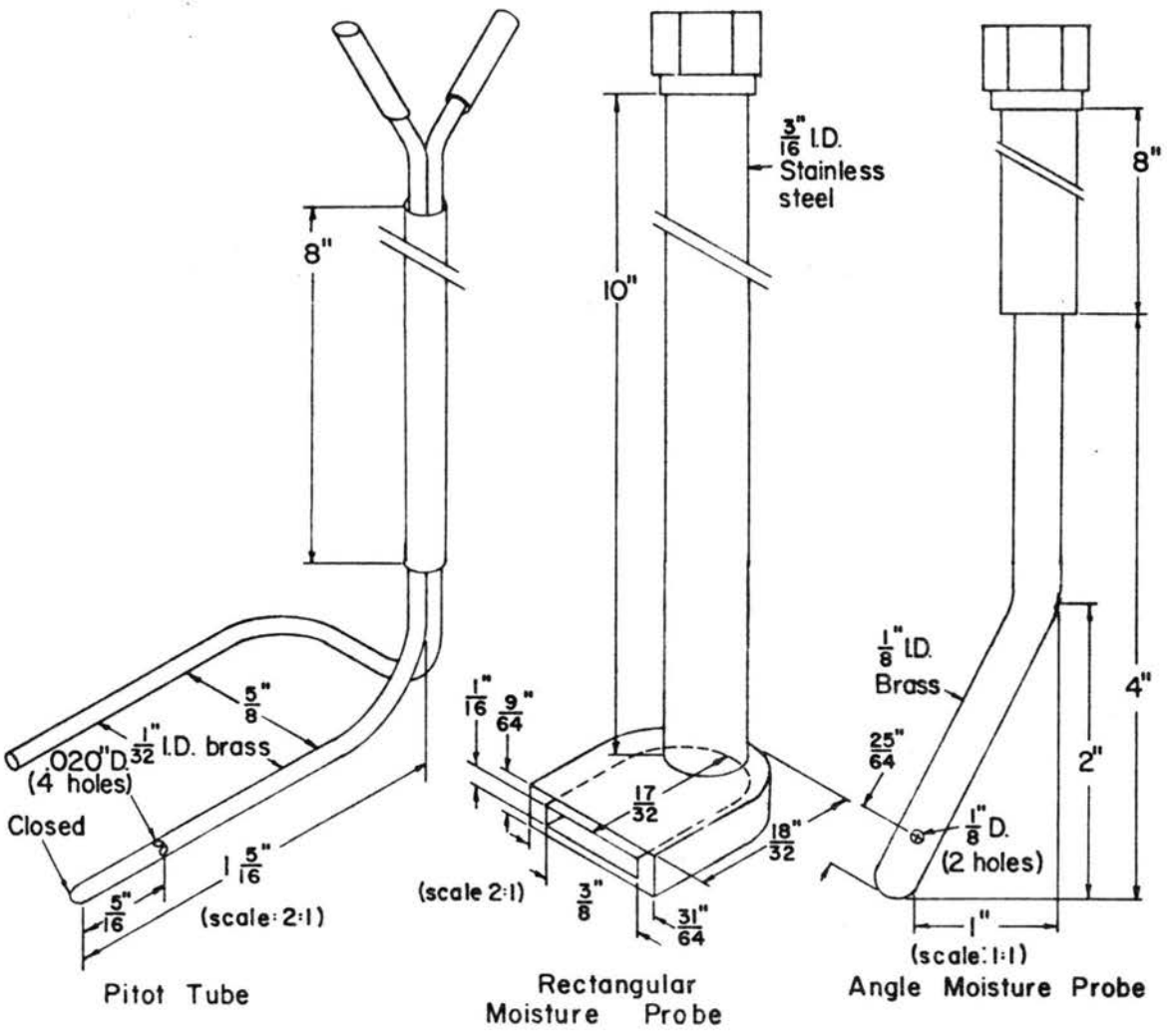

Fig. 11. Probes.

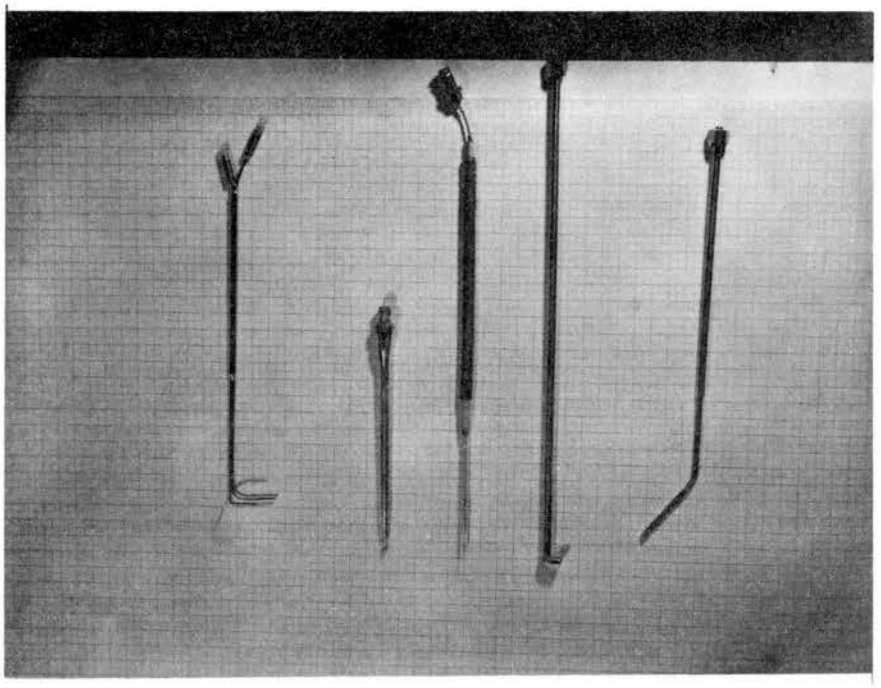

a b c d e

a: Pitot tube, b: Disa Type F13 Hot Wire Probe c: Disa Type 55A22 Hot Wire Probe, d: Moisture Probe, e: Reference Moisture Probe

Fig. 12 Photograph of Probes

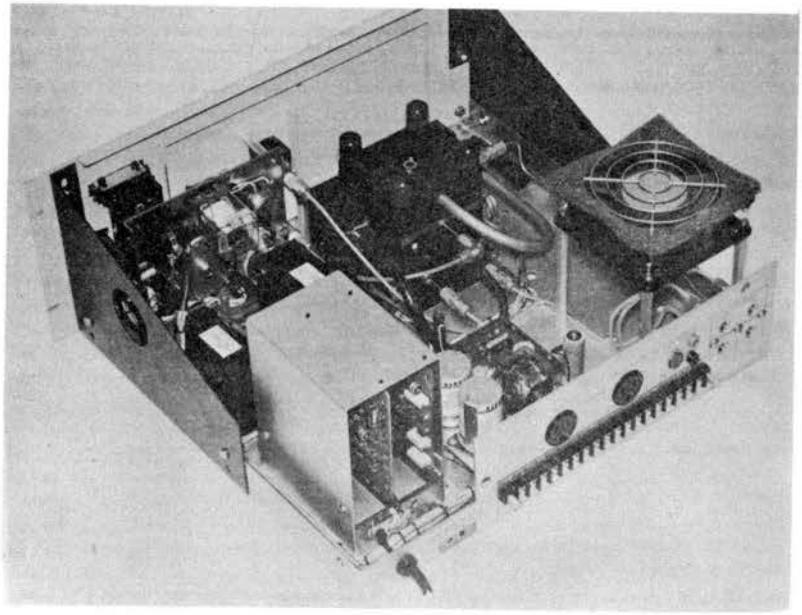

Fig. 13 Interior view of the dew point hygrometer (Cambridge Systems Model 992).

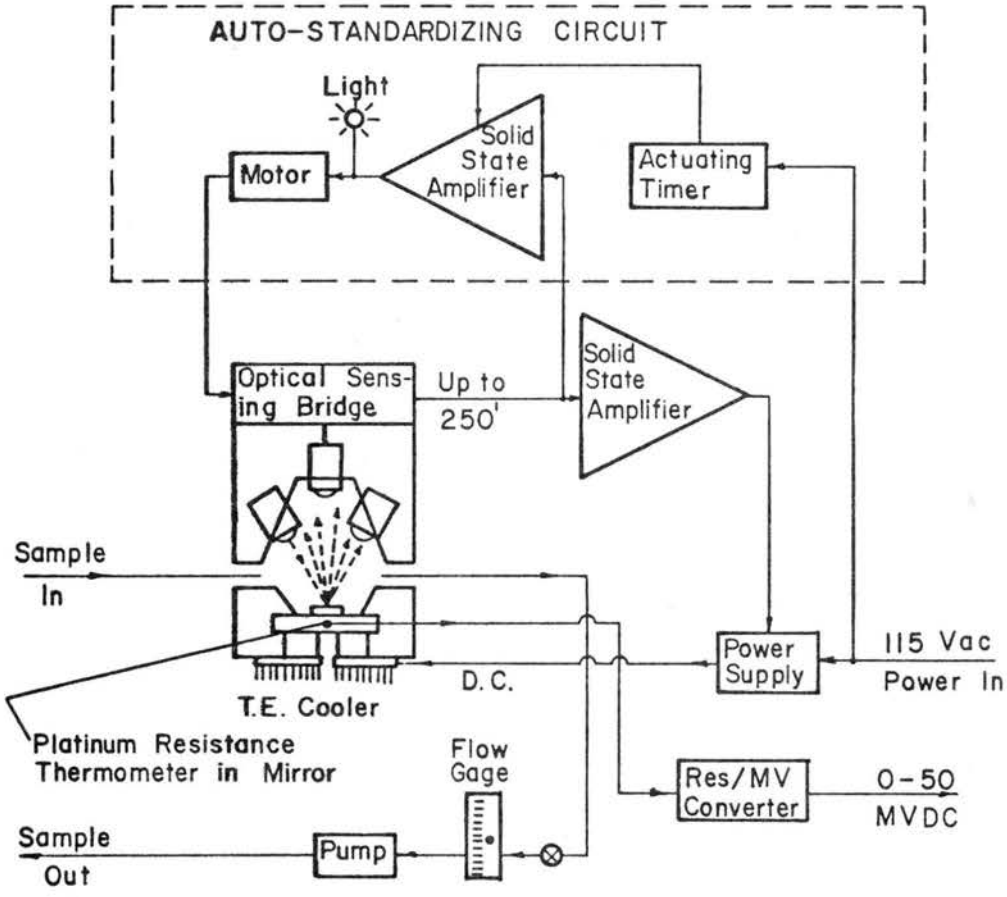

Fig. 14 Simplified block diagram of the dew point hygrometer (Cambridge Systems Model 992).

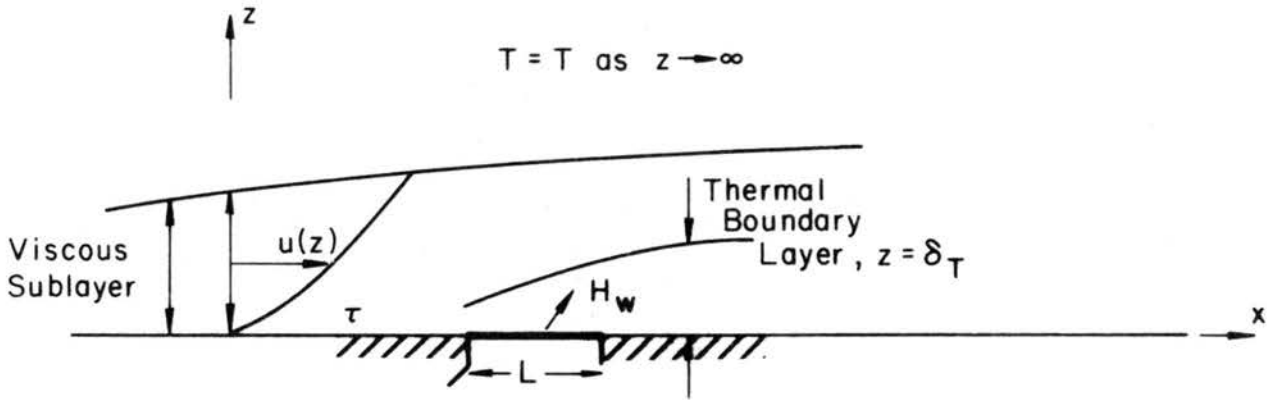

L : Physical Length of Film

L_e: Effective Length of Film of Film for Heating

($L_e > L$)

T : Temperature Distribution Around Film

H_w: Power Lost By Film To Flow

Fig. 15. Flow conditions for hot film response.

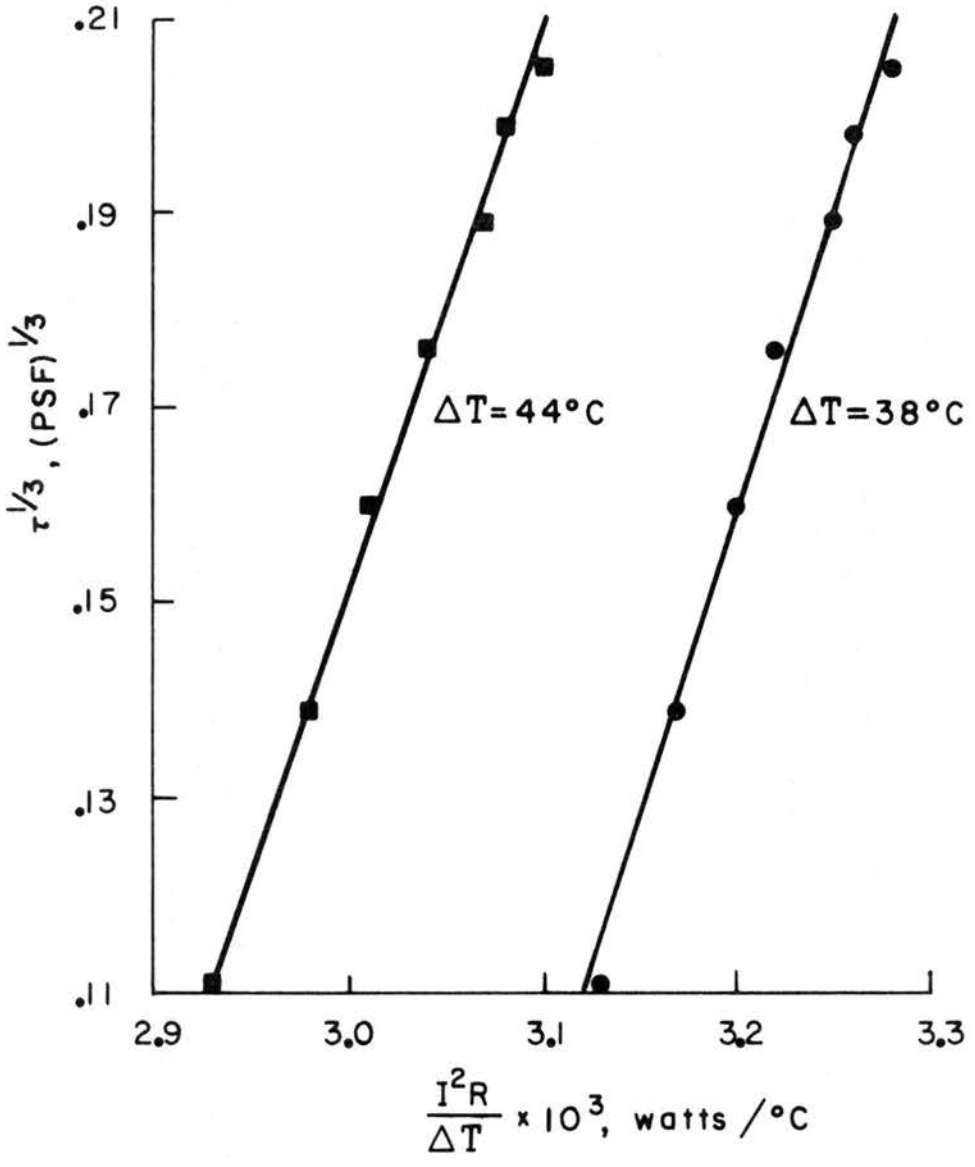

Fig. 16. Typical hot-film calibrations.

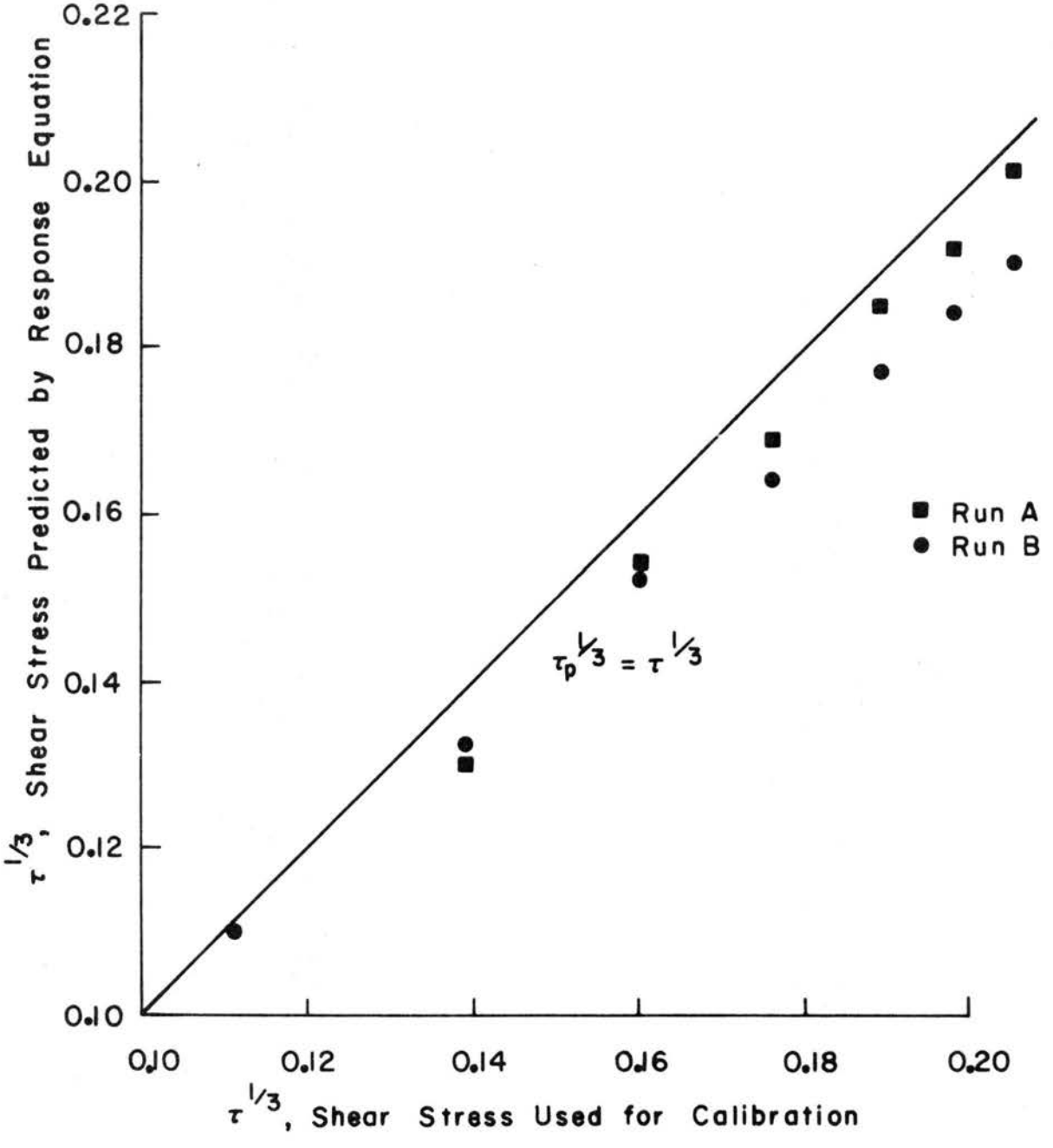

Fig. 17. Prediction by response equation for hot-film.

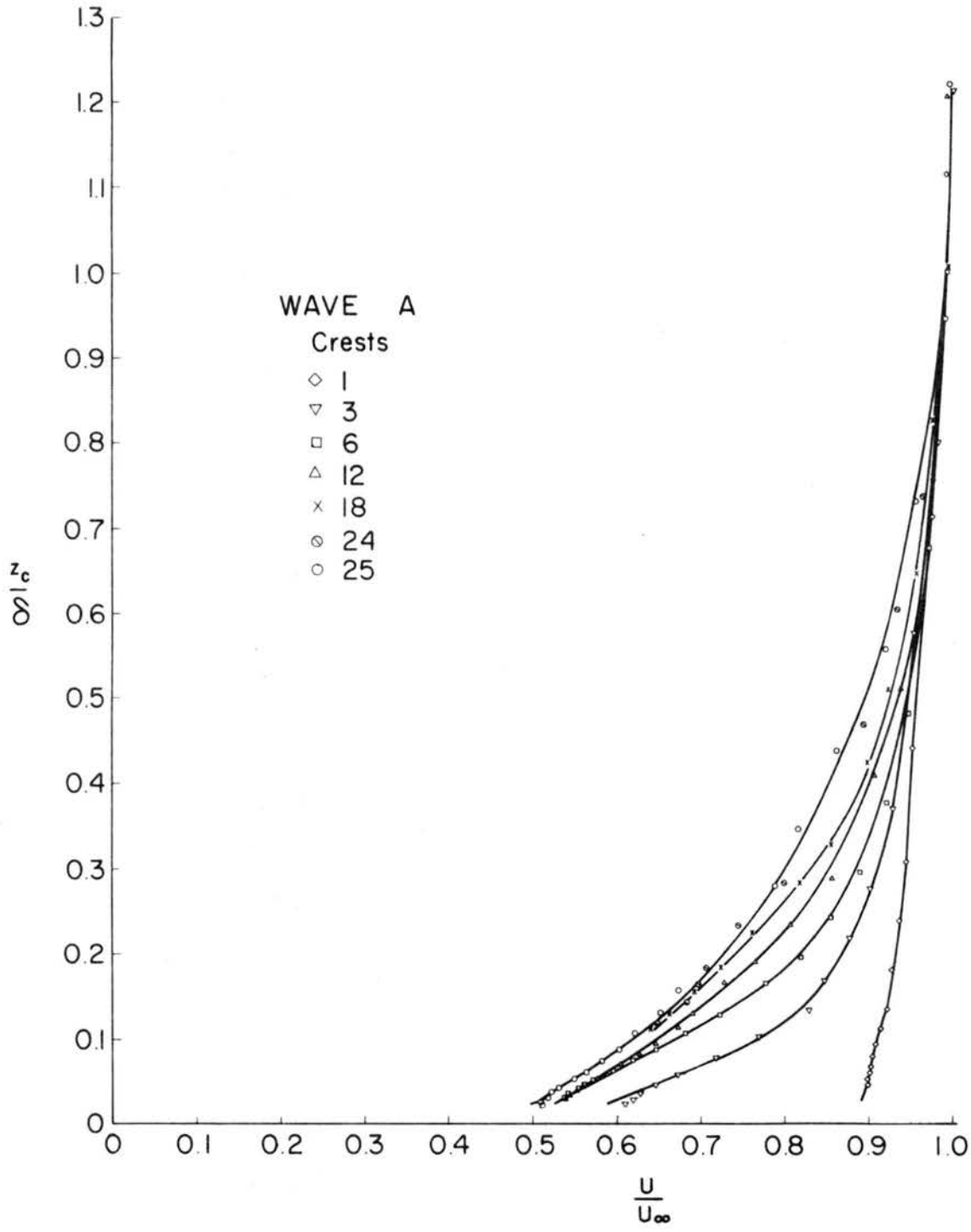

Fig. 18. Mean velocity profiles, wave A.

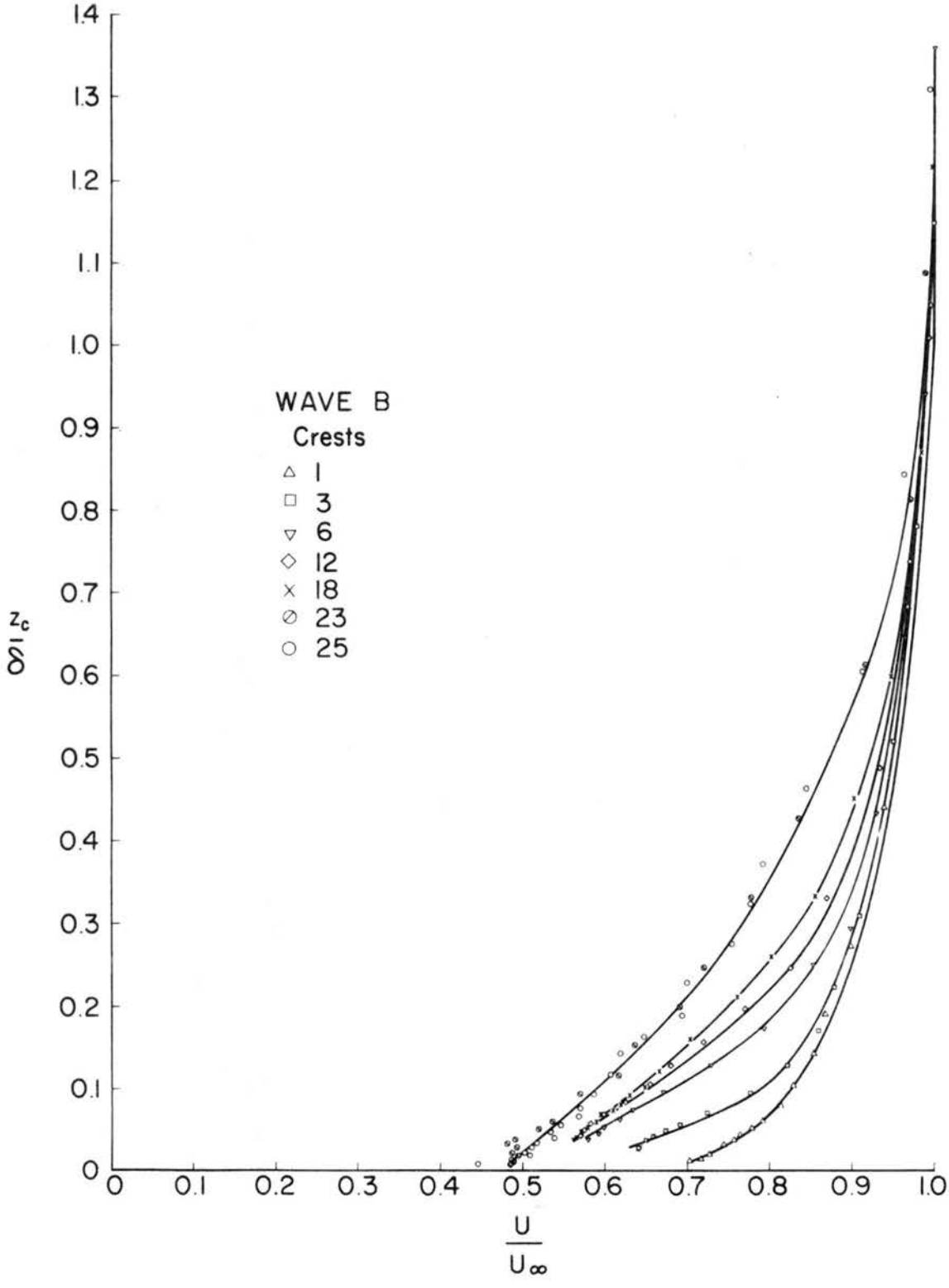

Fig. 19. Mean velocity profiles, wave B.

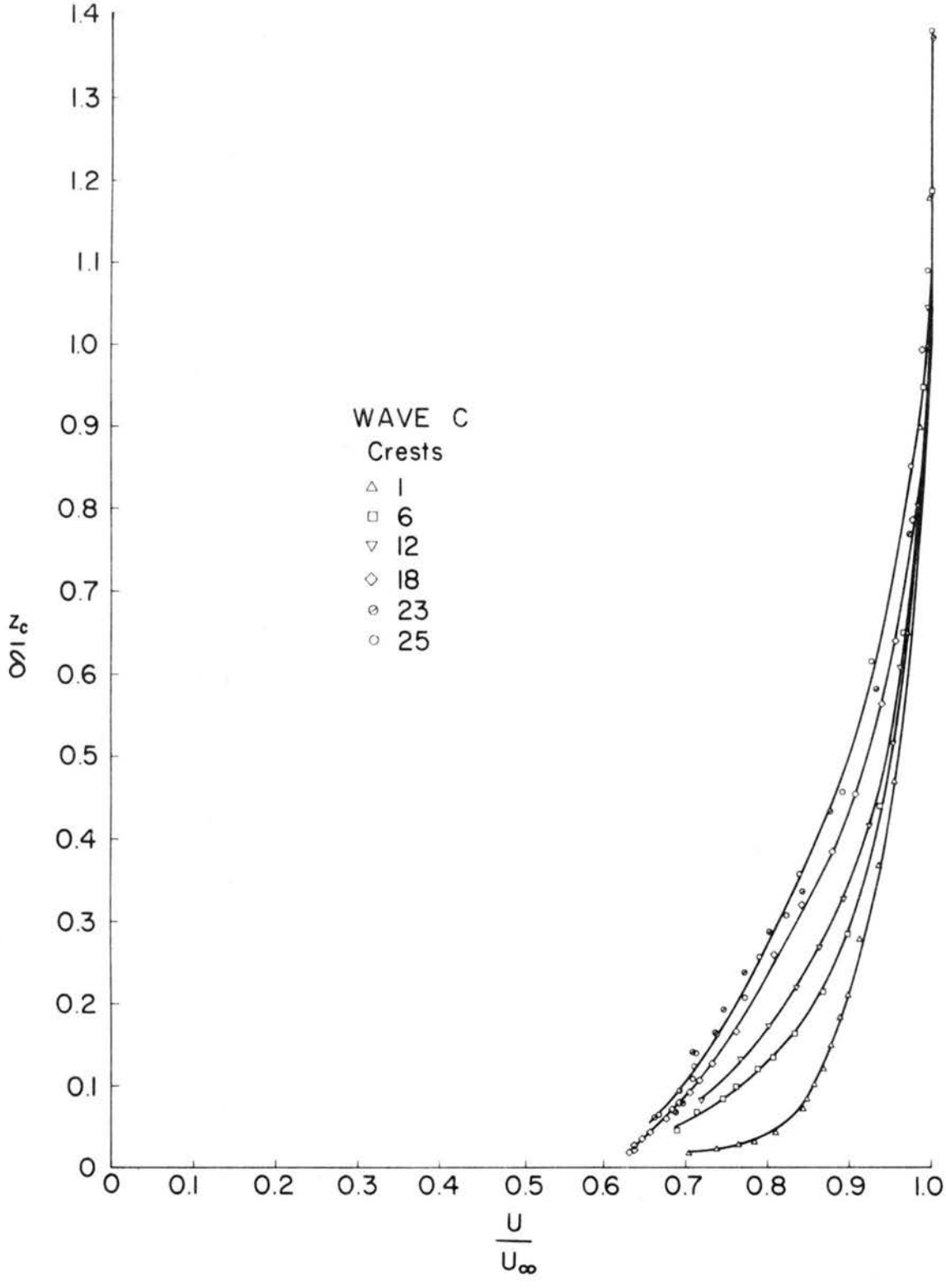

Fig. 20. Mean velocity profiles, wave C.

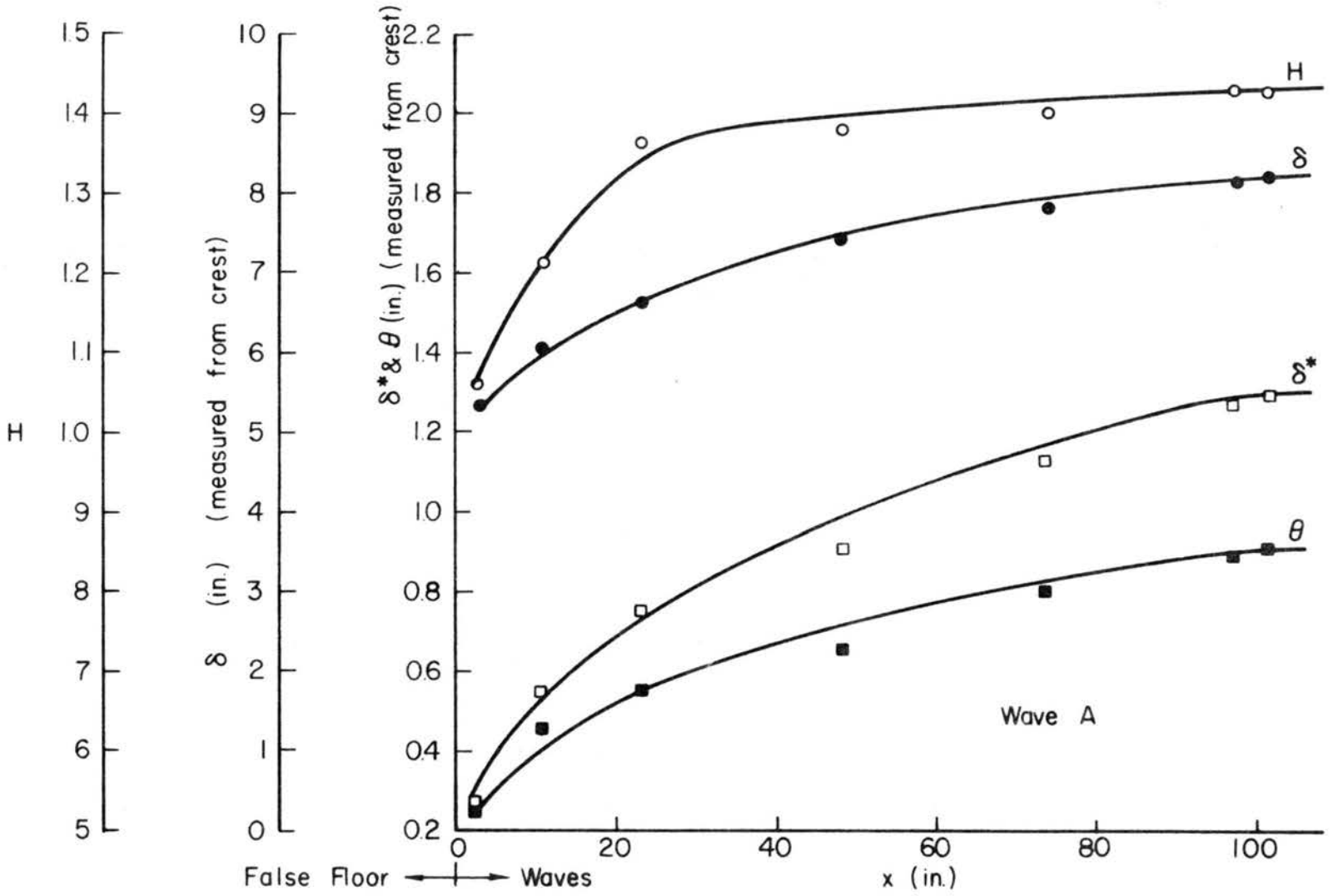

Fig. 21. Plots of δ, δ^*, θ and H, wave A.

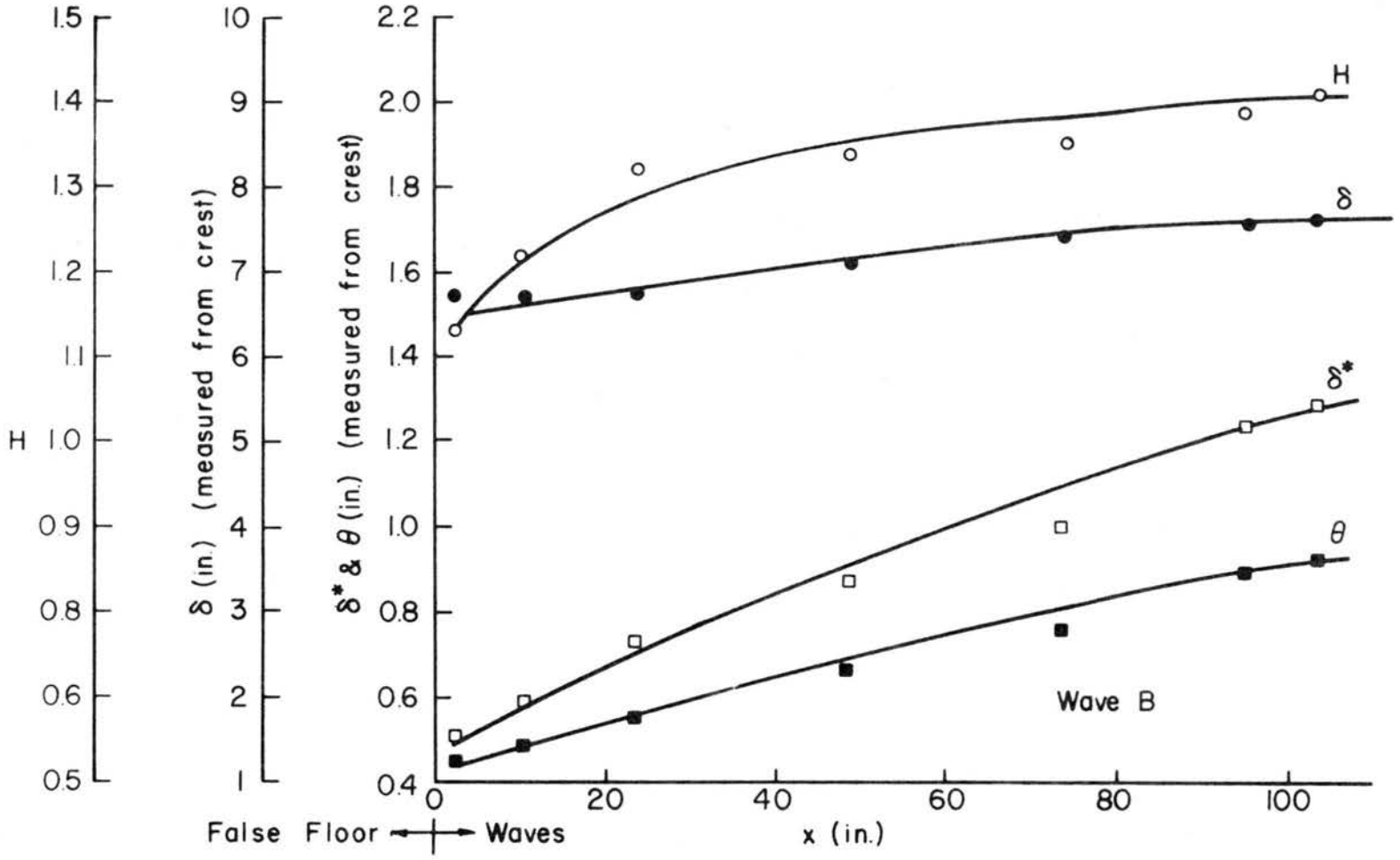

Fig. 22. Plots of δ, δ^*, θ and H, wave B.

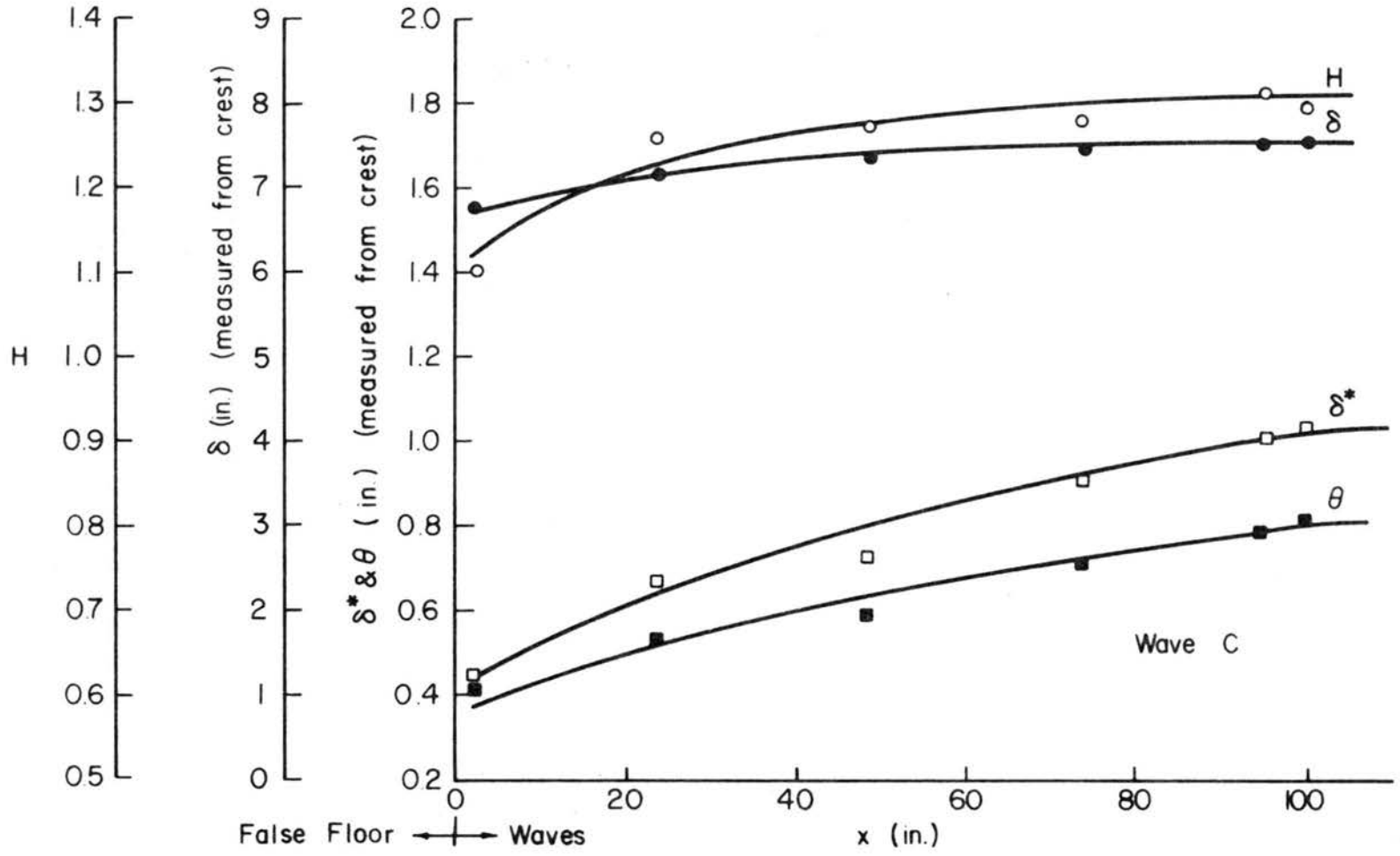

Fig. 23. Plots of δ, δ^*, θ and H, wave C.

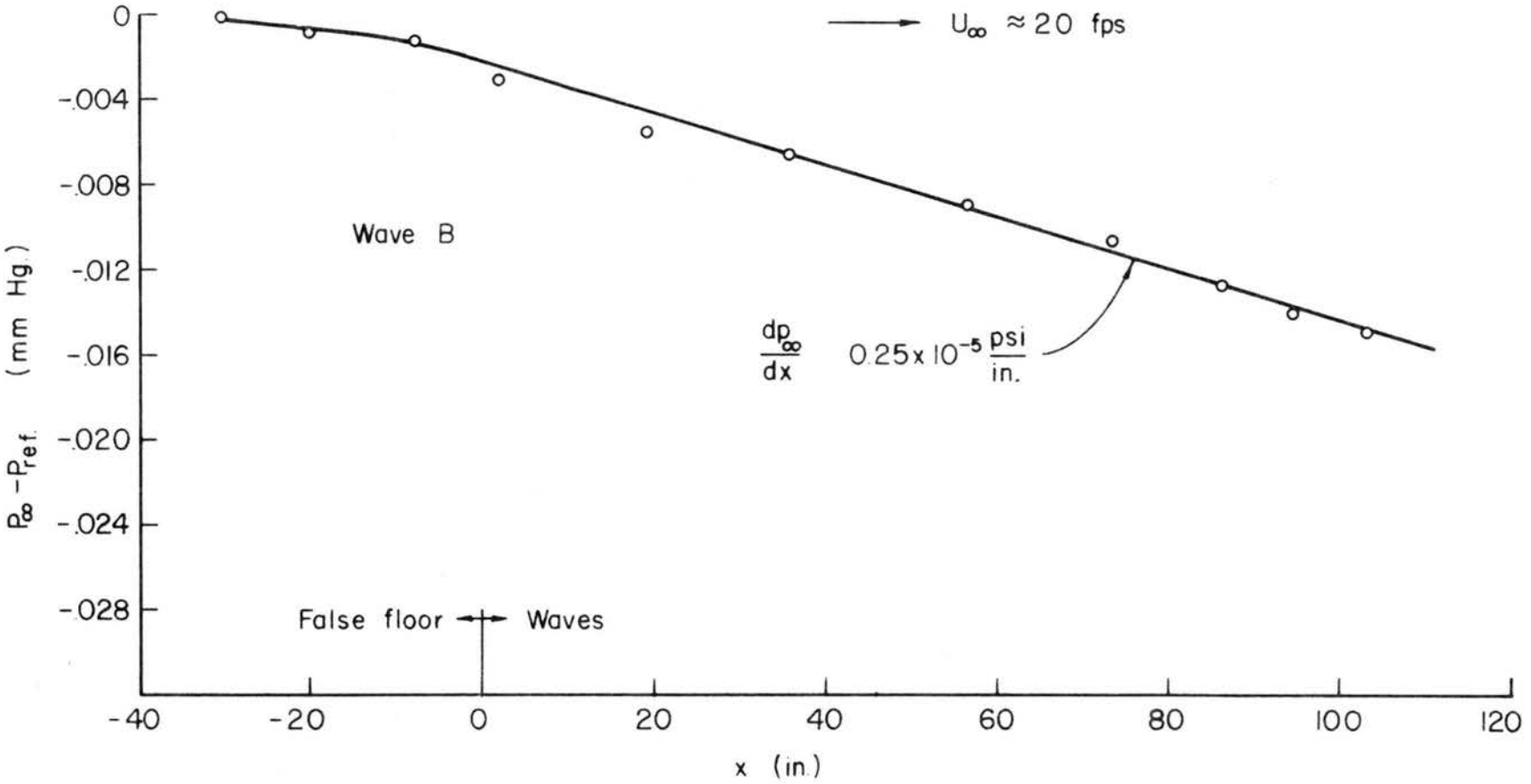

Fig. 24. Free stream static pressure distribution (waves) - typical case.

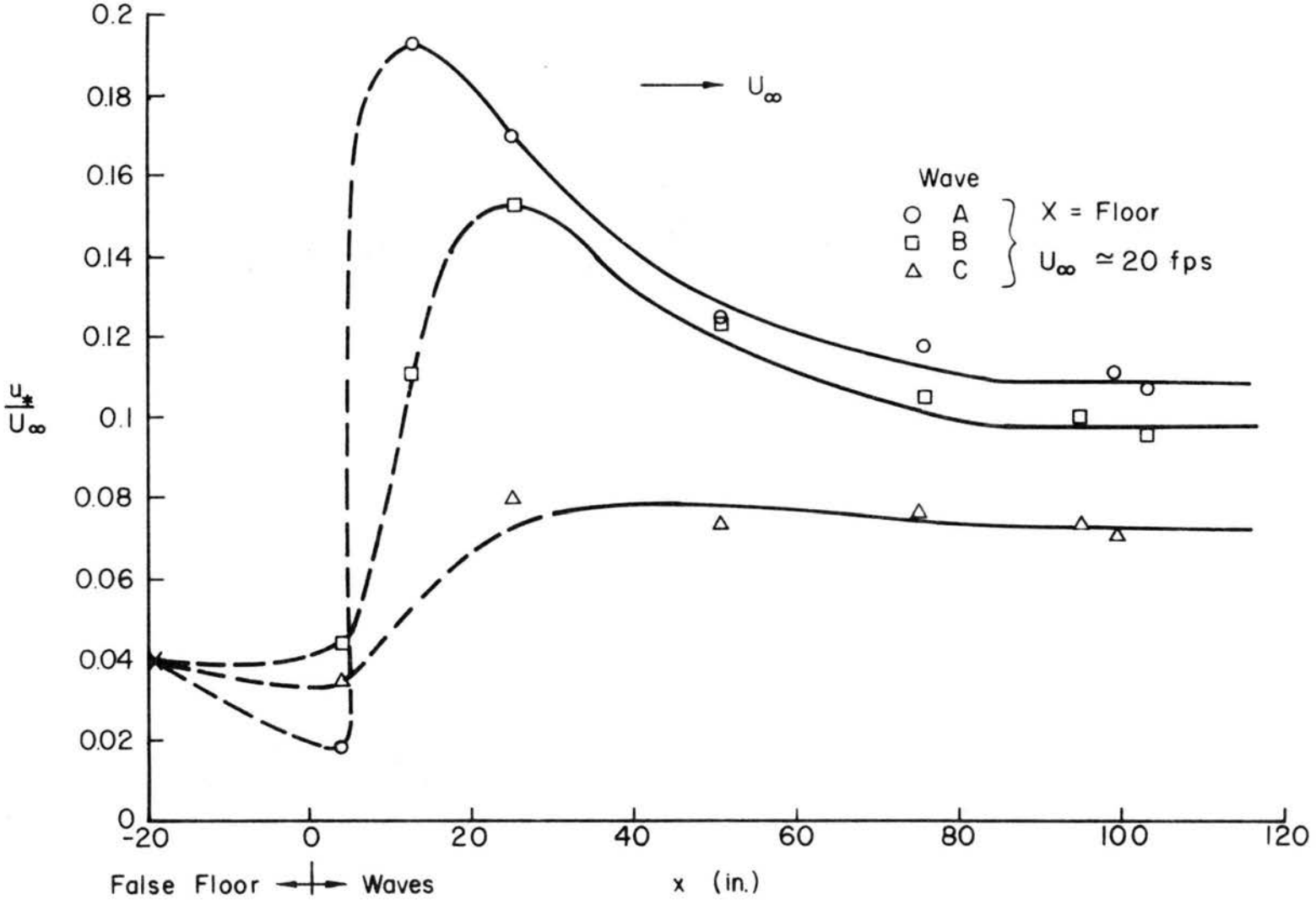

Fig. 25. Variation of friction velocity u_* with fetch (waves).

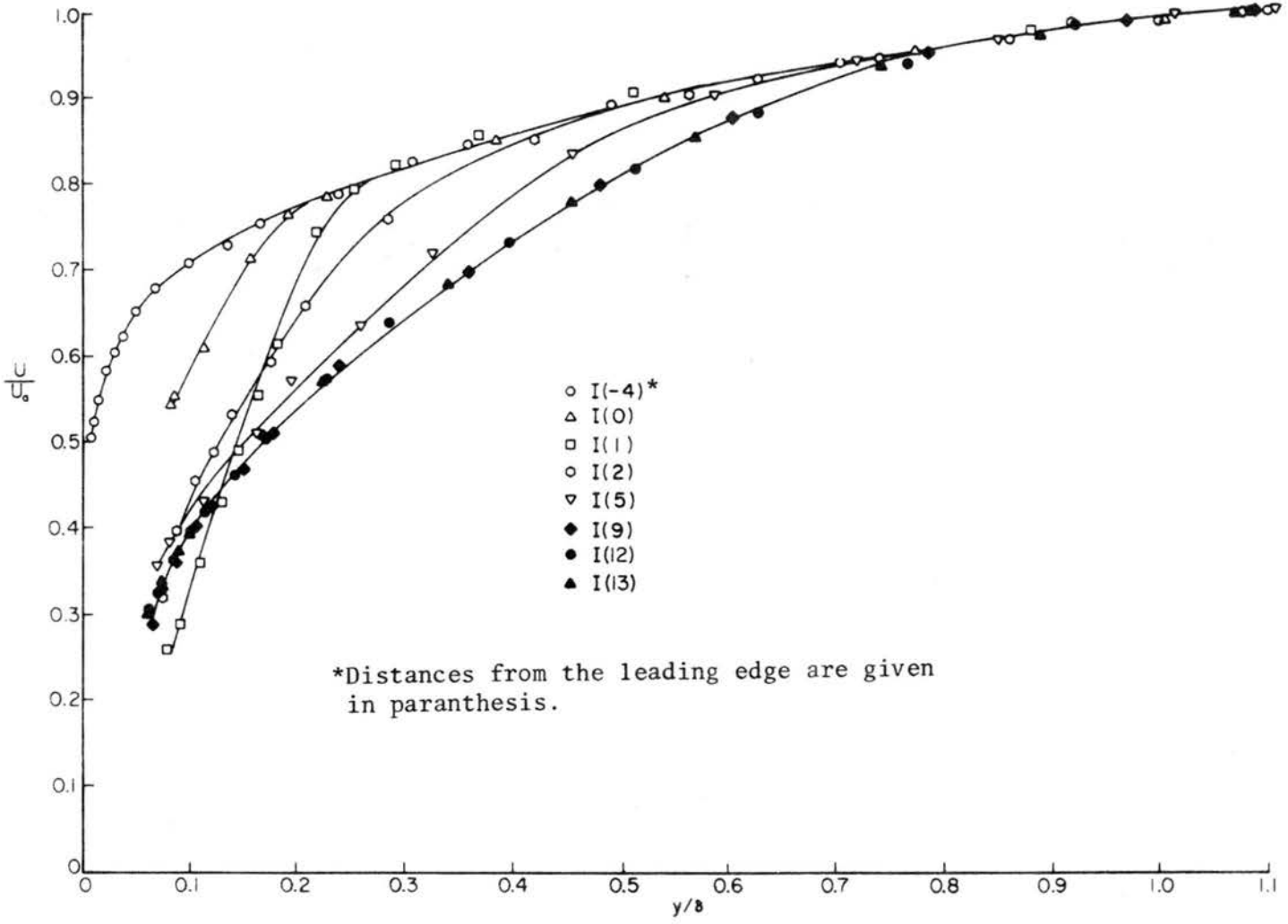

Fig. 26. Typical plots of velocity profiles on fences.

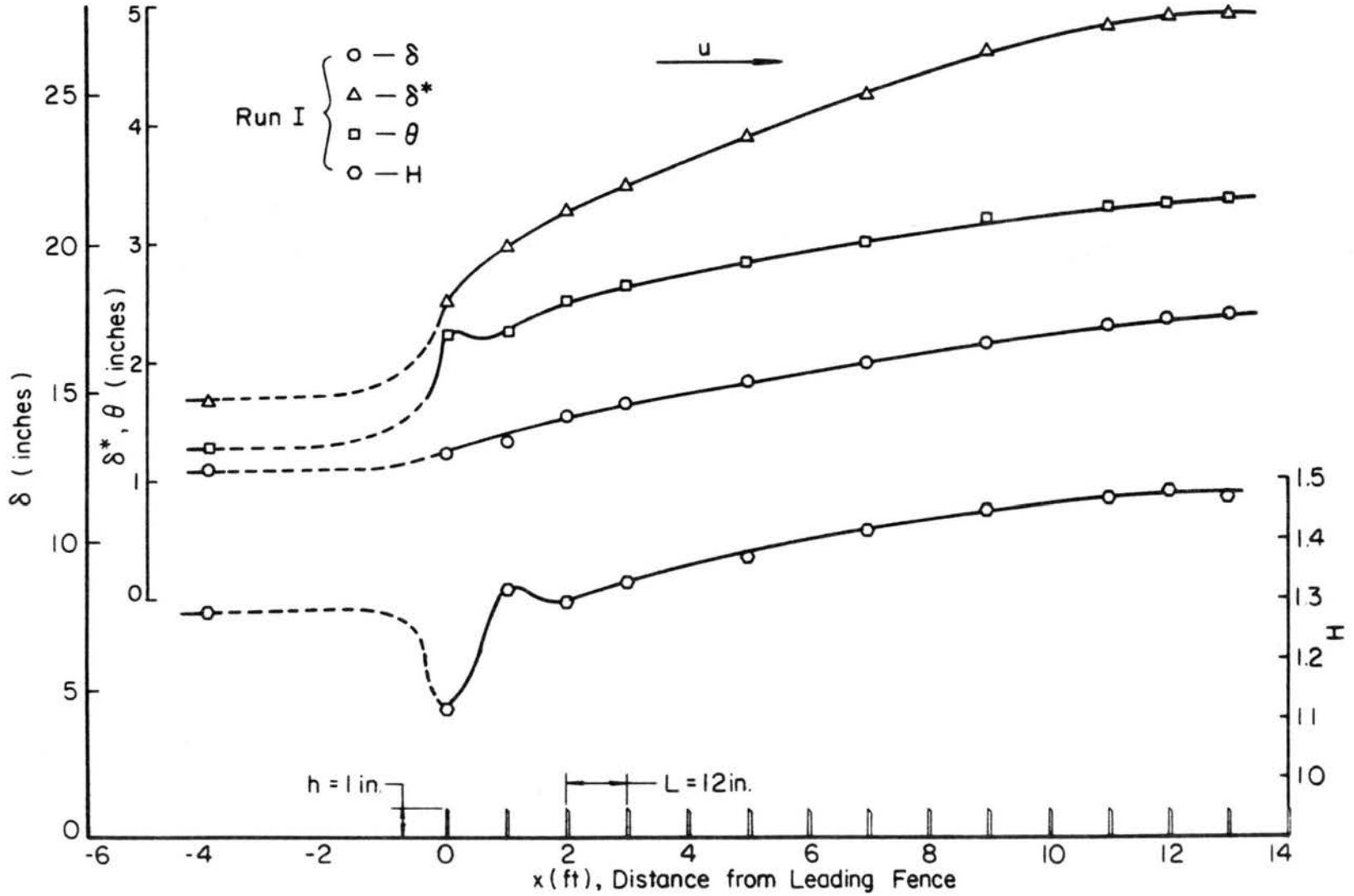

Fig. 27. Plots of boundary-layer parameters for fences (typical).

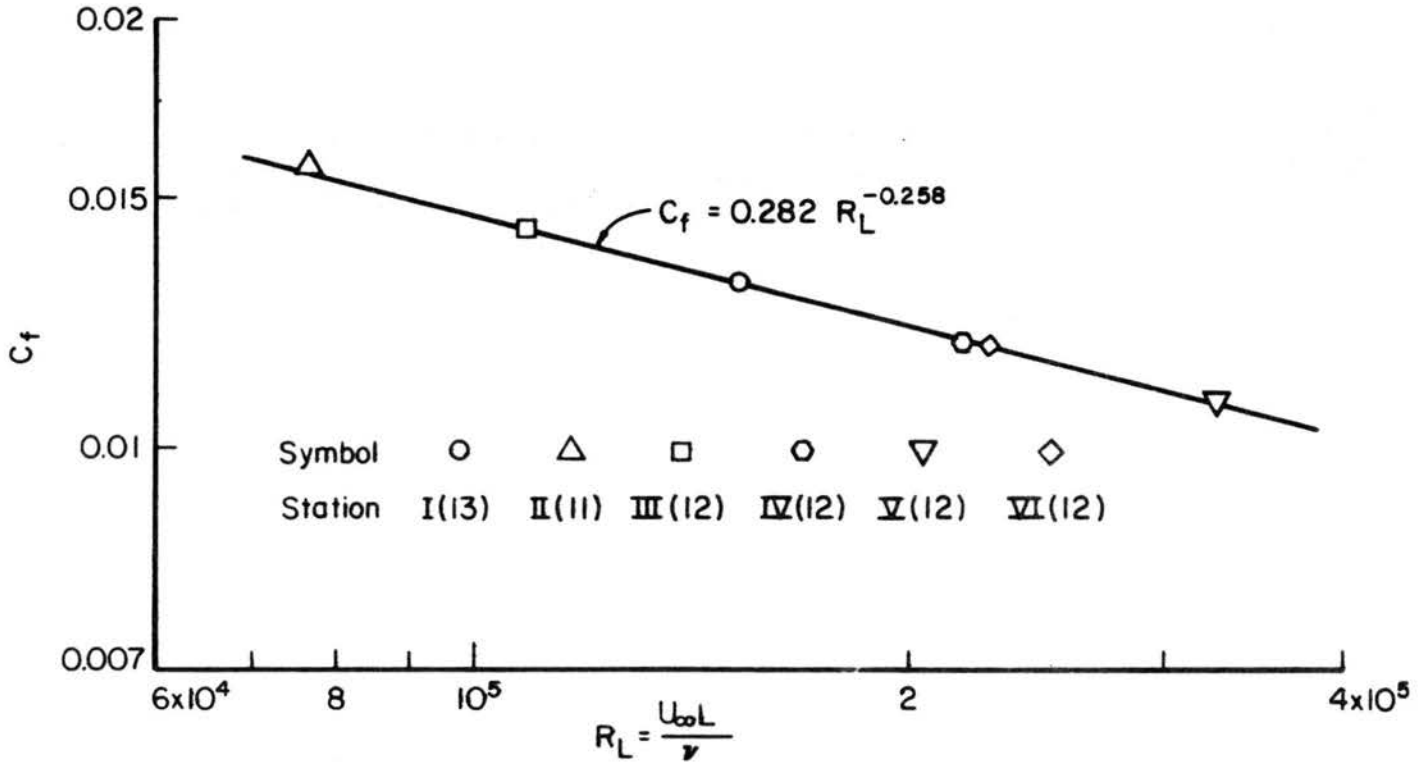

Fig. 28. C_f as a function of R_L (fences).

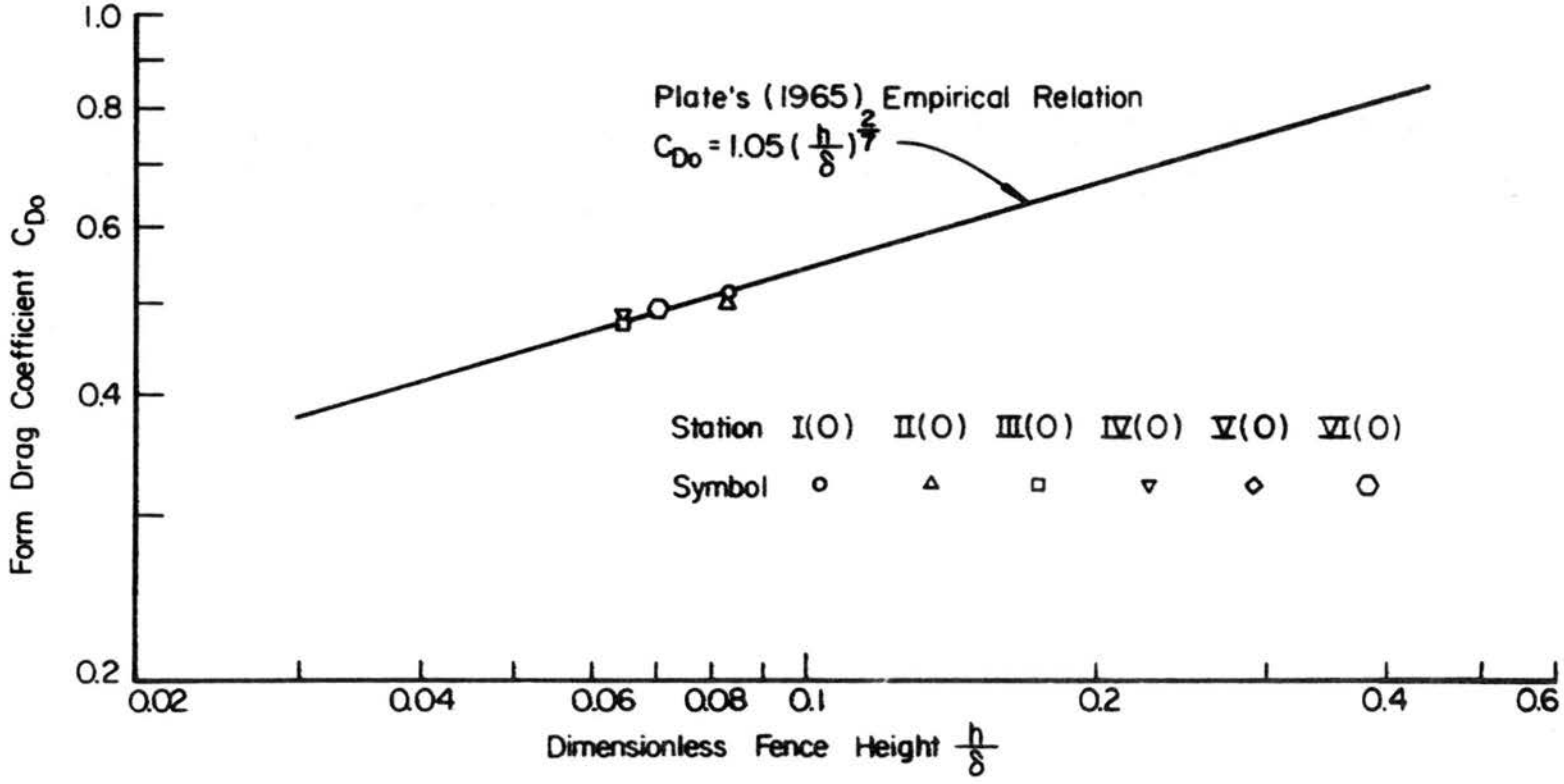

Fig. 29. Comparing C_{Do} (fences) to Plate's empirical relation.

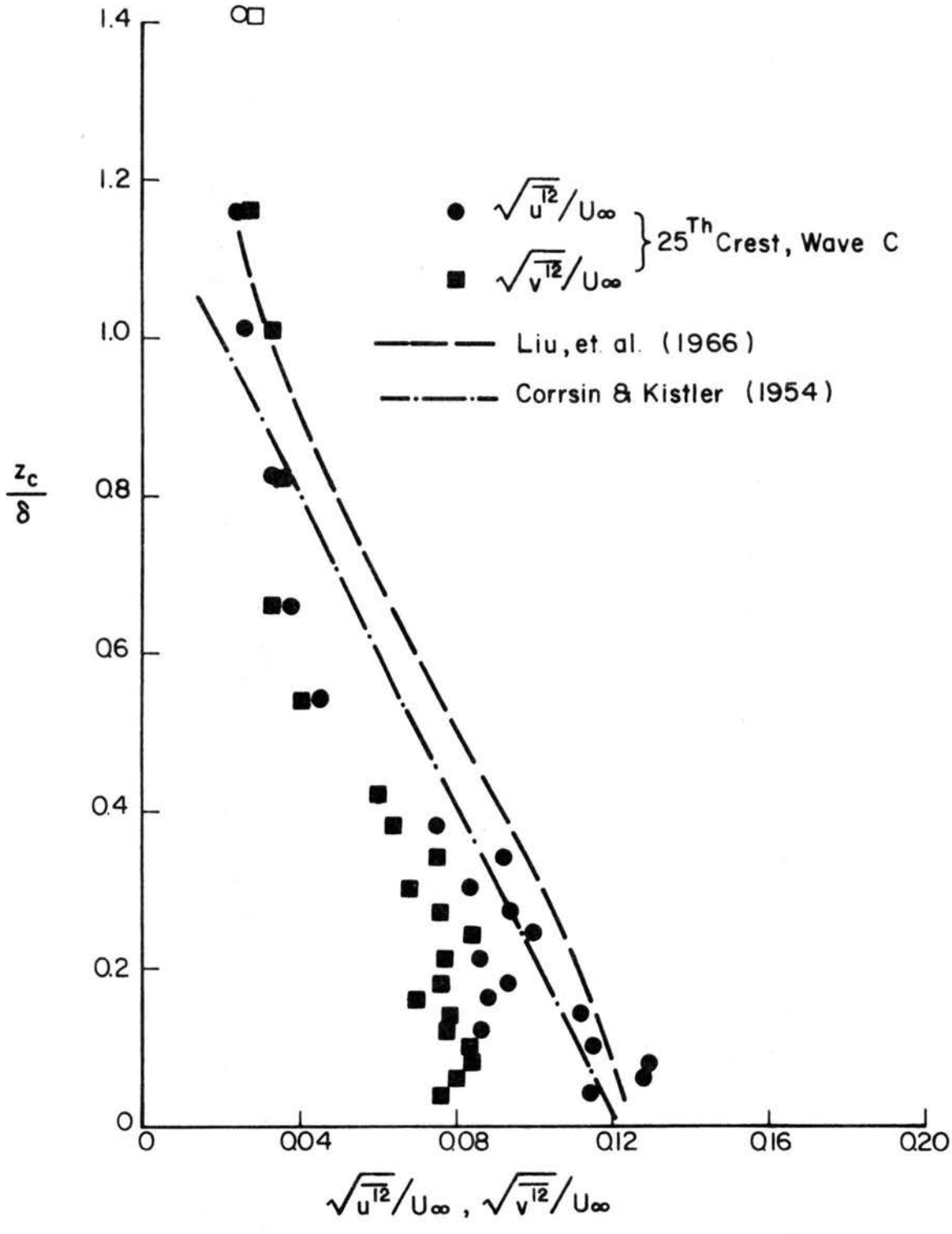

Fig. 30. Turbulent intensities over waves (typical).

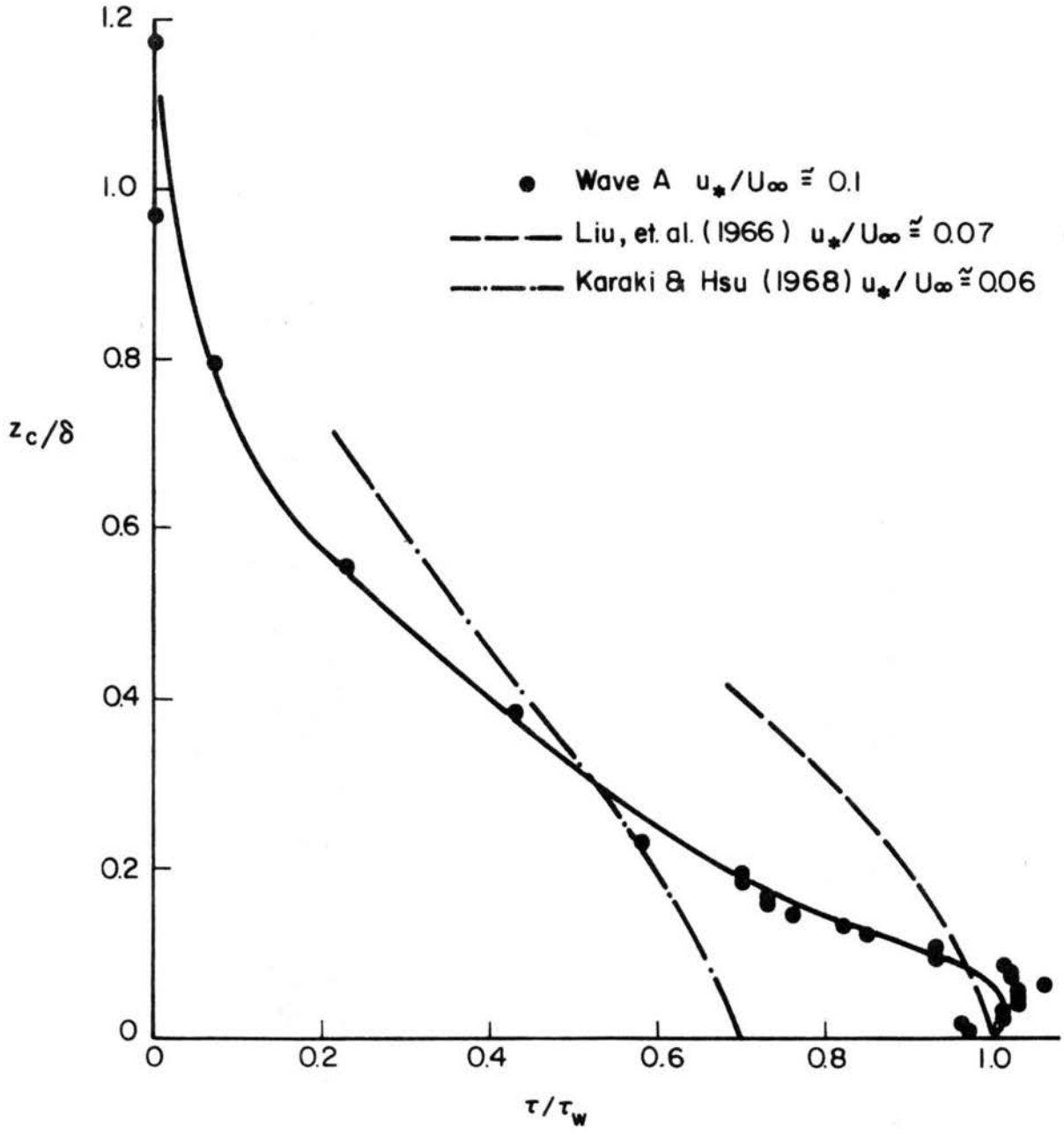

Fig. 31. Shear-stress profile over waves (typical).

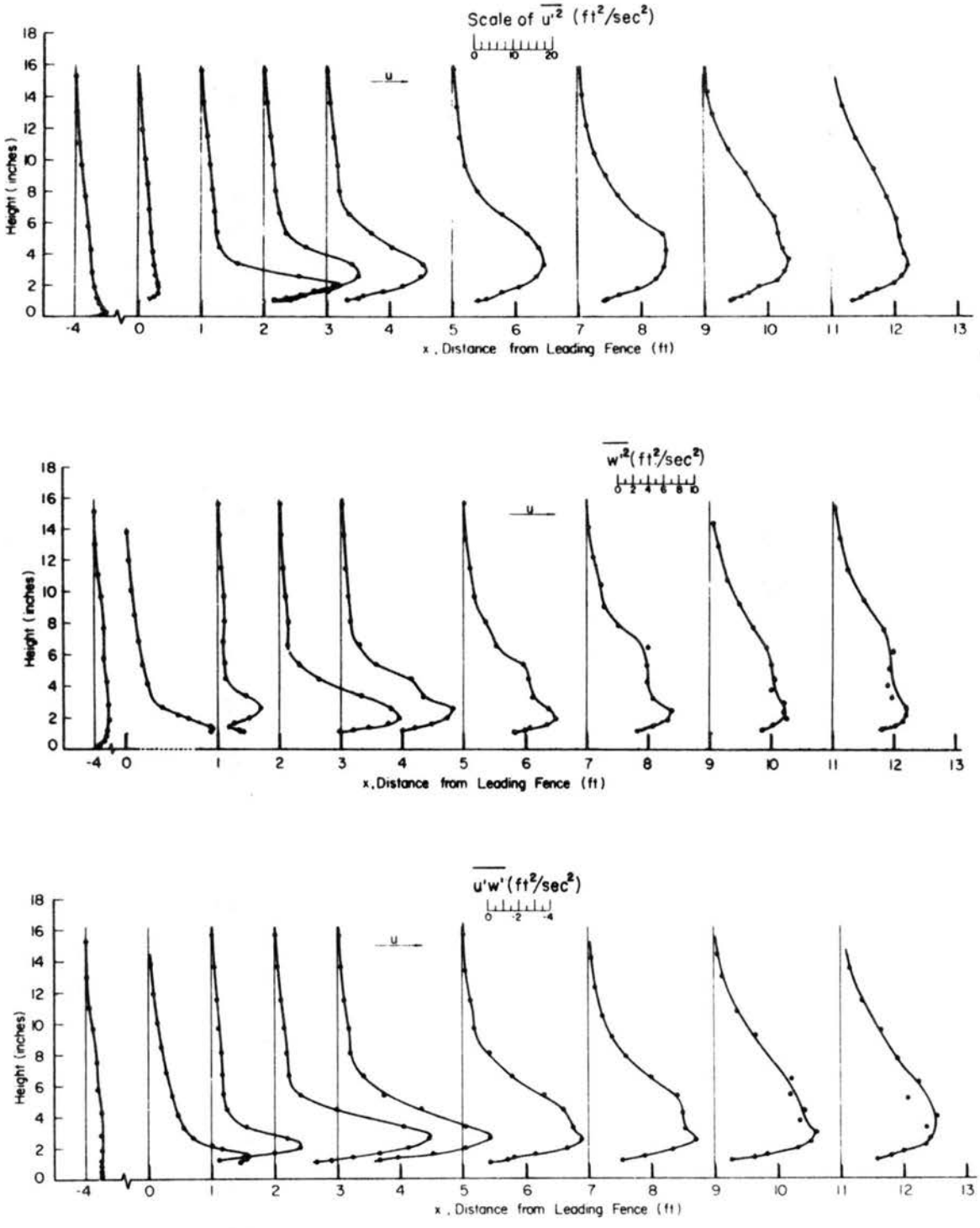

Fig. 32. Turbulence distributions over fences (typical).

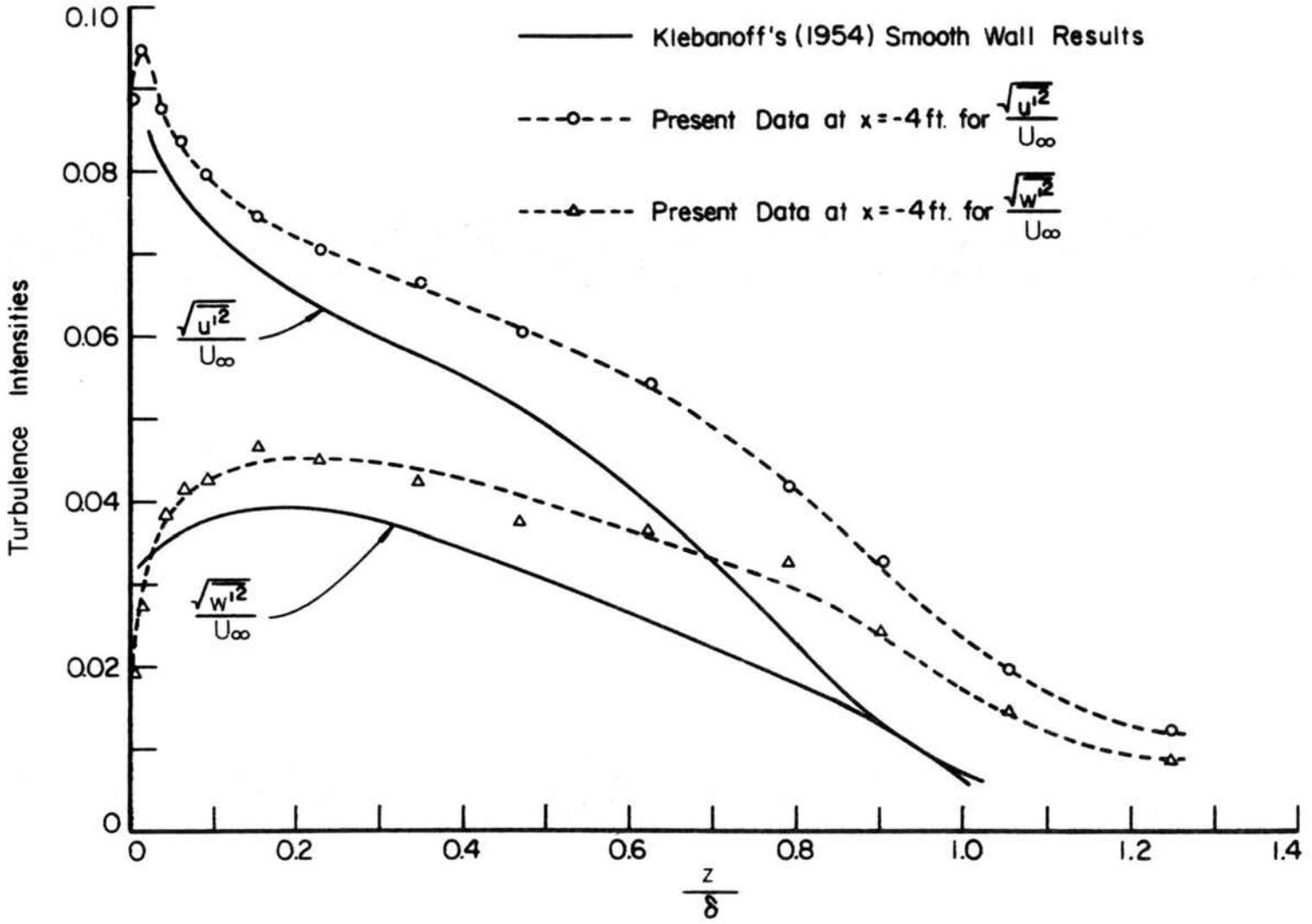

Fig. 33. Turbulence intensities upstream of fences.

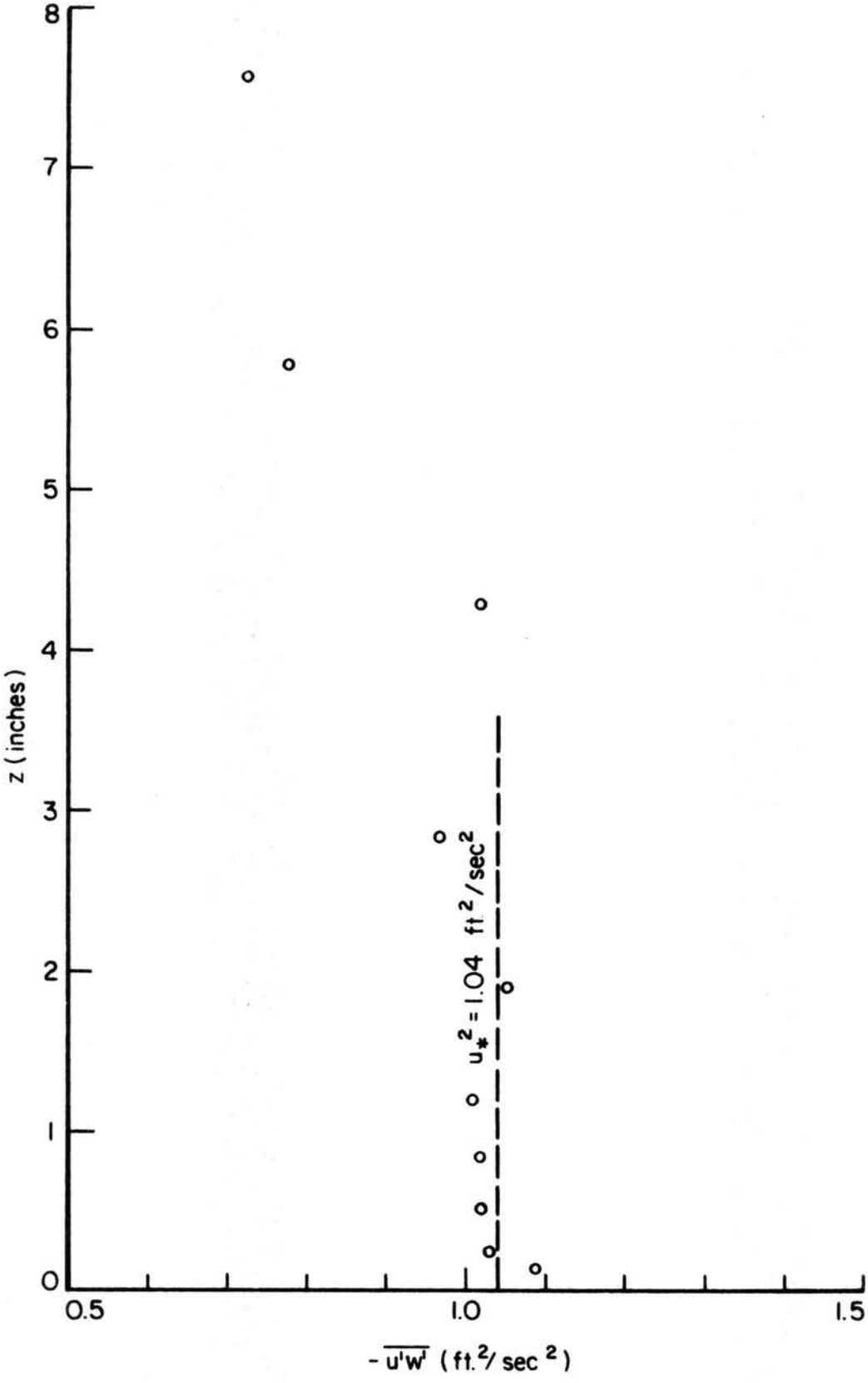

Fig. 34. Turbulent shear stress distribution upstream of fences.

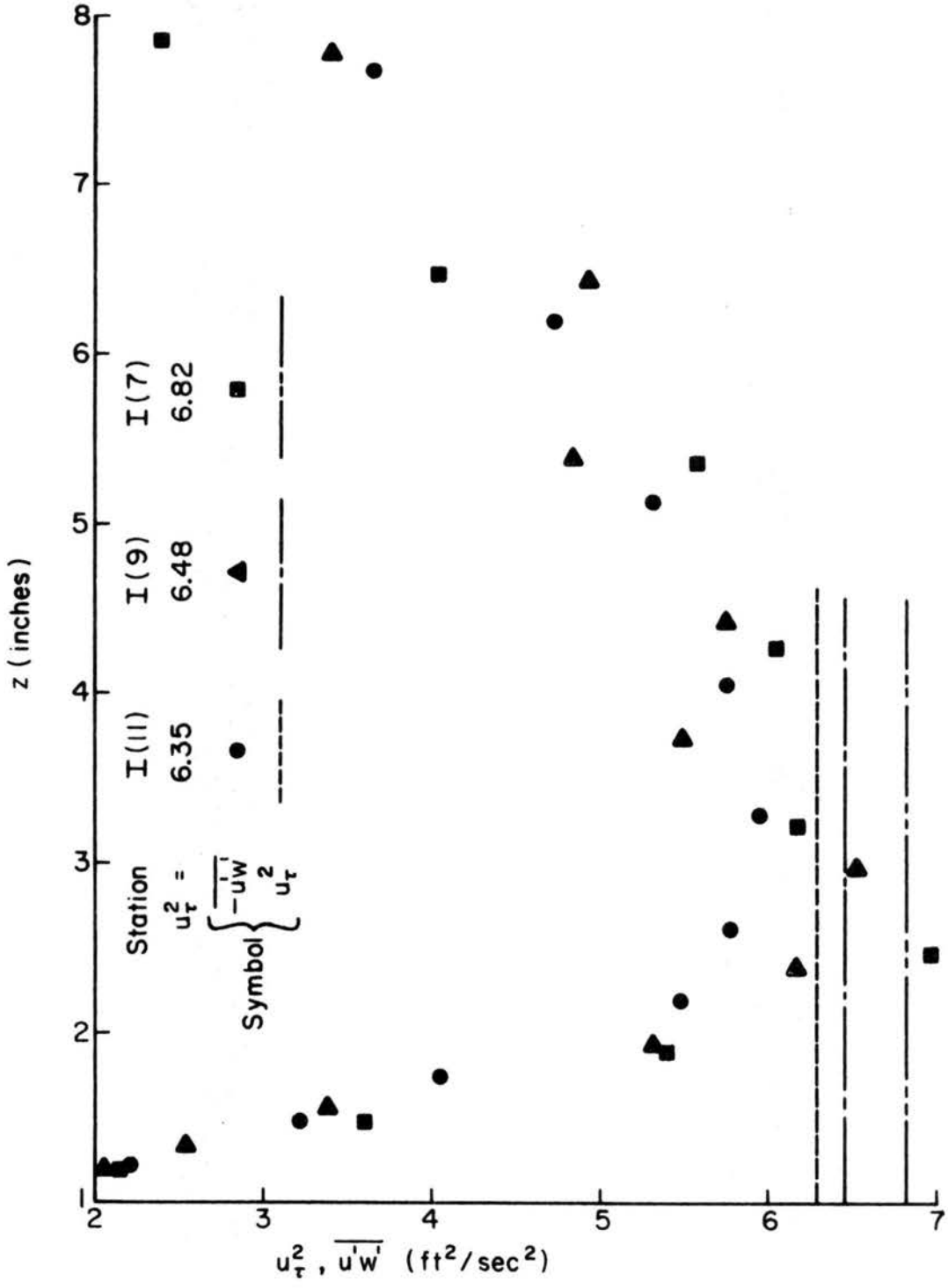

Fig. 35. Turbulent shear-stress distribution over fences (typical).

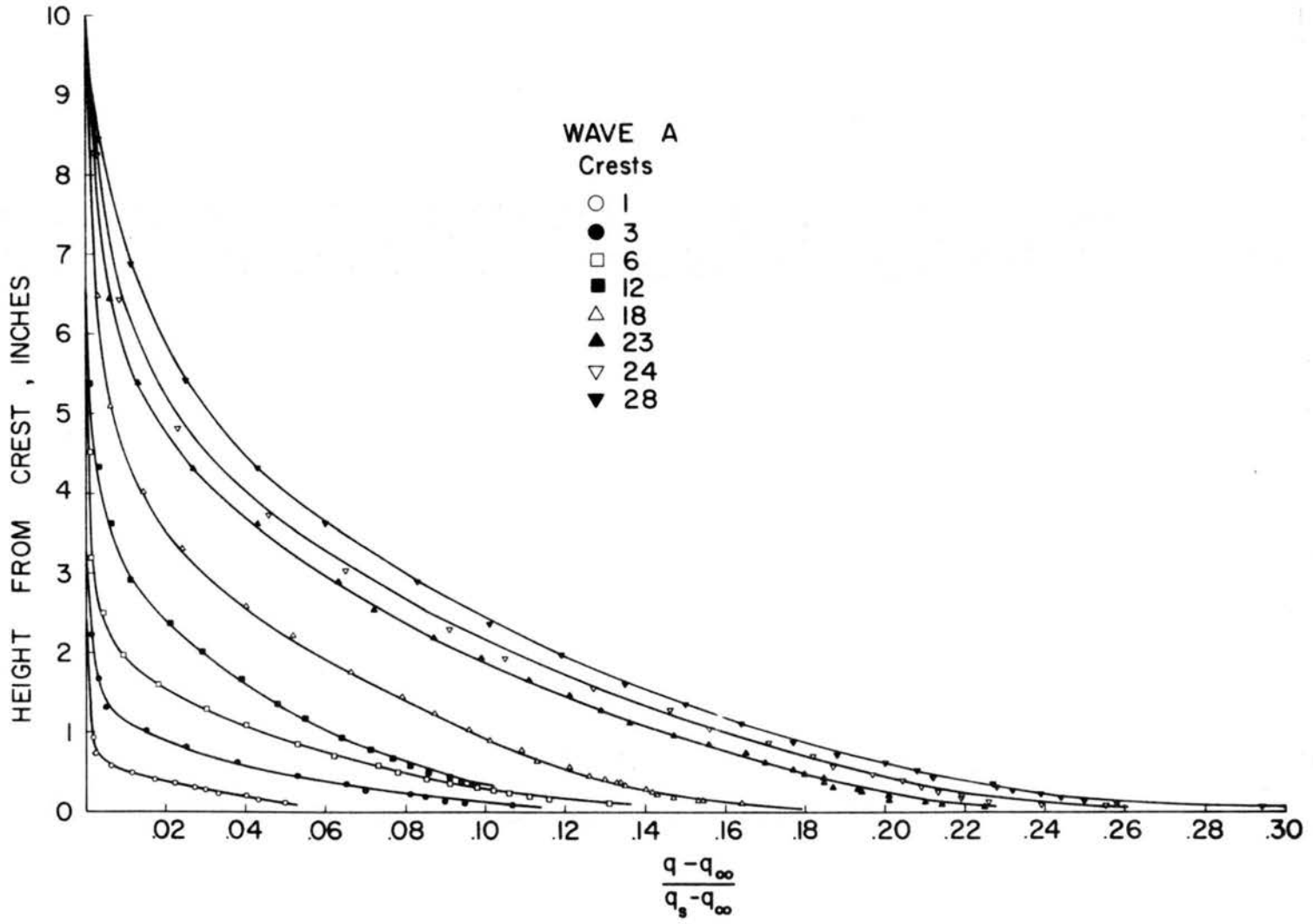

Fig. 36. Mean humidity profiles at various longitudinal positions, wave A.

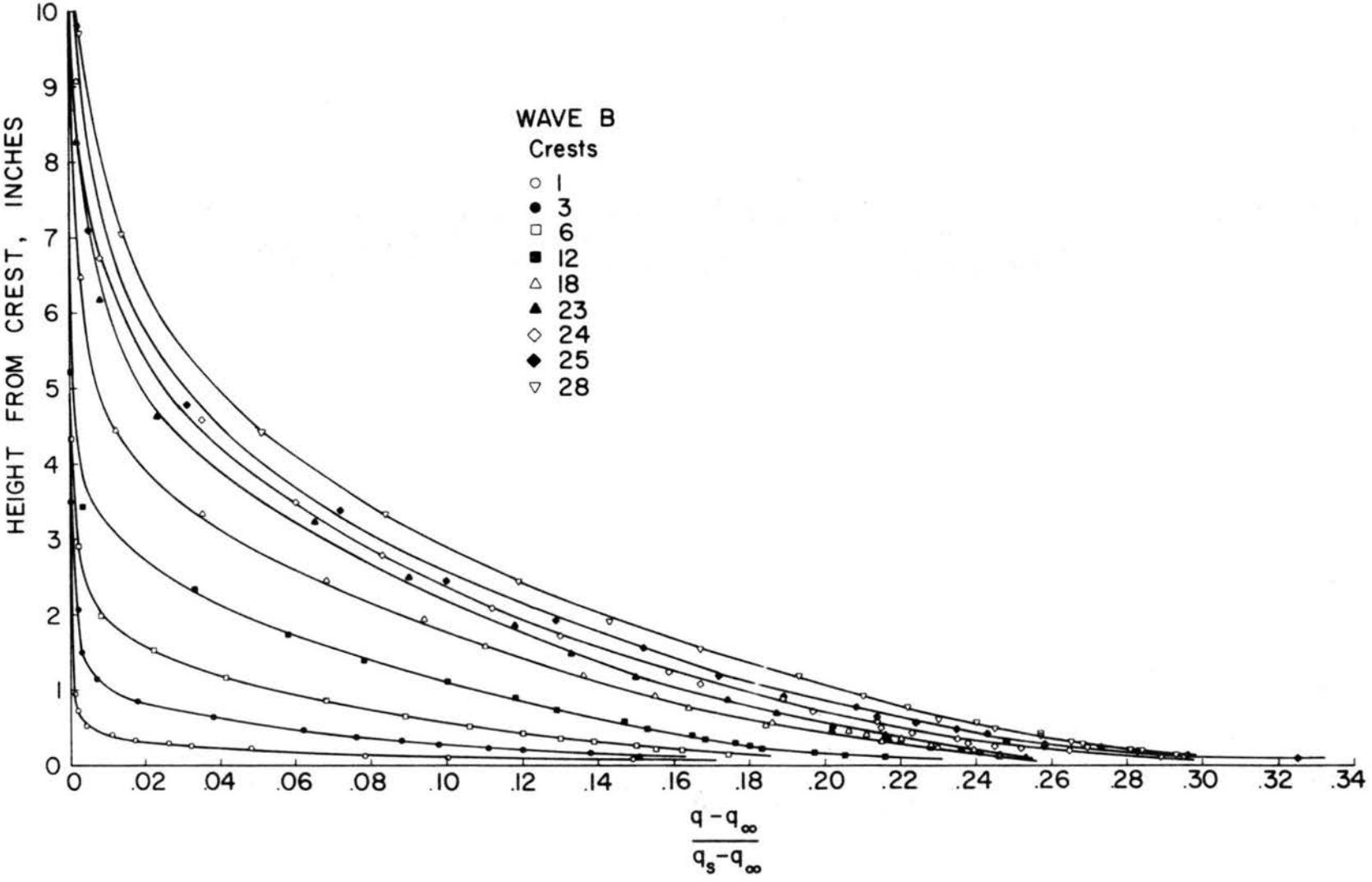

Fig. 37. Mean humidity profiles at various longitudinal positions, wave B.

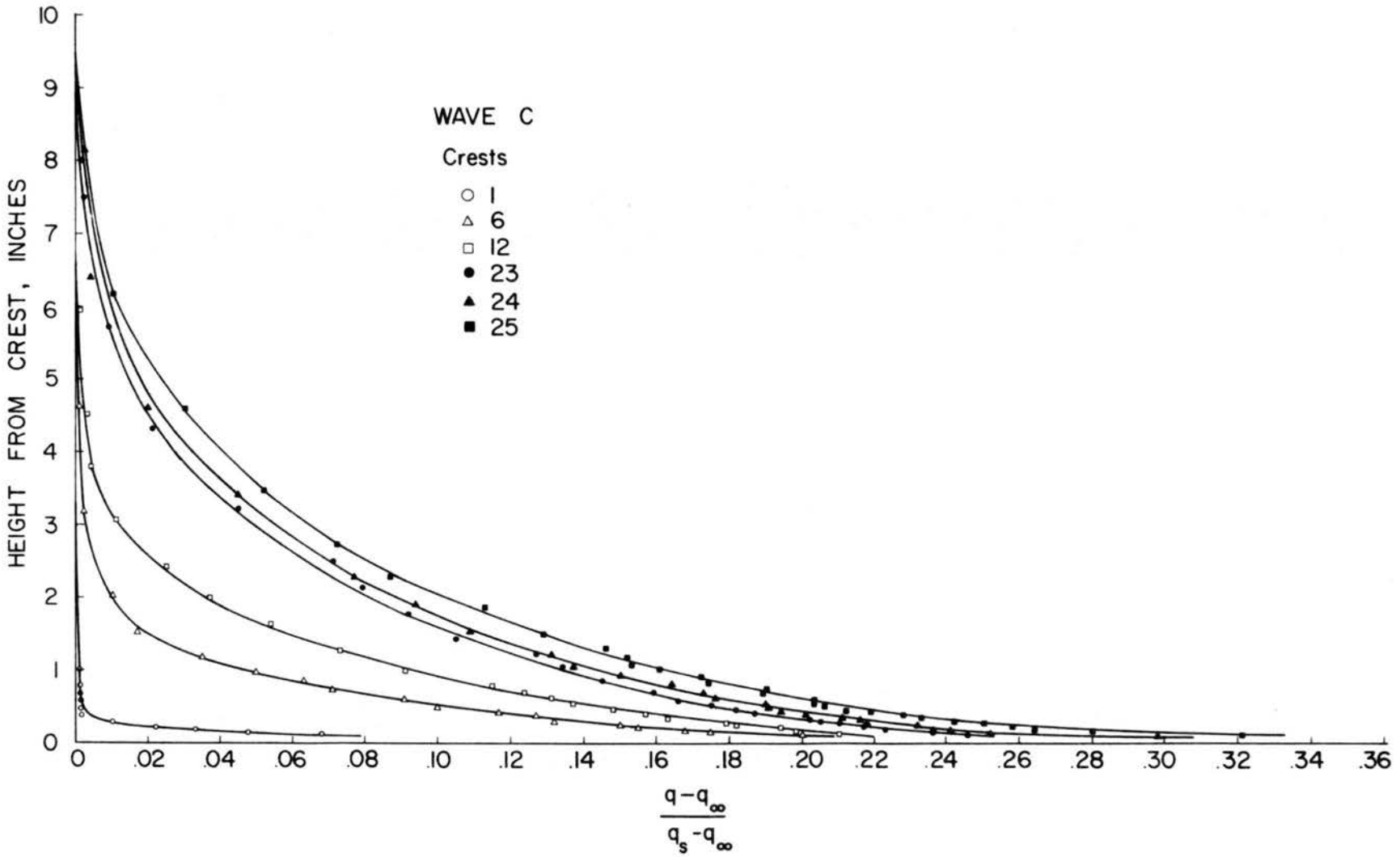

Fig. 38. Mean humidity profiles at various longitudinal positions, wave C.

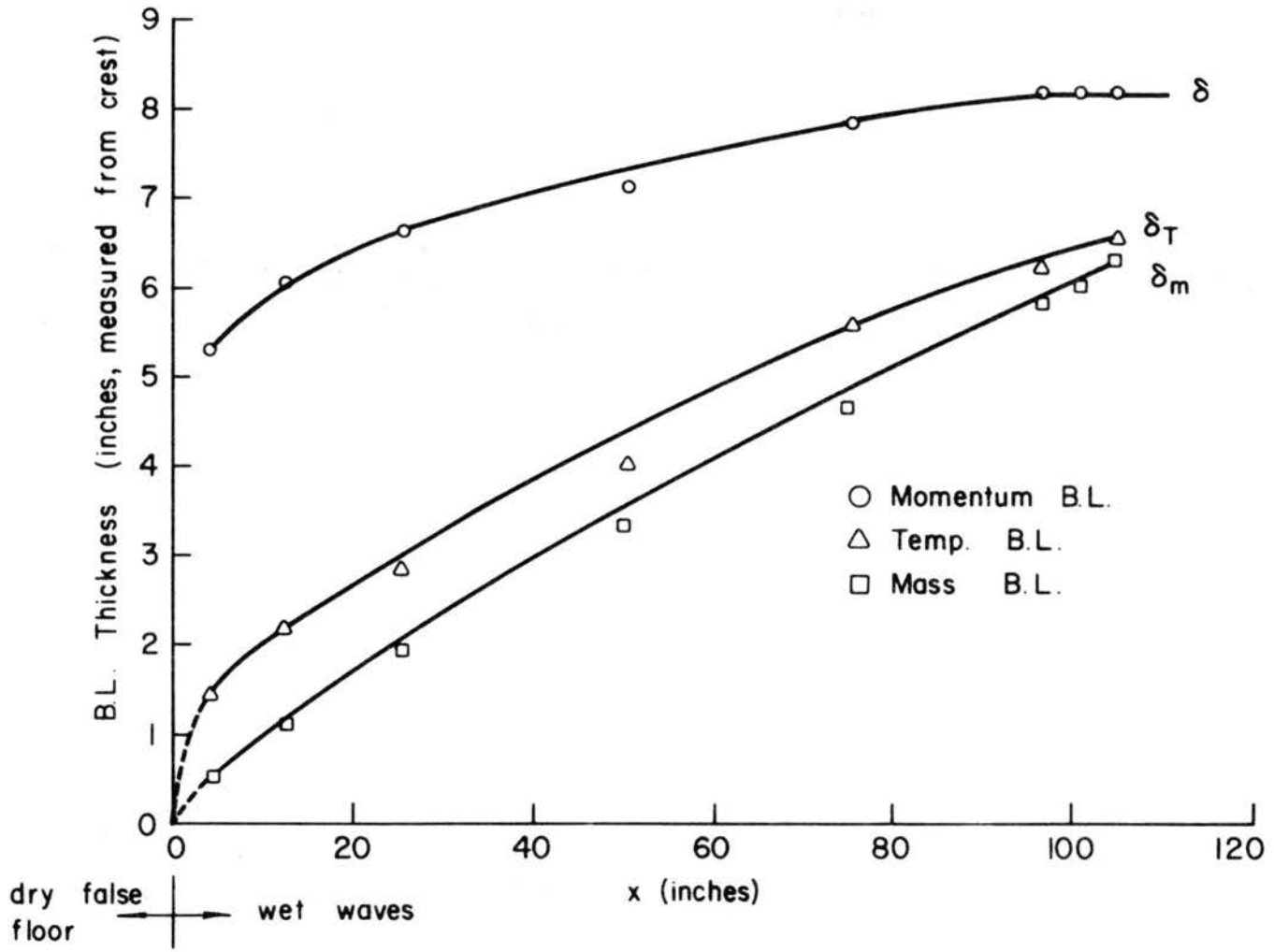

Fig. 39. Development of mass, momentum & temperature boundary layers over waves (typical case).

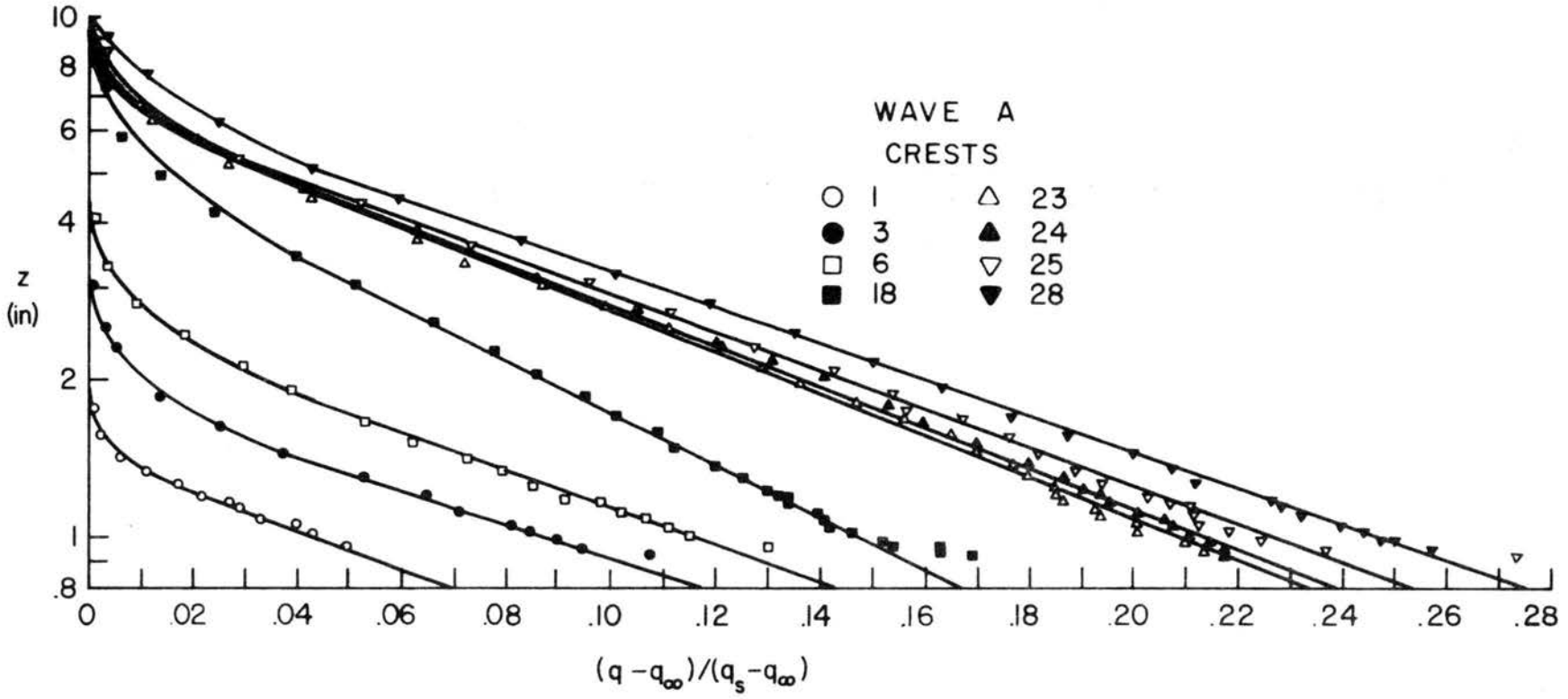

Fig. 40. Semilogarithmic plots of humidity distributions, wave A.

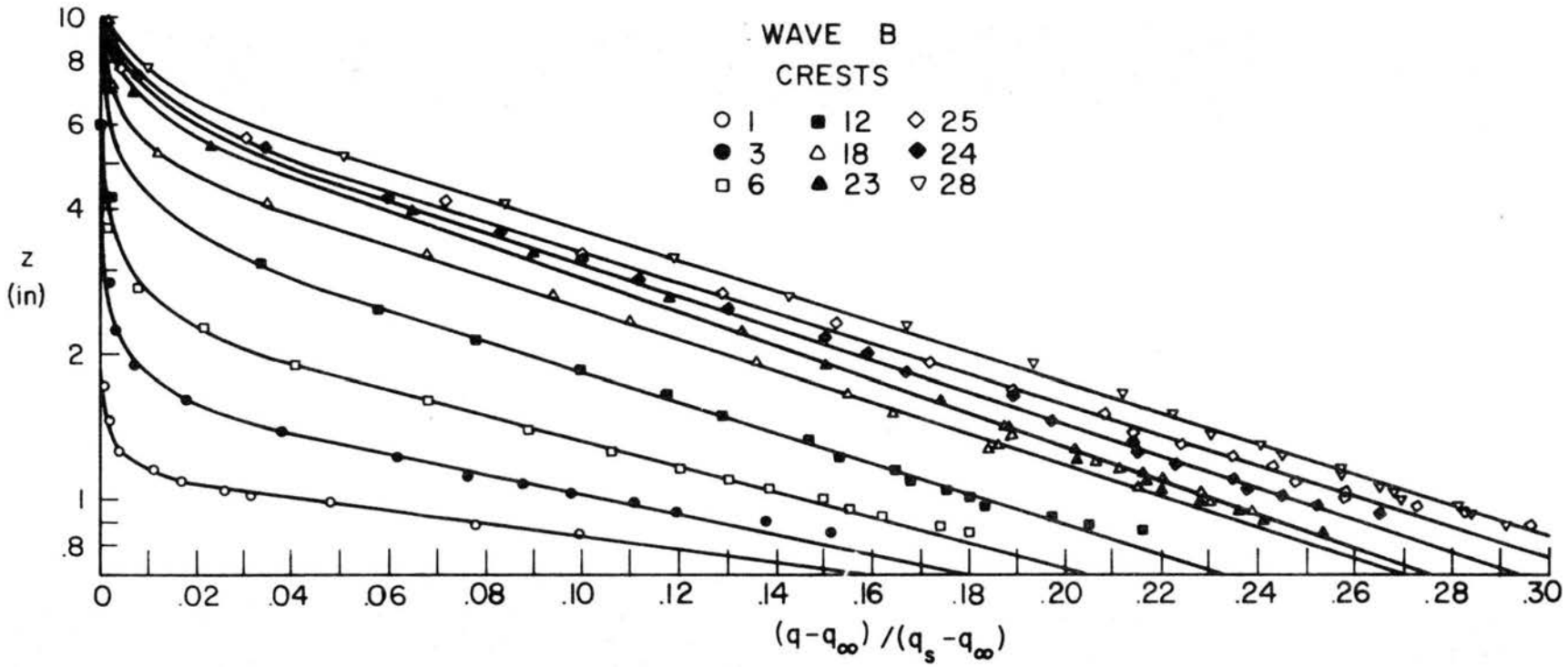

Fig. 41. Semilogarithmic plots of humidity distributions, wave B.

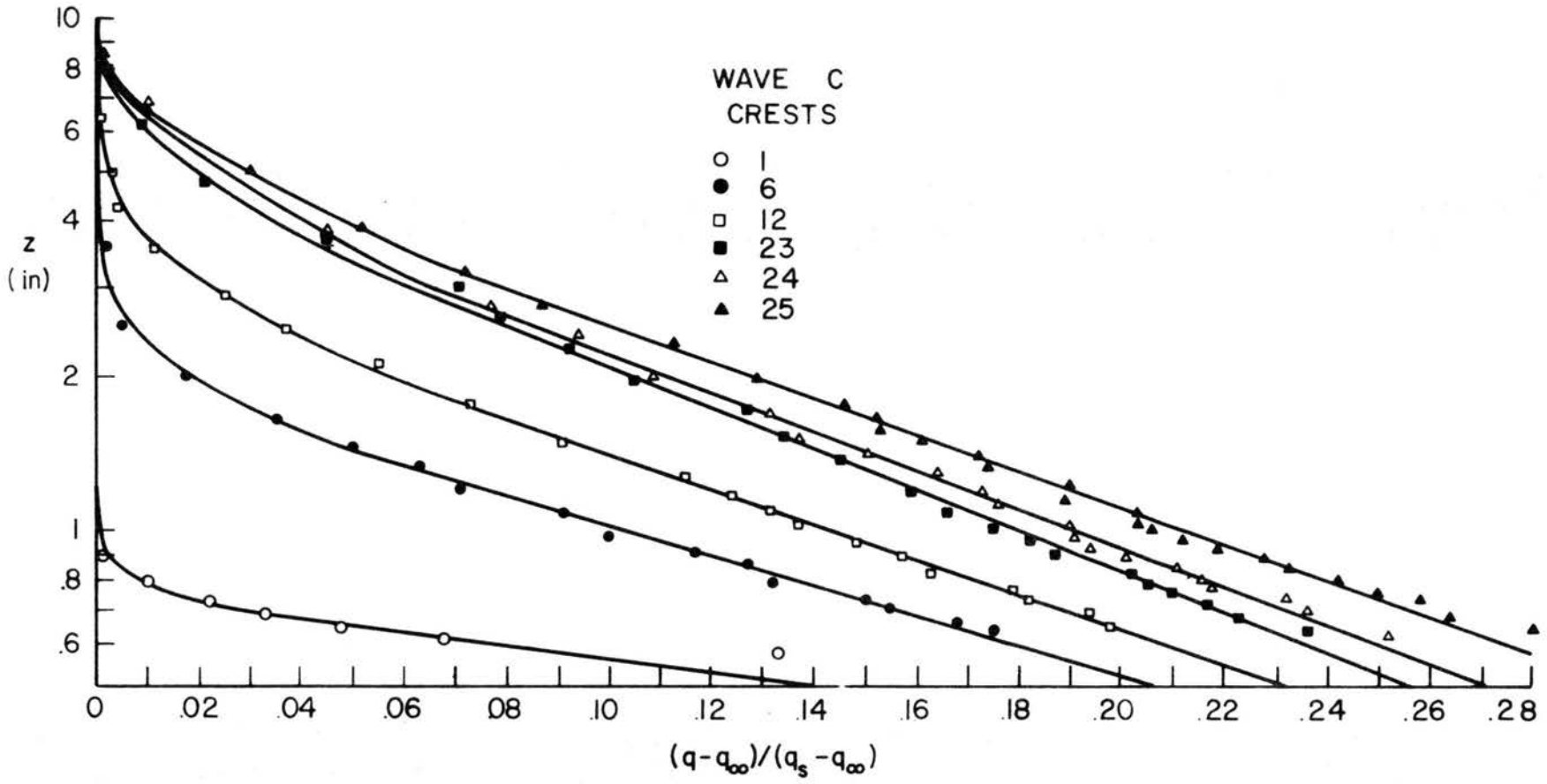

Fig. 42. Semilogarithmic plots of humidity distributions, wave C.

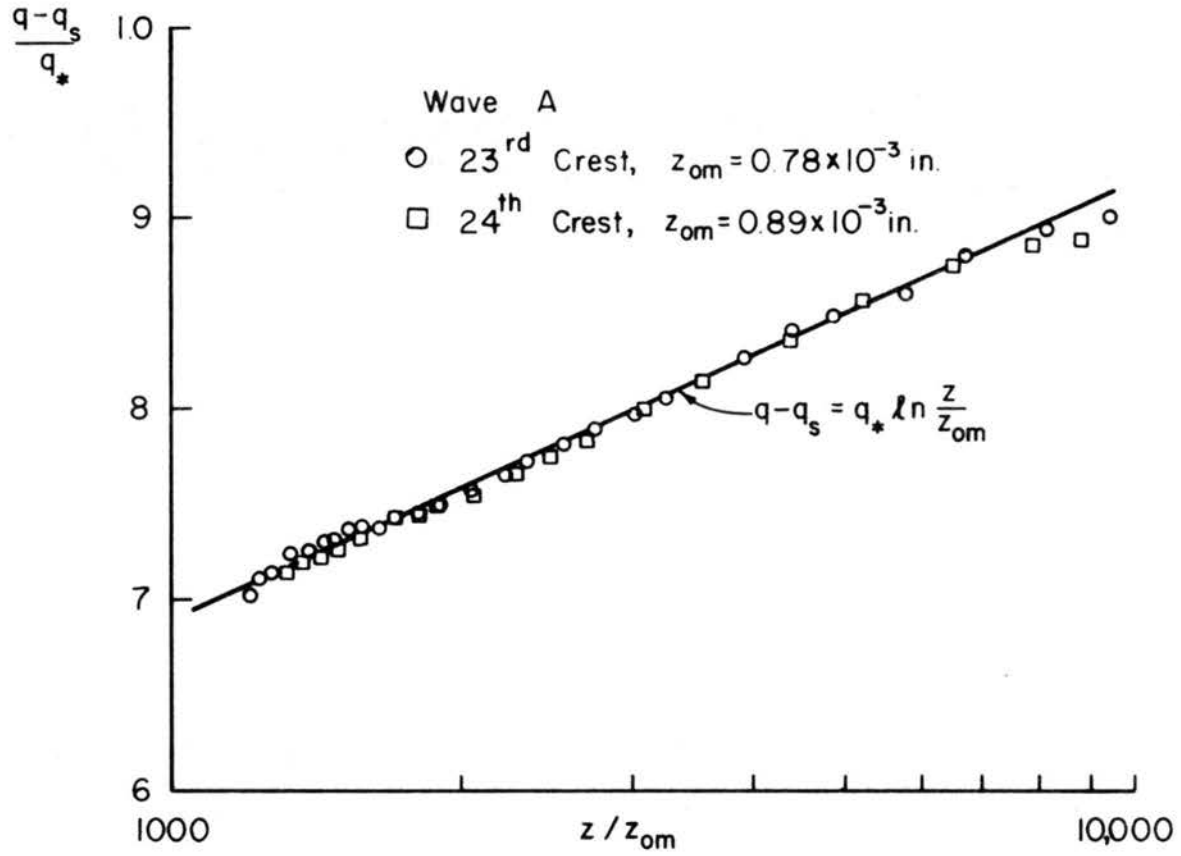

Fig. 43. Plots of $\frac{q-q_s}{q_*}$ vs $\frac{z}{z_{om}}$ (far downstream region), Wave A.

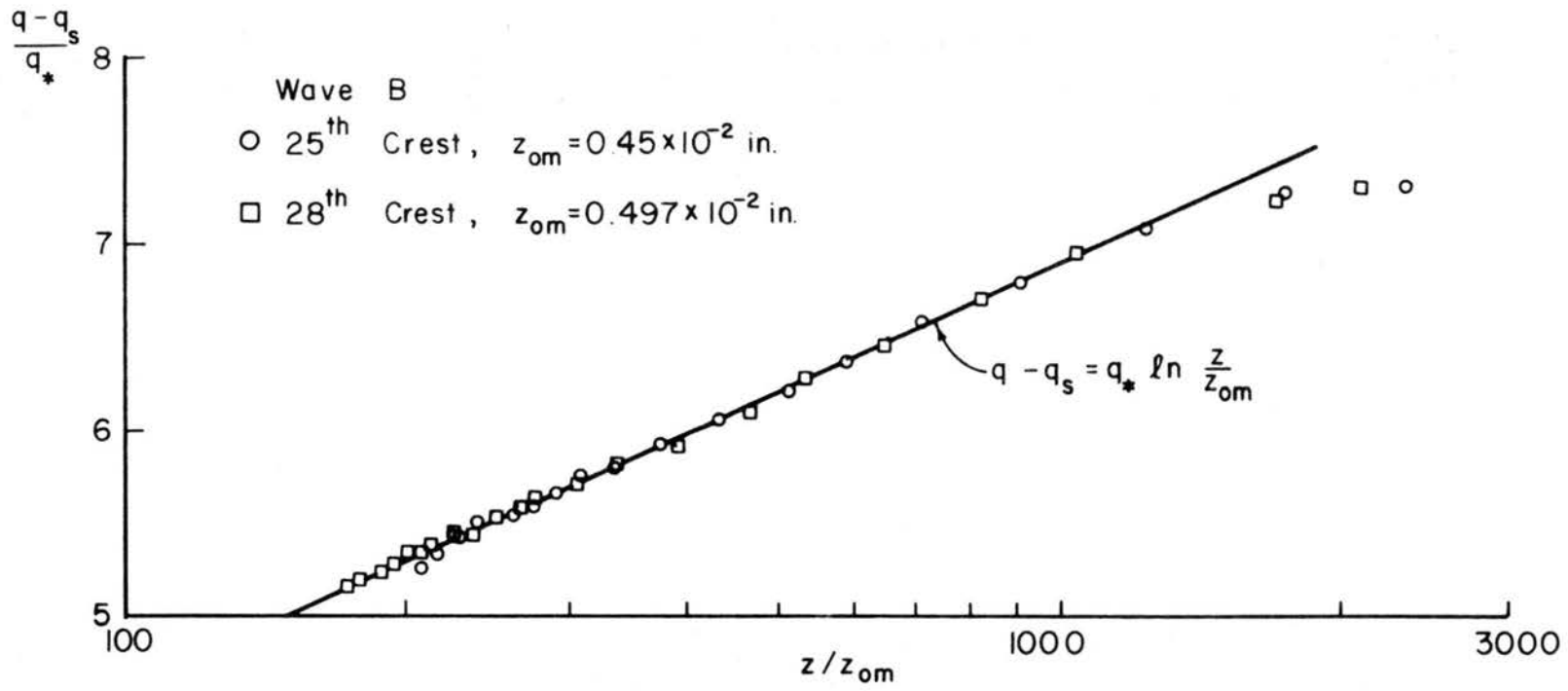

Fig. 44. Plots of $\frac{q-q_s}{q_*}$ vs $\frac{z}{z_{om}}$ (far downstream region), Wave B.

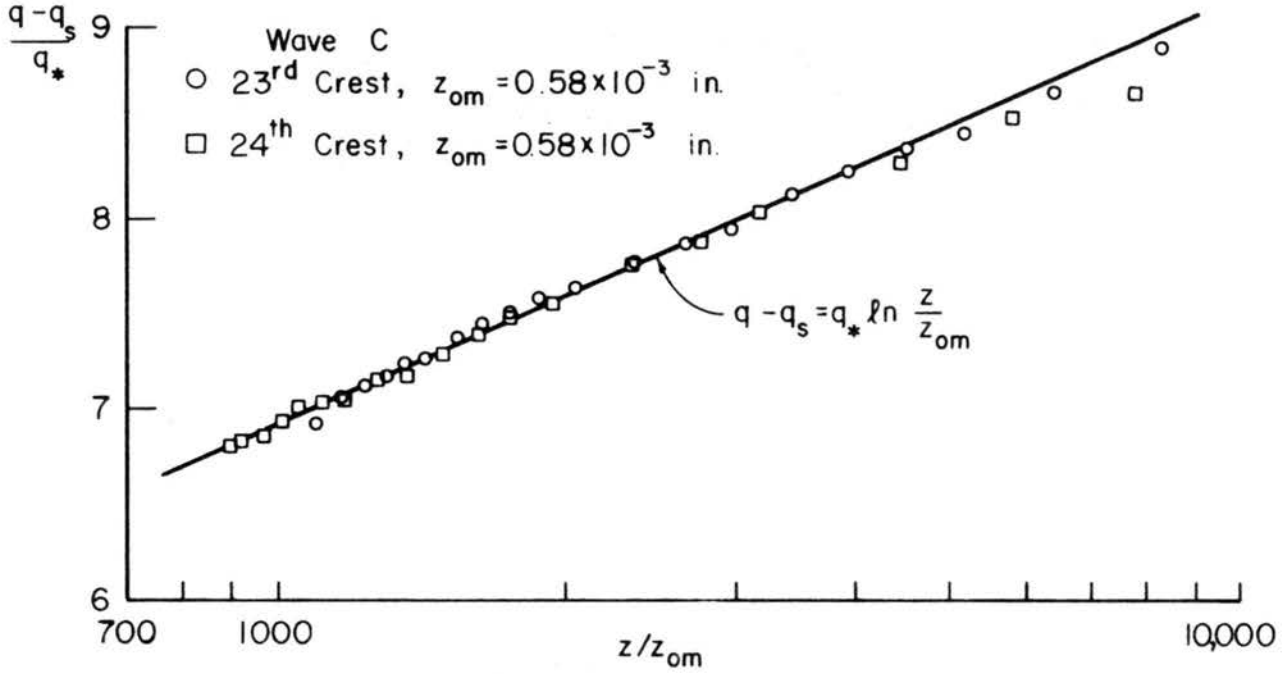

Fig. 45. Plots of $\frac{q-q_s}{q_*}$ vs $\frac{z}{z_{om}}$ (far downstream region), Wave C.

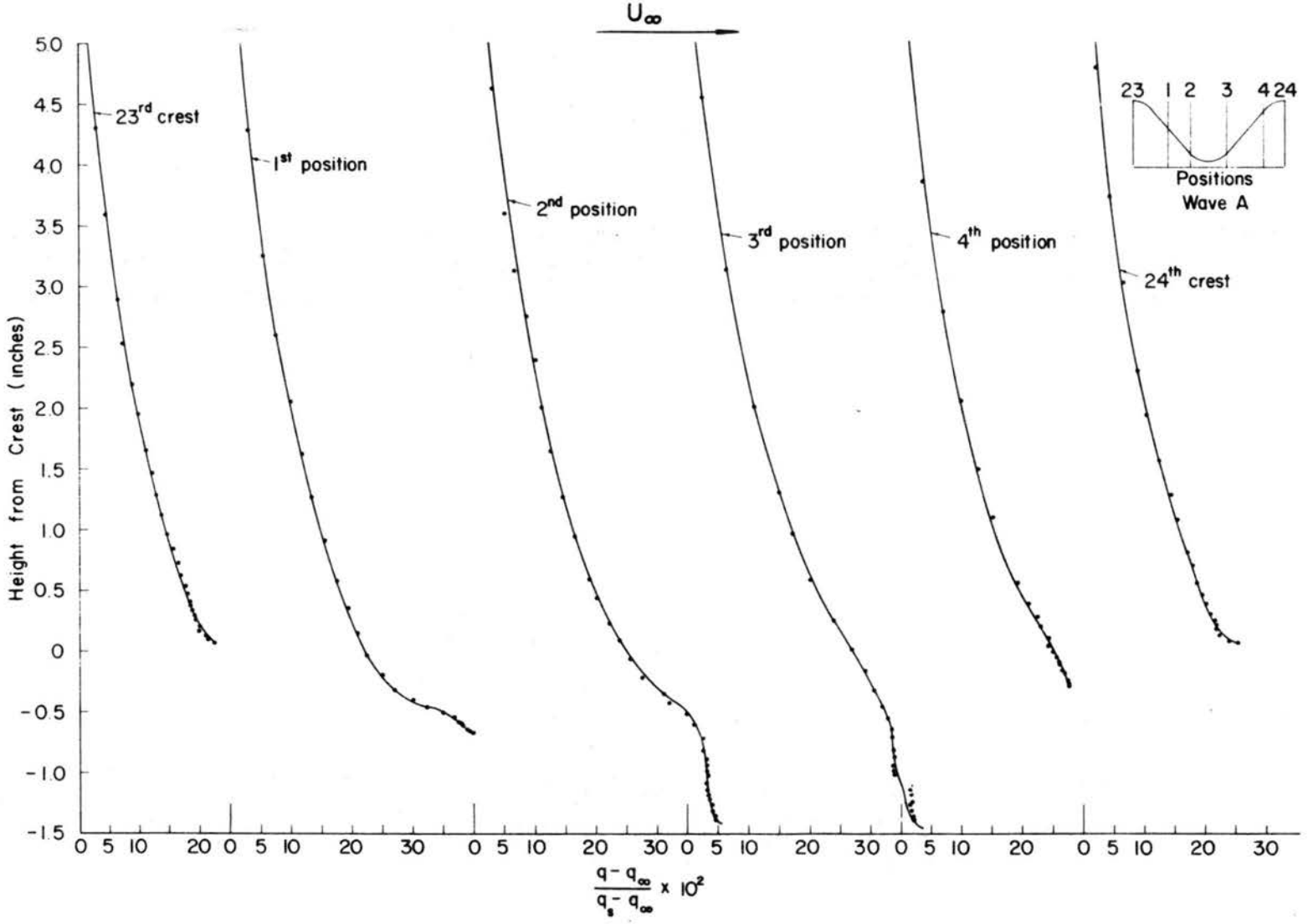

Fig. 46. Vertical humidity profiles at various positions inside a wave trough, Wave A.

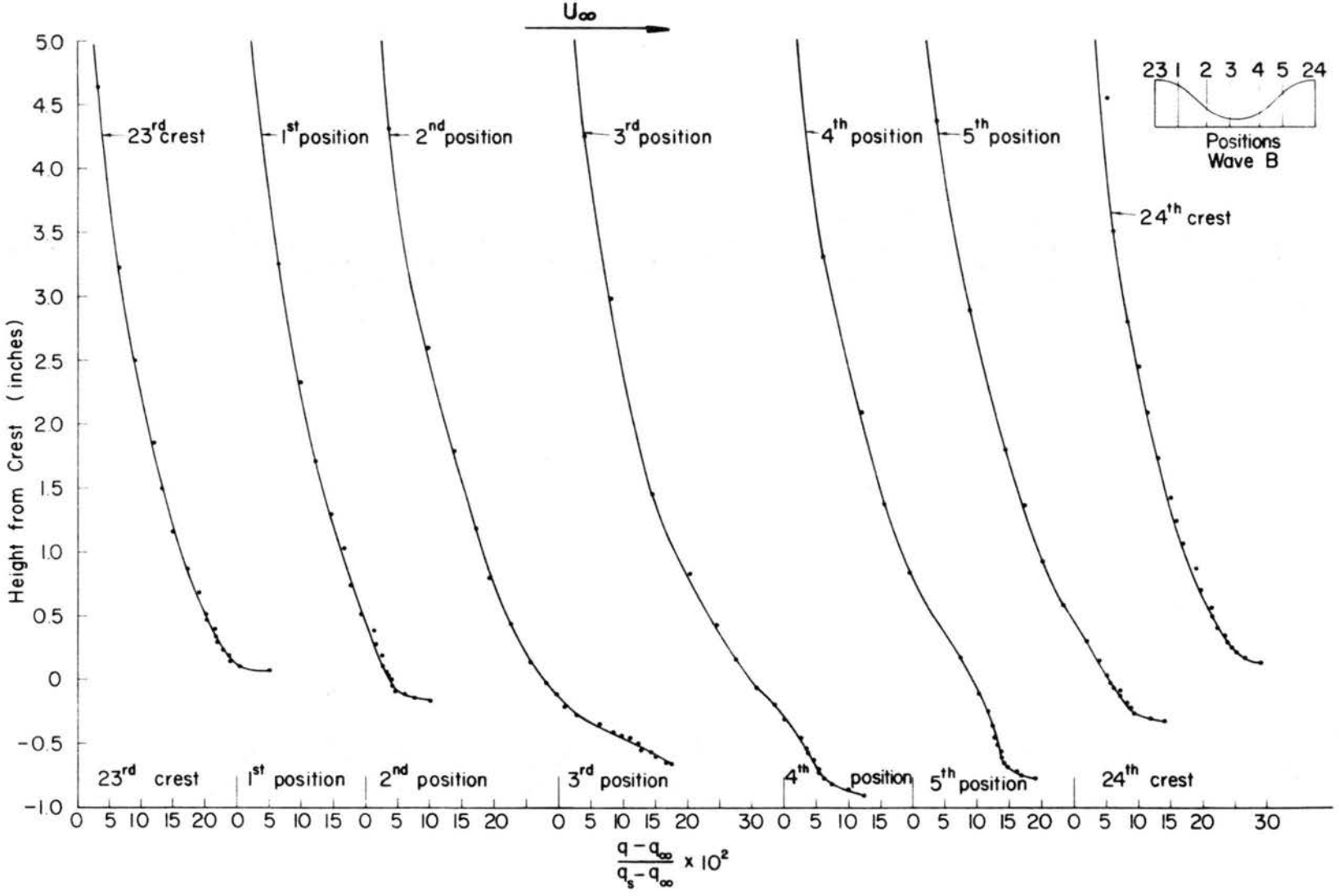

Fig. 47. Vertical humidity profiles at various positions inside a wave trough, Wave B.

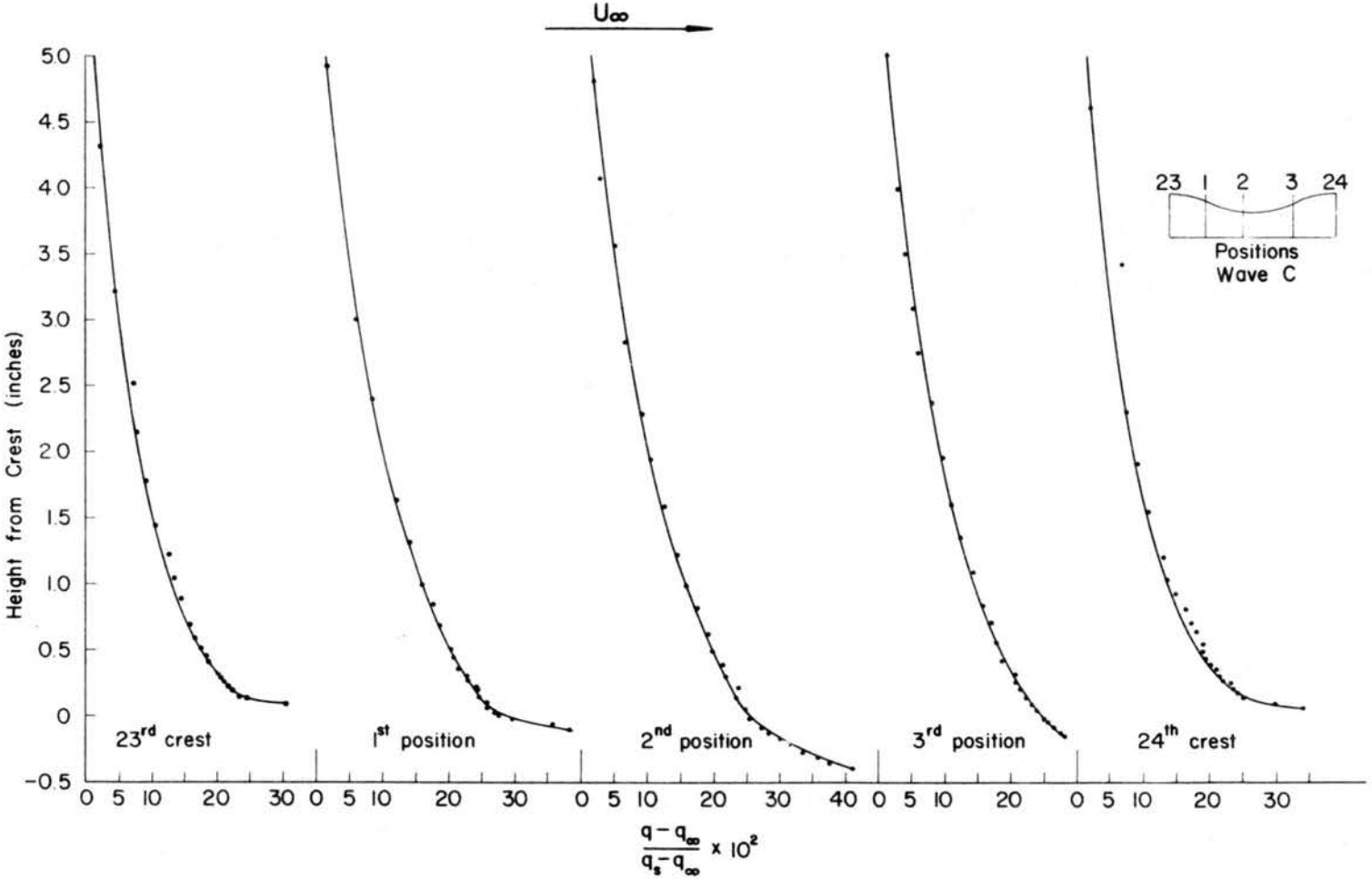

Fig. 48. Vertical humidity profiles at various positions inside a wave trough, wave C.

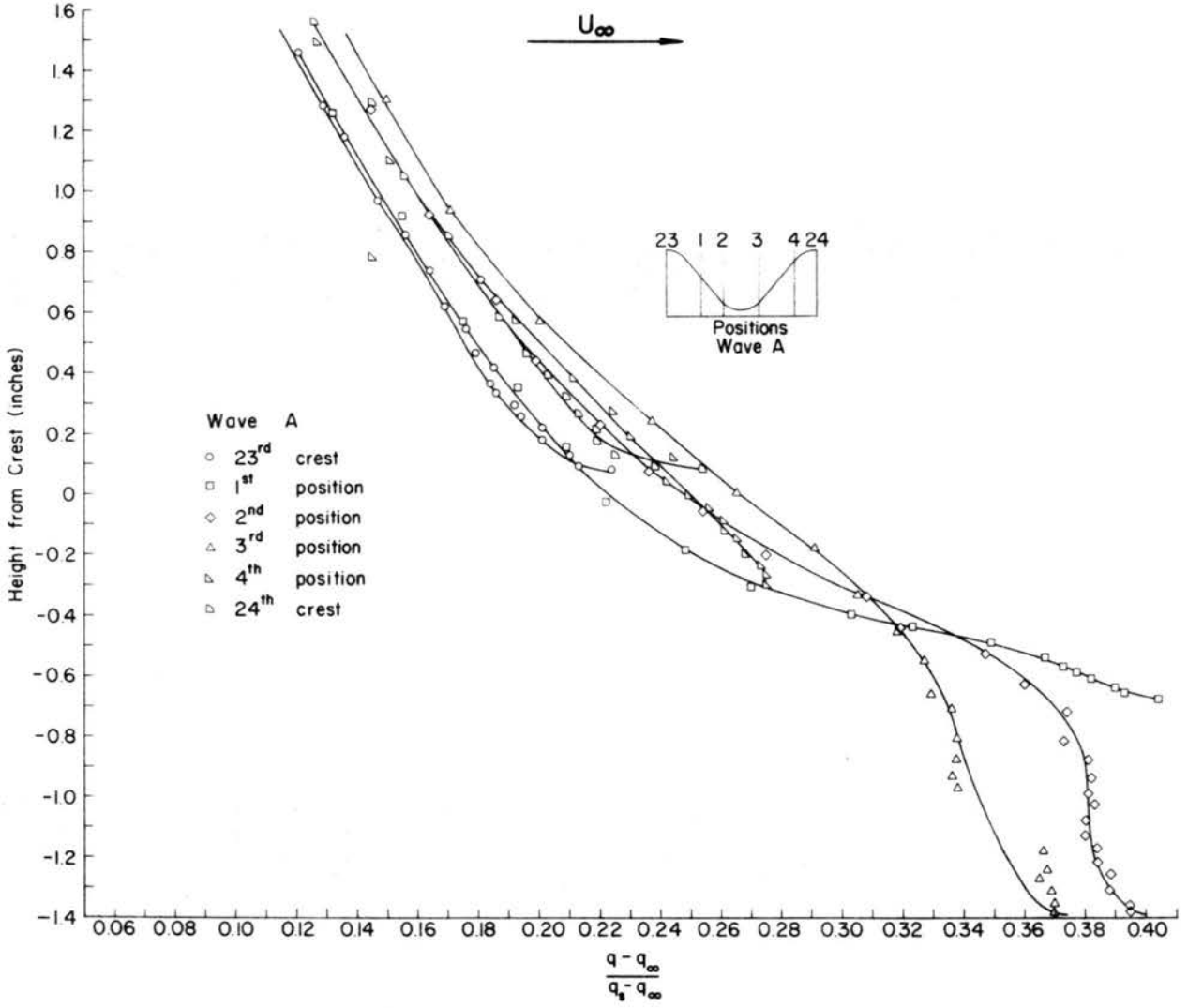

Fig. 49. Enlarged view of lower portion of humidity distributions in Fig. 46.

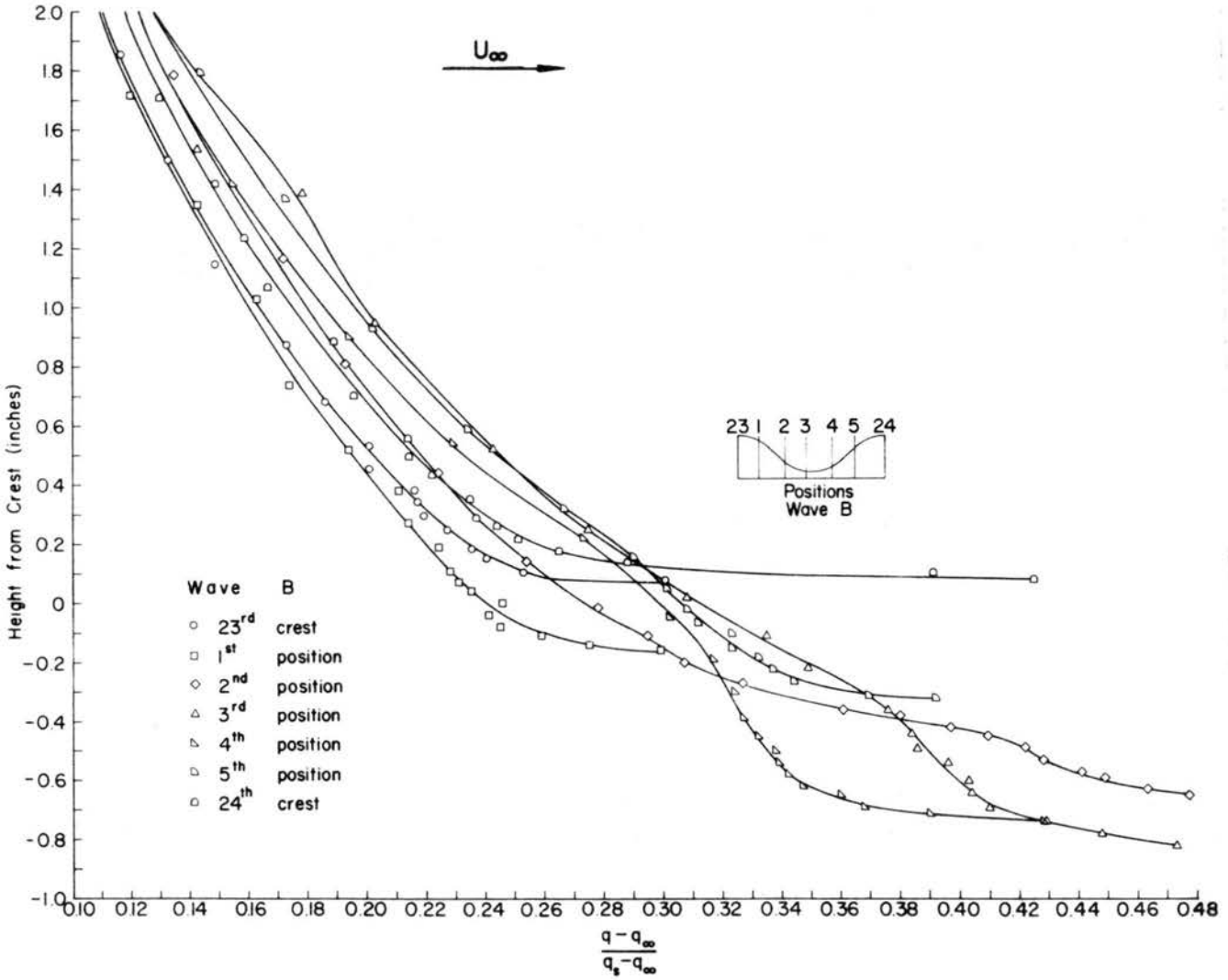

Fig. 50. Enlarged view of lower portion of humidity distributions in Fig. 47.

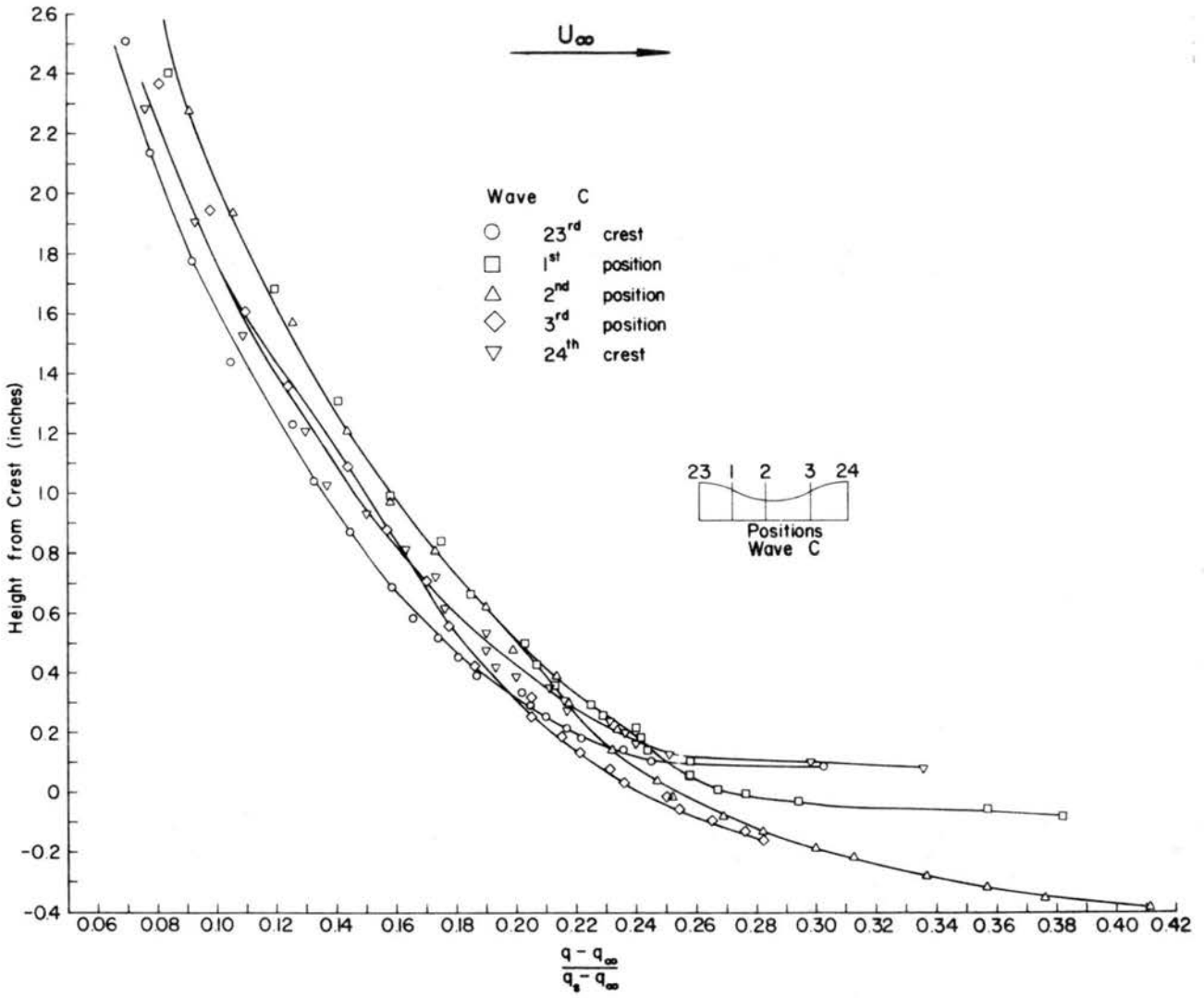

Fig. 51. Enlarged view of lower portion of humidity distributions in Fig. 48.

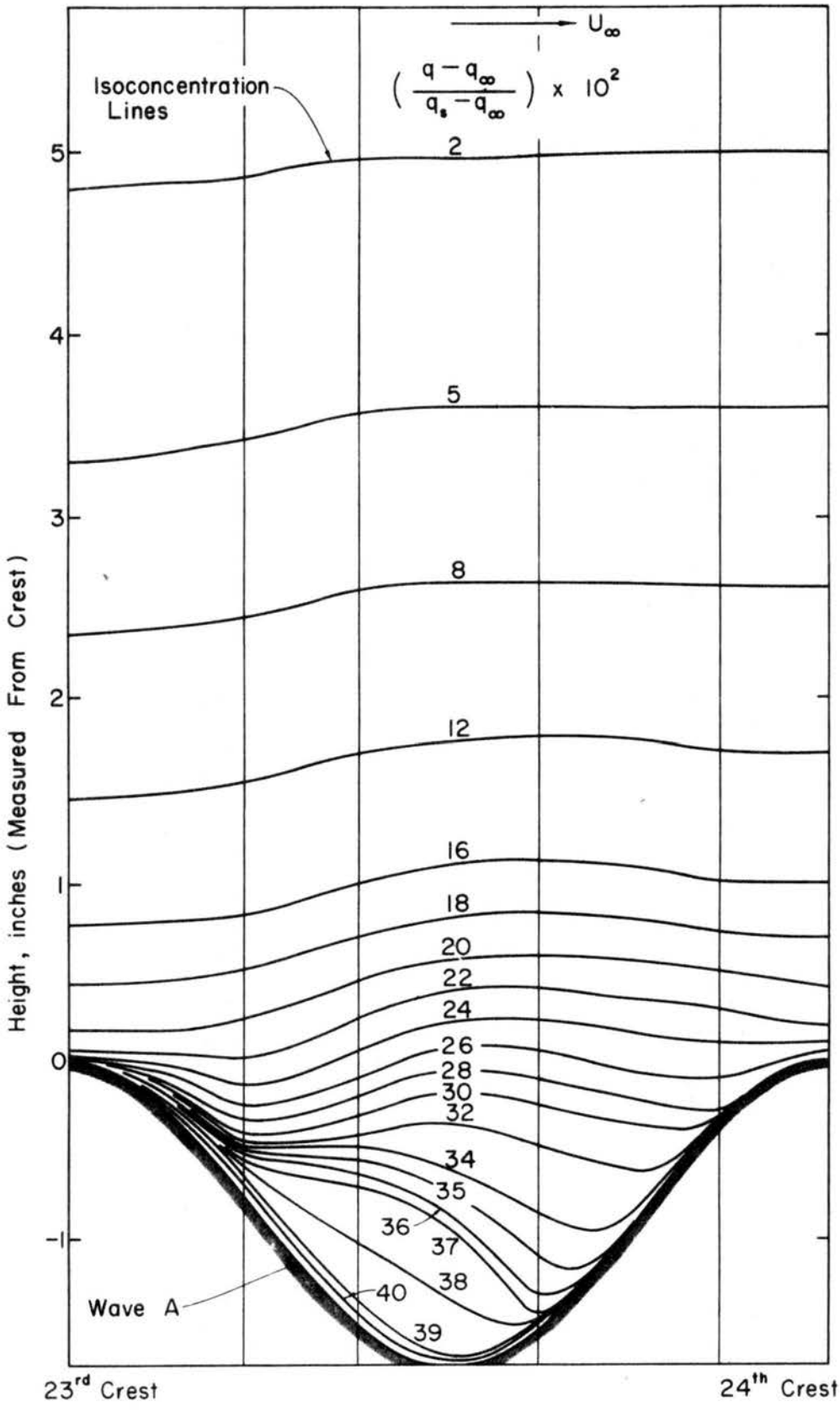

Fig. 52. Isoconcentration lines inside a wave trough, Wave A.

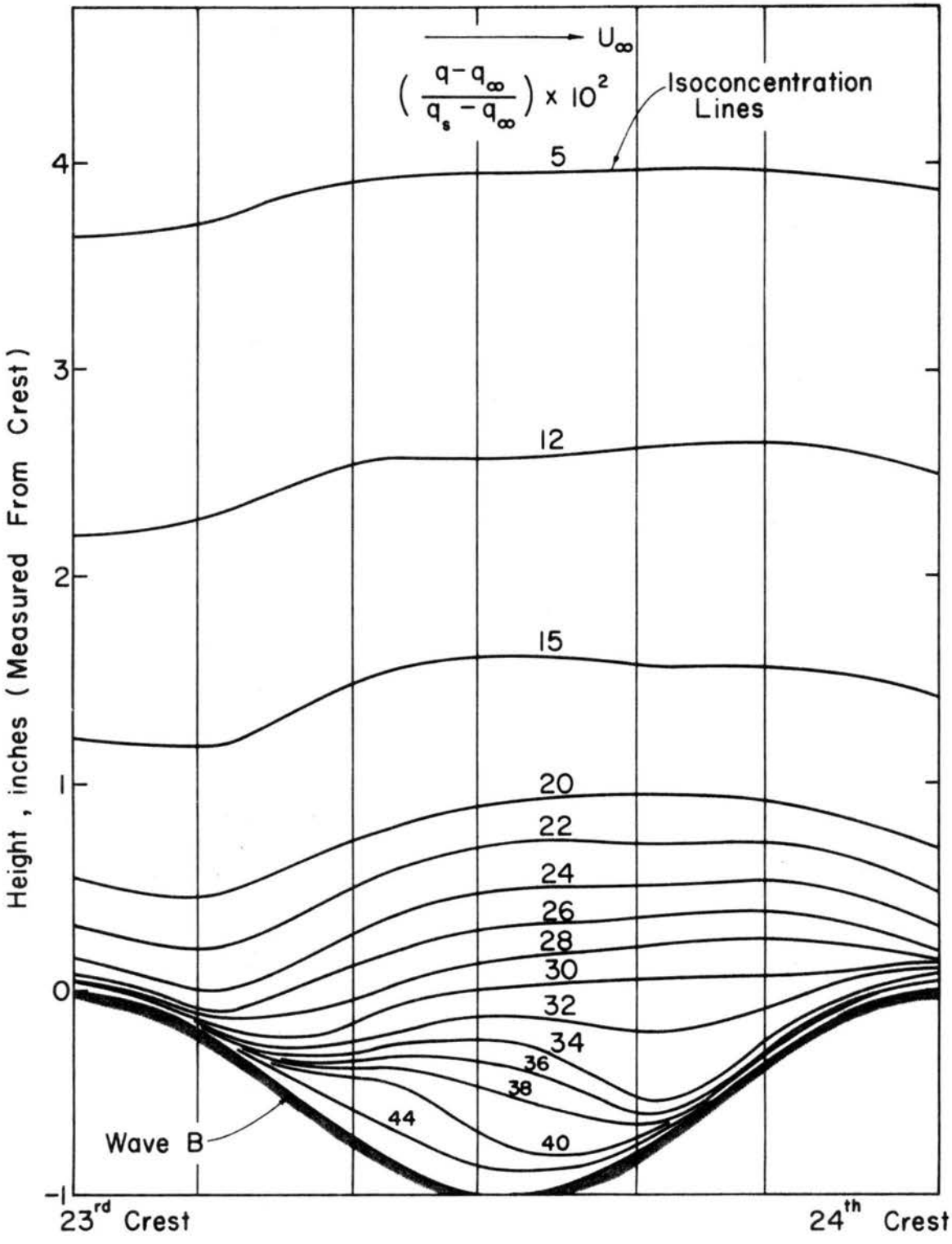

Fig. 53. Isoconcentration lines inside a wave trough, Wave B.

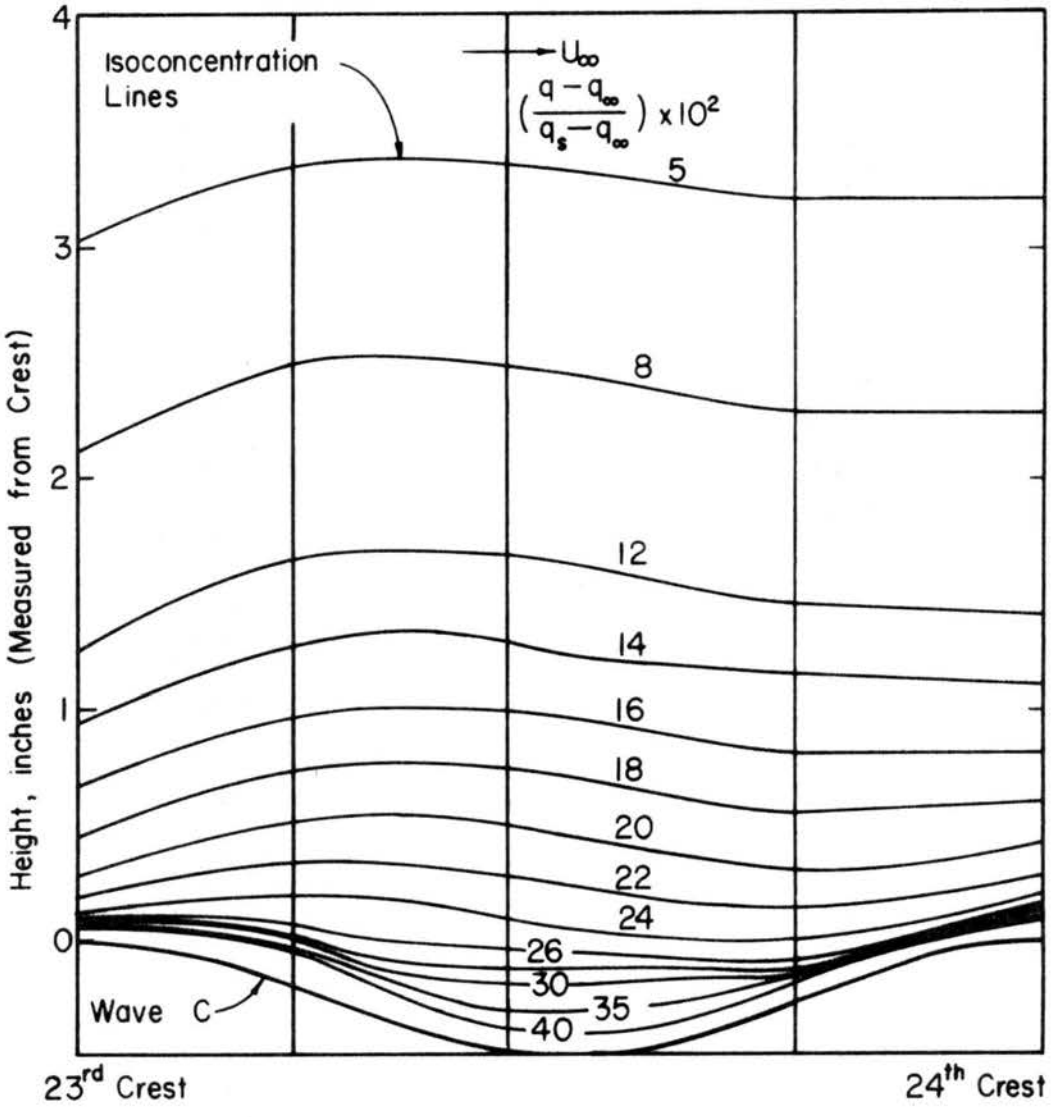

Fig. 54. Isoconcentration lines inside a wave trough, Wave C.

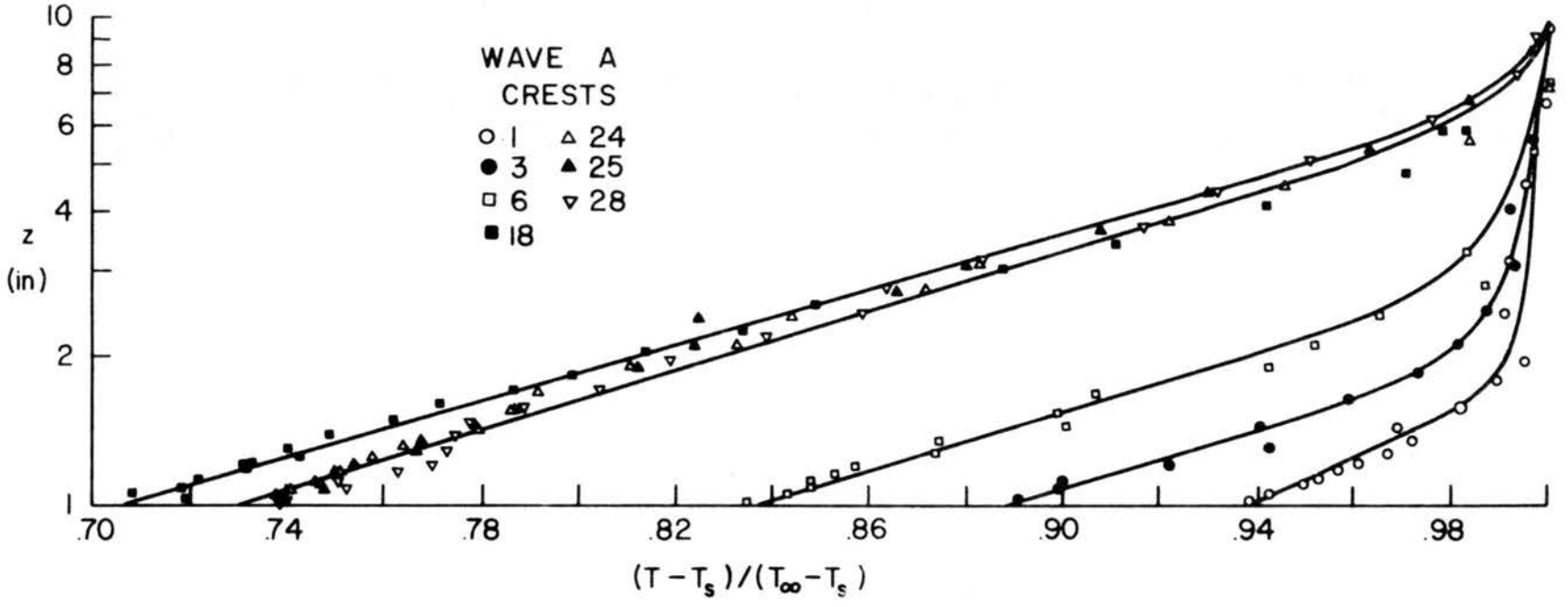

Fig. 55. Mean temperature distributions at various longitudinal positions (Typical case).

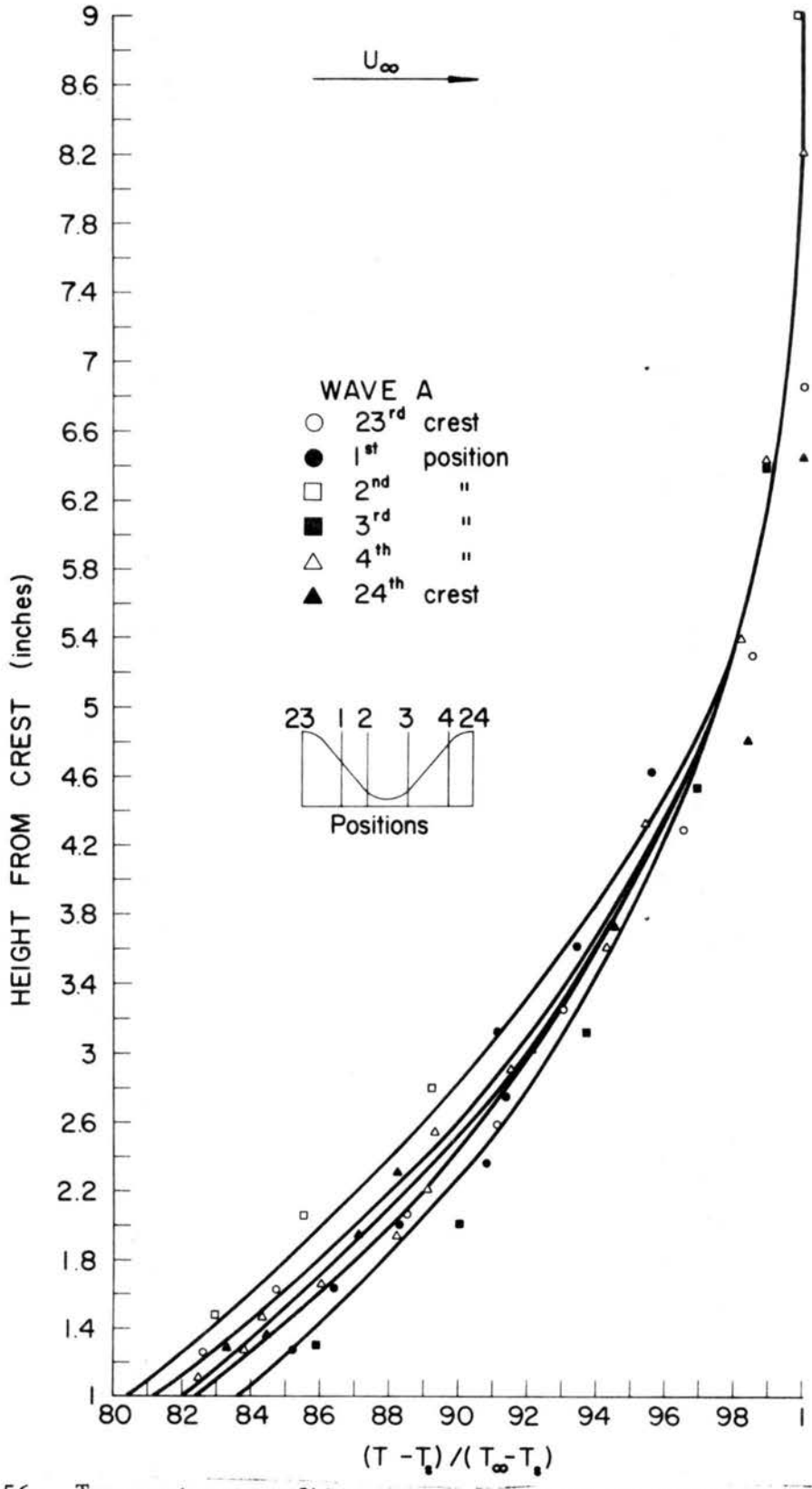

Fig. 56. Temperature profiles (upper portion) at various positions inside a wave trough (Typical case).

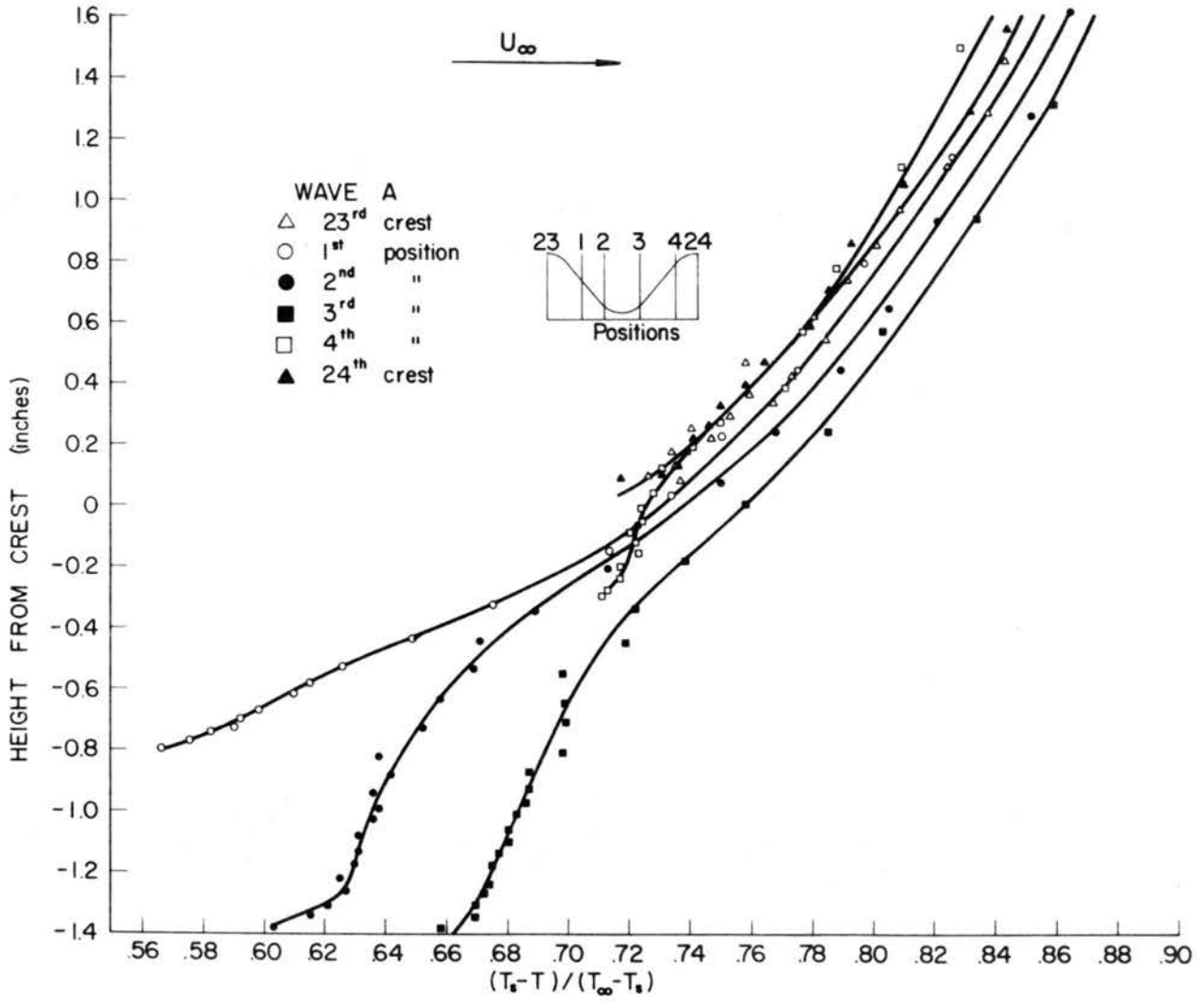

Fig. 57. Enlarged view of lower portion of temperature profiles in Fig. 56.

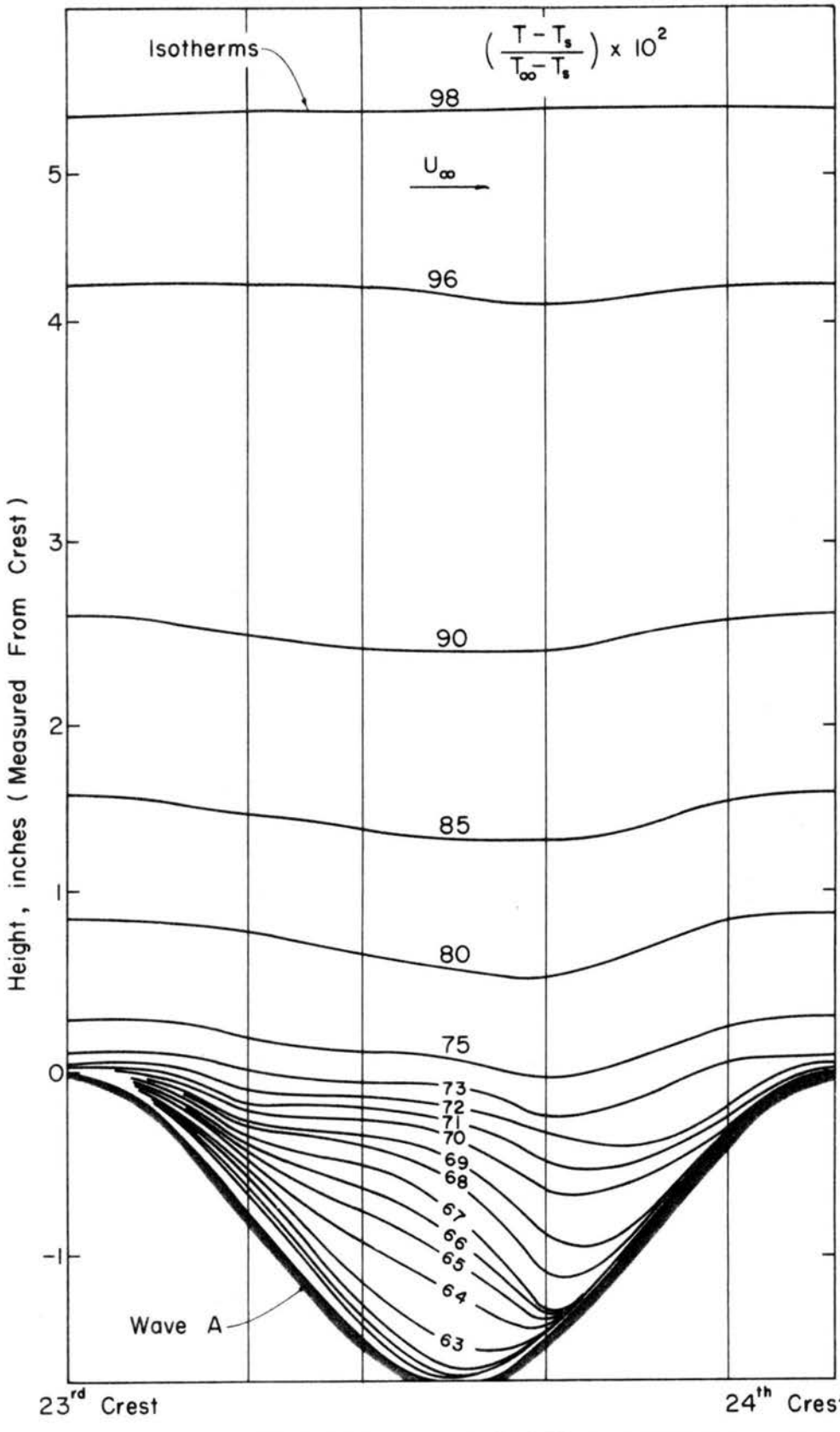

Fig. 58. Isotherms inside a wave trough (Typical case).

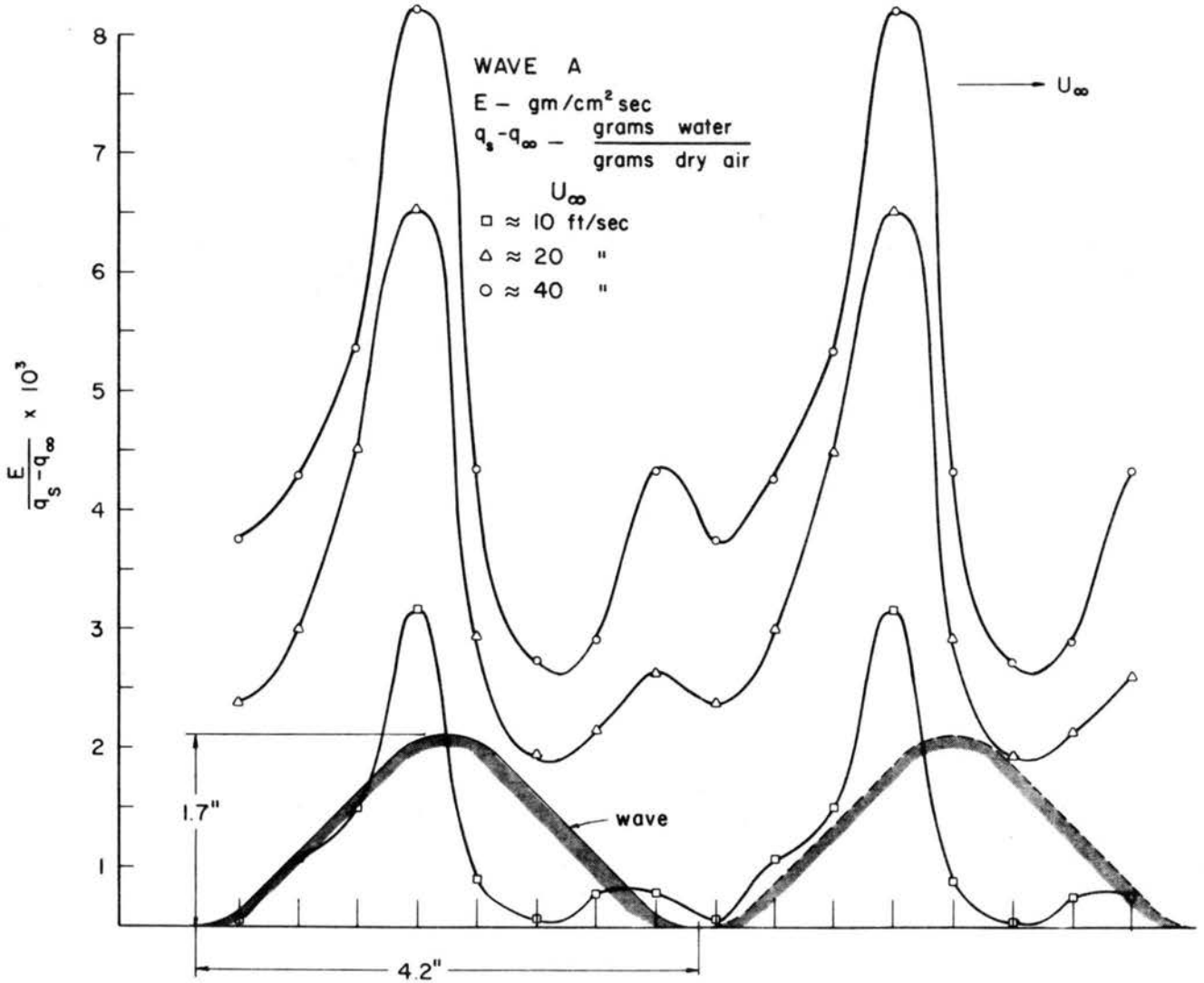

Fig. 59. Distribution of local mass transfer coefficients, Wave A.

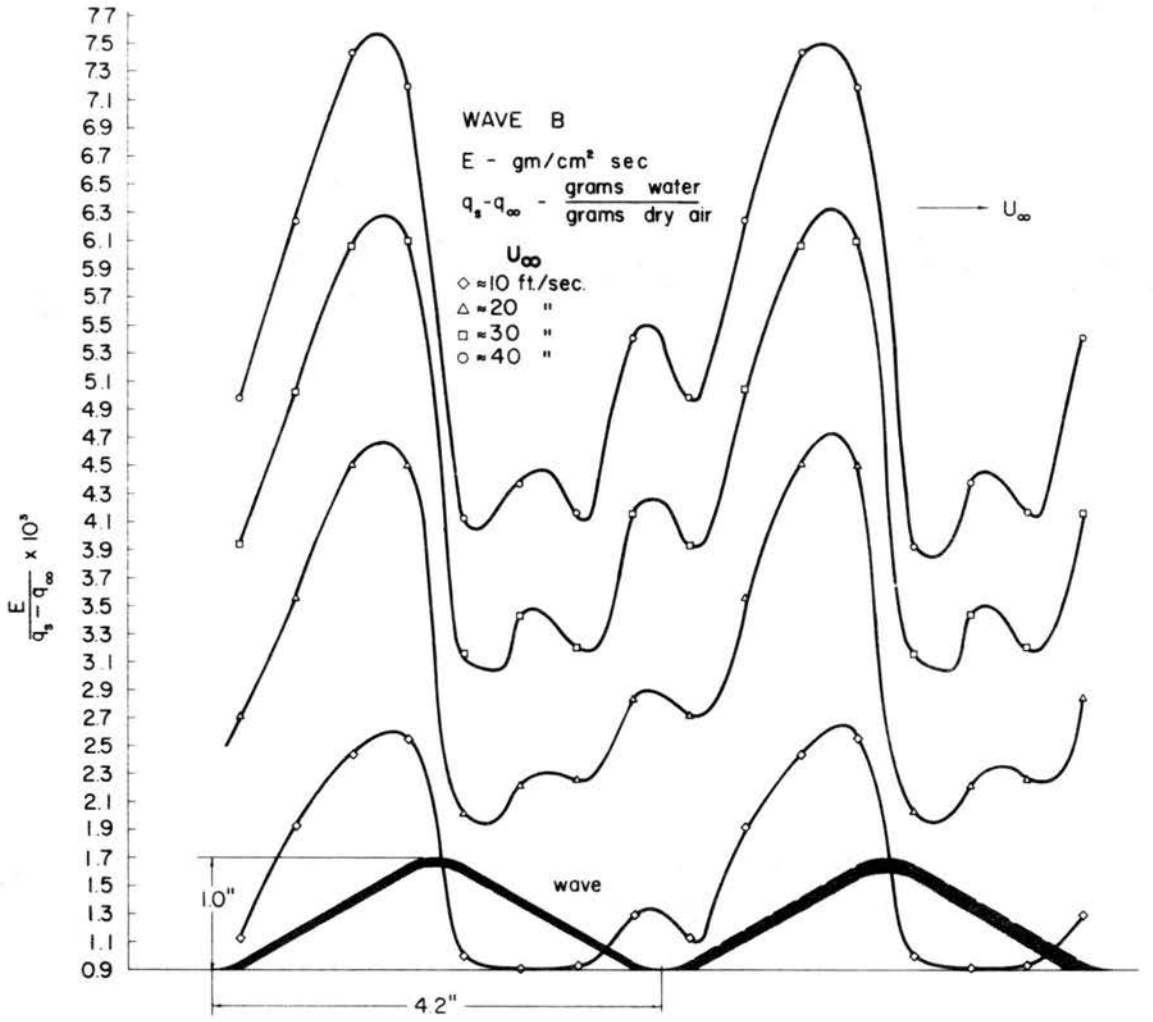

Fig. 60. Distributions of local mass transfer coefficients, Wave B.

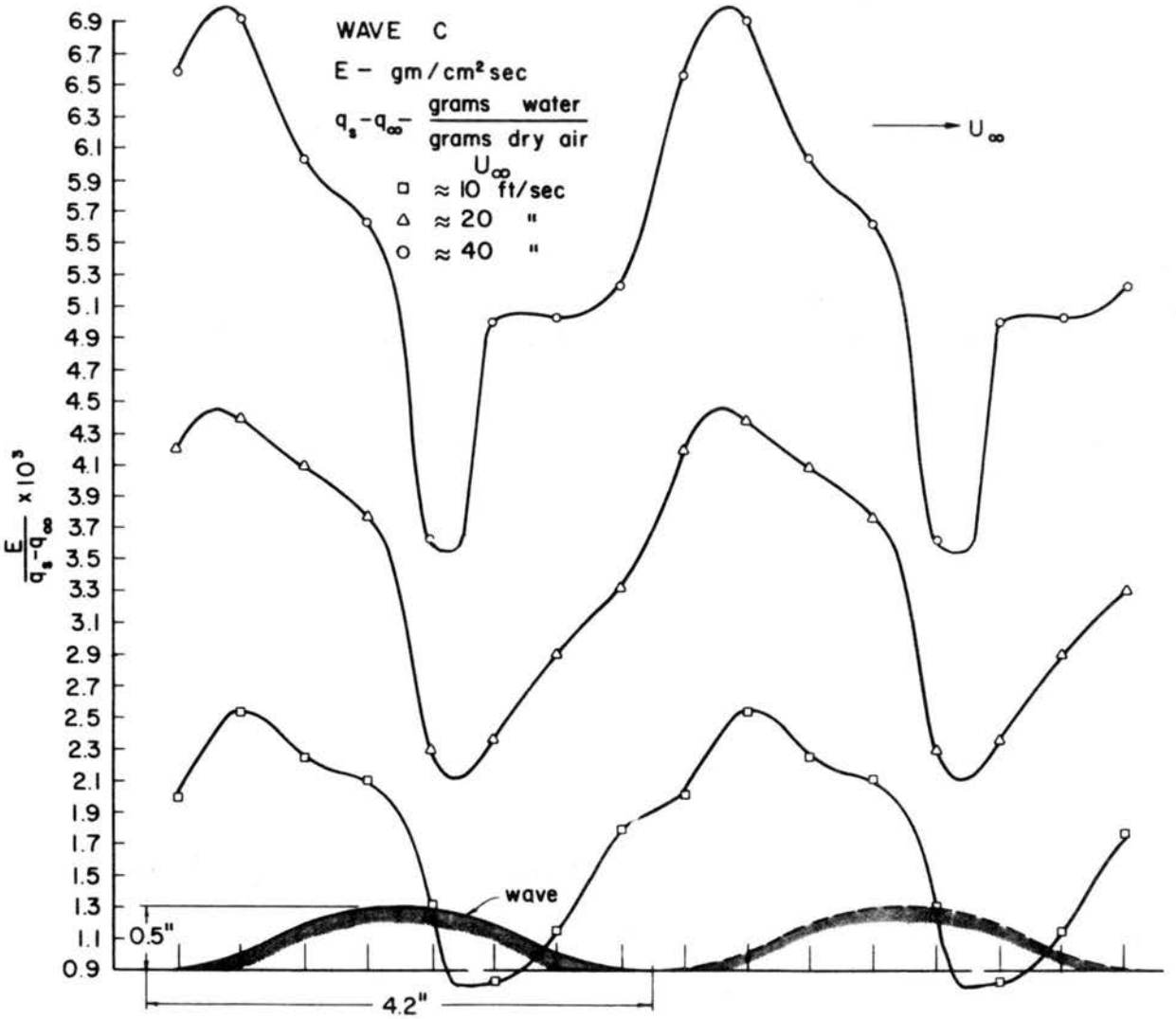

Fig. 61. Distribution of local mass transfer coefficients, Wave C

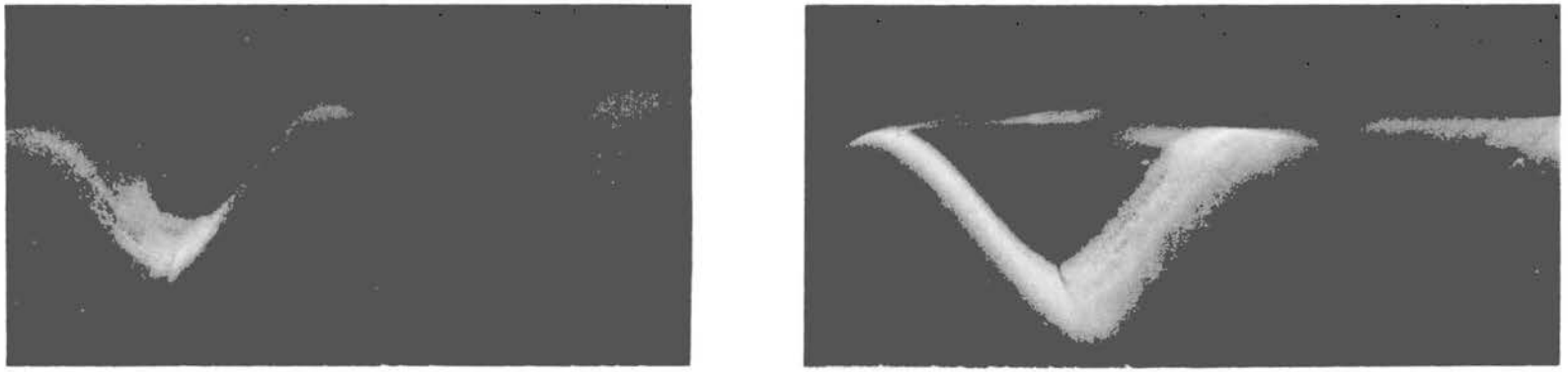

Fig. 62 Photographs of visualization study, Wave A.

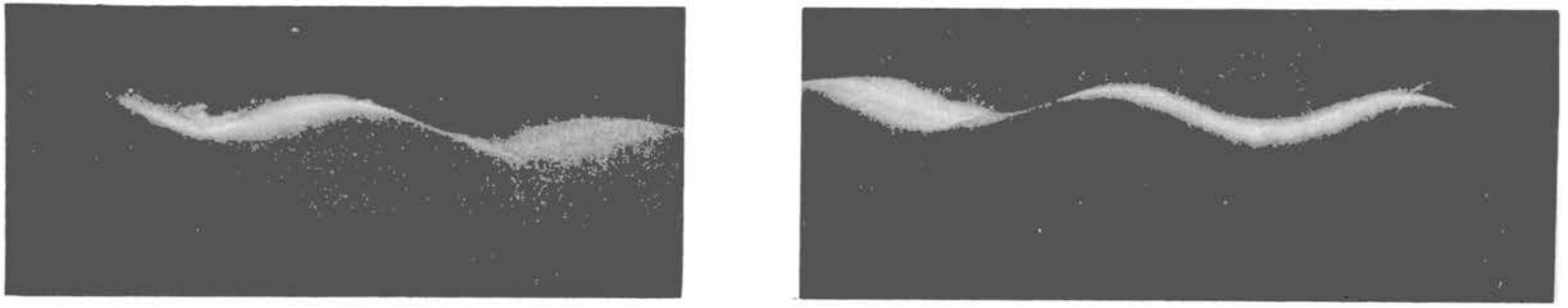

Fig. 63 Photographs of visualization study, Wave C.

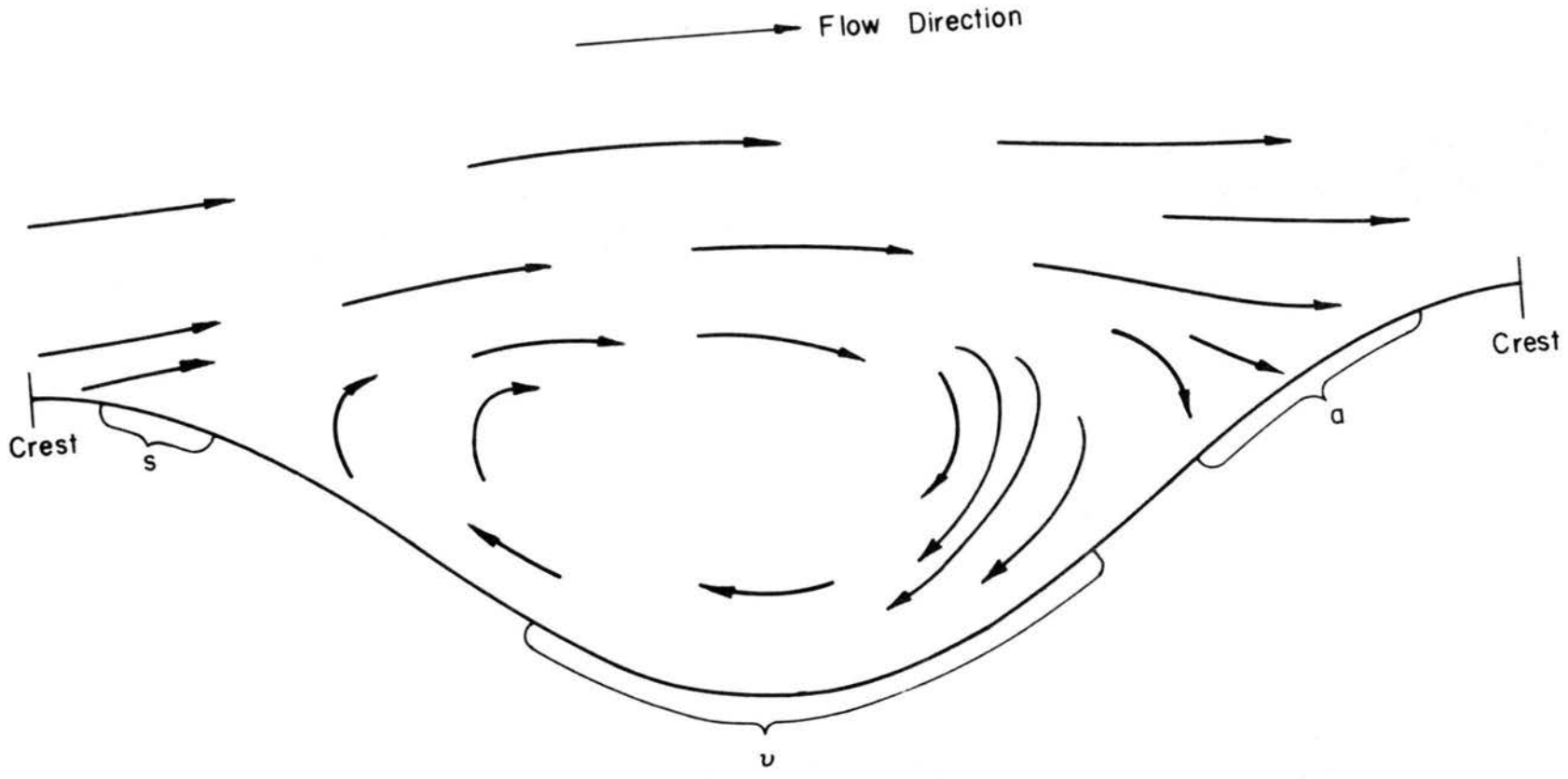

Fig. 64. Approximate flow pattern.

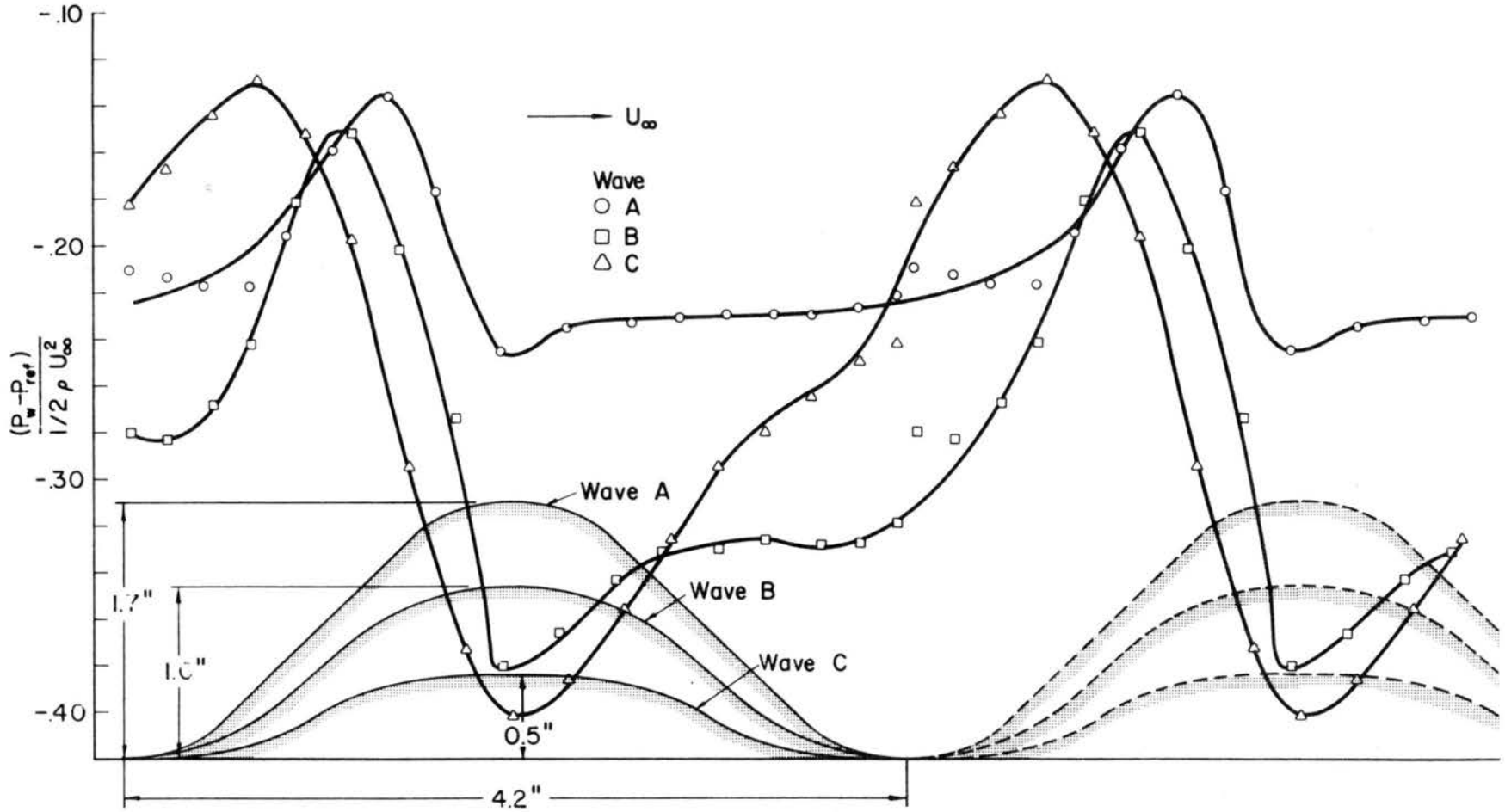

Fig. 65. Wall pressure distributions, waves A, B, & C.

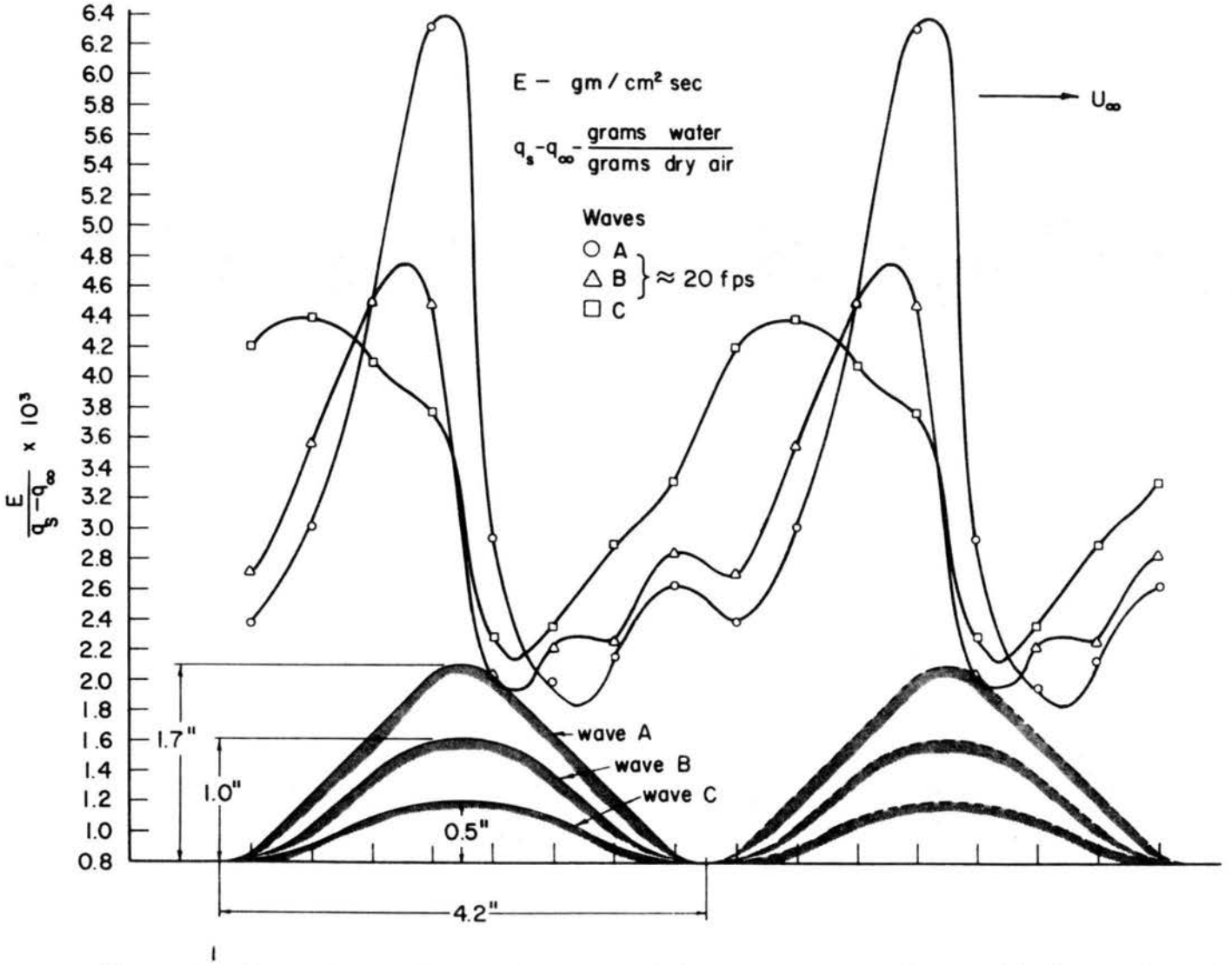

Fig. 66. Comparison of distributions of local mass transfer coefficients for the three wave sets.

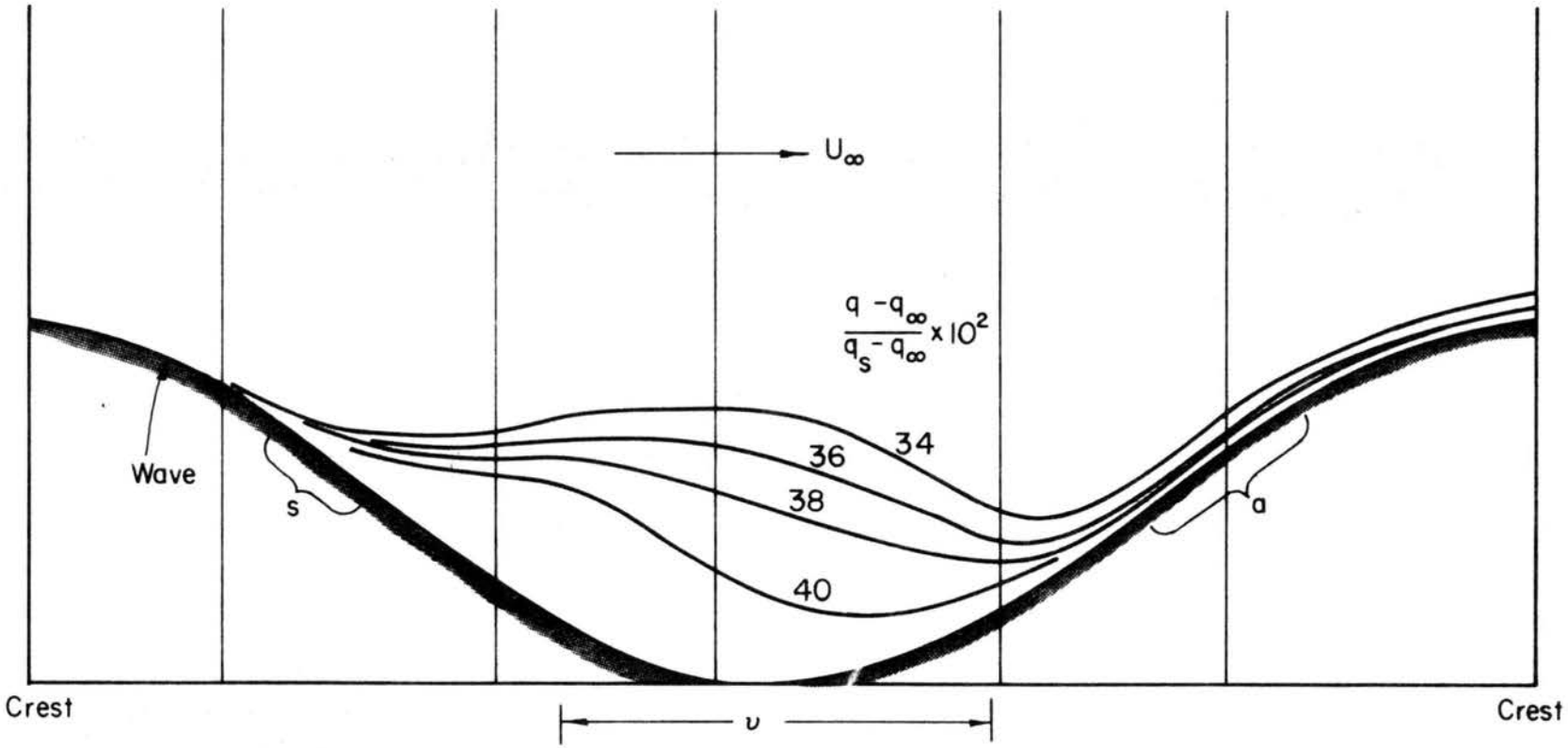

Fig. 67. Typical set of isoconcentration lines in a wave trough.

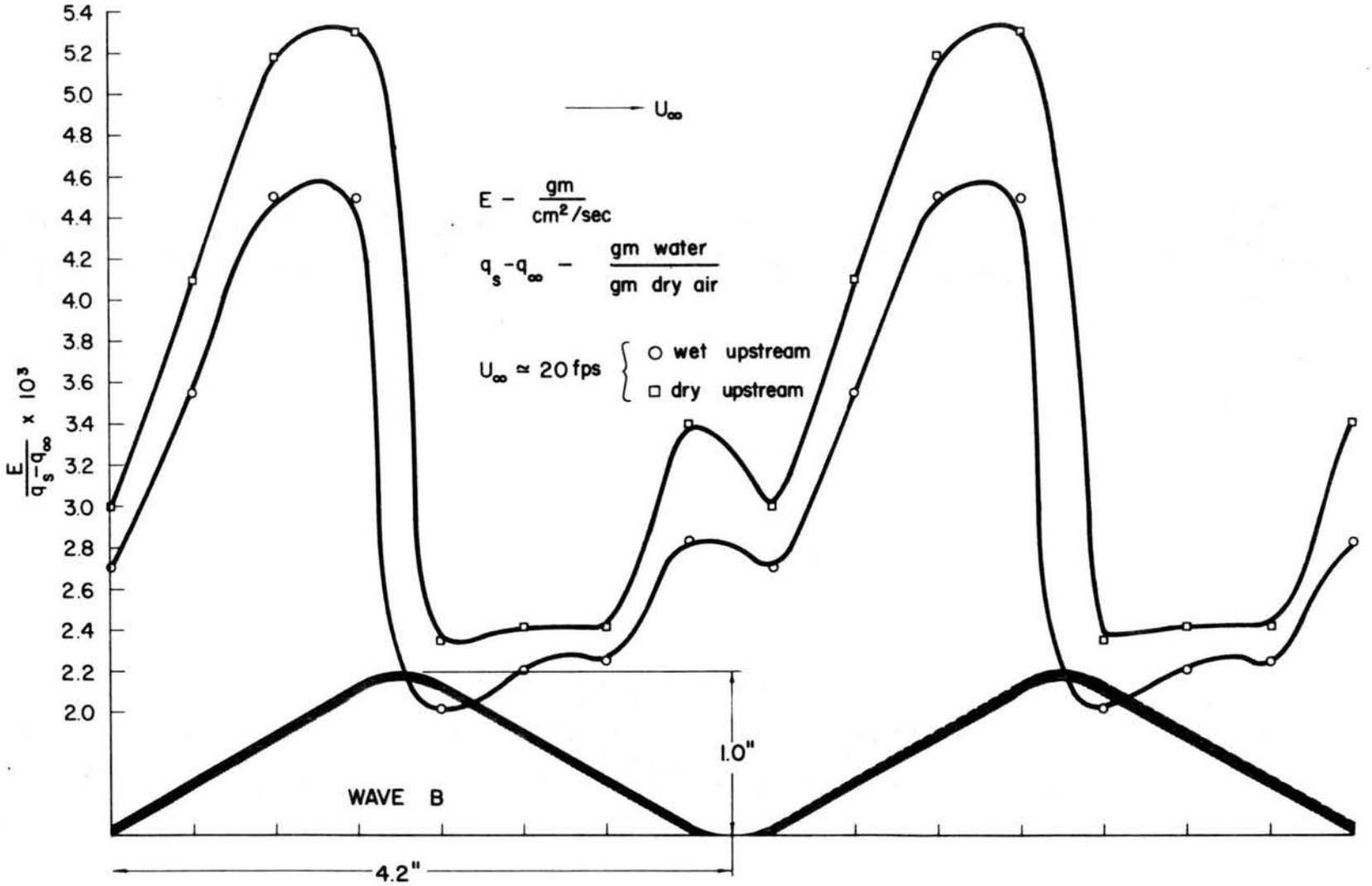

Fig. 68. Comparison of local mass coefficient distributions for wet and dry upstream cases, (Typical case).

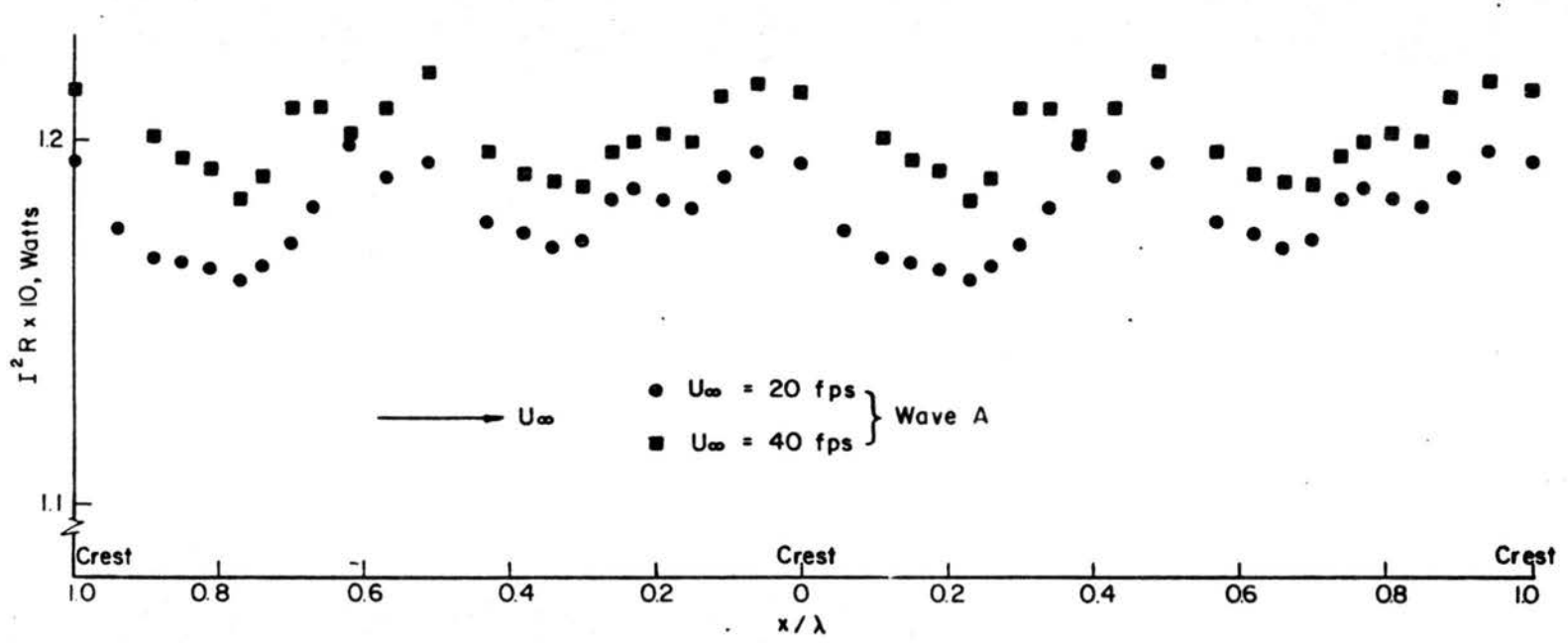

Fig. 69. Wall heat-flux profiles (waves), wave A.

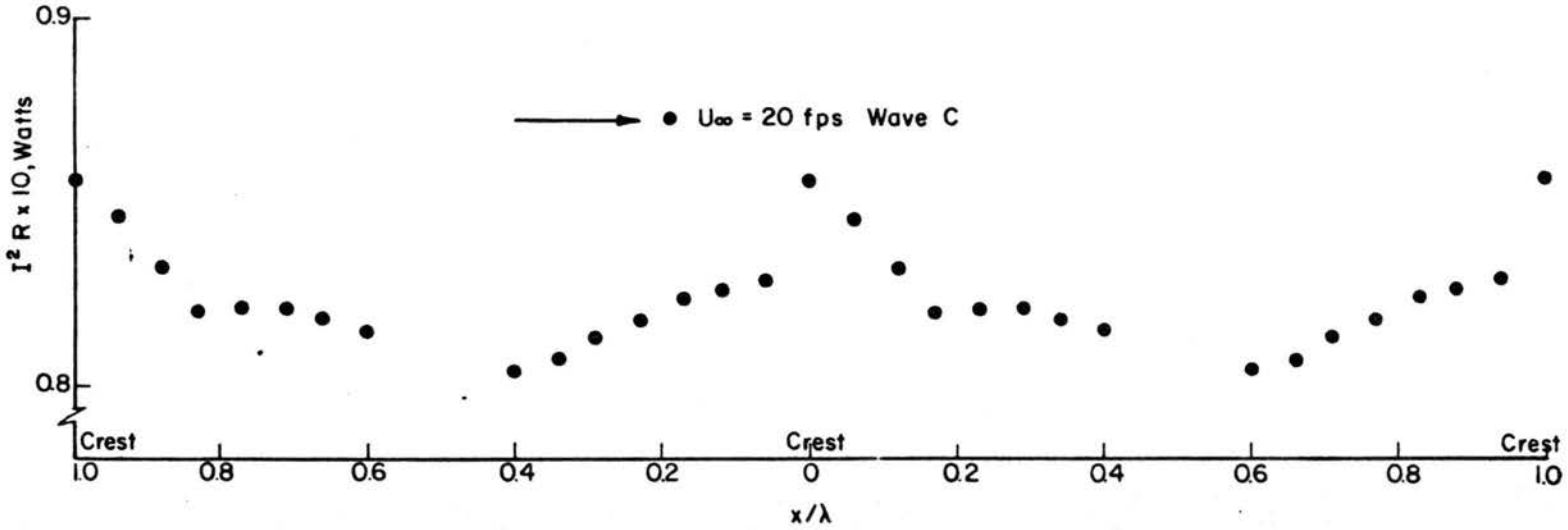

Fig. 70. Wall heat flux profiles (waves), wave C.

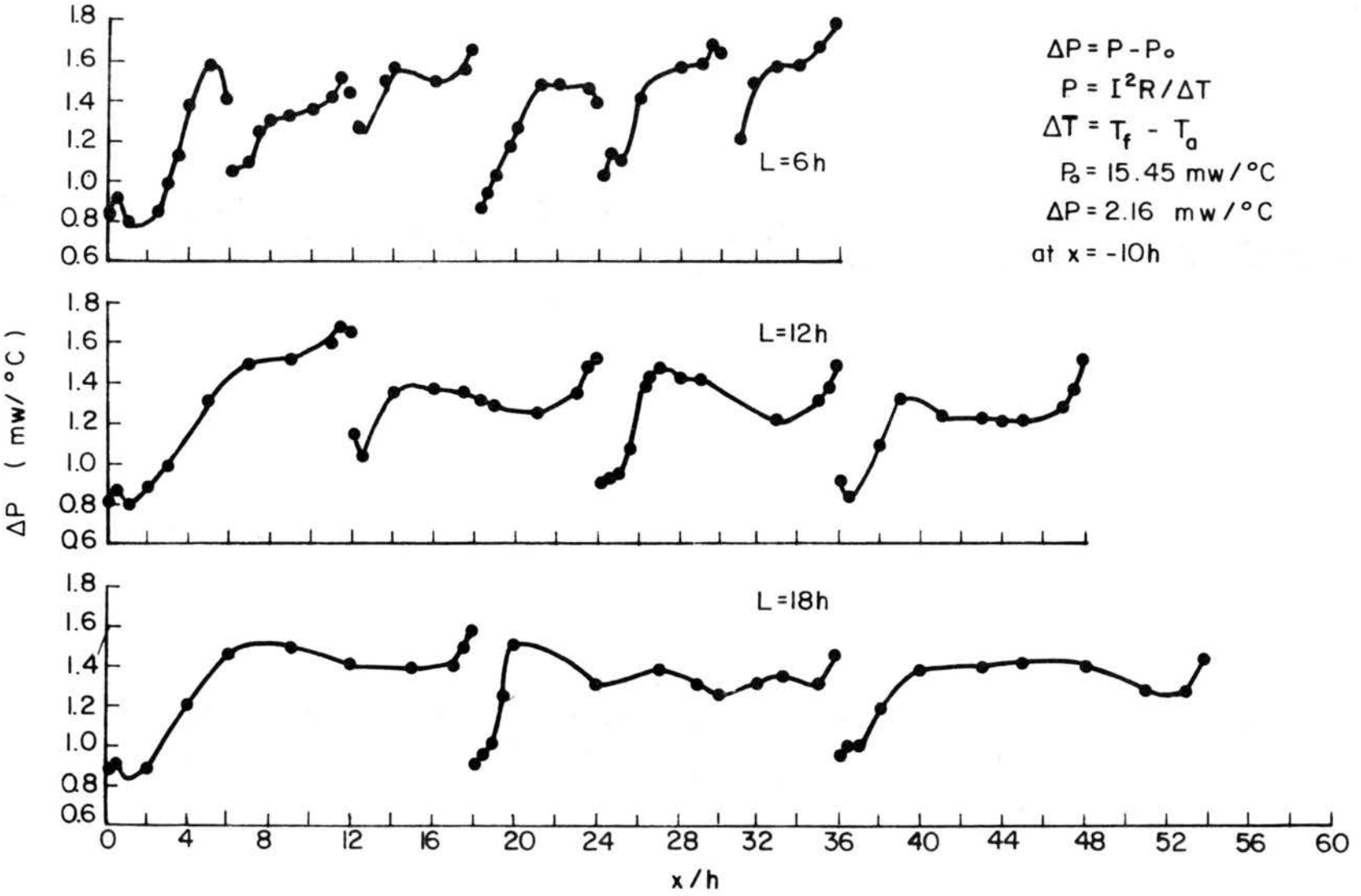

Fig. 71. Wall heat-flux profiles (fences).

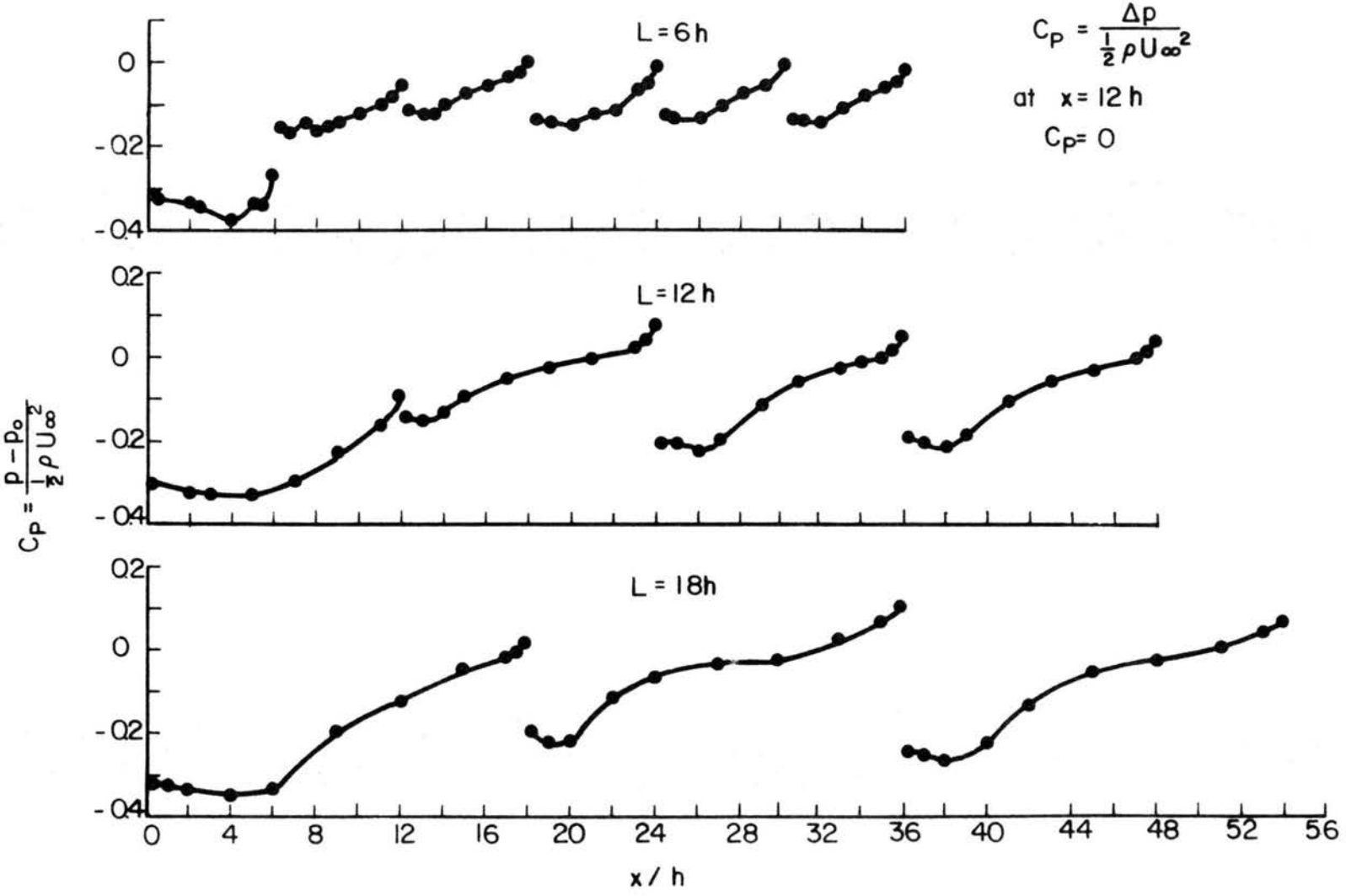

Fig. 72. Local static pressure distributions (fences).

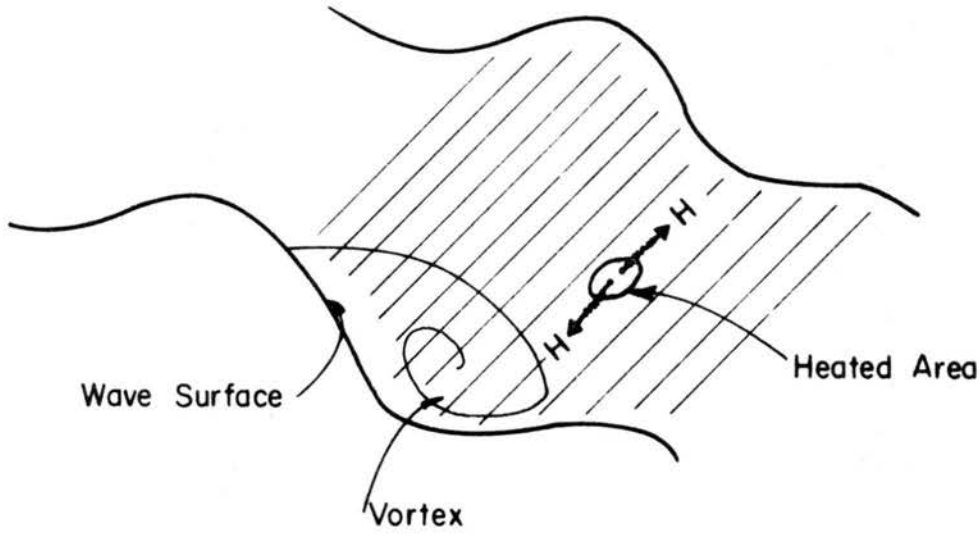

Fig. 73. Removal of heat by cellular vortices in wave troughs (a sketch).

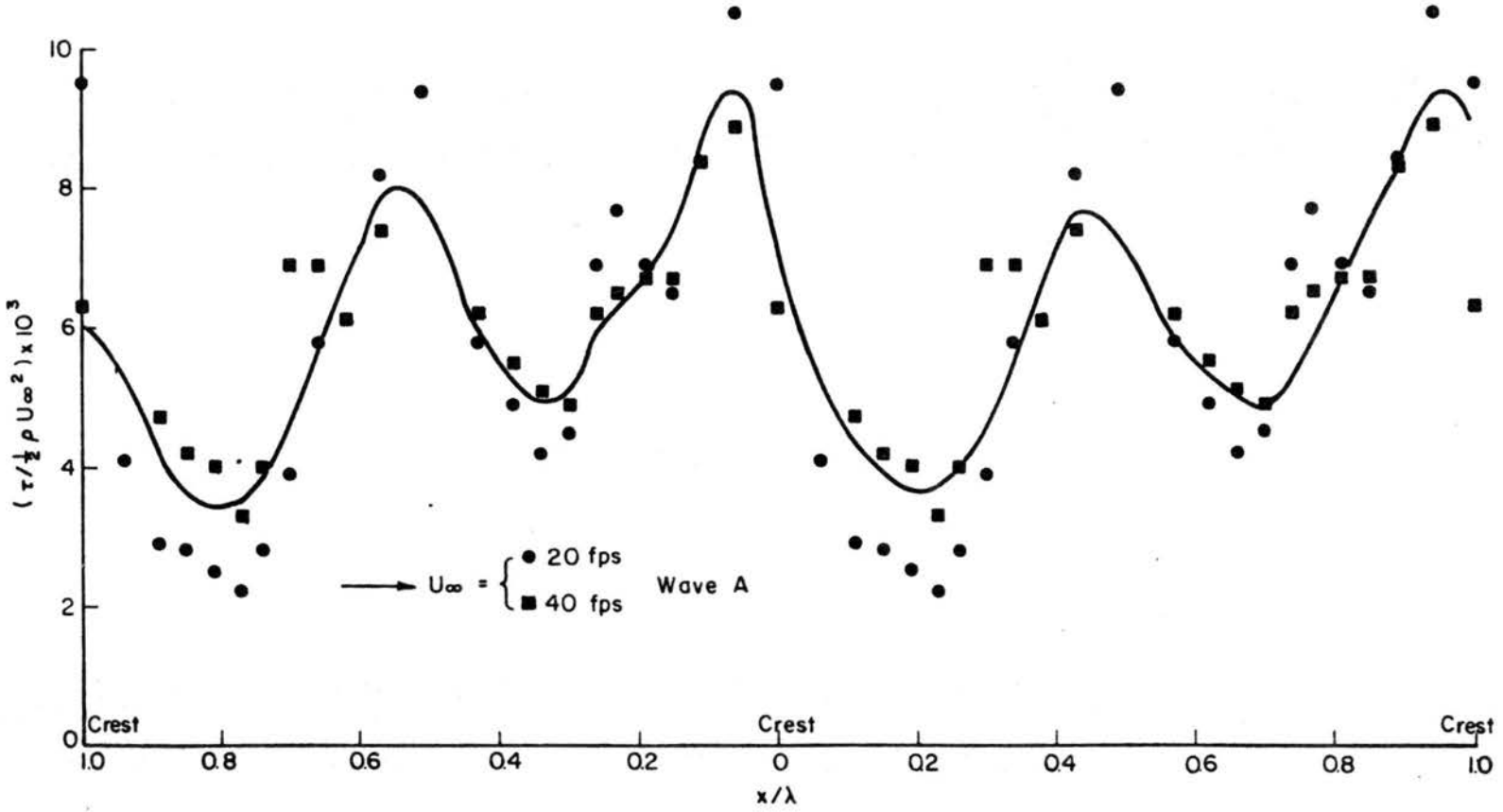

Fig. 74. Wall "shear-stress" profiles (waves), wave A.

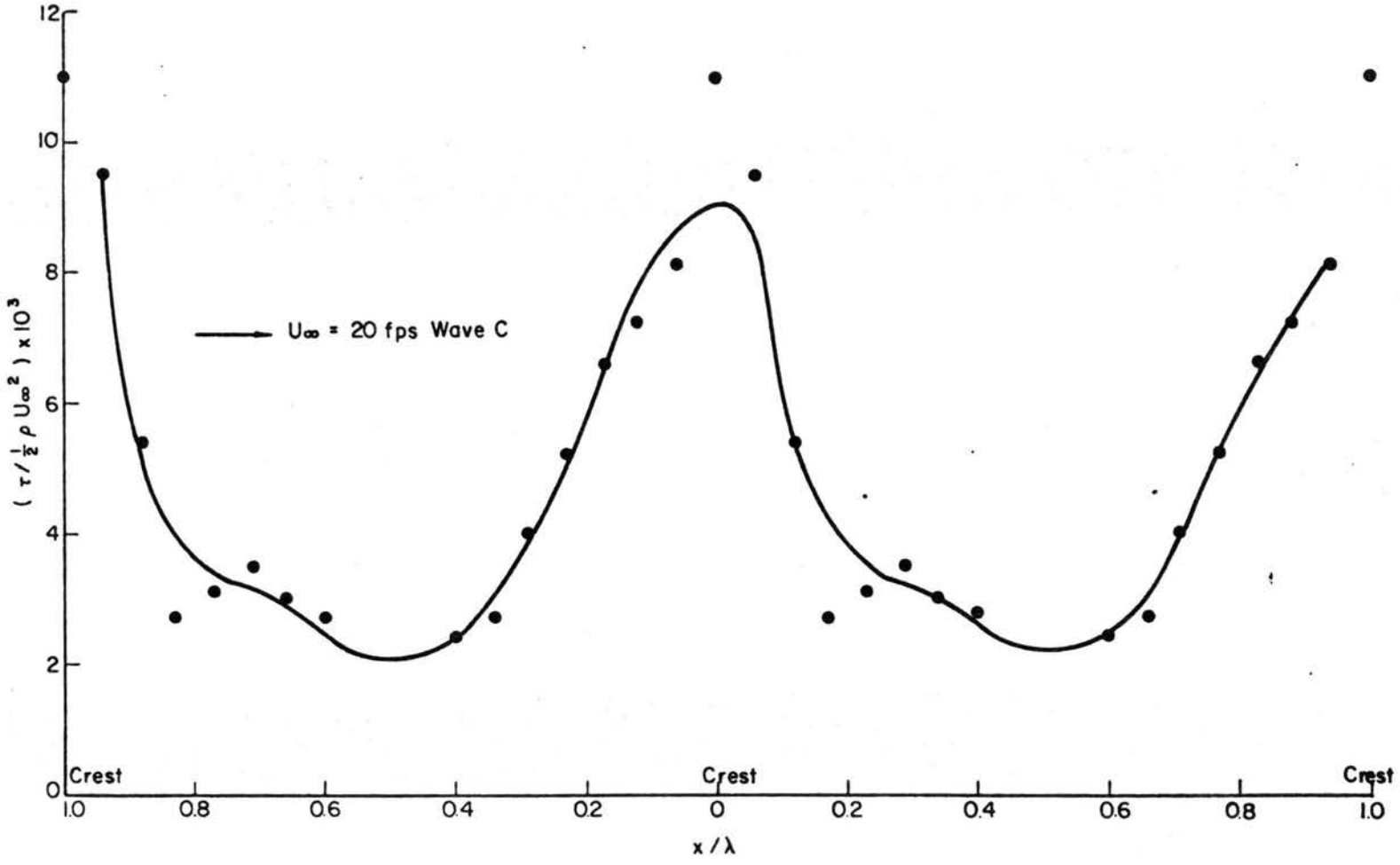

Fig. 75. Wall "shear stress" profiles (waves), wave C.

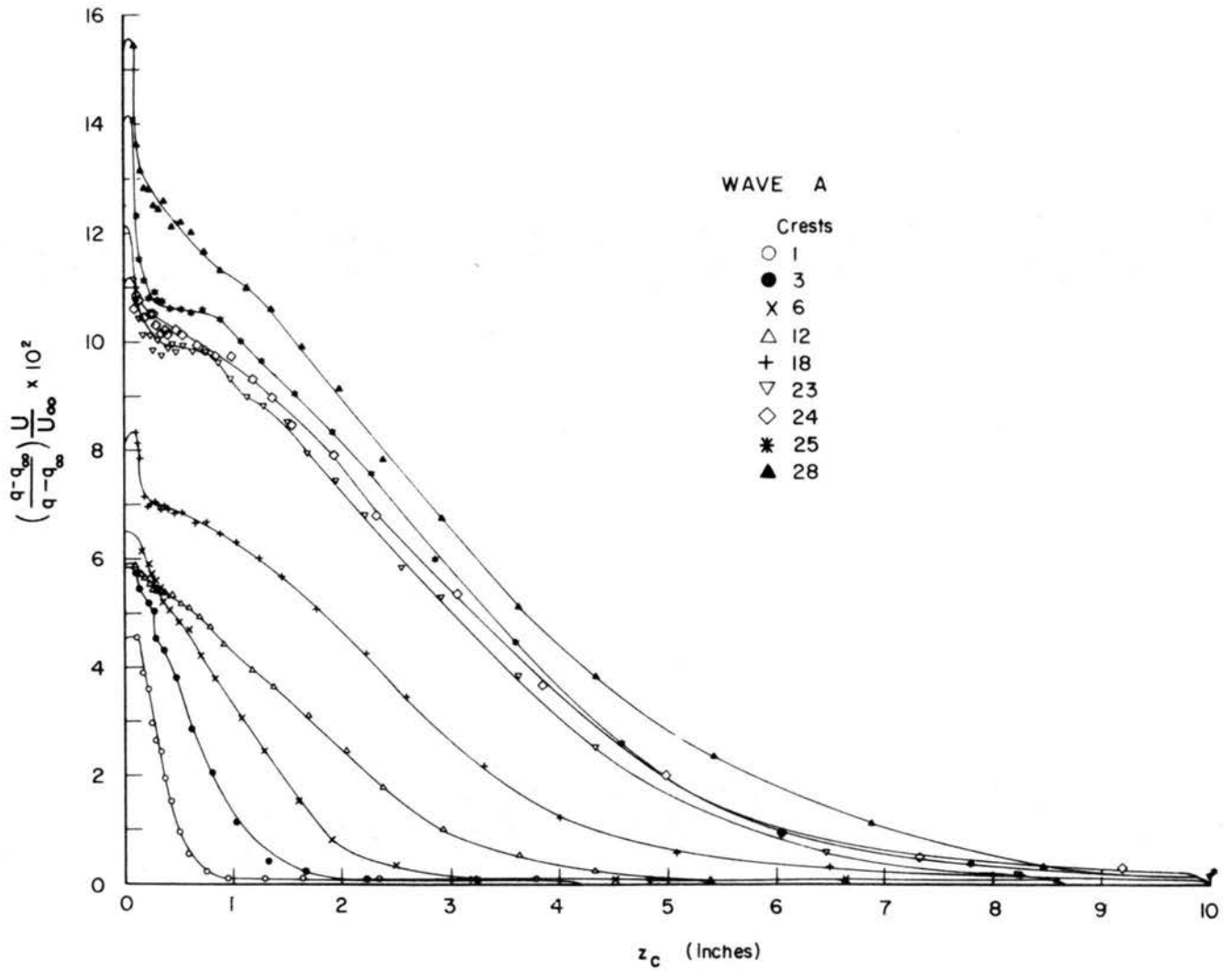

Fig. 76. Variation of $\left(\frac{q-q_\infty}{q_s-q_\infty}\right)\ \frac{u}{u}$ vs z_c over waves (typical case).

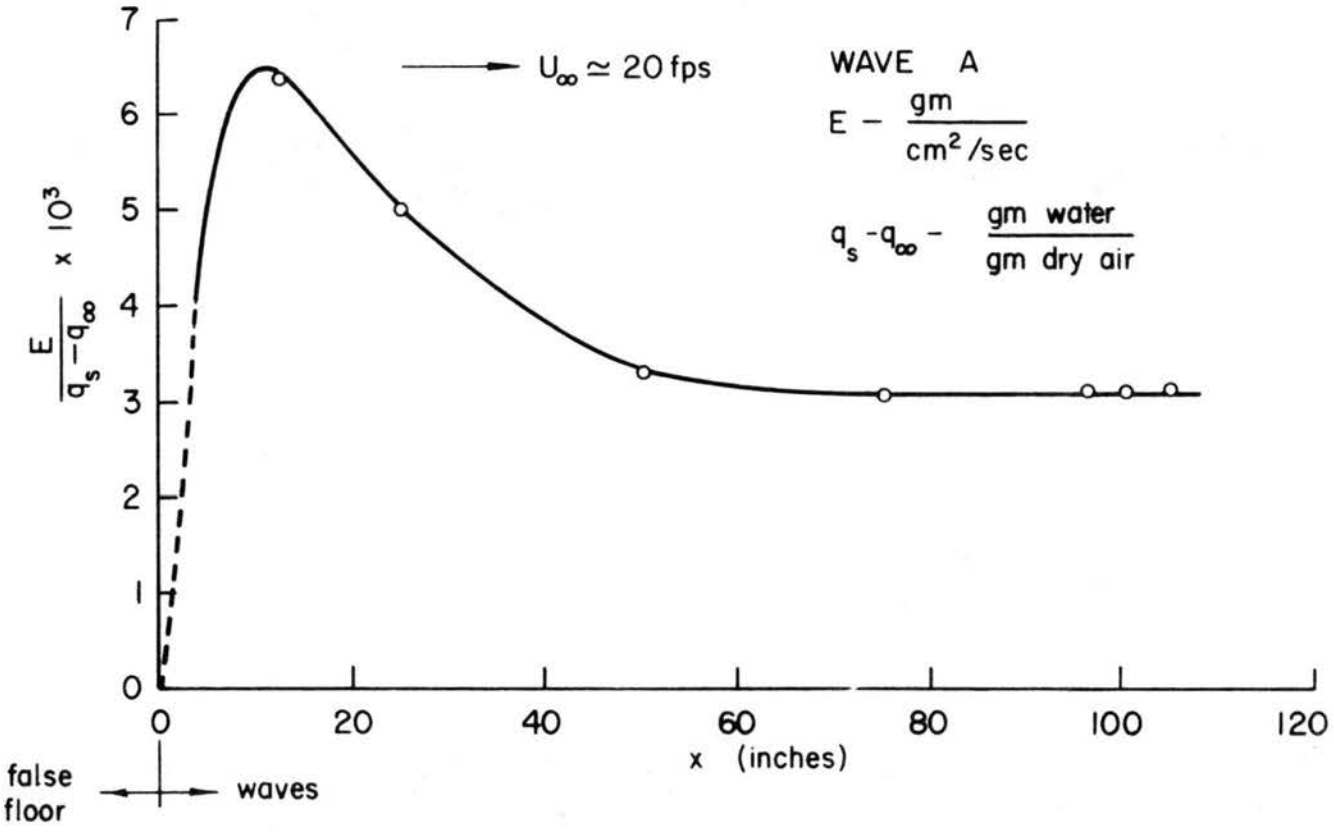

Fig. 77. Variation of average evaporation rate with fetch, wave A.

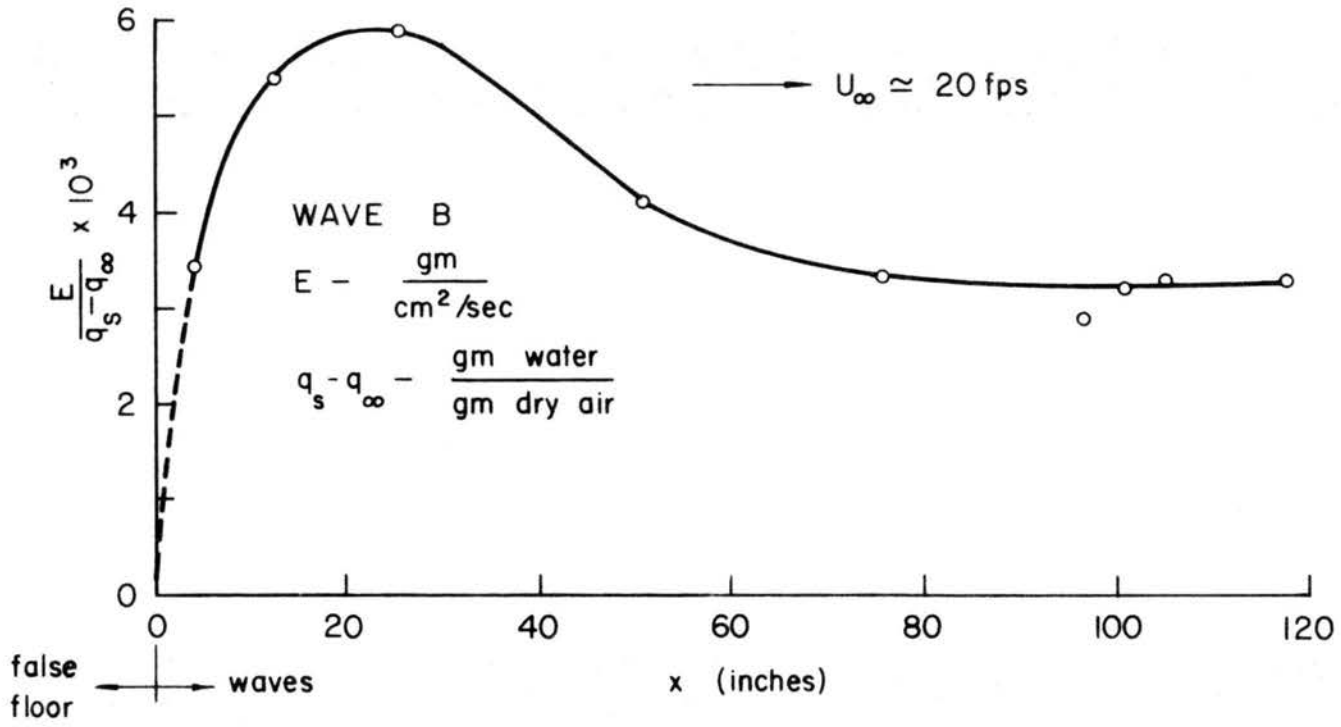

Fig. 78. Variation of average evaporation rates with fetch, Wave B.

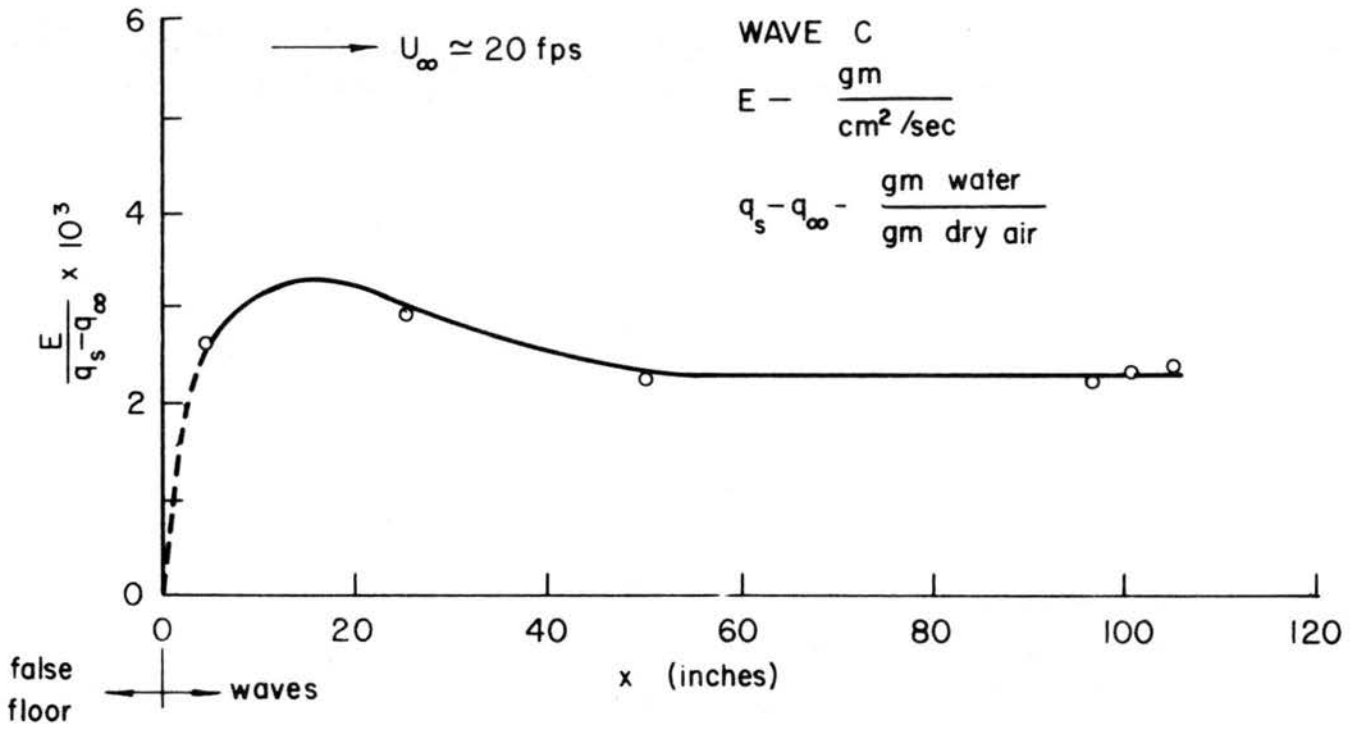

Fig. 79. Variation of average evaporation rates with fetch, Wave C.

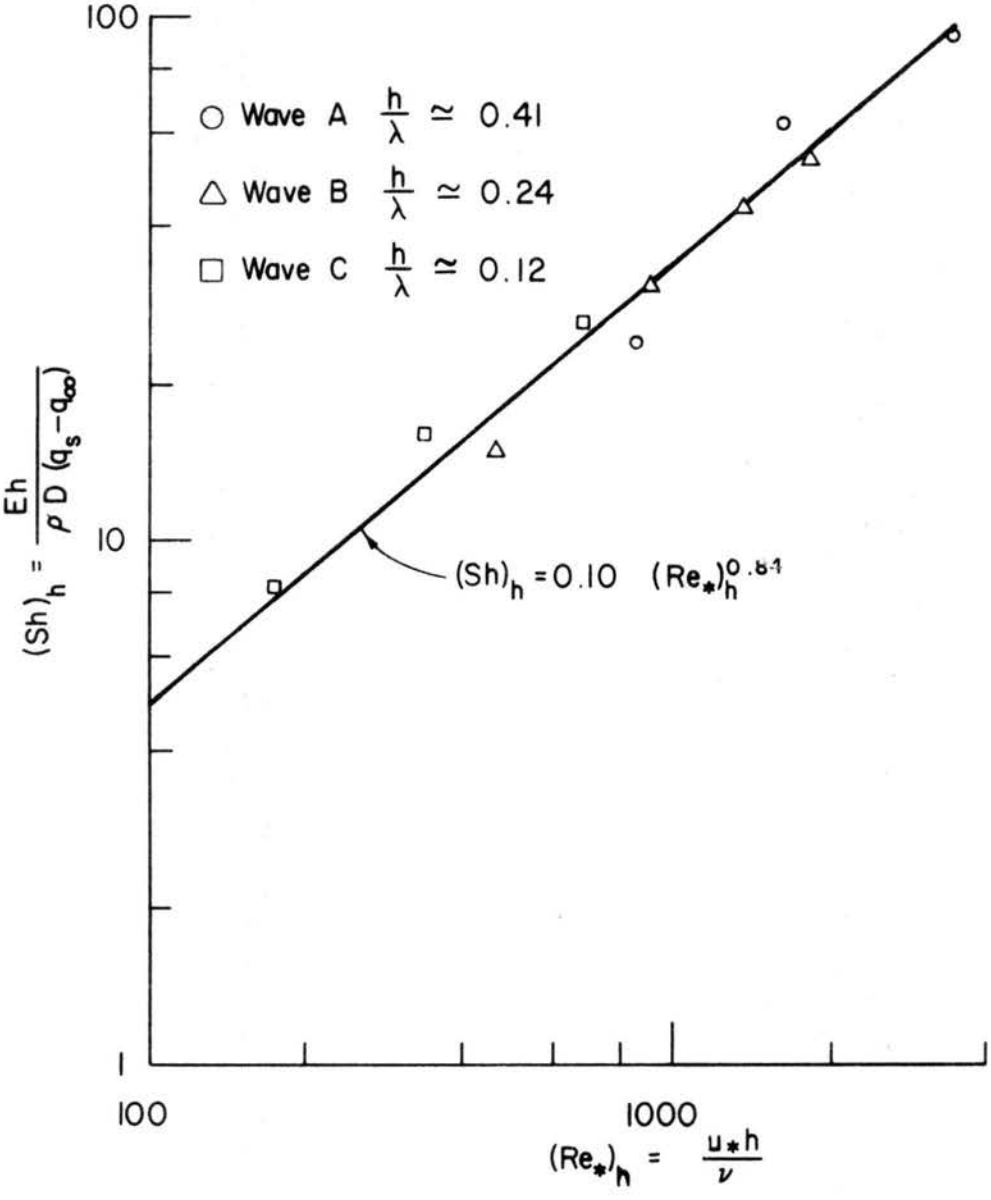

Fig. 80. Correlation of evaporation data with h as the characteristic length.

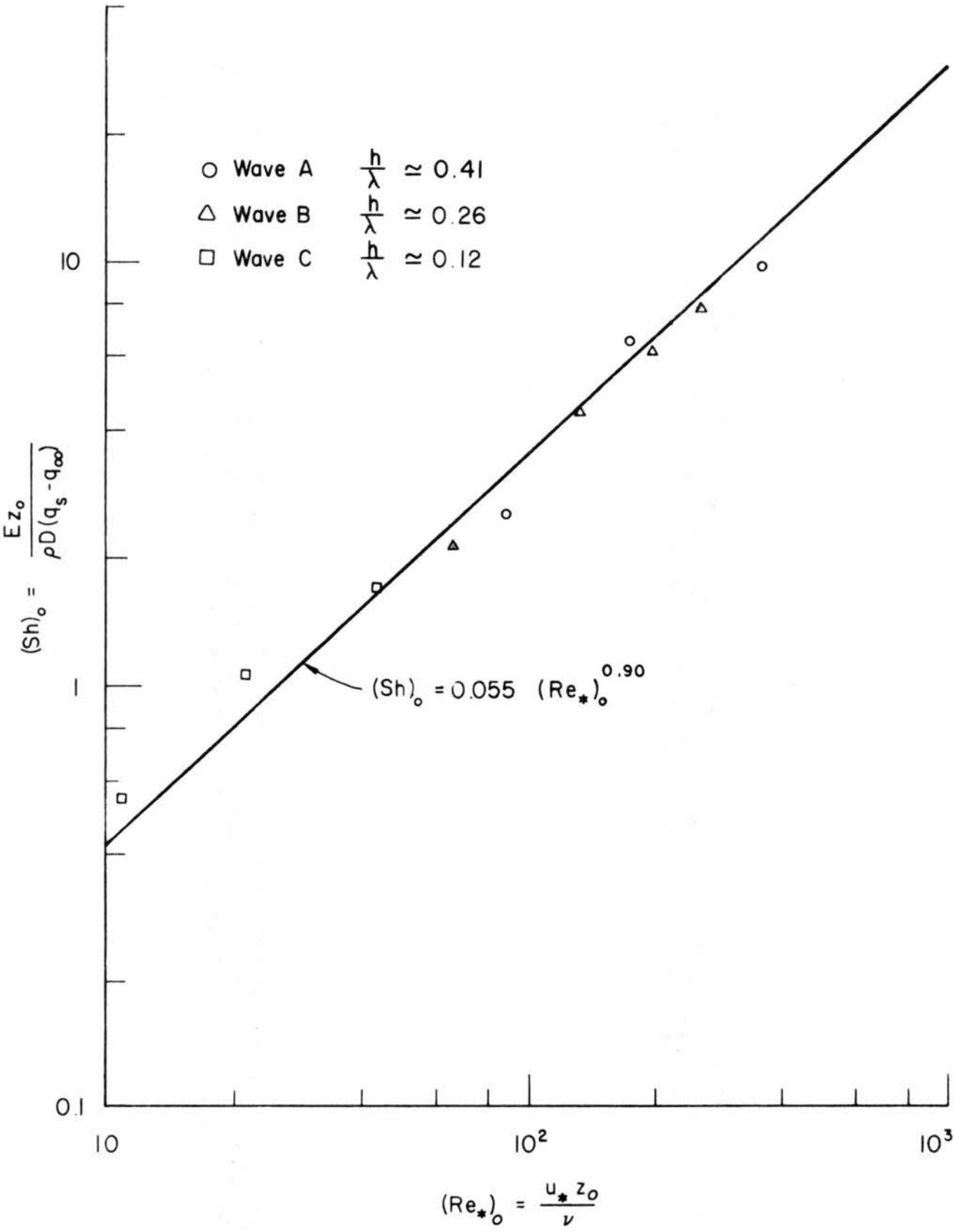

Fig. 81. Correlation of evaporation data with z_o as the characteristic length.

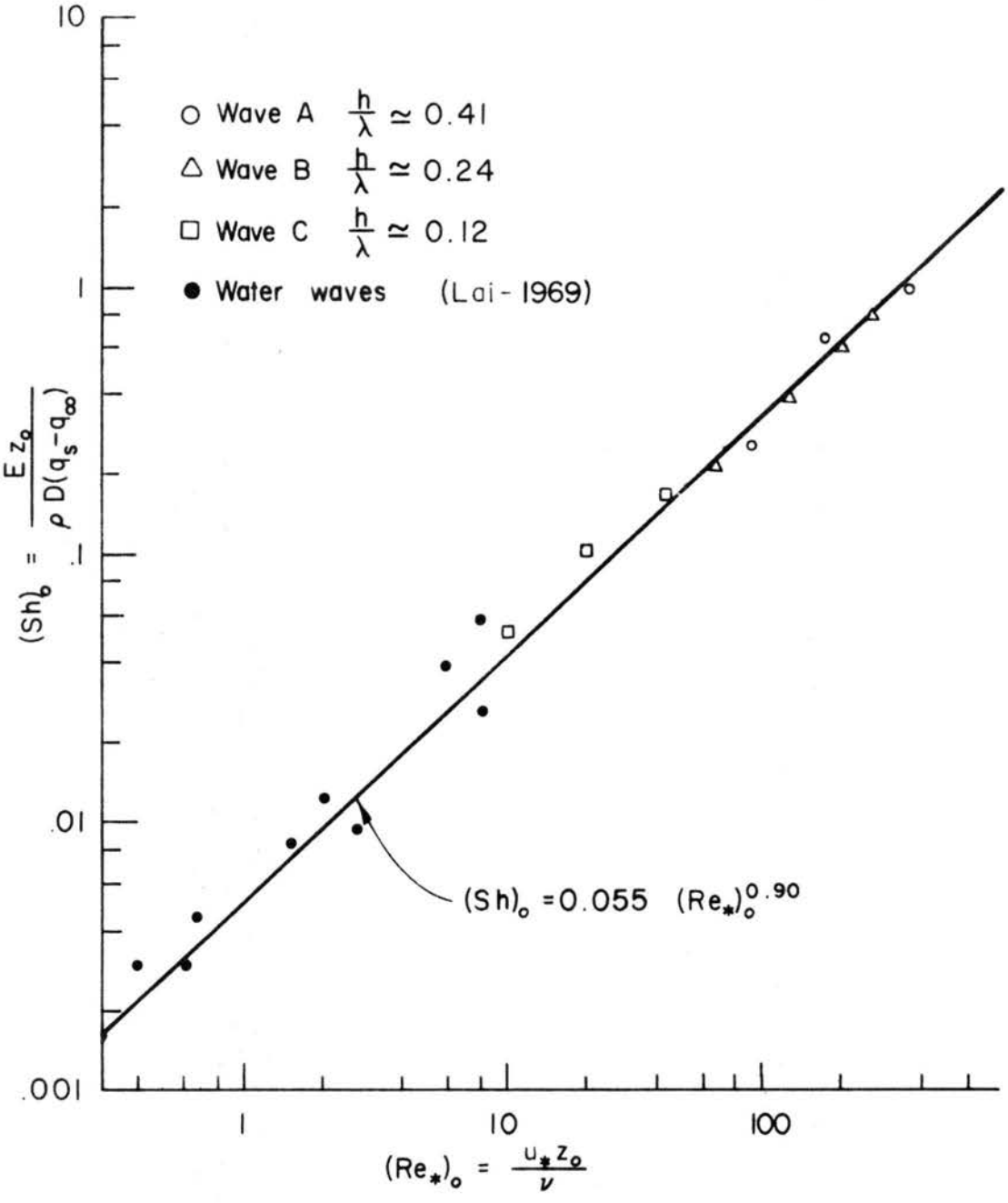

Fig. 82. Correlation of water waves data with the data of this study.

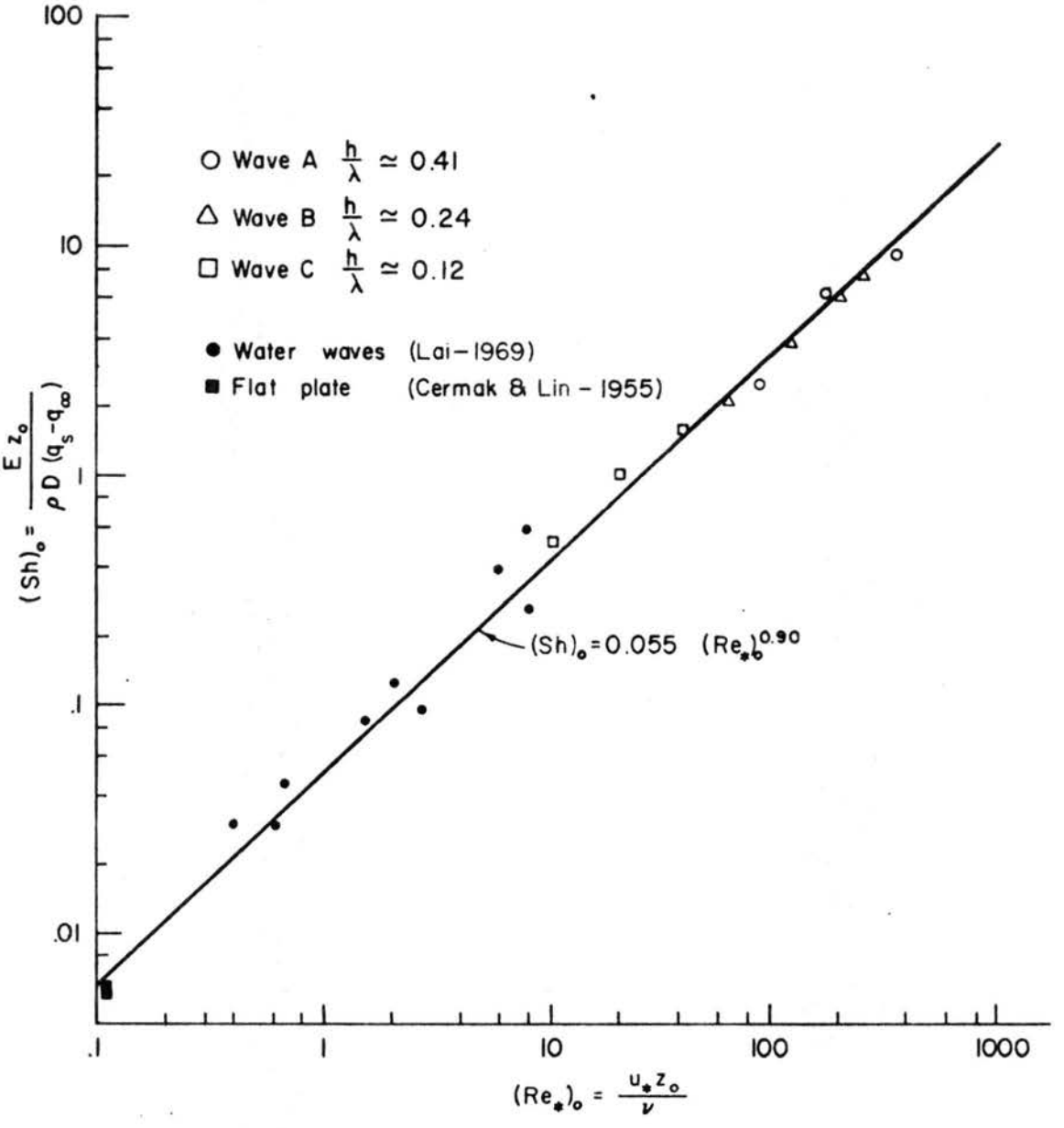

Fig. 83. Correlation of flat plate and water waves data with the data of this study.

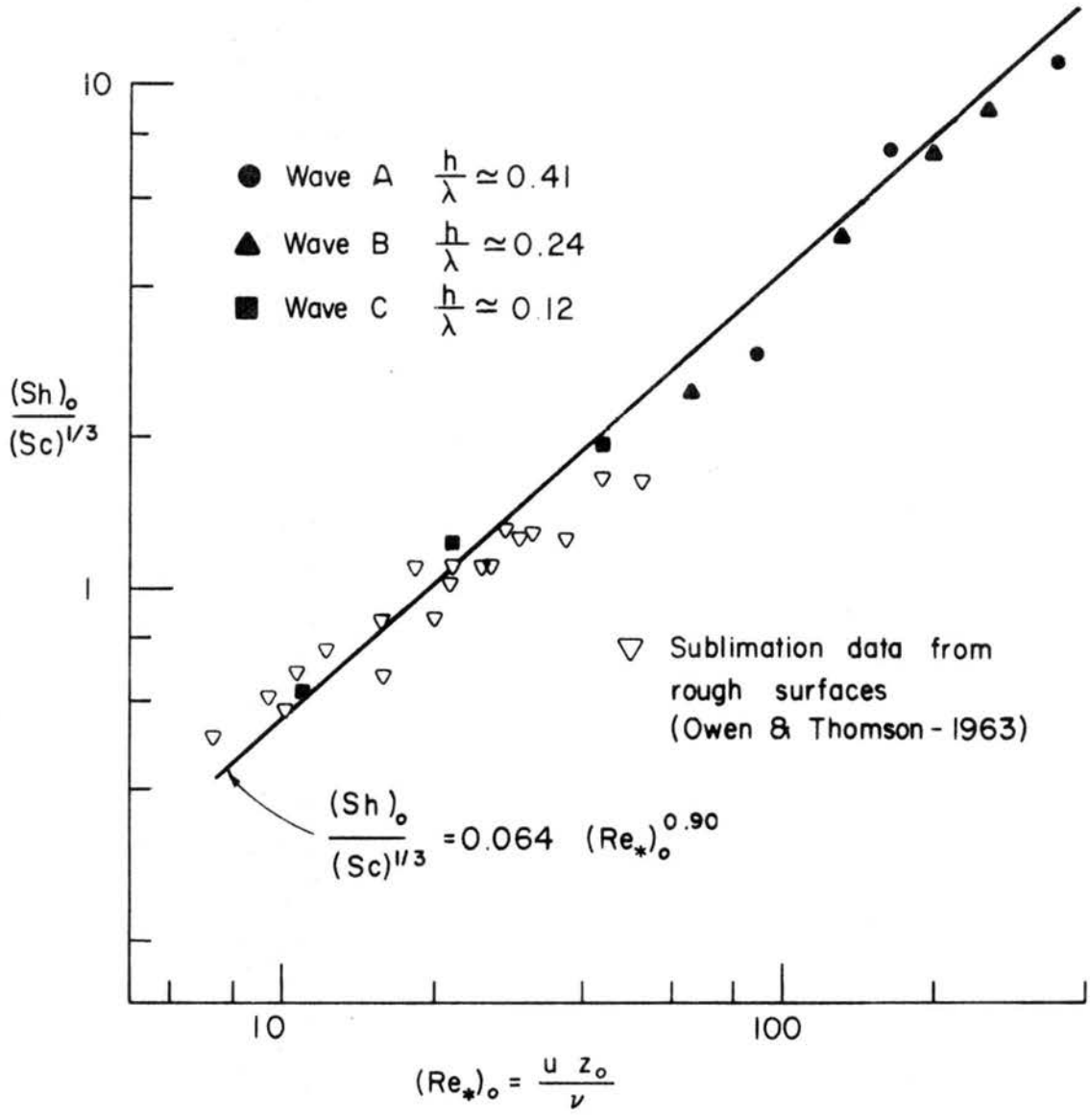

Fig. 84. Correlation of sublimation data from different kinds of rough surfaces (Owen and Thomson - 1963) with the evaporation data of this study.

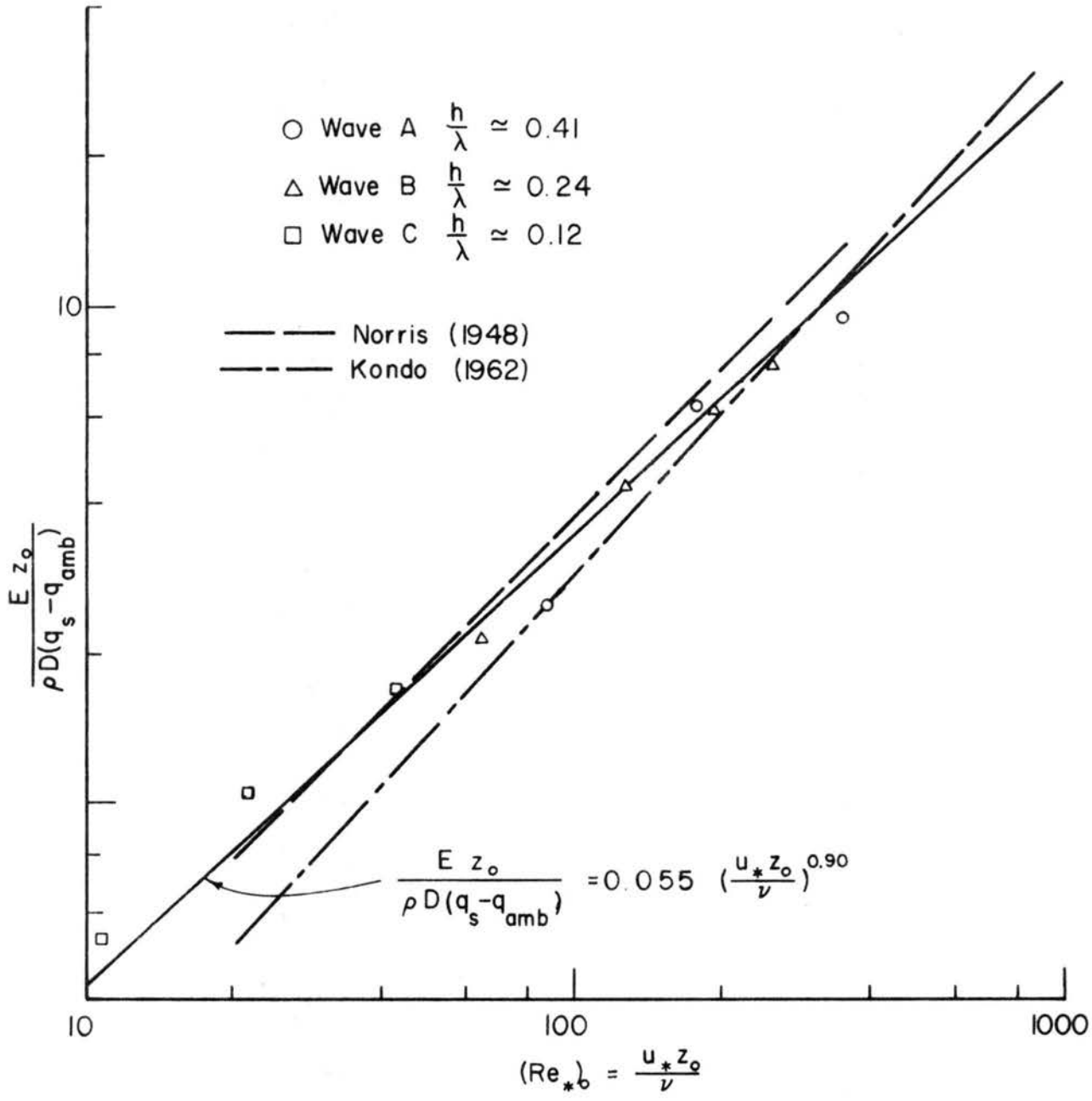

Fig. 85. Comparison with Norris' (1948) and Kondo's (1962) results.

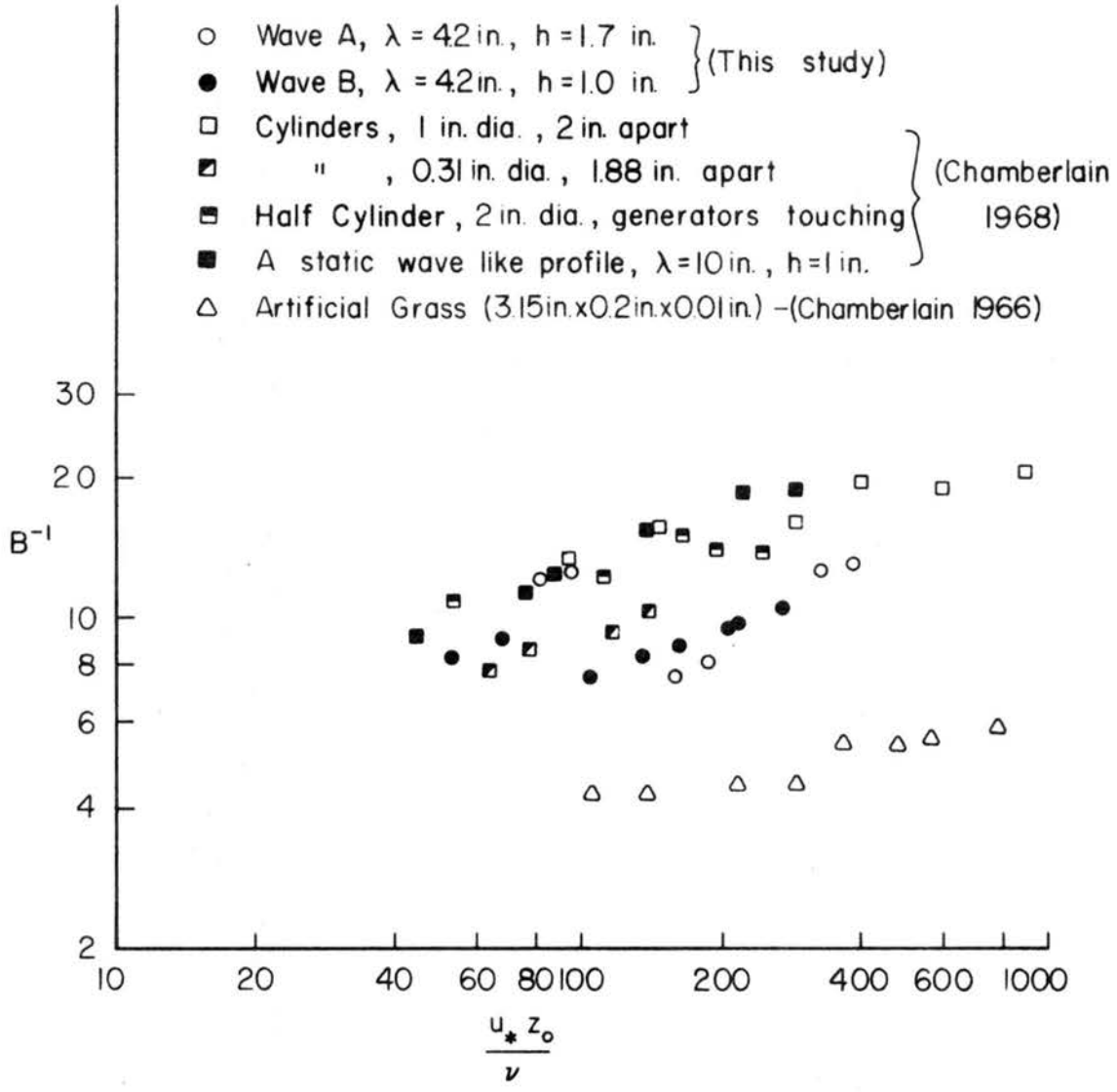

Fig. 86. Plot B^{-1} vs $\frac{u_* z_o}{\nu}$ for this study along with Chamberlain's (1966 and 1968) data.

Wave	h/λ	Region D
A	0.41	-0.43λ to 0.15λ
B	0.24	-0.46λ to 0.08λ
C	0.12	-0.48λ to 0.17λ

$U_\infty \approx 20$ ft./sec

Region D $\approx$ Region Over Which $\dfrac{(\frac{E}{\Delta q}) - (\frac{E}{\Delta q})_{min.}}{(\frac{E}{\Delta q})_{max.} - (\frac{E}{\Delta q})_{min.}} < 0.25$

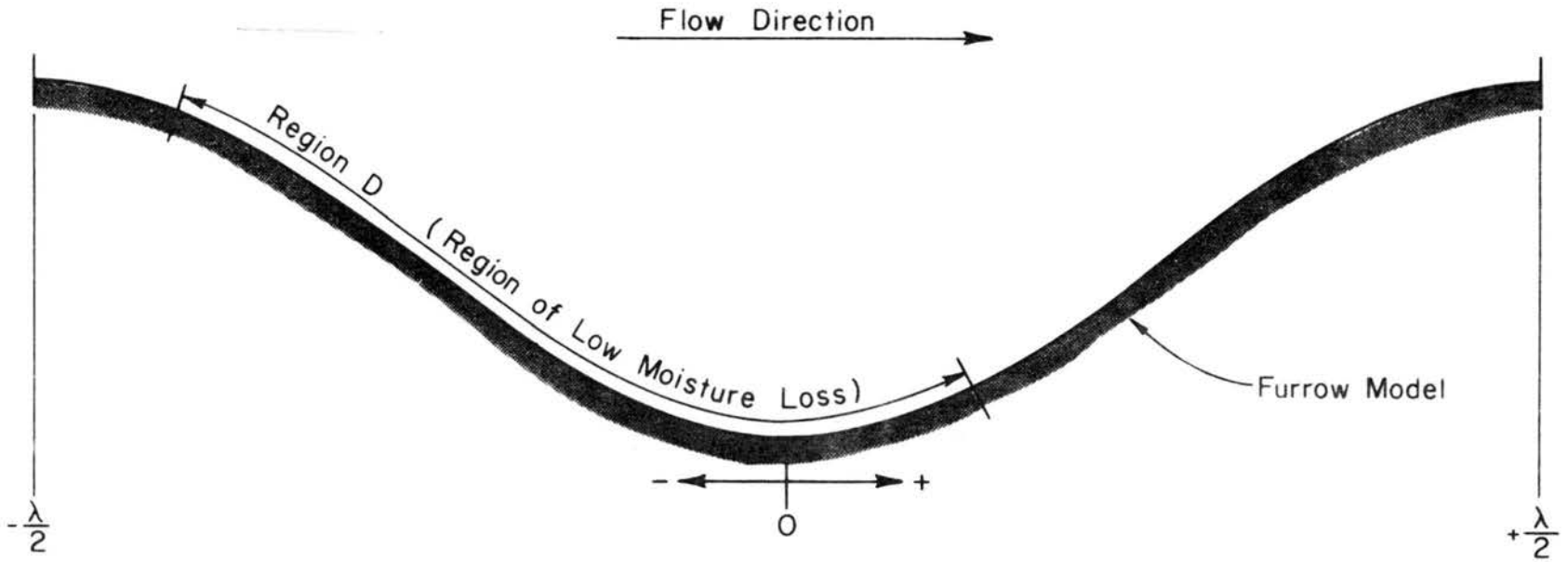

Fig. 87. Model of a field furrow.

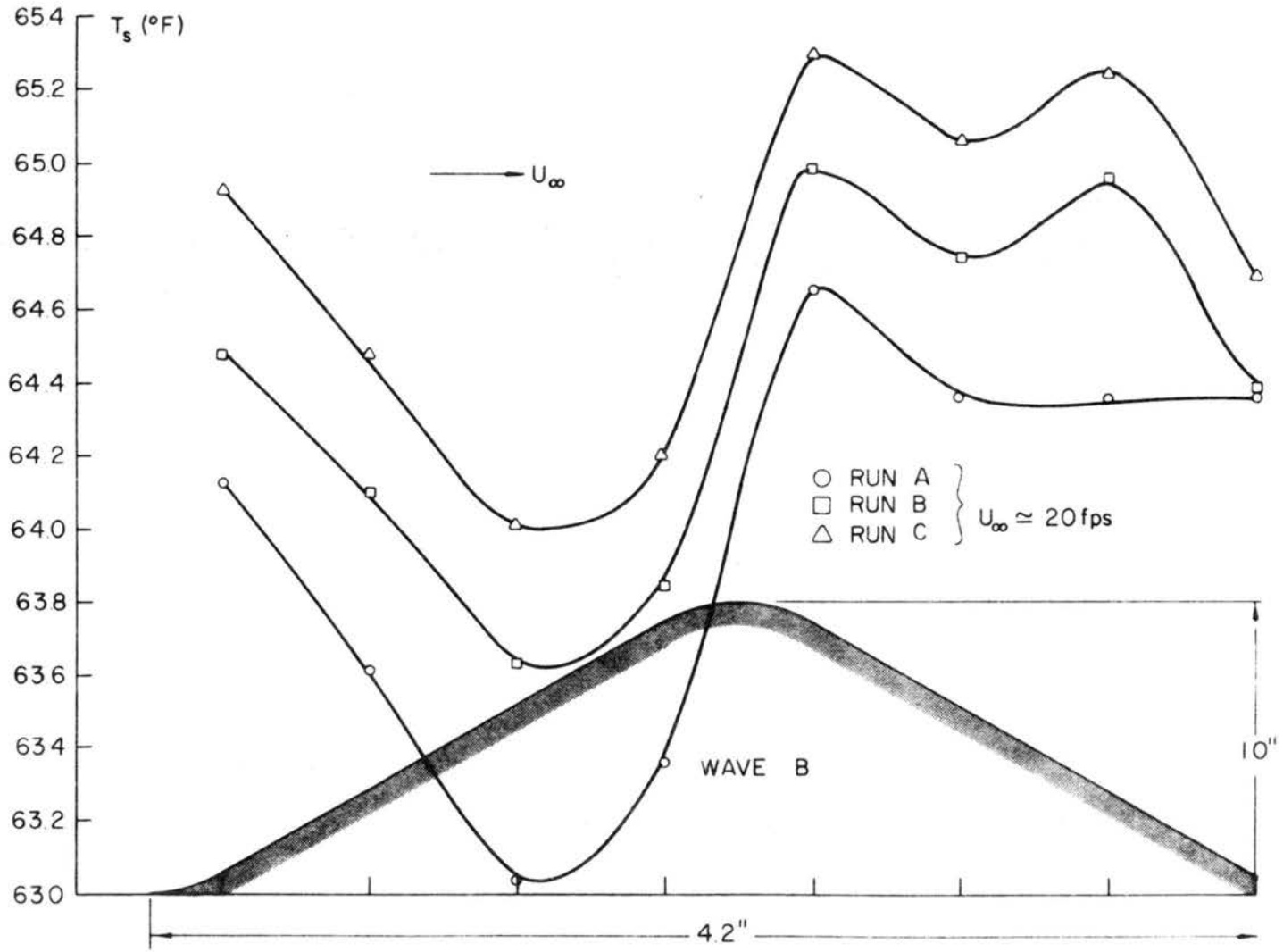

Fig. 88. **Variation** of surface temperature on a saturated wavy surface (Typical case).

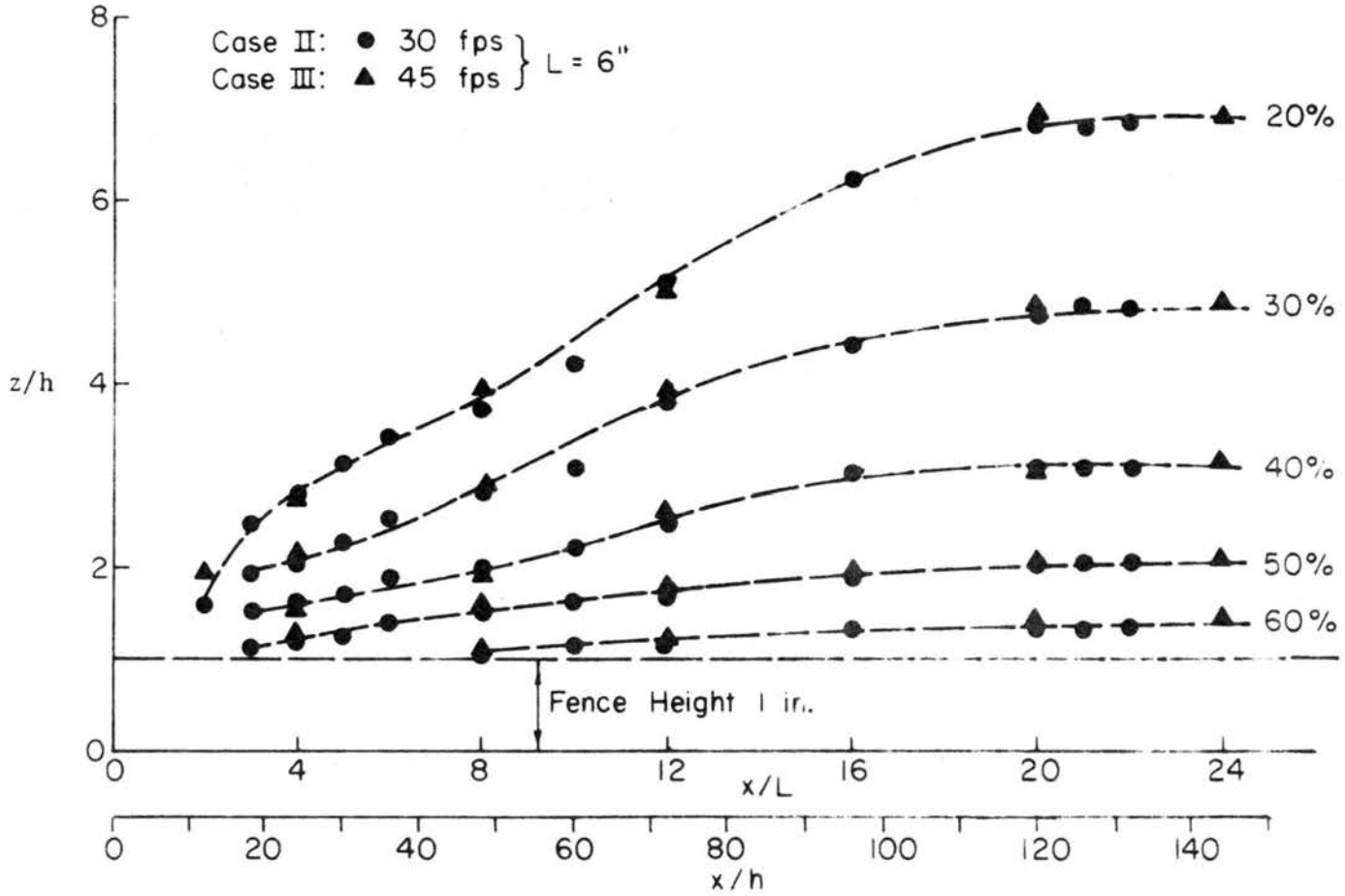

Fig. 89. Wind reduction factors (fences), L = 6 in.

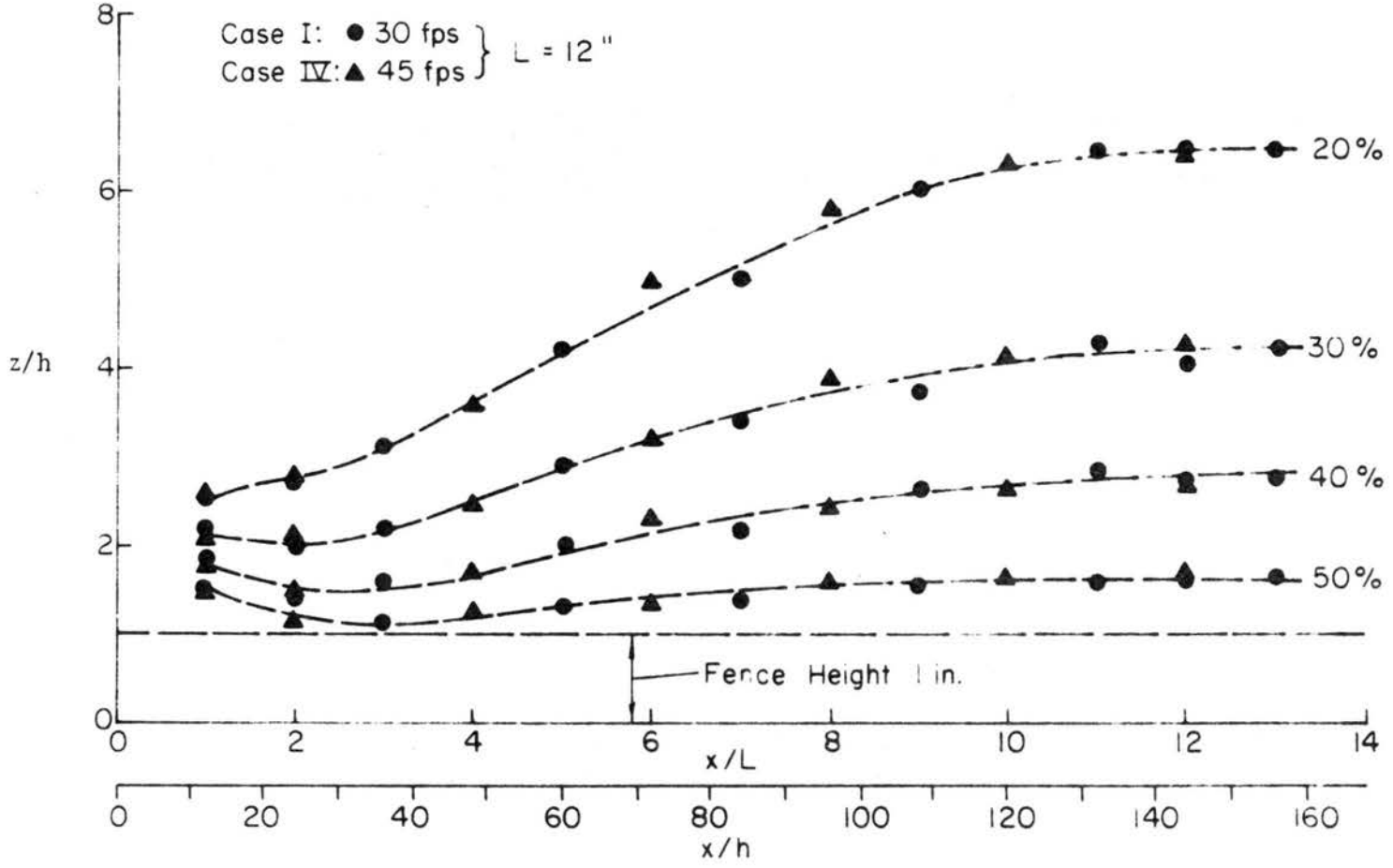

Fig. 90. Wind reduction factors (fences), L = 12 in.

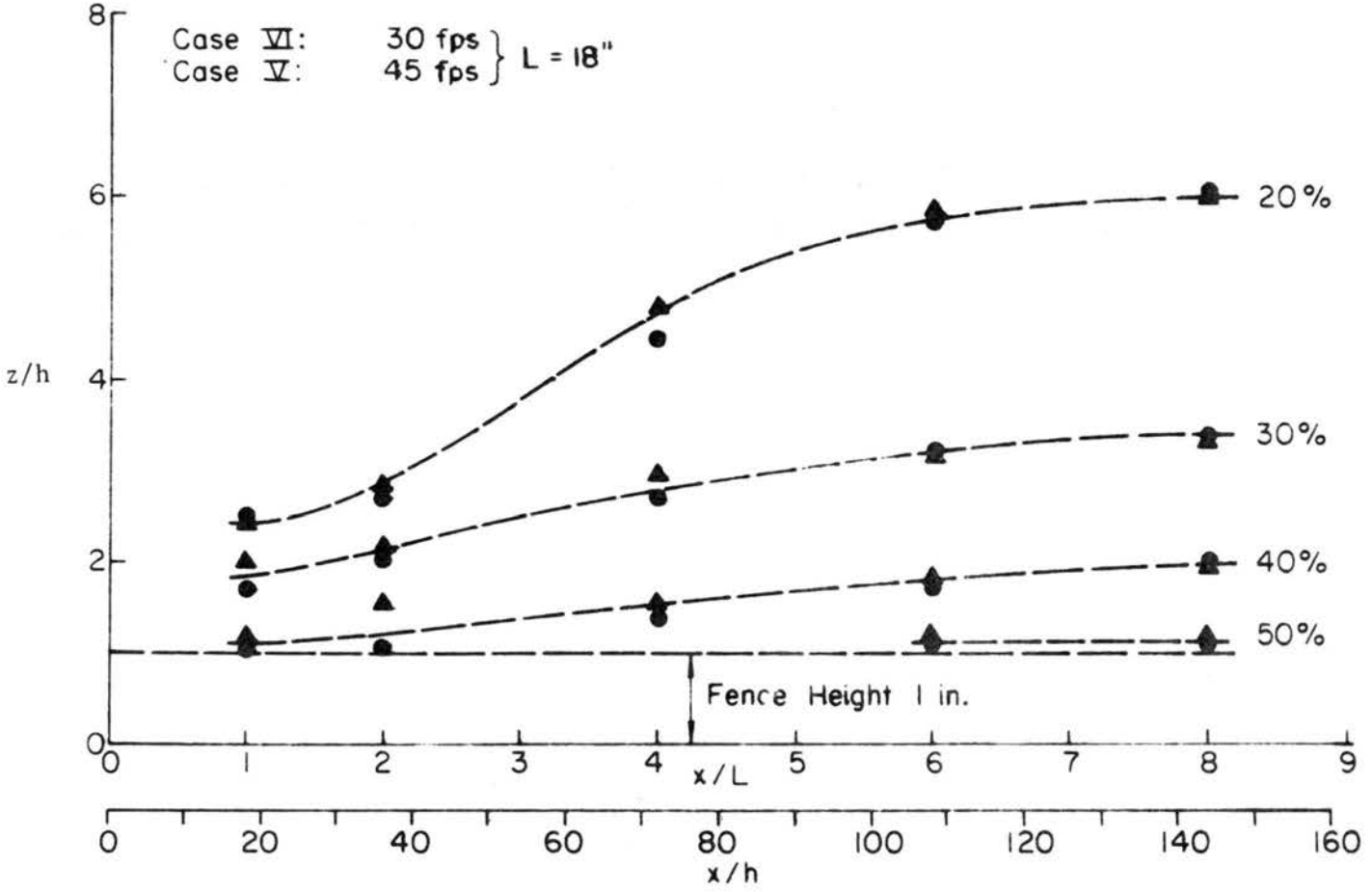

Fig. 91. Wind reduction factors (fences), L = 18 in.

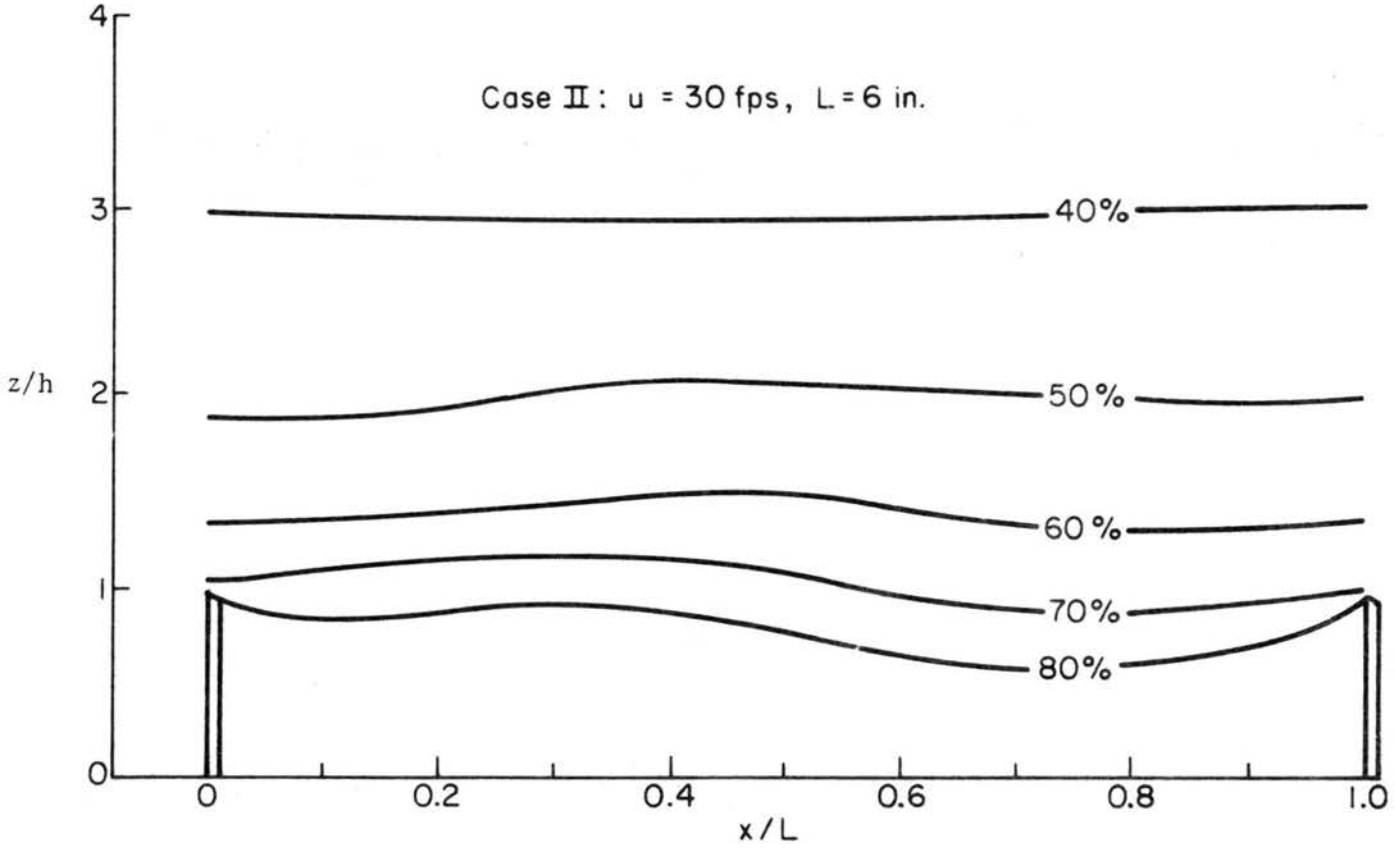

Fig. 92. Wind reduction factor between x = 10 ft and x = 10.5 ft fences and between x = 10.5 ft and x = 11 ft fences.

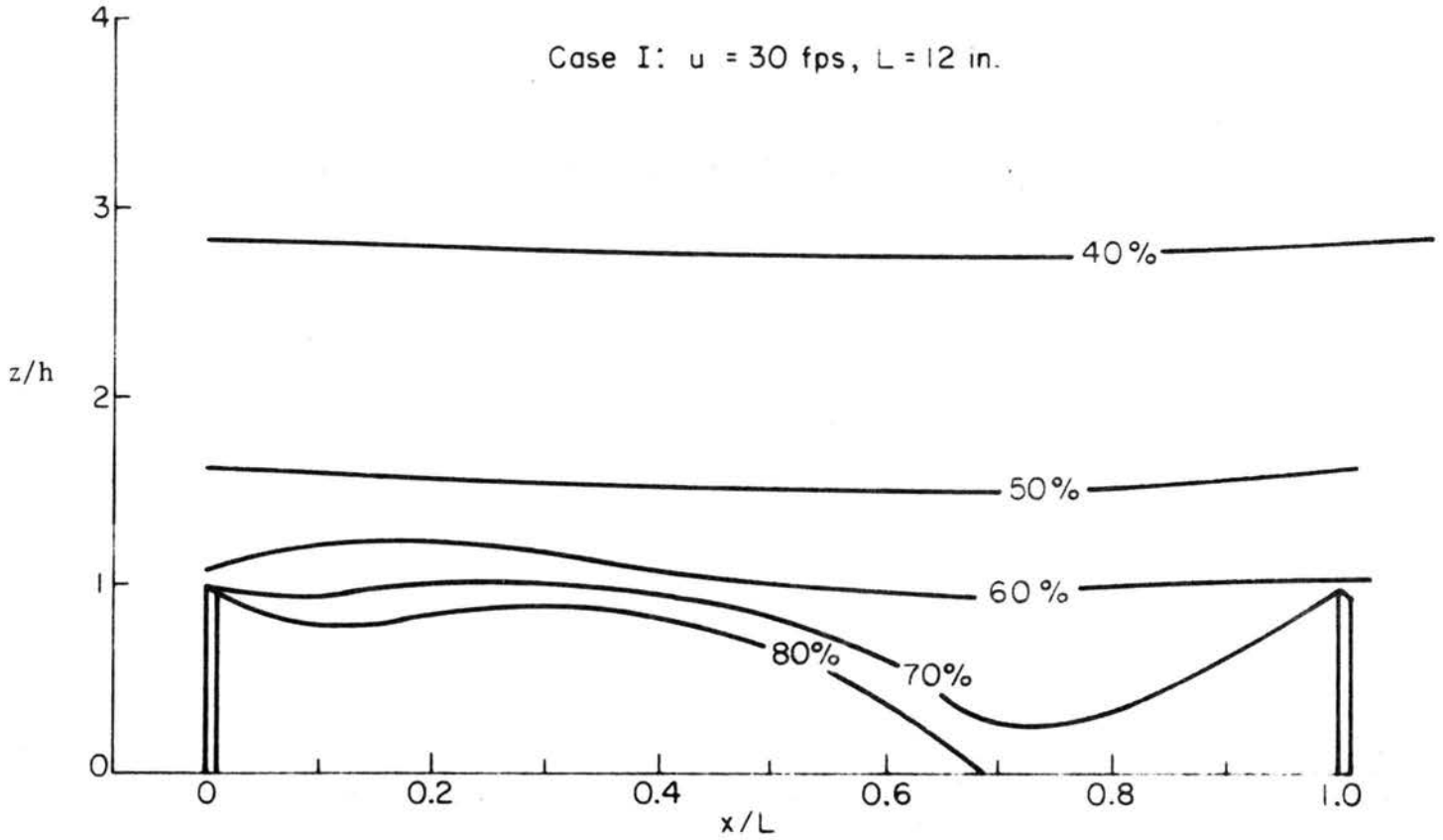

Fig. 93. Wind reduction factor between x = 11 ft and x = 12 ft fences and between x = 12 ft and x = 13 ft fences.

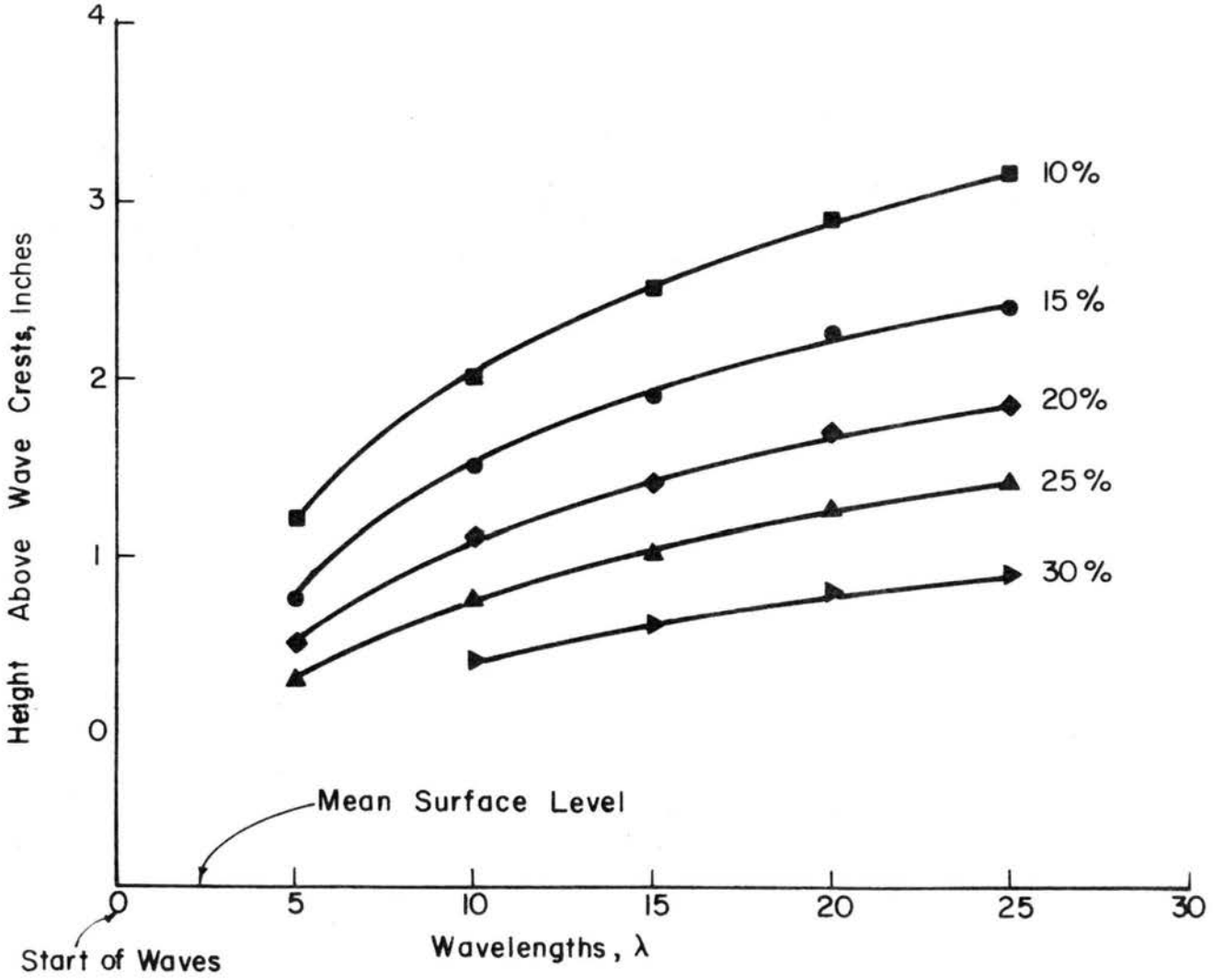

Fig. 94. Wind reduction factors (waves), wave A.

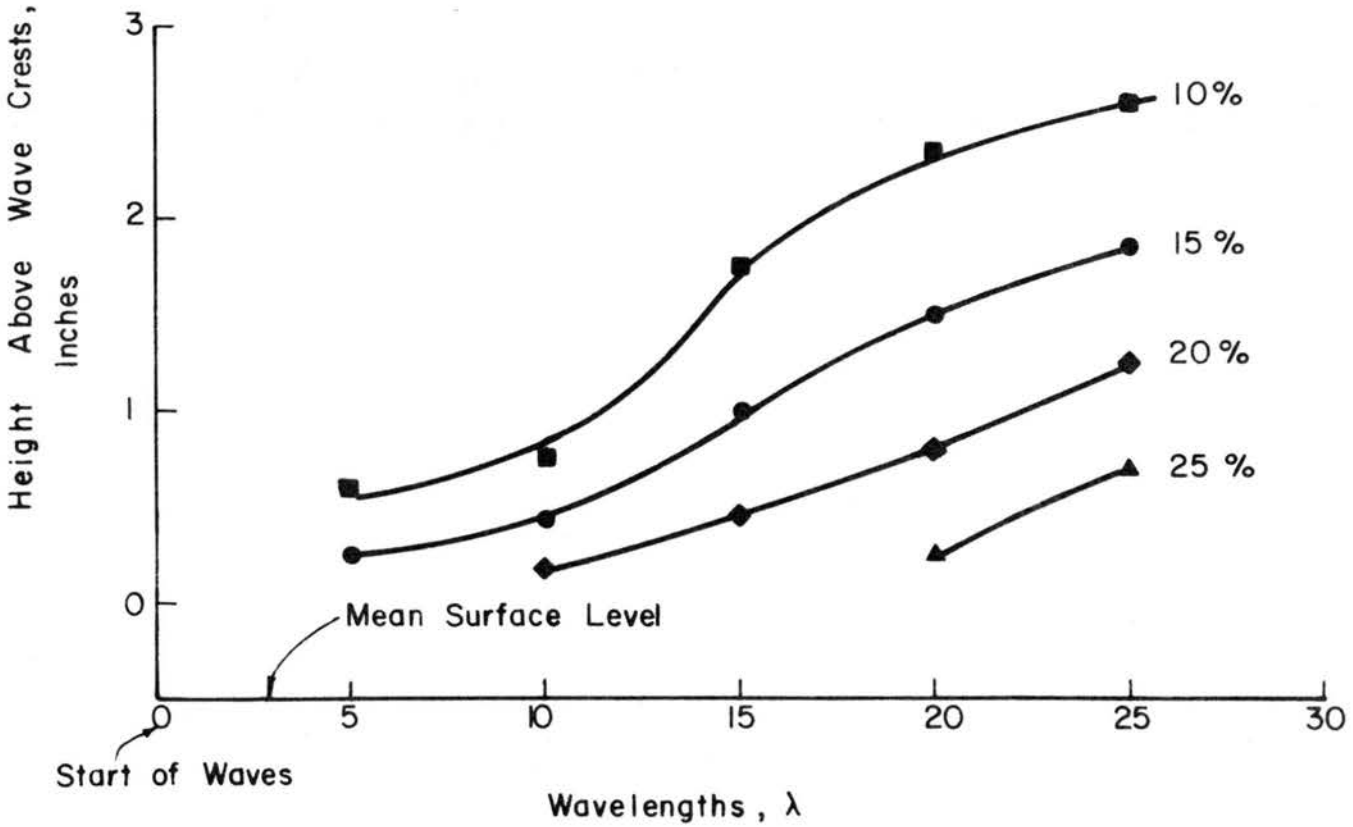

Fig. 95. Wind reduction factors (waves), wave B.

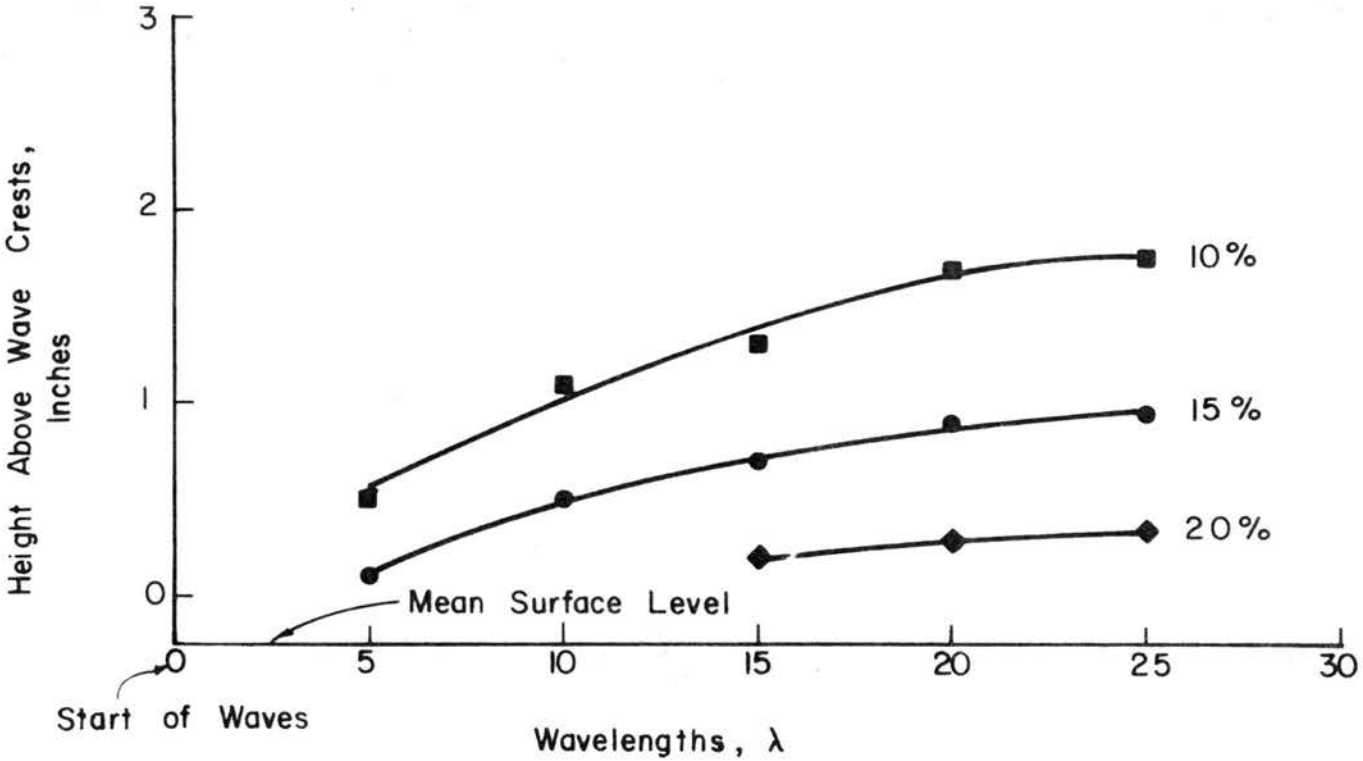

Fig. 96. Wind reduction factors (waves), wave C.

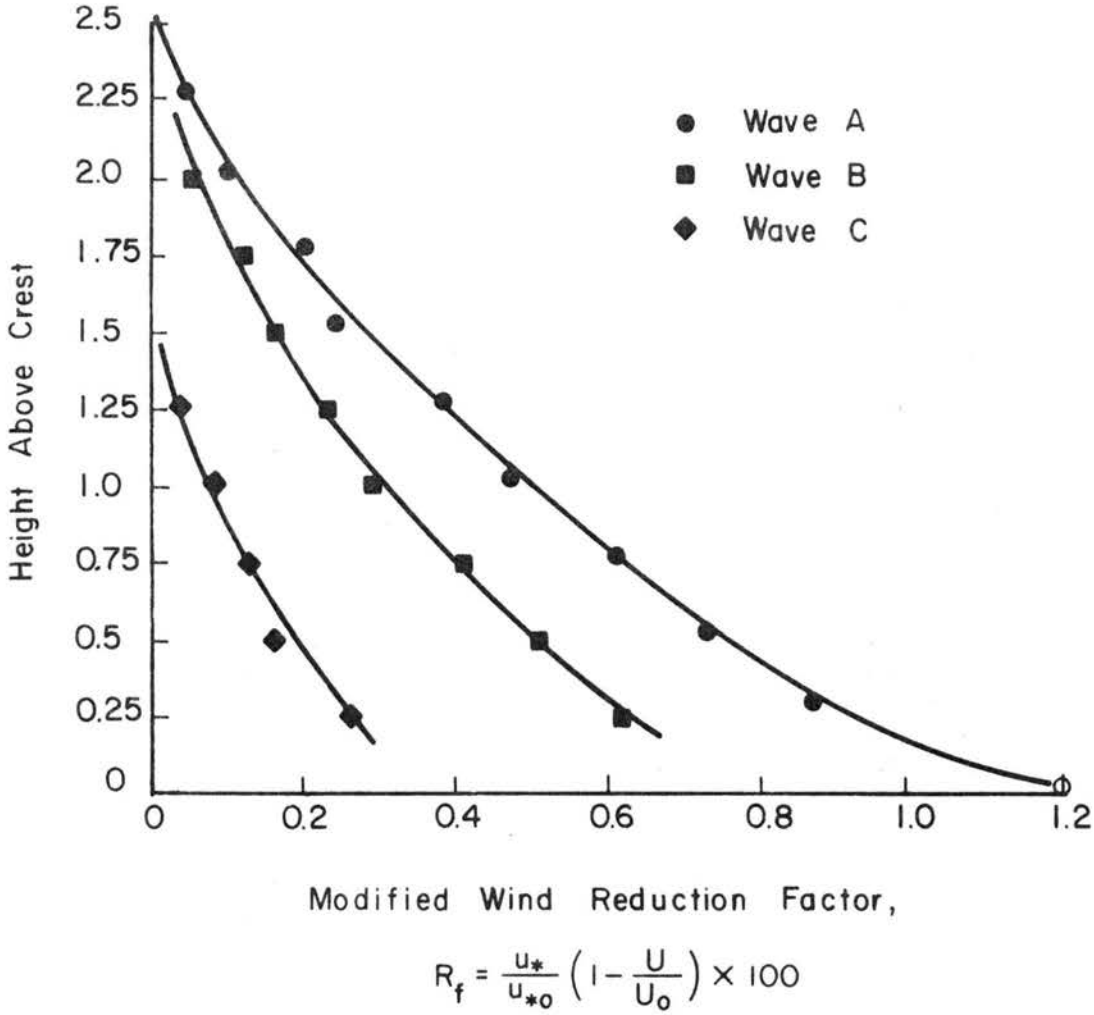

Fig. 97. Modified wind reduction factors (waves A, B, & C).